Simulations of the thermo-chemical evolution of the Earth's core with stable stratification.

Samuel Michael Greenwood

Submitted in accordance with the requirements for the degree of
Doctor of Philosophy

The University of Leeds
School of Earth and Environment

July 2020

The candidate confirms that the work submitted is his own and that appropriate credit has been given where reference has been made to the work of others.

Acknowledgements

First and foremost I thank my supervisors, Jon Mound and Chris Davies, for their patience, encouragement and support over the years. Both during this PhD and during my undergraduate years, you have always given me time to advise on, explain, and proofread the work I've brought you, even with my complete lack of respect for official office hours (sorry). I genuinely cannot think of how you could have managed a PhD student better, so no pressure for the future. I would like to thank the rest of the teaching staff in IGT for helping develop me towards the stage I am at today, including Phil Livermore with whom I completed my undergraduate dissertation and helped me grow my interest in geomagnetism.

I'd like to acknowledge the Deep Earth Research Group for many fruitful discussions and always providing an inclusive and encouraging platform. I also thank the other members of office 8.152 and IGT coffee/beers attendees for just as many fruitful discussions, both related to science and not. Thanks to my family for supporting me throughout life to reach this stage and for always asking about my work, even if you know you'll forget whatever over-complicated explanation I give you.

Finally, I'd like to thank Sarah, who I sit next to whilst writing this due to the work at home rules during this pandemic. You've made my time as a PhD student infinitely more enjoyable and worthwhile, supporting me at every turn.

The Advanced Research Computing team at Leeds have provided me with support and the computing facilities to produce my results. This work was funded by the NERC SPHERES Doctoral Training Programme.

Abstract

The Earth's magnetic field is generated inside the liquid outer core via a dynamo process, converting the kinetic energy of fluid motions into magnetic energy. Stratified fluid at the top of the outer core inhibits fluid motions however, there is a lack of consensus on the volume of stratified fluid and its thermal and chemical structure. In this study I consider different scenarios of the very long term evolution of the core that result in present day stable stratification.

I first construct a numerical model for a parameterised representation of the core, including a time dependent stratified layer beneath the Core-Mantle Boundary (CMB), which is evolved over the age of the Earth. This model, unlike previous models, has a general framework for both thermal and chemical stratification, allowing a range of scenarios to be tested. Successful models produce a layer compatible with seismic observations, 100-400 km thick, match the present inner core radius, and generate sufficient entropy to power the geodynamo for billions of years.

My model is applied to investigate thermally stratified layers resulting from a sub-adiabatic CMB heat flow using recent high thermal conductivity estimates. I find that viable models require a rapid decrease in Q_c, > 3 TW Gyr^{-1}, over the inner core age, which is required to be even larger if entrainment is not negligible. This rate is difficult to reconcile with coupled core and mantle evolution models.

When investigating a chemical layer resulting from a downward flux of oxygen from the mantle, very large fluxes inhibit the ability of the core to generate a dynamo for much of its history, providing upper bounds on the flux. The stratified layer is relatively insensitive to the thermal evolution of the core and so layers up to 150 km thick are consistently found for a range of parameters. Finally, I produce the first thermal history calculations of a chemical layer formed during core formation, demonstrating that a relatively thick chemical layer can persist until the present day, whilst always permitting a dynamo.

Brunt-Väisälä frequencies resulting from thermal stratification gives periods of 8-28 hours, from mass transfer with the mantle ∼30 minutes, and finally from a primordial layer 1.5-4 hours. Additional future constraints upon the Brunt-Väisälä frequency may

therefore allow distinction between the mechanisms.

Contents

List of Figures

Nomenclature

Acronyms

ADR	Adiabatic Ratio
CMB	Core Mantle Boundary
ICB	Inner Core Boundary
ICN	Inner Core Nucleation
LE	Light Elements
SV	Secular Variation

Mathematical Notation

$\mathrm{d}\mathbf{S}$	Area element of a surface
$\mathrm{d}V$	Volume element of a volume
Δ	Change
δ	Small change
$\frac{\mathrm{D}}{\mathrm{D}t}$	Advective time derivative
$\frac{\mathrm{d}}{\mathrm{d}t}$	Time derivative
$\frac{\partial}{\partial t}$	Partial derivative with respect to time
$\frac{\partial}{\partial x}$	Partial derivative with respect to x
$\int$	Integral
$\hat{\mathbf{n}}$	Unit vector normal to a surface
$\mathcal{O}(x)$	Order of magnitude of x
∇	Gradient
$\nabla\cdot$	Divergence
$\oint$	Surface integral

$\sum$ Summation

Symbols

α_c Chemical expansivity

α_T Thermal expansivity

α_{D} Barodiffusion coefficient

$\bar{c}$ Mole fraction of light element

$\boldsymbol{\tau'}$ Viscous stress tensor

E_α Entropy of mass diffusion

E_{H} Entropy of heat of reaction

E_{J} Entropy of ohmic dissipation

E_{k} Entropy of thermal conduction

E_{L} Entropy of latent heat

E_{P} Entropy of pressure heating

E_{r} Entropy of radiogenic heating

E_{s} Entropy of secular cooling

η Magnetic diffusivity

γ Grüneisen parameter

κ Thermal diffusivity

λ Linear correction to ideal solution

$\mathbf{i}$ Mass flux

$\mathbf{B}$ Magnetic field

$\mathbf{E}$ Electric field

μ Chemical potential

Φ_{s} Seismic parameter

ψ Gravitational potential

Q_{c} CMB heat flow

$\mathbf{q}$ Heat flux

Q_{g} Gravitational energy

Q_{H} Energy of heat of reaction

Q_{l} Energy of Latent heat

$Q_{\mathrm{r_s}}^{+}$ Heat flow into stable layer

Q_{P} Pressure heating

Q_{r} Radiogenic heat

$Q_{\mathrm{r_s}}^{-}$ Heat flow out of isentropic region

r_{c} Radius of the core

ρ Density

ρ_θ Potential density

r_{i} Inner core radius

r_{s} Stable layer interface

Δs_{Fe} Entropy of melting

σ Electrical conductivity

T_{a} Adiabatic temperature

τ Time scale

$T_{\mathrm{m,Fe}}$ Melting temperature

Θ Potential temperature

T_{m} Melting temperature of pure iron

$\mathbf{u}$ Slow contractional velocity

$\mathbf{v}$ Velocity

$\mathbf{v}'$ Velocity of convective fluctuations

c Mass fraction of light element

D Mass diffusivity

E Entrainment coefficient

e Internal energy

g Gravity

H Enthalpy

h Rate of internal heating

k	Thermal conductivity
L	Latent heat
M	Mass
N	Brunt-Väisälä frequency
P	Pressure
r	Radius
R_{H}	Heat of reaction
s	Entropy
T	Temperature
t	Time

Units and Prefixes

eV	Electron volt
G	Giga, 1×10^9
J	Joule
K	Degrees Kelvin
kg	Kilogram
M	Mega, 1×10^6
m	Meter
mol	Moles
Pa	Pascal
s	Seconds
T	Terra, 1×10^{12}
W	Watts
wt%	Weight percent
yr	Calendar year

Chapter 1

Introduction

1.1 Overview

This thesis concerns the structure and evolution of the Earth's core, specifically in the long term evolution of stable stratification at the top of the core. The Earth's magnetic field is generated by convection in the core and is therefore dependent upon the dynamics, composition and thermal structure of the core. Observational data proposes stable stratification at the top of the core, which has implications for the interpretation of the magnetic field, core-mantle interactions and the long term evolution of the core. This chapter provides the background knowledge for the theme of this thesis and sets out the aims and objectives.

1.2 The Geomagnetic Field

The magnetic field of the Earth permeates throughout the entire planet and stretches far out into space. Our magnetic field shields us from the charged particles of the solar wind and has provided humans with a navigation tool that has been utilised for centuries. The magnetic field of the Earth is the total field arising from a number of sources, such as electrical currents in the magnetosphere or permanent magnetisation within crustal rocks. The main contribution to the total field is the geomagnetic field, which is actively generated within the Earth. Figure 1.1 shows a map of the radial component of the geomagnetic field and the inclination at the Earth's surface based on the 2015 IGRF model (Thébault et al., 2015). For a pure dipole field aligned with the rotation axis of the Earth, the magnetic equator (inclination = 0°) and the magnetic poles (inclination ± 90°) would match perfectly with the geographic equator and poles, a state the Earth's field is close to but not exact. Some significant deviations from a dipole can be seen in the high latitude lobes of field and the more anomalous field in the South Atlantic (Fig. 1.1).

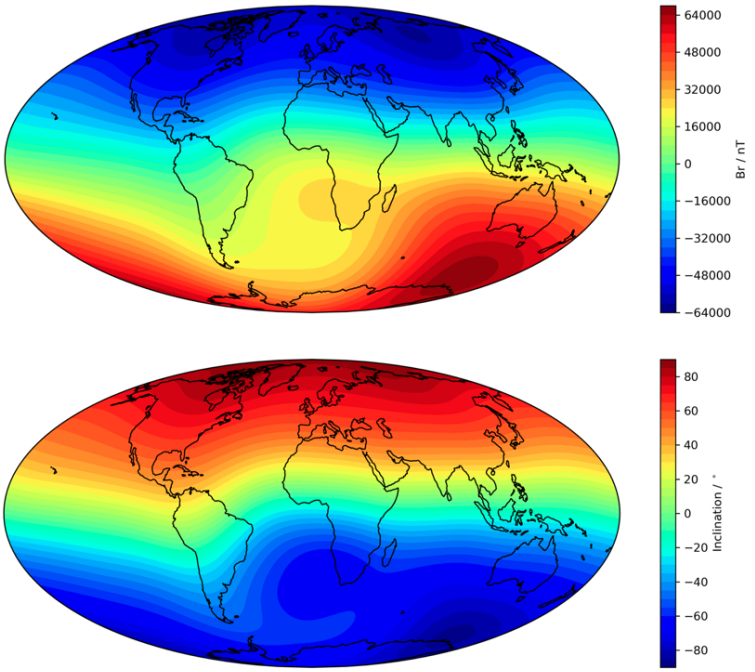

Figure 1.1: Radial component of the magnetic field (top) and magnetic inclination (bottom) of the 2015 IGRF model (Thébault et al., 2015) at the Earth's surface.

Measurements of the magnetic field began for the purpose of navigation and were widespread enough that ship's logs dating back to the 16th century have been utilised for construction of global field models (Jackson et al., 2000). Magnetic observatories at fixed locations have provided more accurate continuous records since the 18th century, with the downside of generally poor global coverage due to the uneven distribution of land mass (and scientific funding!). The highest resolution data have come from satellites which are able to collect precise measurements with an even coverage. The first mission providing continuous satellite data, the Ørsted satellite, was launched in 1999 enabling, with subsequent missions, accurate spatial and temporal reconstructions of the geomagnetic field (e.g. the IGRF (Thébault et al., 2015)).

The geomagnetic field varies on a wide range of timescales. Examples of shorter time scales captured by human observations are geomagnetic storms due to solar activity lasting hours (Lui, 1996) and Secular Variation (SV) associated with internal dynamics within the core over the last 400 years (Jackson and Finlay, 2015). Variation on timescales longer than this must be inferred indirectly from archeomagnetic and paleomagnetic data. Rocks containing magnetic minerals may attain a remnant magnetisation from the geomagnetic field at the time that they are formed (Tauxe, 2010) and provided they are able to retain that magnetisation unperturbed, they may provide a representative record of the geomagnetic field in the distant past.

The availability of rocks suitable for obtaining paleomagnetic data decreases rapidly

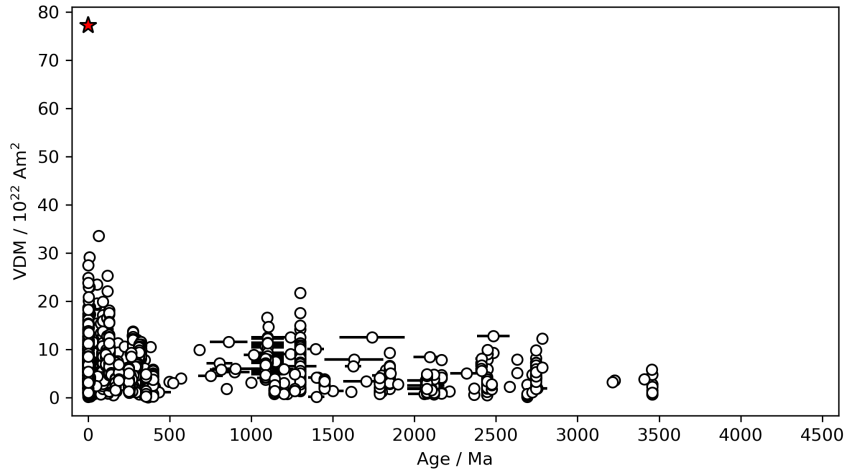

Figure 1.2: Virtual Dipole Moment (VDM) from the PINT database for paleomagnetic data (Biggin et al., 2009) shown by white circles with available age uncertainties. The present day value according to the 2015 IGRF model (Thébault et al., 2015) is shown as the red star.

with age (Biggin et al., 2009) since older rocks are less common due to the constant recycling of material on Earth from plate tectonics. The more recent Holocene field can be represented by time dependent global models (Korte et al., 2011) able to represent spatial variations in the field to a similar degree as the present day geomagnetic field (albeit with much reduced accuracy). A recent time dependent regularised model (Panovska et al., 2019) has extended a global model of the field back 100 thousand years but this is the current limit for a continuous global representation for the magnetic field until the present. Going back further, directional data associated with the remnant magnetisation becomes harder to obtain due to fewer data and larger uncertainties in necessary corrections to be applied based on the tectonic history of the outcrop (Tauxe, 2010). Studies therefore typically focus upon the paleointensity data, the magnitude of the remnant magnetisation vector. Figure 1.2 shows paleointensity data over the age of the Earth, 4.5 Gyrs, taken from the PINT database (Biggin et al., 2009). Although scatter in the data exists, they allow a key observation to be made: the geomagnetic field appears to have persisted for at least the last 3.5 Gyrs. The possibility of a magnetic field prior to 3.5 Ga is debated (Tarduno et al., 2015; Borlina et al., 2020) since only limited individual crystals from Australian sedimentary rocks have so far been identified to examine this period in time (Fu et al., 2017; Valley et al., 2014).

Carl Friedrich Gauss established the source for the magnetic field was internal to the Earth before Larmor (1919) reasoned it was constantly generated by fluid motions. The leading theory is that the kinetic energy of convection is converted to magnetic energy producing the geomagnetic field, a process termed the geodynamo (Jones, 2015), driven by cooling of the core and freezing of the inner core (discussed more in section

1.4). A dynamo is not unique to Earth and an equivalent process is often invoked to explain the large scale magnetic fields for other planets such as Mercury, Jupiter and Saturn (Wicht and Tilgner, 2010) and the Sun (Charbonneau, 2014). It is worth noting that other origins for driving the fluid flow generating the magnetic field aside from convection have been proposed, such as precessional and tidal forces (Tilgner, 2005; Tilgner, 2007). It is not yet established if these origins are consistent with the observed spatial and temporal variations in the magnetic field at the surface (Jones, 2015) and so theses effects are not included in this thesis.

To investigate the geomagnetic field further requires understanding of the structure and nature of convection in the core, as well as the lower mantle where heat is extracted, cooling the core.

1.3 Earth's internal structure

The majority of our knowledge on the interior of Earth comes from global seismology, which takes advantage of large earthquakes sending seismic waves deep into the Earth before returning to the surface where they are observed. The Preliminary Reference Earth Model (PREM) (Dziewonski and Anderson, 1981) constructs a mathematical parameterisation of radially varying parameters, e.g. P/S wave velocities and density, and inverts for the model that best matches normal mode frequencies, body wave travel times, the mass of the Earth and the Earth's moment of inertia. The resulting model represents the average 1D structure of the Earth as a function of radius, highlighting the main regions: the solid inner core, liquid outer core and solid mantle (Fig. 1.3). Density jumps at the Core Mantle Boundary (CMB) and the Inner Core Boundary (ICB) indicate the sharp transition from silicate minerals in the mantle to liquid iron in the outer core, and the transition from liquid to solid iron alloy in the inner core. The outer core is known to be liquid given its inability to support shear waves producing the S-wave 'shadow zone' from observed teleseismic events (Oldham, 1906).

The Adams-Williamson equation predicts the increase in density with depth for a chemically uniform material under self compression in a hydrostatic pressure gradient, with the Bullen parameter measuring the ratio of the observed density gradient with this theoretical density gradient (Bullen, 1963). Throughout the lower mantle, the Bullen parameter is between 0.97-1.01, although may locally deviate significantly (Matyska and Yuen, 2002), and throughout the core is within 1% of 1 (Dziewonski and Anderson, 1981). The 1D structure in the core and lower mantle are therefore reasonably well represented by a well mixed state although this is only true for the large scale horizontally averaged 1D state in PREM.

Deviations from PREM provides key information about dynamic processes in the interior. Some of the most obvious exceptions to the well mixed state in the mantle

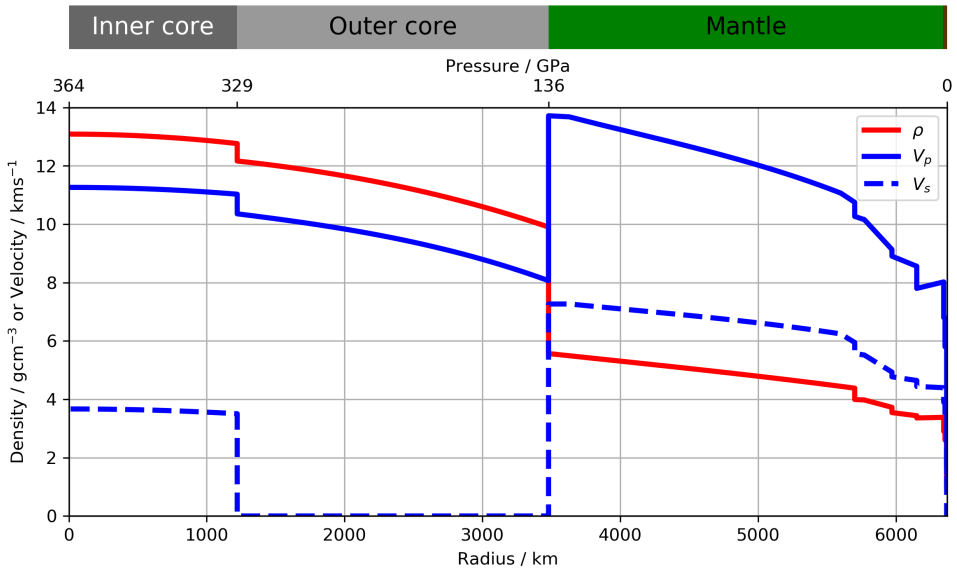

Figure 1.3: Densities (red), P-wave velocities (V_p, blue) and S-wave velocities (V_s, blue dashed) in PREM (Dziewonski and Anderson, 1981). The y-axis is in units of g cm^{-3} for density or km s^{-1} for seismic velocity.

manifest as the Large Low Shear Velocity Provinces (LLSVP's) (Koelemeijer et al., 2016) and small Ultra Low Velocity Zones (ULVZ's) (Rost et al., 2006) observed seismically, potentially representing reservoirs of chemically distinct material. In the core, regions at both the top and bottom of the outer core have been identified to deviate from PREM (Lay and Young, 1990; Souriau and Poupinet, 1991) in their seismic velocity, inferred as layering within the fluid. These layers raise interesting questions since there must be a stable density stratification sufficiently resisting mixing with the bulk of core allowing them to persist.

The upper layer in the core, beneath the CMB, will be a focus in this thesis and a full discussion will be given in sections 1.6 and 1.7, however first the more general chemical and thermal structure of the core is reviewed.

1.4 Core composition

The composition of the Earth can be inferred via two key lines of evidence. Firstly, understanding of solar system formation and planetary accretion suggests that both chondritic meteorites, the most common type to impact Earth, and the Earth itself share a similar source and should match in their relative chemical abundance (McDonough and Sun, 1995). Secondly, any model of the composition of the Earth must predict seismic velocities and densities that match those observed.

The Earth underwent planetary differentiation in the first 1-100 Myrs (Walter and

Trønnes, 2004) after its formation, when heavy iron and nickel sank to form the Earth's core, separating the planet into the silicate mantle and metallic core. The Ni content of the Earth's core is assumed to be the same as observed in chondritic meteorites at an atomic ratio of Fe/Ni $\approx$ 17 (McDonough and Sun, 1995). When the proportion of Ni is small, FeNi alloys have minor differences from pure Fe in their seismic wave speeds and properties at inner core conditions (Martorell et al., 2013) and in oxygen or sulphur bearing iron alloys, nickel behaves equivalently to iron (Helffrich and Kaneshima, 2010). Therefore for simplicity, proposed outer core compositions often forego including nickel.

The observed density of the outer core is lower than for a pure Fe-Ni alloy and so other, lighter, elements must be present (Birch, 1952). Typically this core density deficit is taken to be in the range of 5-10% (Birch, 1952; Hirst and Carter, 2002; Shanker et al., 2004; Hirose et al., 2013, and references therein.), limiting the amount of light element that could be present in the core. Therefore, elements other than iron and nickel must have sufficient abundances in accreted material, partition into iron at the relevant temperatures and pressures in the early Earth, remain soluble throughout the homogeneous bulk of the outer core, and predict observed seismic and density models of the core (Poirier, 1994). Based on these constraints, the core is thought to contain significant amounts of one or more of O, Si, S, C or H (Poirier, 1994; Hirose et al., 2013).

There is great difficulty in achieving the extreme core temperatures ($T > 3500$ K) and pressures ($P > 136$ GPa) experimentally. Shock experiments may reach very high pressures and so have been used to investigate the inner core and its melting but can require large temperature extrapolations from the Hugoniot (the experiment temperature) to the relevant P/T conditions in the core (Boehler, 2000). Laser heated Diamond Anvil Cells (LDAC) allow for tighter control on both temperature and pressure although require costly sophisticated equipment and have only recently managed to reach the P/T conditions of the inner core (Tateno et al., 2010). Without laser heating, DAC experiments are more accessible but do not represent the relevant high temperatures. This difficulty in achieving simultaneously high pressures and temperature means the majority of the data acquired by experiments are limited in number and usually require extrapolation to the relevant conditions.

In combination to these experiments, studies also employ *ab initio* simulations to more easily probe the extreme conditions, since they allow arbitrary pressures and temperatures by directly modelling the inter-atomic interactions of a substance. The simulations are however very computationally expensive restricting parameter searches over pressure, temperature and composition, and so are still used sparingly. More complicated alloys with more light elements makes the simulations even more expensive therefore fewer numbers of light elements are preferred (Alfè et al., 2007).

Carbon and hydrogen are highly volatile and so are difficult to incorporate into the core in a large amount (Morard et al., 2014). Inclusion of hydrogen may better explain seismic velocities at a low core temperature (Umemoto and Hirose, 2020), although the feasibility of the amount of H required for this are still debated (Li et al., 2020). Therefore the main focus on for suitable models of the composition consider O, S, and Si. Sulphur and silicon behave in a similar manner with respect to the density of the alloy (Alfè et al., 2002b) however the depletion of Si in the mantle, coupled with the volatility of S, could suggest significant quantities of Si over S in the core (Allègre et al., 2001). The solubility of oxygen in liquid iron increases rapidly with pressure above 40 GPa (Hirose et al., 2013) and has been found necessary to provide the best fits to PREM data (Badro et al., 2014). Candidates for the core, therefore, often consider Fe-O, Fe-S/Si binary mixtures, yet proposed compositions can significantly vary due to the temperature used in the study, along with the non-unique solution of fitting velocity and density data (see Hirose et al. (2013) for an extensive list of proposed compositions).

The density jump at the ICB can be determined by different methods. PREM inverts for the density jump, trading off with all other parameters inverted against the various constraints in the model, giving the density jump as $\Delta\rho = 600$ kgm^{-3}, whilst Shearer and Masters (1990) suggest a value of 1000 kgm^{-3} based on the amplitude of the PKiKP (the seismic phase that reflects off the ICB). More recently, Masters and Gubbins (2003) argue that normal modes more accurately determine $\Delta\rho$ rather than the rarely seen and weak PKiKP phases, and propose a value of 820 ± 180 kgm^{-3}.

Due to the phase change from solid to liquid alone, $\Delta\rho$ is predicted to be $\sim$220 kg m^{-3} (Hirose et al., 2013), which is not enough to explain the total $\Delta\rho$ observed. Therefore the compositions of the inner and outer cores must differ with a relative enrichment of light elements in the outer core, meaning the density jump provides a useful constraint on core composition models, if the partitioning behaviour of light elements can be estimated. *Ab initio* calculations of the partitioning of O/S/Si between solid and liquid iron show that oxygen is strongly rejected by the solid, whereas S/Si only weakly partition into the liquid (Alfè et al., 2007). As the inner core grows, the liquid at the ICB is enriched with these rejected light elements, mostly oxygen creating compositionally buoyant fluid which helps drive convection and hence the geodynamo (Braginsky, 1964; Gubbins, 1977; Buffett et al., 1996a). This source of power will later be shown to be important for the long term evolution of the core.

In this thesis I will consider the proposed core compositions given by Alfè et al. (2002b) and Alfè et al. (2007) for the range of $\Delta\rho$= 600, 800, 1000 kgm^{-3} given in the table 1.1 for core compositions with O and Si in terms of their mole fraction in the liquid alloy, $\bar{c}$. O/Si are chosen because sulphur behaves similarly to silicon and so can replace Si with little change (Alfè et al., 2002b; Alfè et al., 2007). A higher $\Delta\rho$

correlates to a larger difference in light element between the inner and outer cores and so oxygen must account for a larger proportion of the total light element progressively replacing Si, given the strong rejection of oxygen from the solid. The benefit of using their data is that the same group have published self consistent data for core properties (Davies et al., 2015) and the melting temperature of iron (Alfè et al., 2002c) evaluated at relevent T/P conditions (discussed in the next section).

Table 1.1: Core compositions for 3 different ICB density jump, $\Delta\rho$, used in this thesis.

Symbol	Meaning	Element	$\Delta\rho$=600	$\Delta\rho$=800	$\Delta\rho$=1000 kgm^{-3}
$\bar{c}_x$	Mole fraction of light element 'x'	O	0.08	0.13	0.17
		Si	0.10	0.08	0.02

In summary, in this thesis, the core is taken to be iron alloyed to oxygen and silicon. The outer core is enriched in O/Si relative to the inner core by an amount dictated by the partitioning behaviour of O/Si and the density jump at the ICB (800 ± 200 kgm^{-3}). Silicon partitions almost evenly between solid and liquid whilst nearly all oxygen is rejected by the solid. The chemistry associated with stable layers based on observations will be discussed in section 1.6 but first it is also important to consider the thermal structure of the core.

1.5 Temperature of the core

The Rayleigh number, a measure of the vigour of convection, is larger than the critical value estimated to be necessary to initiate convective motions by a factor of $\sim 10^3 - 10^6$ (Gubbins, 2001) and the Reynolds number is also very high at round 10^8 (*Encyclopedia of Geomagnetism and Paleomagnetism* 2007, pg 101.) indicating the fluid vigorously convecting and highly turbulent. This dynamical regime strongly mixes the fluid and reduces the density anomalies associated with convective fluctuations. The anomalies required to provide the heat extracted from the core at the CMB, of $\mathcal{O}(1-10)$ TW, are estimated to be very small at around 10^{-7} % of the density of the fluid (Stevenson, 1987; Jones, 2015). These small density perturbations only correspond to either a 0.1 mK temperature anomaly or a 10^{-7} wt% light element anomaly (taking appropriate thermal and chemical expansivities of 10^{-5} K^{-1} and 1, respectively). The thermal anomalies associated with convection are therefore very small compared to the total temperature which is > 3500 K.

Fluid at greater depths experiences greater compression which leads to adiabatic heating. Assuming that fluid motions are quick relative to thermal and mass diffusion timescales then no heat or mass is exchanged with a fluid parcels surroundings (adiabatic process) when advected in a pressure field. With the change in pressure, there

is a change in volume and work is done on the parcel by its surroundings. A decrease in the volume of the parcel results in an increase in the temperature and the opposite is true for when the pressure on the parcel is reduced. This leads to a temperature gradient described by the thermodynamic relation (Stacey, 2010)

$$\left(\frac{\partial \ln T}{\partial \ln \rho}\right)_s = \gamma, \tag{1.1}$$

where γ is the Grüneisen parameter, approximately a constant value of 1.5 throughout the core (Alfè et al., 2002a; Gubbins et al., 2003), and the subscript s is entropy indicating that this is valid during an isentropic process. An isentropic process is a process that is both adiabatic and reversible, which the pressure work on fluid parcels during adiabatic compression is. The Adams-Williamson equation, which assumes a homogeneous body with adiabatic compression under a hydrostatic pressure gradient, gives a density gradient of

$$\frac{\mathrm{d}\rho}{\mathrm{d}r} = -\frac{\rho g(r)}{\Phi_\mathrm{s}(r)}, \tag{1.2}$$

where $g(r)$ and $\Phi_\mathrm{s}(r)$ are gravity (determined from a density model of the core) and the seismic parameter (calculated from waves speeds in the core), which when combined with 1.1 gives the adiabatic temperature, T_a

$$T_\mathrm{a}(r) = T_\mathrm{c} \exp\left(-\int_{r_\mathrm{c}}^{r} \frac{g(r)\gamma}{\Phi_\mathrm{s}(r)} \mathrm{d}r\right), \tag{1.3}$$

where the constant of integration has been used to define T_a relative to $T_\mathrm{a}(r_\mathrm{c}) = T_\mathrm{c}$, the temperature at the CMB (radius r_c). This temperature profile is neutrally stable, any fluid that is adiabatically displaced vertically maintains thermal equilirium with the ambient fluid, therefore the core cannot precisely have this adiabatic temperature everywhere (Stacey, 2010). It is the deviations away from the adiabat that drive convection however core convection is constantly acting to mix the thermal profile back towards the adiabat, however as mentioned these deviations are small.

In the thermal boundary layers at the ICB and CMB the fluid cannot vigorously convect assuming no fluid penetrates the surfaces, however these layers are only predicted to be ~ 40 cm (Jones, 2015). Therefore, for a given melting temperature at the ICB the temperature profile in the core can be assumed to be an extrapolation along the adiabat up to the CMB.

The melting temperature of pure iron at ICB pressures is still debated, with estimates spanning over 1000 K. *Ab initio* calculations have suggested either 6350 K (Alfè, 2009) or 5400 K (Laio, 2000), LDAC data has yielded 5500-6200 K (Anzellini et al., 2013; Sinmyo et al., 2019), low pressure experiments give 4900 K (Boehler, 1993),

dislocation theory predicts 6200 K (Poirier and Shankland, 1993), and finally shock experiments suggest >5700 K (Nguyen and Holmes, 2004; Tateno et al., 2010). In general more recent work has supported higher melting temperatures (although see Sinmyo et al., 2019) and so I will be using values of core properties derived from these larger estimates (Davies et al., 2015).

These estimates are for pure iron, whereas the presence of light elements depresses the melting temperature by several hundred degrees (Hirose et al., 2013). For the compositions I will be using, the light elements in the core reduce the melting temperature by ∼700 K (Alfè et al., 2002b) to finally give the temperature at the ICB of around 5500 K at present.

1.6 Observations of stratification in the core

As mentioned previously, although the bulk of the core is assumed adiabatically stratified, both the base and the top of the liquid appear to deviate from this trend in seismic studies focusing upon these regions.

The focus of this thesis is on the upper side of the outer core at the CMB, where seismic studies have looked to constrain the seismic velocity. These studies have primarily considered SmKS waves, waves that have m number of legs in the outer core reflecting m-1 times on the underside of the CMB (Fig. 1.4). For an increasing m, the waves sample progressively shallower depths of the core allowing a radial velocity model to be constructed.

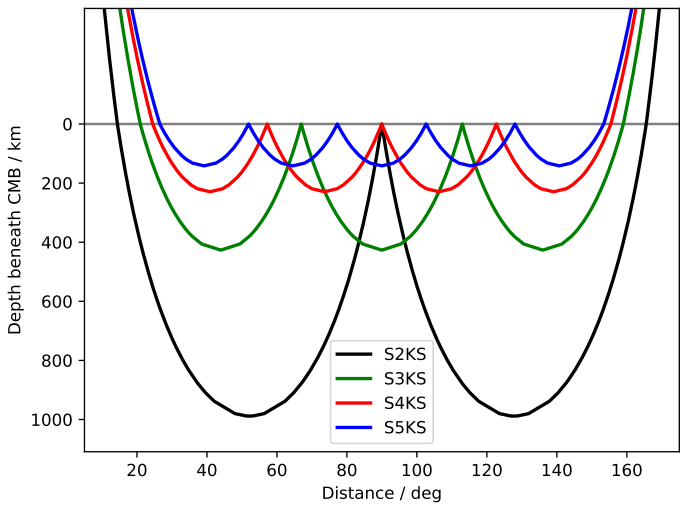

Figure 1.4: Calculated ray paths for SmKS waves using PREM for a source-receiver distance of 180°.

The velocity profile in PREM closely matches that predicted by a body with a con-

stant composition at the top of the core (Helffrich and Kaneshima, 2010) and so significant deviations from PREM are interpreted as a deviation from a homogeneous adiabatically stratified body. Using SmKS waves many authors, although not all (Alexandrakis and Eaton, 2010), find a velocity model deviating from PREM by a reduction in seismic velocity by 1-2% beneath the CMB to varying depths in the core. Lay and Young (1990) and Garnero et al. (1993) find relatively thin regions of 50-100 km, Tanaka (2007) proposes 150 km, whilst the work by Helffrich and Kaneshima (2010), Helffrich and Kaneshima (2013), Kaneshima and Helffrich (2013), and Kaneshima (2018) favour thicker layers 300-400 km in size (Fig. 1.5).

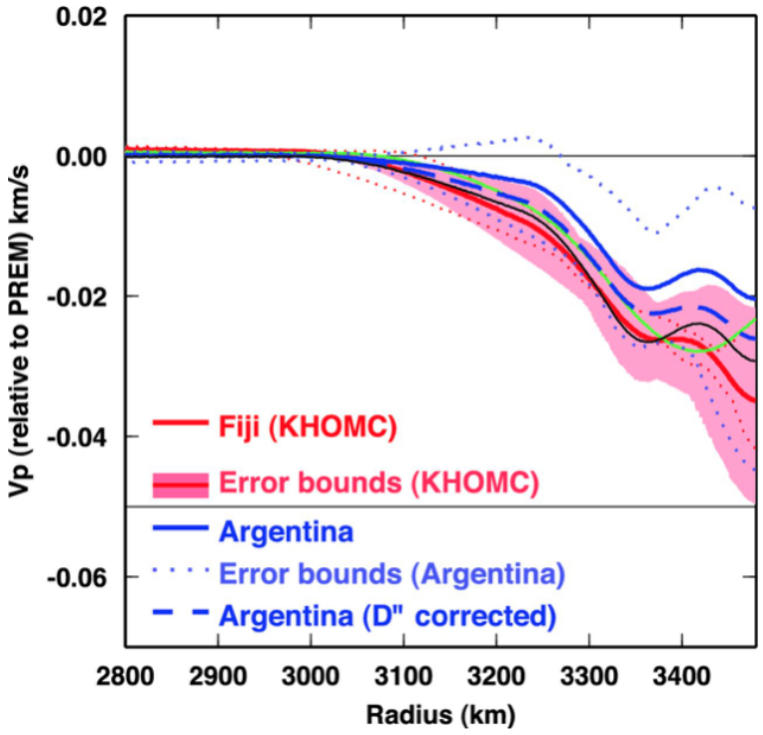

Figure 1.5: Figure taken from Kaneshima and Helffrich (2013) showing their velocity model KHOMC predicts a velocity drop relative to PREM

A recent paper by Irving et al. (2018) uses normal mode data to calculate the equation of state (EoS) for the core, which predicts a different velocity structure for a homogeneous body that need not include a layer. This model however just inverted for the core density, which resulted in a higher density than PREM, however they also assumed PREM densities in the mantle. PREM is constrained to the mass of the Earth and so increasing the density just in the core results in a model no longer consistent with this constraint

In order for a layer at the top of the core to not be mixed away, the density must be relatively low and so the velocity low must be primarily due to a drop in the bulk modulus, K, of the fluid since $V_\mathrm{p} = \sqrt{K/\rho}$. The stratification could be due to a positive

thermal anomaly, a positive light element anomaly, or some positive/negative combination of the two as long as the fluid is overall sufficiently lighter than the underlying convecting fluid. Increases in temperature have a relatively weak reduction on seismic wave speed (Helffrich and Kaneshima, 2010) and Komabayashi (2014) showed additional oxygen in the layer may decrease V_p. Helffrich and Kaneshima (2010) calculate best fitting oxygen and sulphur enrichment to a model of a Fe-O-S liquid finding an enrichment of O and S by 3.7 and 1.9 wt%, respectively, fit their SmKS data best.

More recently however, Brodholt and Badro (2017) suggest that an increase in any one light element will always increase V_p. They consider a range of pairs of light elements (O, S, Si, C) finding a requirement that at least one light element must be relatively depleted to ensure an overall reduction in seismic velocity. They limit themselves to just 2 light elements, finding a wide range of combinations of enrichment/depletion that produce both a velocity and density drop, for example an increase (decrease) in oxygen (silicon) by 15 (9) mol%, around 5 wt% for both producing a 1% velocity drop. These anomalies differ by around a factor of 2 from Helffrich and Kaneshima (2010), demonstrating that the solution to explaining the velocity anomaly is not trivial due to the non-unique solution coupled with different method yielding significantly different results.

Aside from seismic studies, there are limited ways in which the layer may be observationally constrained. As the core generates the magnetic field, the presence of the layer may have a signature in the observed magnetic field which must be generated within or pass through the layer. In the stable layer, vertical motions are inhibited producing reduced or no veritcal motion of fluid. Whaler (1980) neglects diffusion from the magnetic induction equation, showing that in a toroidal flow (no vertical fluid motion) the radial magnetic field at local extrema must be time invariant. Selecting relevant points in the observed geomagnetic SV Whaler (1980) argues the field is statistically consistent with a toroidal flow field. Subsequently Whaler (1986) reexamines the issue, finding velocity fields that include radial motions (poloidal and toroidal flow) at the CMB provide an acceptable fit the observed SV and that toroidal flows do not.

More recently Amit (2014) and Lesur et al. (2015) also find that allowing poloidal flow increases the fit to SV, however both note that observations are not necessarily inconsistent with a very limited amount of radial motion, as could be the case with stable stratification. These studies have all assumed the frozen flux hypothesis where magnetic diffusion is assumed negligible on the spatial and temporal timescales of interest for SV (Roberts and Scott, 1965). Magnetic diffusion however is not necessarily negligible and potentially could explain much of the observed SV (Metman et al., 2019). In fact, areas of radial magnetic field on the CMB that have a reversed sign to the dipole state (reversed flux patches) are thought to be diffusive features but one that requires upwelling in the vicinity of the CMB (Bloxham, 1986). Gubbins (2007) suggests that

any stratification should be 100 km or less to allow radial flow sufficiently close to the CMB in order to produce observed reversed flux patches. Alternatively, Gubbins (2007) note that shear flows within a layer containing strong gradients in a poloidal field exist could produce observations of the reversed flux patches but either mechanism requires further dynamical study (Gubbins, 2007). At present stable stratification cannot be conclusively confirmed or ruled out by observations of SV.

Aside from investigating global SV, periodic variations may be present resulting from waves excited in a stable layer. MAC waves operate on a force balance between magnetic, buoyancy and Coriolis forces and so are sensitive to the size of the layer and the strength of the density stratification. Buffett et al. (2016) fit a model of the azimuthal flow field derived from geomagnetic observations to predict the dipole and length of day variations (minus their linear trend) to a reasonable degree with MAC waves. The best fitting model, a linear combination of MAC waves, required a 140 km thick layer with a Brunt-Väisälä frequency, N, yielding a period around 1 day. N is the frequency at which gravity waves will oscillate and is a common measure of the strength of stratification, dependent upon the stabilising density gradient and given by

$$N = \sqrt{-\frac{g}{\rho}\frac{\mathrm{d}\rho'}{\mathrm{d}r}}, \tag{1.4}$$

where ρ' is the density anomaly within the layer. MAC waves are also sensitive to the magnetic field in the core and these stratification parameters do trade off with magnetic field strength and electrical conductivity. Hardy et al. (2020) have recently proposed very high values for magnetic field within a stratified layer of 8 mT, compared to 0.86 mT assumed in Buffett et al. (2016), which would require thicker stratification to retain MAC waves that fit the observations (Buffett et al., 2016).

The observations are so far inconclusive of the nature of stratification beneath the CMB. Seismic observations tend to favour stratification on the order of 100-300 km in size caused by an excess of light element at the top of the core, although fitting compositional profiles to reproduce modelled velocities is non-unique. Expected buoyancy frequencies from the excess light element are quite large, 10-50 times larger than is predicted by considering geomagnetic observations (Helffrich and Kaneshima, 2013; Buffett et al., 2016). Geomagnetic considerations are therefore more consistent with a thermal origin for the layer since temperature has a much weaker impact on the density giving larger frequencies (Lister and Buffett, 1998) and predicts a layer size at the lower end of the range of thicknesses inferred by seismology.

1.7 Origins of the layer

The range of proposals for the potential mechanisms generating the layer have been proposed. As the fluid in the stable layer remains distinct from the convecting fluid below, and assuming negligible vertical mixing within the layer itself, the radial thermal and compositional fields evolve slowly by diffusion on the millions to billions of years timescale. This timescale is much longer than currently attainable by 3D dynamical simulations ($> 10^5$ yrs) and so parameterised thermal history models are needed instead to investigate this long term evolution of the core.

Thermal history models are thermodynamic models that reduce the core to a 1D time averaged state on a timescale that is long relative to the convective motions but short relative to its very slow cooling (Gubbins et al., 1979; Buffett et al., 1996b; Labrosse et al., 1997; Gubbins et al., 2003; Nimmo, 2015). Heat flow at the CMB is balanced against energy sources within the core and hence evolve the cooling rate, evolving the 1D thermal and chemical structure of the core over the age of the Earth. Typically the entire core is assumed to be convecting which is not the case with stable stratification, and so the more traditional formulations for the thermal history must be adapted in order to investigate the origin and long term evolution of the layer.

Aside from representing the long term evolution of the core, a key use of thermal history models is to estimate the energy sources powering generation of magnetic field by calculating the ohmic dissipation in the core over time. If the ohmic dissipation is greater than some minimum requirement, then the generation of magnetic field is thermodynamically viable (Nimmo, 2015). Since we have strong observational evidence for an internally generated magnetic field for the last 3.5 Gyrs, the requirement that the ohmic dissipation be greater than the lower bound during this time provides a key constraint on the thermal history.

The standard model for the thermal evolution is that at present the inner core is growing, releasing both latent heat and gravitational energy from uneven partitioning of light elements between solid and liquid (Nimmo, 2015). The light element release liberates gravitational energy which is thermodynamically efficient and so significantly contributes towards powering the dynamo (Gubbins et al., 2004). Prior to the inner core, convection is purely thermally driven by the secular cooling of the core and so the core must have cooled rapidly enough to provide sufficient power to the dynamo (Davies, 2014). The entire fluid outer core is assumed to be convecting which would not be the case if stable stratification is present. Models that include stratification therefore need to alter the standard model to compute the evolution of the core. Thermal history models are discussed in detail in chapter 2.

Proposed origins for the layer fall into two catagories, a chemically stratified layer or a thermally stratified layer, discussed in the following two sections. Results from

cited studies are summarised in table 1.2

1.7.1 Chemical Stratification

Chemical stratification requires a mechanism to enrich the upper region of the core with light element. The partitioning of oxygen, or potentially other light elements, into the liquid as the inner core grows produces chemically light plumes from the ICB that may pool beneath the CMB (Moffatt and Loper, 1994) over the age of the inner core due to the low mass diffusivity restricting the equalisation of the chemical anomaly with the ambient fluid. Bouffard et al. (2019) performed 3D dynamical simulations to show that, in the limit of zero chemical diffusion, this effect could begin to form a layer. However, the simulations cannot be carried out over a long enough time scale to show this effect persists over the lifetime of the inner core, and hence how large the layer would have grown to by the present day. Furthermore the layer only becomes enriched in light element and so, barring an additional effect that could remove another light element, cannot be consistent with Brodholt and Badro (2017), which requires one light element decreases in such a way that the seismic velocity also decreases.

Alternatively, the diffusion of light element along a pressure gradient, barodiffusion, may accumulate a chemical layer over the age of the Earth (Fearn and Loper, 1981; Gubbins and Davies, 2013). The mass diffusivity of light elements is small, on the order of $10^{-8} - 10^{-9}$ $m^2 s^{-1}$ (Pozzo et al., 2013), and so such a layer may take billions of years to reach 100 km in size. Gubbins and Davies (2013) model the radial diffusion of O, S and Si under barodiffusion, assuming no mass flux at the CMB, to infer an $\sim$100 km thick layer forms in the first 4 Gyrs of Earths history. The stabilising gradients are very strong although they do not simulate the most recent part of Earth's history when the inner core grows, which would likely destabilise some amount of the lower region of the layer whilst the outer core fluid becomes steadily enriched in oxygen. Furthermore, like the previous mechanism, the stable layer becomes enriched in all light elements and so is also not consistent with Brodholt and Badro (2017).

A further suggestion for the origin of the chemical layer is the consequence of incomplete mixing from Earth's accretion. The accretionary process involved many collisions with planetesimals (Rubie et al., 2011), including some giant collisions (O'Brien et al., 2006) that may be responsible for Moon formation (Asphaug, 2014). These high energy collisions deliver large amounts material to the Earth (Rubie et al., 2011) whilst melting the mantle (Nakajima and Stevenson, 2015), allowing the cores of the colliding bodies to merge. If the impactor core was less dense than that of the proto-Earth's due to a different composition, a long lived chemical layer could be produced from incomplete mixing of the two cores (Jacobson et al., 2017; Landeau et al., 2016).

This impactor core could have a range of possible compositions and so might have

a depletion of some elements and enrichments in others, allowing consistency with the results of Brodholt and Badro (2017). Unfortunately, both the initial size and composition of the impactor core are quite unconstrained. Thermal history models for a range of initial layers formed via this process that find scenarios which are compatible with observations would provide a useful constraint but has so far not been published. Performing such simulations will be a focus within this thesis.

Finally, the core could be undersaturated in oxygen relative to the mantle giving rise to Fe-O partitioning into the core through the CMB as determined experimentally (Frost et al., 2010; Fischer et al., 2015) and predicted by ab-initio simulations (Davies et al., 2018; Pozzo et al., 2019). This increase in oxygen at the CMB, assuming inefficient mixing by entrainment, would diffuse downwards, encroaching deeper into the convecting core (Buffett and Seagle, 2010; Nakagawa, 2018; Davies et al., 2018; Davies et al., 2020).

Buffett and Seagle (2010) develop a numerical method for evolving the time dependent thickness of the layer. They modelled the radial mass diffusion of excess oxygen introduced via the mantle to grow a stable layer over 4.5 Gyrs. The diffusion of oxygen produced an $\sim$80 km layer by the present day, which included a period when the layer is partially eroded during inner core growth, due to the slow oxygen enrichment of the convecting fluid beneath. For simplicity, Buffett and Seagle (2010) assumed a constant super-adiabatic thermal gradient throughout the layer and the evolution for the underlying bulk of the core was treated as an input to the model and so the evolution of the stable layer caused no feedback into the global evolution of the core.

Nakagawa (2018) extended this study by removing this simplifying assumption of a constant super-adiabatic gradient, coupling the evolution of the bulk of the core to the evolution of the stable layer and allowing feedback between the two regions. Additionally a steady state solution was used to solve for the thermal profile throughout the layer. The ohmic dissipation was calculated however the procedure of how the stratification altered the calculated from the standard model was not specified and so the impact upon the dynamo from a stable layer remains undetermined. Otherwise the same partitioning data of Frost et al. (2010) and an equivalent method for evolving the layer thickness in time as Buffett and Seagle (2010) was used leading to similar conclusions, an approximately 80km thick layer. When using higher proposed values for the mass diffusivity of oxygen in the core (Ichikawa and Tsuchiya, 2014; Posner et al., 2017) Nakagawa (2018) shows the layer may grow to up to 270 km in size at present, more in line with estimates from seismic and geomagnetic observations.

New data from both experimental and *ab initio* calculations (Fischer et al., 2015; Davies et al., 2018; Pozzo et al., 2019) is available on the partitioning behaviour of Fe-O between mantle and core, which has been considered by Davies et al. (2020) in

producing chemical stratification; however, they focus on the evolution of a magma ocean and so the full implications for the core are as of yet unknown and will be addressed in this thesis.

1.7.2 Thermal Stratification

Stable thermal stratification must originate from a sub-adiabatic heat flow at the CMB. When the CMB heat flow becomes sub-adiabatic, the thermal profile at the top of the core must adjust to satisfy the conductive heat flow, producing a stable thermal gradient. The effect is to heat up the top of the core and to decrease the volume of the core that is able to maintain a well mixed adiabatic thermal profile.

An early paper by Gubbins et al. (1982) solves for time dependent thermal diffusion producing thermal stratification due to a sub-adiabatic heat flow. The inner core is assumed to grow over all 4.5 Gyrs simulated but does not provide any compositional buoyancy by oxygen partitioning into the liquid. They find an >1000 km thick layer forms, using a (now) relatively low thermal conductivity of 15 $\mathrm{WK^{-1}m^{-1}}$. Labrosse et al. (1997) take an alternative approach, instead treating the moving interface as a Stefan problem, which has the benefit of providing solutions to the thermal diffusion equatino explicitly in a domain that changes size over time, but requires the inclusion of a ficticious latent heat term at the base of the layer. They found that for a linearly decreasing CMB heat flow which becomes sub-adiabatic at around 3 Gyrs, a stable layer grows to ∼600 km in the remaining 1.5 Gyrs of the simulation, about double the rate of growth in Gubbins et al. (1982), most likely owing to the larger thermal conductivity of 60 $\mathrm{WK^{-1}m^{-1}}$ they used.

Building on these studies, Lister and Buffett (1998) solve for both temperature and composition within the stable layer, arguing that thermal diffusion is fast enough to be approximated by a steady state solution and that doubly diffusive salt finger instabilities act to mix the composition uniformly across the layer. By including the compositional profile in the layer, the layer is less buoyant than a purely thermal layer due to a relative depletion of light element relative to the underlying convective region which is being enriched in oxygen from inner core growth. Including this chemical profile within the layer has the impact of slowing down the growth rate of the layer and so, using similar parameters to Labrosse et al. (1997), the stable layer grows to just 400 km thick in nearly 3 Gyrs. In all of these models of thermal stratification, the stratification grows after the inner core begins to grow, either from the beginning of the simulation (Gubbins et al., 1982; Lister and Buffett, 1998) or at ∼1.7 Gyrs (Labrosse et al., 1997). However, recent revisions to the thermal conductivity, k, of the core significantly alter this picture.

Traditional estimates take k ∼30 $\mathrm{WK^{-1}m^{-1}}$ (Stacey and Loper, 2007), however

a number of recent studies (De Koker et al., 2012; Pozzo et al., 2012; Pozzo et al., 2013; Gomi et al., 2013; Pourovskii et al., 2017), though not all (Konôpková et al., 2016; Xu et al., 2018), propose much higher values of >80 $\mathrm{WK^{-1}m^{-1}}$ at the CMB and increasing up to ∼150 $\mathrm{WK^{-1}m^{-1}}$ at the ICB. The adiabatic heat flow is the heat conducted along the adiabatic temperature profile, which using Fourier's law is given as: $Q_\mathrm{a} = -4\pi r_\mathrm{c}^2 k \mathrm{d}T_\mathrm{a}/\mathrm{d}r$. High values for k have therefore drastically increased the estimate of the adiabatic heat flow by 2-3× to ∼15 TW (Pozzo et al., 2013).

Prior to Inner Core Nucleation (ICN) there is no source of compositional buoyancy or latent heat, which helps to power the geodynamo, only thermal convection driven by the secular cooling of the core (Buffett et al., 1996b; Gubbins et al., 2003) as heat is extracted at the CMB. Heat conducted down the adiabat cannot be used to drive convection, and hence magnetic field generation, and so if the heat flow extracted from the convecting fluid becomes less than that conducted down the adiabat, a dynamo cannot be sustained under the assumption of an adiabatically stratified fluid.

Given the new estimates of the adiabatic heat flow, higher CMB heat flow must be necessary to power the geodynamo prior to ICN, which in turn cool the core faster resulting in a younger inner core. An inner core that is only 500 Myrs old places a constraint upon the timing of thermal stratification since it may only originate after ICN. Furthermore, the thermal diffusivity is proportional to the thermal conductivity and so the layer growth might be expected to be faster. Revisiting thermal stratification in the core with these higher estimates is needed to reassess the previous conclusions. New models including high k will be performed in this thesis.

Table 1.2: Previous results for the growth of a stably stratified layer in parameterised models, where values are for present day layer thickness, h, and period of gravity waves, $2\pi/N$. A single T/C in the second column indicates that only temperature (T) or composition (C) was solved for within the layer. T(C) indicates that both were solved for where the thermal gradient was stabilising, C(T) is the reverse where the chemical gradient was stabilising. Buoyancy period is the period of gravity waves as given by the Brunt-Väisälä frequency. Note that Gubbins et al. (1982) was omitted since their study focussed on demonstrating the growth behaviour of the layer but were not advocating for a >1000 km thick layer in the Earth. Buoyancy periods for any studies that are not quoted in the text are left blank.

Publication	Stratification type	h (km)	$\frac{2\pi}{N}$ (hours)
Labrosse et al. (1997)	T	600	-
Lister and Buffett (1998)	T(C)	400	>17
Buffett and Seagle (2010)	C	80	0.5
Nakagawa (2018)	C(T)	80-270	0.05
Gubbins and Davies (2013)	C	100	1.2
Davies et al. (2020)	C	60-140	-

At present only a relatively small number of thermal history models have been

published on stratification in the Earth's core. Previous models of thermal stratification do not specify the impact upon the ohmic dissipation generated in the core when a stable layer is included. Nakagawa (2018) calculated the ohmic dissipation for their chemical layer, however does not specify how the presence of a stable layer is accounted for in the calculation, making the impact of the layer opaque. Every study has also used a unique method for computing the time evolution of the layer for the specific use case of their study. A more flexible, transparent method for computing the thermal history of the core with applications to both thermal and chemical stratification, calculating the full entropy budget therefore has great utility. This model should be easily adapted to take advantage of new data when available and represent new physical processes not currently modelled since there is still lots more to learn about the stable layer.

1.8 Aims and structure of the thesis

The nature of the stratified layer is still unknown with a range of properties suggested by observations and several proposals for its origin. The stratified layer properties have broad implications for a range of research areas from planetary formation, global seismology, high pressure/temperature mineral physics to planetary evolution, CMB interactions to the geodynamo, geomagnetic observations, and magneto-hydrodynamic waves. Furthermore, all these research areas may be relevant for both Earth and potentially other planets (Fig. 1.6).

In this thesis I aim to investigate the long term evolution and present day structure of stratification at the top of the core under a range of scenarios by way of the following objectives:

1. Develop a thermal history model, with a generalised representation of thermal and chemical stratification.
2. Constrain the structure and evolution of stable layers resulting from purely thermal stratification, focusing on the implications of high core thermal conductivity.
3. Constrain the structure and evolution of stable layers resulting from chemical stratification due to FeO enrichment and incomplete mixing at core formation.

This thesis is organised as follows. Chapter 2 develops the bespoke thermal history model requiring new numerical schemes to couple the evolution of a stable layer to the rest of the core. Chapter 3 applies this to model thermal stratification and Chapter 4 investigates chemical stratification by FeO enrichment and incomplete mixing. Finally in chapter 5 concluding remarks and potential avenues for future work are discussed.

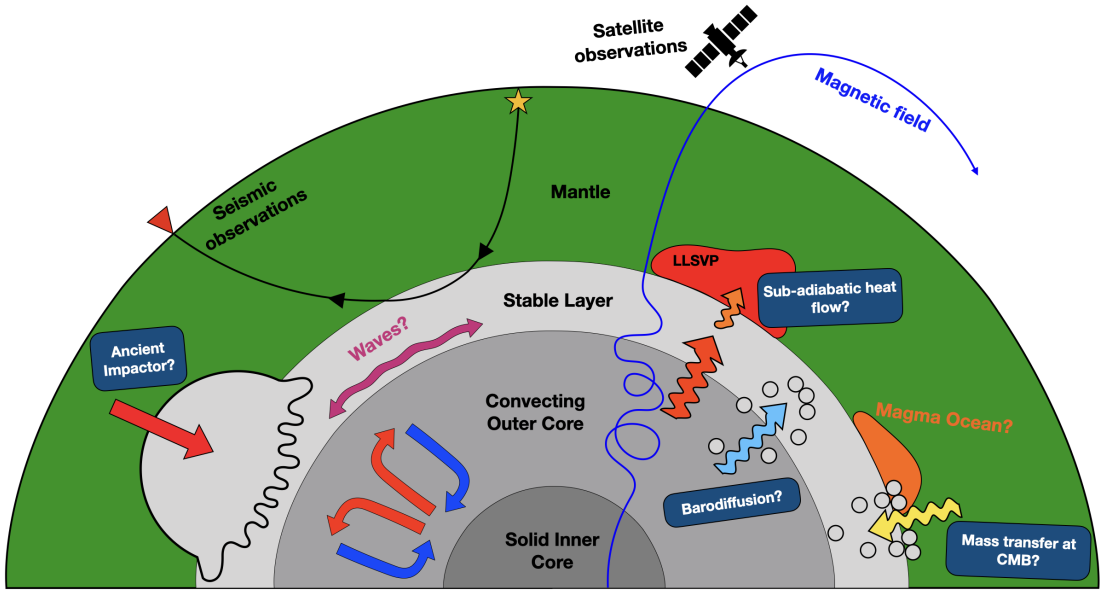

Figure 1.6: Cartoon highlighting the wide range of complex processes and impacts associated with a stratified layer. Potential origins of the layer are highlighted in the blue boxes.

Chapter 2

Model Development

2.1 Introduction

Chapter 1 introduced the theme of this thesis and set out the aims and objectives. The first objective, which will enable the subsequent objectives, is to construct a parameterised model for the long term evolution of the core. This model will be developed in this chapter and will include stable stratification beneath the CMB of both a thermal and chemical origin.

In all of the proposed origins for stratification (discussed in section 1.7), the stable layer is a relatively long lived feature of the Earth's core. To grow to the size predicted for the layer at present, 100-400 km (Garnero et al., 1993; Tanaka, 2007; Helffrich and Kaneshima, 2010; Kaneshima, 2018), driven by the diffusion of temperature and/or light element takes a long time owing to the small diffusivities for both temperature and mass. The thermal diffusivity, κ, is much higher than mass diffusivities in the core (Gubbins et al., 2004), yet taking an order of magnitude estimate of κ at the top of the outer core where the density is 10^4 kg m^{-3}, the specific heat capacity is 800 J K^{-1} kg^{-1} and a generously high thermal conductivity of 150 W K^{-1} m^{-1} gives

$$\kappa = \frac{k}{\rho C_p} \approx \frac{150}{10^4 \times 800} \approx 10^{-5}\mathrm{m}^2\mathrm{s}^{-1}. \tag{2.1}$$

A diffusivity of $10^{-5}\mathrm{m}^2\mathrm{s}^{-1}$ corresponds to a time scale (L^2/κ) of around 30 million years for a $L = 100$ km thick layer, a timescale much longer than other processes on the 100km scale. Taking a velocity of $U = 13$ km yr^{-1} (Holme, 2015) gives a fluid advection time (L/U) ∼8 years and assuming an electrical conductivity of $\sigma = 1.1 \times 10^6$ S m^{-1} (Pozzo et al., 2013), the magnetic diffusion time is $(L^2/\eta) = (L^2\mu_0\sigma) \sim 500$ years, where η, μ_0 are the magnetic diffusivity and permeability of free space respectively. The time evolution of the stable layer is therefore on an intermediate timescale, long

relative to fluid motions and magnetic field fluctuations on the same length scale, but short relative to the very slow cooling of the core over the age of the Earth.

The slow evolution of the Earth can be modelled using thermal history models (e.g. Buffett et al., 1996b; Labrosse et al., 1997; Gubbins et al., 2004; Davies, 2014). These 1D parameterised models evolve a time averaged state, evolving over geological time on the same intermediate timescale as the stable layer will evolve. Modelling the evolution of the stable layer should therefore take into account the thermal evolution of the core that thermal history models seek to describe.

Previous authors have simulated the growth of a stable layer to varying degrees and under a number of scenarios for the origin of the layer. Previous models of thermal stratification (Gubbins et al., 1982; Labrosse et al., 1997; Lister and Buffett, 1998) compute solutions for the diffusion of temperature in the layer, coupled to a thermal history model for the rest of the core, but do not specify the impact upon the ohmic dissipation generated in the core when a stable layer is included. A focus of the model derived here will be to explicitly allow the evolution of the stable layer to impact the production of ohmic dissipation and hence infer the impact on the power available to drive the geodynamo.

Models for a chemical origin for the layer are more varied. Gubbins and Davies (2013) compute the mass diffusion of light elements from the CMB into an infinite halfspace due to barodiffusion to infer a 100 km thick layer would form. However they do not calculate the evolution of the whole core and so cannot evaluate the layer's influence on its thermal evolution or the power available to the geodynamo. A few models have been published regarding a mass transfer of oxygen into the core from either solid ferropericlase (Buffett and Seagle, 2010; Nakagawa, 2018; Davies et al., 2018) or liquid silicates in a magma ocean (Davies et al., 2020). Davies et al. (2018) and Davies et al. (2020) use the same method as Gubbins and Davies (2013), to infer a mass flux into the core at the CMB from either ferropericlase or liquid silicates producing a stable layer. Their studies showed the plausibility that a layer $\mathcal{O}(100)$ km may form, however like Gubbins and Davies (2013) they do not simulate the coupled interaction with the evolution of the rest of the core since they focus on the partitioning behaviour.

Buffett and Seagle (2010) simulates the stable layer evolution from partitioning of oxygen from ferropericlase and allows the evolution of the core to impact the stable layer evolution. This is most notable during inner core growth when the layer size is reduced due to the slow enrichment of the underlying convective region in oxygen rejected by the inner core. The evolution of the bulk of the core however is an input to the model, based upon previous thermal history calculations that do not include a stable layer (Buffett et al., 1996b). Nakagawa (2018) extends Buffett and Seagle (2010) by coupling the

evolution of the rest of the core to the stable layer and also solves for temperature within the layer with a steady state solution. The ohmic dissipation is calculated in Nakagawa (2018) although the method is not detailed and so the contribution from the layer is not yet clear.

A general framework to model the evolution of either a thermal or chemical origin for the layer and to simulate the long term evolution of the entire core, whilst estimating the ohmic dissipation therefore has great utility.

This chapter is organised as follows. Section 2.2 lays out the development for the general energy and entropy budgets for the core as has been done in previous work. Sections after 2.2 therefore contain my original work. Section 2.3 outlines the 1D representation for a stable layer and section 2.4 details the global energy and entropy balances including this representation. Section 2.5 details the numerical method for evaluating the terms in the global balances with the numerical representation of core properties in section 2.6. Section 2.7 develops the scheme for numerically solving the diffusion equations within the layer and how the time evolution of layer growth is handled. Finally Section 2.8 provides benchmarking cases against known solutions with a summary provided in section 2.9, recapping the main governing equations and method that has been developed.

2.2 Existing thermal history model framework

In order to solve for the cooling history of the core, conservation of energy is used as a condition to relate the heat extracted from the core to its cooling rate. The density gradients within the core are well described by the Adams-Williamson equation for a homogeneous medium under self-compression (Dziewonski and Anderson, 1981). The density fluctuations associated with convection are very small at around $\delta\rho/\rho \approx 10^{-8}$ (Stevenson, 1987) corresponding to thermal anomalies $\mathcal{O}(10^{-3})$ K or light element anomalies of $\mathcal{O}(10^{-6})$ wt%. Convection is therefore assumed to keep the outer core well-mixed, hydrostatic, and close to isentropic outside of thin boundary layers (Gubbins et al., 1979; Braginsky and Roberts, 1995).

The convective perturbations will evolve on the timescale of convection, τ_{conv}. Inferred core motions at the top of the core derived from observations of the secular variation of the magnetic field suggest velocities on the order of 10 km/yr (Holme, 2015). An order of magnitude estimate of τ_{conv} can be taken as the convective turnover time L/v, where L is the height of the outer core and v is 10 km yr^{-1}, yielding $\tau_{\text{conv}} \approx 226$ years. The hydrostatic, isentropic basic state on the other hand, evolves slowly at the rate of core cooling, τ_{cool} over the age of the Earth. When taking a time average of the core on a timescale $\tau_{\text{conv}} \ll \tau \ll \tau_{\text{cool}}$ it is assumed that the perturbations around the basic state due to convection average to zero (Braginsky and Roberts, 1995; Buffett

et al., 1996b; Gubbins et al., 2003; Nimmo, 2015), where τ is on the order of 1 Myrs. Convection still plays an important role in maintaining the basic state, transporting heat and generating a magnetic field, however under this assumption the specifics of the dynamics are omitted creating a spherically symmetric 1D representation of the core.

The inner core is assumed to also be sufficiently described by this basic state. Convective motions in the inner core are still debated as more data on the viscosity of the crystalline structure becomes available (Belonoshko et al., 2019), otherwise in the absence of convection heat will be transported solely by conduction. Labrosse et al. (1997) show that assuming the inner core to also be isentropic with an adiabatic temperature profile, rather than a conductive profile introduces little error when computing the cooling rate of the core.

After averaging out the short time scale fluctuations associated with convection, the core is assumed to be represented by a 1D basic state that is hydrostatic, isentropic and chemically uniform. The following equations will be derived for an iron core containing just a single alloying light element, where the concentration of light element is described by a mass fraction, c, defined as the fraction of mass in the alloy attributed to the specific light element. Occasionally it is necessary to specify the mole fraction instead, $\bar{c}$, the fraction of moles of solute (light element) in one mole of solution (iron alloy). Multiple light elements are more than likely to be present in the core (Poirier, 1994; Hirose et al., 2013), and so should feature in the model. Additional light elements are easily included later on by taking the summation across all light element species in any term dependent upon c or $\bar{c}$, but for simplicity just one light element is considered to begin with.

2.2.1 Energy balance of the core

Within the core, energy is conserved (Landau and Lifshitz, 1987; Gubbins et al., 2003):

$$\frac{\partial}{\partial t}\left(\rho e + \frac{1}{2}\rho|\mathbf{v}|^2 + \frac{|\mathbf{B}|^2}{2\mu_0}\right) = -\nabla\cdot\left[\rho\mathbf{v}\left(\frac{1}{2}|\mathbf{v}|^2 + e + \frac{P}{\rho}\right) + \frac{\mathbf{E}\times\mathbf{B}}{\mu_0} - \mathbf{v}\cdot\boldsymbol{\tau'} + \mathbf{q}\right] + \rho h + \rho\mathbf{v}\cdot\nabla\psi, \tag{2.2}$$

which equates the rate of change in time, t, of energy on the LHS with internal sources and the divergence of energy on the RHS. ρ, e, $\mathbf{v}$, $\mathbf{B}$, μ_0, are the density, internal energy, velocity, magnetic field, and permeability of free space. P, $\mathbf{E}$, $\boldsymbol{\tau'}$, $\mathbf{q}$, h and ψ are the pressure, electric field, stress tensor, heat flux vector, rate of internal heating and gravitational potential respectively. The LHS represents the rate of change of internal, kinetic and magnetic energy. On the RHS the divergence term shows, in

order, the flux of energies due to kinetic energy, internal energy, work done by pressure, electromagnetic energy, work done by shear stresses, and the heat flux. Finally on the RHS are energies arising from internal heating and work done by gravity.

The following identities will be used to manipulate this equation. The Reynolds transport theorem relates the rate of change of an integral over a volume, V, of some material property, $\mathcal{A}$, to the intrinsic rate of change of $\mathcal{A}$ and the flux of that material property in/out the volume:

$$\frac{\mathrm{d}}{\mathrm{d}t}\int \rho\mathcal{A}\mathrm{d}V = \int \frac{\partial(\rho\mathcal{A})}{\partial t}\mathrm{d}V + \oint \rho\mathcal{A}\mathbf{v}\cdot\mathrm{d}\mathbf{S}. \tag{2.3}$$

The divergence vector identity for some vector $\mathcal{B}$ and some scalar ϕ is given as:

$$\nabla\cdot(\phi\mathcal{B}) = \mathcal{B}\cdot\nabla\phi + \phi\nabla\cdot\mathcal{B}. \tag{2.4}$$

The integration over a volume, V, of 2.2 using 2.3 and 2.4 gives:

$$\begin{aligned}\frac{\mathrm{d}}{\mathrm{d}t}\int \rho e\mathrm{d}V + \frac{\mathrm{d}}{\mathrm{d}t}\int \frac{1}{2}\rho|\mathbf{v}|^2\mathrm{d}V + \int \frac{\partial}{\partial t}\frac{|\mathbf{B}|^2}{2\mu_0}\mathrm{d}V = \\ -\oint P\mathbf{v}\cdot\mathrm{d}\mathbf{S} - \oint \frac{\mathbf{E}\times\mathbf{B}}{\mu_0}\cdot\mathrm{d}\mathbf{S} + \oint \mathbf{v}\cdot\boldsymbol{\tau'}\cdot\mathrm{d}\mathbf{S} - \oint \mathbf{q}\cdot\mathrm{d}\mathbf{S} + \int \rho h\mathrm{d}V + \int \rho\mathbf{v}\cdot\nabla\psi\mathrm{d}V,\end{aligned} \tag{2.5}$$

where $\mathbf{S}$ is the area element of the bounding surfaces of V.

Fluctuations of kinetic and magnetic energy on the LHS of Eq 2.5 are assumed to average to zero on the timescale we are interested in. We have limited sources to be able to estimate these terms from observational data. Magnetic energy is produced via the conversion of the kinetic energy of convection by the dynamo process (Buffett and Bloxham, 2002) and so fluctuations in both are expected to anti-correlate. PADM2M (Ziegler et al., 2011) models the axial dipole moment of the magnetic field over the last 2 Myrs based on paleomagnetic intensity data (Fig. 2.1), showing fluctuations on a shorter timescale than our averaging procedure has used and that they approximately average to zero. Assuming that the time variance in PADM2M is associated with the fluctuations in magnetic energy in the core (Avery et al., 2019), which are in turn associated with fluctuations in the kinetic energy then all may be assumed to average to zero.

Long trends in the kinetic and magnetic energies, beyond PADM2M might be significant and so estimating the total kinetic and magnetic energy in the core today may reveal likely orders of magnitude of their long term trend. The leading order

terms in the energy balance are $\mathcal{O}(1\text{ TW})$, which when sustained for 1 Myrs represents $\mathcal{O}(10^{25}\text{ J})$. The fluid velocity in the core can be estimated by fitting the secular variation of the magnetic field, giving a RMS velocity of around 13 km yr^{-1} (Holme, 2015). Assumptions are required to invert for the fluid flow and is only representative of velocity beneath the CMB but should serve as an appropriate order of magnitude for the whole core (Jones, 2015). Taking 13 km yr^{-1} across the entire core, the kinetic energy is $\sim 2 \times 10^{17}$ J. Considering an unreasonably extreme case, bringing the entire core to a halt and removing all available kinetic energy over 1 Myrs, only corresponds to a sustained energy output of 6.3 KW.

One avenue of estimating the magnetic field strength in the core is by fitting models of torsional waves to observed varations in the magnetic field (Cox et al., 2014). These waves are only sensitive to magnetic field in the radial direction (in cylindrical coordinates) and so the total RMS field strength can be estimated if one assumes the field is isotropic. Gillet et al. (2010) give a large field strength estimate of 4 mT and so assuming this is constant across the core yields a total magnetic energy of $\sim 4 \times 10^{21}$, larger than the kinetic energy. Considering an equivalently extreme scenario, removing all magnetic field in just 1 Myrs, would only produce a sustained 0.13 GW. While somewhat crude estimates, they demonstrate that long term trends in the kinetic and magnetic energies are not reasonably large enough to be significant for my purposes. It is worth noting that this assumption is also required for practicality, since we cannot know the magnetic field and velocity throughout the core.

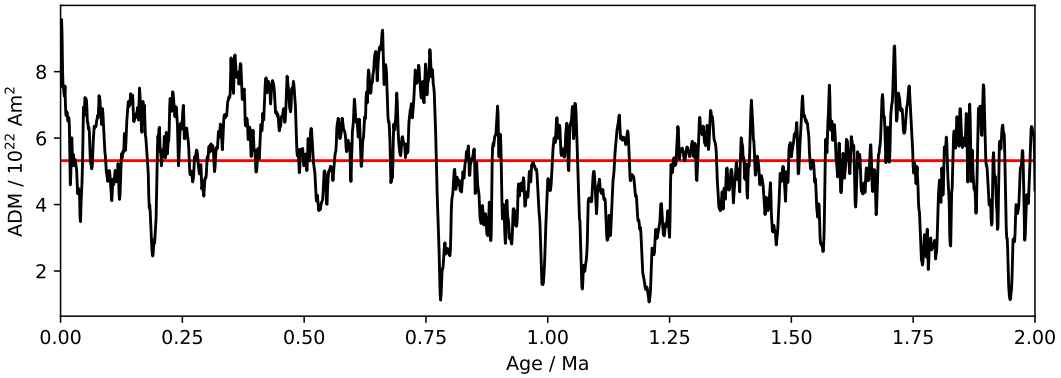

Figure 2.1: Axial Dipole Moment (ADM) plotted as a function of age from the PADM2M model (Ziegler et al., 2011). The mean value for the entire time series is shown by the red line.

The mantle is also assumed to be perfectly electrically insulating, reducing the surface flux of electromagnetic energy to zero. In reality the mantle does have a non-zero electrical conductivity and has been considered to have a large enough when molten to support a small dynamo region in a past basal magma ocean (Ziegler and Stegman, 2013; Blanc et al., 2020), although that is assumed not the case here. Assuming stress-free boundaries there can be no surface tractions and so $\boldsymbol{\tau}' = 0$ on any surfaces. A

slip-free condition might be more physically reasonable (Roberts and Glatzmaier, 2000) but allowing the shear stresses to disappear makes it possible to avoid introducing unconstrained estimates of them in this analysis. All of these assumptions reduce Eq 2.5 to

$$\oint \mathbf{q} \cdot \mathrm{d}\mathbf{S} = -\int \rho \frac{\mathrm{D}e}{\mathrm{D}t} \mathrm{d}V + \int \rho h \mathrm{d}V - \int \nabla \cdot (P\mathbf{v}) \mathrm{d}V + \int \rho \mathbf{v} \cdot \nabla \psi \mathrm{d}V. \tag{2.6}$$

The first term on the RHS, the changing internal energy, will now be manipulated using thermodynamic relations and conservation of mass.

The fundamental equation of thermodynamics for a two component mixture expresses a change in internal energy in terms of the conjugate variables temperature and entropy, pressure and volume, and finally chemical potential and mass fraction of light element (Gubbins et al., 2004)

$$de = T\mathrm{d}s - P\mathrm{d}V + \mu \mathrm{d}c, \tag{2.7}$$

where T, s are temperature and entropy, and μ is the chemical potential. For unit mass, $\mathrm{d}V = -\rho^{-2}\mathrm{d}\rho$, therefore

$$de = Tds + P\frac{\mathrm{d}\rho}{\rho^2} + \mu \mathrm{d}c. \tag{2.8}$$

The fluctuations in internal energy can therefore be written

$$\rho \frac{\mathrm{D}e}{\mathrm{D}t} = \rho T \frac{\mathrm{D}s}{\mathrm{D}t} + \frac{P}{\rho}\frac{\mathrm{D}\rho}{\mathrm{D}t} + \rho\mu \frac{\mathrm{D}c}{\mathrm{D}t}. \tag{2.9}$$

Assuming mass is conserved in the core (Gubbins et al., 2003; Nimmo, 2015)

$$\begin{aligned} &\frac{\partial \rho}{\partial t} + \nabla \cdot (\rho \mathbf{v}) = 0 \quad \text{and} \quad \frac{\mathrm{D}\rho}{\mathrm{D}t} = \frac{\partial \rho}{\partial t} + \mathbf{v} \cdot \nabla \rho \\ &\Rightarrow \quad \frac{\mathrm{D}\rho}{\mathrm{D}t} = -\rho(\nabla \cdot \mathbf{v}), \end{aligned} \tag{2.10}$$

which can be used to substitute in for the density derivative in 2.9 to give:

$$\rho \frac{\mathrm{D}e}{\mathrm{D}t} = \rho T \frac{\mathrm{D}s}{\mathrm{D}t} - P\nabla \cdot \mathbf{v} + \rho\mu \frac{\mathrm{D}c}{\mathrm{D}t}. \tag{2.11}$$

Entropy is an extensive state function and so considering changes in temperature,

pressure and light element, its derivative may be written

$$\frac{\mathrm{D}s}{\mathrm{D}t} = \left(\frac{\partial s}{\partial T}\right)_{P,c} \frac{\mathrm{D}T}{\mathrm{D}t} + \left(\frac{\partial s}{\partial P}\right)_{T,c} \frac{\mathrm{D}P}{\mathrm{D}t} + \left(\frac{\partial s}{\partial c}\right)_{P,T} \frac{\mathrm{D}c}{\mathrm{D}t}. \tag{2.12}$$

The definitions of the specific heat capacity, C_p and thermal expansivity, α_T are (Gubbins et al., 2003; Nimmo, 2015)

$$C_p = T\left(\frac{\partial s}{\partial T}\right)_{P,c} \tag{2.13}$$

$$\alpha_T = -\rho\left(\frac{\partial s}{\partial P}\right)_{T,c} = -\frac{1}{\rho}\left(\frac{\partial \rho}{\partial T}.\right)_{P,c} \tag{2.14}$$

Using 2.12-2.14 and the Maxwell relation

$$\left(\frac{\partial s}{\partial c}\right)_{P,T} = -\left(\frac{\partial \mu}{\partial T}\right)_{P,c}, \tag{2.15}$$

allows 2.11 to be rewritten as

$$\rho\frac{\mathrm{D}e}{\mathrm{D}t} = \rho C_p \frac{\mathrm{D}T}{\mathrm{d}t} - \alpha_T T\frac{\mathrm{D}P}{\mathrm{D}t} + \rho\left(\mu - T\left(\frac{\partial \mu}{\partial T}\right)_{P,c}\right)\frac{\mathrm{D}c}{\mathrm{D}t} - P\nabla\cdot\mathbf{v}. \tag{2.16}$$

Substitution of 2.16 back into 2.6 gives

$$\begin{aligned}\oint \mathbf{q}\cdot\mathrm{d}\mathbf{S} = &-\int \rho C_p \frac{\mathrm{D}T}{\mathrm{d}t}\mathrm{d}V + \int \alpha_T T\frac{\mathrm{D}P}{\mathrm{D}t}\mathrm{d}V - \int \rho\left(\mu - T\left(\frac{\partial \mu}{\partial T}\right)_{P,c}\right)\frac{\mathrm{D}c}{\mathrm{D}t}\mathrm{d}V \\ &+ \int P\nabla\cdot\mathbf{v}\mathrm{d}V + \int \rho h\mathrm{d}V - \int \nabla\cdot(P\mathbf{v})\mathrm{d}V + \int \rho\mathbf{v}\cdot\nabla\psi\mathrm{d}V.\end{aligned} \tag{2.17}$$

The total energy budget for the core is achieved by applying 2.17 to the volumes of the inner core and outer core with appropriate boundary conditions at the ICB and CMB. The heat flux vector, $\mathbf{q}$, is dependent on both thermal conduction and the mass flux (Landau and Lifshitz, 1987).

$$\mathbf{q} = -k\nabla T + \mathbf{i}\left(\mu + \frac{\beta T}{\alpha_D}\right) \tag{2.18}$$

$$\mathbf{i} = -\alpha_D\nabla\mu - \beta\nabla T, \tag{2.19}$$

where k is the thermal conductivity, β is a material constant, and α_D is the barodiffusion

coefficient given as (Gubbins et al., 2004)

$$\alpha_D = \frac{\rho D}{(\partial \mu / \partial c)_{P,T}}, \tag{2.20}$$

where D as the mass diffusivity of light element.

Assuming no mass flux at the CMB, the heat flux vector is simply the heat conducted along the temperature gradient in the upper boundary layer of the core.

$$Q_{\mathrm{c}} = \oint \mathbf{q} \cdot \mathrm{d}\mathbf{S} = \oint -k \nabla T \cdot \mathrm{d}\mathbf{S}. \tag{2.21}$$

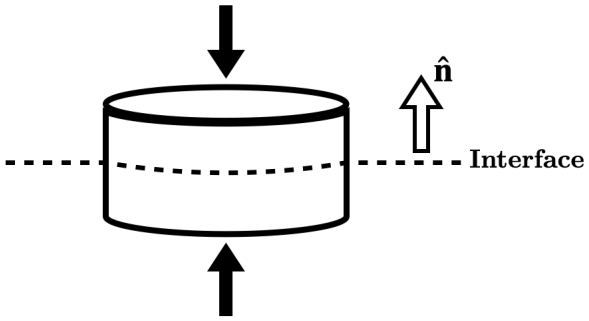

Figure 2.2: Pill box shaped volume that is placed on an interface and its height reduced to zero. The top and bottom surfaces are then located on the top and underside of the interface.

To determine the conditions at the ICB, a pill box argument is used. Consider a small cylindrical volume centered on the ICB such that the top face is in the outer core and the bottom face is in the inner core shown in figure 2.2. The height of the volume is reduced such that the cylinder is infinitesimally thin with the top face on the outer core side of the ICB and the lower face is on the inner core side of the ICB. The volume of the pill box approaches zero but its surface area does not and so integration of continuity equations over this volume, reduces all volume integrals to zero but retains surface integrals. $\langle X \rangle$ will denote the jump in the quantity X across the ICB defined here as $X_{\mathbf{2}} - X_{\mathbf{1}}$ with subscripts 1, 2 referring to the value on the ICB in the solid inner core or liquid outer core respectively.

Under this notation Braginsky and Roberts (1995) give the corresponding continuity condition for mass

$$\hat{\mathbf{n}} \cdot \langle \rho \left(\mathbf{v} - \frac{\mathrm{d}r_{\mathrm{i}}}{\mathrm{d}t} \right) \rangle = 0, \tag{2.22}$$

where r_i is the inner core radius so that velocities are expressed relative to the advancing ICB, and for energy is

$$\hat{\mathbf{n}} \cdot \langle \mathbf{q} + H\rho \left(\mathbf{v} - \frac{\mathrm{d}r_\mathrm{i}}{\mathrm{d}t} \right) \rangle = 0 \tag{2.23}$$

where H is the enthalpy ($H = e + P/\rho$) and $\hat{\mathbf{n}}$ is the unit vector normal to the ICB. Assuming no penetration of fluid in/out the inner core ($\mathbf{v} = \langle \mathbf{v} \rangle = 0$), Equations 2.22 and 2.23 imply

$$\langle H\rho \left(\mathbf{v} - \frac{\mathrm{d}r_\mathrm{i}}{\mathrm{d}t} \right) \rangle = (H_\mathbf{1} - H_\mathbf{2})\rho_\mathbf{1} \frac{\mathrm{d}r_\mathrm{i}}{\mathrm{d}t}. \tag{2.24}$$

Equation 2.23 may therefore be written

$$\hat{\mathbf{n}} \cdot \mathbf{q_2} = \hat{\mathbf{n}} \cdot \mathbf{q_1} + (H_\mathbf{2} - H_\mathbf{1})\rho_\mathbf{1} \frac{\mathrm{d}r_\mathrm{i}}{\mathrm{d}t}. \tag{2.25}$$

The enthalpy differential for a reversible process is defined as

$$\mathrm{d}H = T\mathrm{d}s + V\mathrm{d}P + \mu \mathrm{d}c \tag{2.26}$$

$$= T\mathrm{d}s + \mu \mathrm{d}c, \tag{2.27}$$

where the pressure has been taken as continuous across the ICB ($V\mathrm{d}P = 0$). There are two contributions to the change in entropy, one from a change in c is equal to $-\mathrm{d}c\,(\partial\mu/\partial T)_{P,T}$ (Eq. 2.12) and one from the phase change of liquid to solid of Δs_Fe (positive for melting). The enthalpy change is therefore

$$H_\mathbf{2} - H_\mathbf{1} = T\Delta s_\mathrm{Fe} + \left(\mu - T \left(\frac{\partial \mu}{\partial T} \right)_{P,T} \right) \langle c \rangle \tag{2.28}$$

$$= L + R_H \langle c \rangle \tag{2.29}$$

assuming that both μ and its temperature derivative are continuous across the ICB. L is the latent heat due to the phase change and R_H is the heat of reaction from a change in composition upon freezing. Equation 2.25 becomes

$$\hat{\mathbf{n}} \cdot \mathbf{q_2} = \hat{\mathbf{n}} \cdot \mathbf{q_1} + L\rho_\mathbf{1} \frac{\mathrm{d}r_\mathrm{i}}{\mathrm{d}t} + R_H \langle c \rangle \rho_\mathbf{1} \frac{\mathrm{d}r_\mathrm{i}}{\mathrm{d}t}. \tag{2.30}$$

The heat flux into the outer core is the heat flux out of the inner core plus the heat released from freezing iron and changing composition on the advancing ICB. The difference in composition between the solid and liquid is determined by the partitioning

behaviour of light element where the method of estimating this is shown later in section 2.6.E quating the mass of light element released at the ICB to the mass of light element evenly distributed across the convecting outer core of mass $M_{\mathbf{2}}$ gives the relation

$$\rho_{\mathbf{1}} 4\pi r_{\mathrm{i}}^2 \langle c \rangle \frac{\mathrm{d}r_{\mathrm{i}}}{\mathrm{d}t} = \frac{\mathrm{D}c}{\mathrm{D}t} M_{\mathbf{2}}, \tag{2.31}$$

and so the heat of reaction term in equation 2.30 can be written as

$$R_H \langle c \rangle \rho_{\mathbf{1}} \frac{\mathrm{d}r_{\mathrm{i}}}{\mathrm{d}t} = R_H \frac{\mathrm{D}c}{\mathrm{D}t} M_{\mathbf{2}}. \tag{2.32}$$

The volume integrals across the entire core of conservation of energy, including the boundary conditions at the CMB and at the ICB gives the energy terms

$$\begin{aligned} Q_{\mathrm{c}} = &- \int \rho C_p \frac{\mathrm{D}T}{\mathrm{d}t} \mathrm{d}V_{\mathbf{12}} + \int \alpha_T T \frac{\mathrm{D}P}{\mathrm{D}t} \mathrm{d}V_{\mathbf{12}} + R_H \frac{\mathrm{D}c}{\mathrm{D}t} M_{\mathbf{2}} - \int \rho R_H \frac{\mathrm{D}c}{\mathrm{D}t} \mathrm{d}V_{\mathbf{2}} \\ &+ \int \rho h \mathrm{d}V + 4\pi r_{\mathrm{i}}^2 \rho_{\mathbf{1}} L \frac{\mathrm{d}r_{\mathrm{i}}}{\mathrm{d}t} + \int P \nabla \cdot \mathbf{v} \mathrm{d}V_{\mathbf{12}} \\ &- \int \nabla \cdot (P\mathbf{v}) \mathrm{d}V_{\mathbf{12}} + \int \rho \mathbf{v} \cdot \nabla \psi \mathrm{d}V_{\mathbf{12}}, \end{aligned} \tag{2.33}$$

where $V_{\mathbf{12}}$ is the combined volume of the inner core and convecting outer core.

The final 3 terms on the RHS of 2.33 all involve the fluid velocity, $\mathbf{v}$, which can be separated into the convective fluctuations $\mathbf{v}'$ and the long term contractional velocity as the core shrinks via cooling, $\mathbf{u}$ (Gubbins et al., 2003) such that $\mathbf{v} = \mathbf{u} + \mathbf{v}'$.

In the time averaged basic state it is assumed $\mathbf{v}'$ average to zero, the total velocity averages to $\mathbf{u}$, and the pressure gradient to hydrostatic, $\nabla P = \rho \nabla \psi$ (Gubbins et al., 2003). Substituting these in to the last 3 terms in 2.33, replaces the gravitational potential term and by the vector identity 2.4, they become zero (Gubbins et al., 2003)

$$\begin{aligned} &\int P \nabla \cdot \mathbf{u} \mathrm{d}V_{\mathbf{12}} - \int \nabla \cdot (P\mathbf{u}) \mathrm{d}V_{\mathbf{12}} + \int \rho \mathbf{u} \cdot \nabla \psi \mathrm{d}V_{\mathbf{12}} = \\ &\int P \nabla \cdot \mathbf{u} \mathrm{d}V_{\mathbf{12}} - \int \nabla \cdot (P\mathbf{u}) \mathrm{d}V_{\mathbf{12}} + \int \mathbf{u} \cdot \nabla P \mathrm{d}V_{\mathbf{12}} = 0. \end{aligned} \tag{2.34}$$

Work done by gravitational forces is accommodated by the work done by pressure and hence does not contribute to the global energy budget of the basic state. When light element is excluded from the growing inner core however, the mass is assumed to redistribute evenly across the outer core which requires convective motions. The work done by gravity by the convection in this redistribution does not average to zero since

light element is continuously moved from the inner core across the convecting outer core, therefore must be included in the energy budget and can power the dynamo.

Changes in the gravitational potential within the core may result from sources external to the core since the gravity field is the consequence of all the mass on Earth. The redistribution of mass from mantle convection is not taken into account, such as subduction of lithospheric plates or the possible collection of dense piles on the CMB, instead all gravitational changes are assumed to be from sources within the core.

The gravitational potential term can be expanded with Eq. 2.4 and simplified with the divergence theorem and conservation of mass (Eq. 2.10) to give

$$\begin{aligned}\int \rho\mathbf{v}' \cdot \nabla\psi \mathrm{d}V_{\mathbf{2}} &= \int \nabla \cdot (\rho\mathbf{v}'\psi)\mathrm{d}V_{\mathbf{2}} - \int \psi\nabla \cdot (\rho\mathbf{v}')\mathrm{d}V_{\mathbf{2}} \\ &= \oint \rho\psi\mathbf{v} \cdot dS - \int \psi\nabla \cdot (\rho\mathbf{v})\mathrm{d}V_{\mathbf{2}} \qquad (2.35) \\ &= -\int \psi\frac{\partial\rho}{\partial t}\mathrm{d}V_{\mathbf{2}} \qquad (2.36)\end{aligned}$$

where the surface integral is zero as $\mathbf{v}' \cdot \mathrm{d}\mathbf{S} = 0$ at the CMB. The velocity no longer appears on the RHS but the density derivative implicitly depends upon the velocity. The time averaged density changes are assumed to result from a uniform redistribution of light elements by advection throughout the convective region. Using the definition of α_c

$$\alpha_c = -\frac{1}{\rho}\left(\frac{\partial\rho}{\partial c}\right)_{P,T}, \qquad (2.37)$$

the change in density of the outer core due to the enrichment of light element can therefore be written

$$\frac{\partial\rho}{\partial t} = \left(\frac{\partial\rho}{\partial c}\right)_{P,T}\frac{\mathrm{D}c}{\mathrm{D}t} = -\rho\alpha_c\frac{\mathrm{D}c}{\mathrm{D}t}. \qquad (2.38)$$

The integral over the core is the gravitational energy change from the light element being concentrated at the ICB and evenly mixed across the outer core. The total over the core contains contributions from the volume integral over the outer core and a surface integral at the ICB (since there is assumed no change in c in the inner core) (Gubbins et al., 2004)

$$Q_{\mathrm{g}} = \int \psi\rho\alpha_c \frac{\mathrm{D}c}{\mathrm{D}t}\mathrm{d}V_{\mathbf{2}} - \psi(r_{\mathrm{i}})\alpha_c\rho_{\mathbf{1}}4\pi r_{\mathrm{i}}^2\langle c\rangle\frac{\mathrm{d}r_{\mathrm{i}}}{\mathrm{d}t}$$
$$= \int \psi\rho\alpha_c \frac{\mathrm{D}c}{\mathrm{D}t}\mathrm{d}V_{\mathbf{2}} - \psi(r_{\mathrm{i}})\alpha_c\frac{\mathrm{D}c}{\mathrm{D}t}M_{\mathbf{2}}, \tag{2.39}$$

which defines the total gravitational energy release associated with the uneven partitioning of LE into the inner core, Q_{g}.

The final energy balance is therefore

$$Q_{\mathrm{c}} = -\int \rho C_p \frac{\mathrm{D}T}{\mathrm{d}t}\mathrm{d}V_{\mathbf{12}} + \int \alpha_T T\frac{\mathrm{D}P}{\mathrm{D}t}\mathrm{d}V_{\mathbf{12}} + R_H\frac{\mathrm{D}c}{\mathrm{D}t}M_{\mathbf{2}} - \int \rho R_H\frac{\mathrm{D}c}{\mathrm{D}t}\mathrm{d}V_{\mathbf{2}}$$
$$+ \int \rho h\mathrm{d}V_{\mathbf{12}} + 4\pi r_{\mathrm{i}}^2\rho_{\mathbf{1}}L\frac{\mathrm{d}r_{\mathrm{i}}}{\mathrm{d}t} + \int \psi\rho\alpha_c\frac{\mathrm{D}c}{\mathrm{D}t}\mathrm{d}V_{\mathbf{2}} - \psi(r_{\mathrm{i}})\alpha_c\frac{\mathrm{D}c}{\mathrm{D}t}M_{\mathbf{2}}. \tag{2.40}$$

The first term on the RHS gives the total energy released from secular cooling of the core, Q_{s}

$$Q_{\mathrm{s}} = -\int \rho C_p\frac{\mathrm{D}T}{\mathrm{D}t}\mathrm{d}V_{\mathbf{12}}. \tag{2.41}$$

The next term on the RHS is the pressure heating, Q_{P}, which arises from the slow contraction as the core cools

$$Q_{\mathrm{P}} = \int \alpha_T T\frac{\mathrm{D}P}{\mathrm{D}t}\mathrm{d}V_{\mathbf{12}}. \tag{2.42}$$

In the third term on the RHS is the total heat of reaction, Q_{H}

$$Q_{\mathrm{H}} = R_H\frac{\mathrm{D}c}{\mathrm{D}t}M_{\mathbf{2}} - \int \rho R_H\frac{\mathrm{D}c}{\mathrm{D}t}\mathrm{d}V_{\mathbf{2}}. \tag{2.43}$$

In an ideal solution, there is no change in enthalpy due to mixing (page 97 Keszei, 2013), therefore the heat of reaction only arises in departures from an ideal solution. If R_H is independent of radius then R_H can be taken outside of the integral, as can $\mathrm{D}c/\mathrm{D}t$ since this is always assumed uniform, which would lead to $Q_{\mathrm{H}} = 0$. All heat absorbed (released) by light element rejected from the inner core is balanced out by the heat released (absorbed) as the light element mixes across the outer core (Gubbins et al., 2004). Therefore Q_{H} is non-zero only if the core is not an ideal solution and R_H varies with radius.

The 4th term in Eq. 2.40 is simply the total heat released by the decay of radiogenic

isotopes, Q_r

$$Q_\mathrm{r} = \int \rho h \mathrm{d}V. \tag{2.44}$$

The latent heat release, Q_l, takes the form

$$Q_\mathrm{l} = 4\pi r_\mathrm{i}^2 \rho_\mathbf{1} L \frac{\mathrm{d}r_\mathrm{i}}{\mathrm{d}t} \tag{2.45}$$

The melting point, T_m, is elevated with increasing pressure and so the slow contraction of the core slowly increases the pressure everywhere in the core over time. This small, slow incease will result in additional growth of the inner core which Gubbins et al. (2003) refer to as Q_PL. Gubbins et al. (2004) show that at present the effect is relatively small, less than 2 TW at present, which decreases with inner core radius, becoming zero at times in Earth's history when there is no inner core. Neglecting this term will force an increase in the cooling rate for the present day but quickly becomes insignificant going back in time, particularly if the inner core is young. In light of this I concede to neglect the impact of pressure changes on the inner core growth and so for simplicitity omit their derivation which can be found in Gubbins et al. (2003).

The final term on the RHS of 2.40 is the previously defined gravitational energy, Q_g. Equation 2.40 balances the heat extracted by the mantle at the CMB with the sources of energy within the core, written in the simple manner

$$Q_\mathrm{c} = Q_\mathrm{s} + Q_\mathrm{l} + Q_\mathrm{g} + Q_\mathrm{H} + Q_\mathrm{r} + Q_\mathrm{P} \tag{2.46}$$

The cooling rate is unknown and is the parameter of interest to solve for, section 2.5 details the numerical method by which the energy terms are estimated in order to solve for DT/Dt. Note that the magnetic field, $\mathbf{B}$, does not feature in 2.40 and so evaluation of only the energy terms cannot provide insight into the capacity for the core to generate a magnetic field.

The energy extracted from convection to produce magnetic field is re-dissipated into the core by resistive heating (Braginsky and Roberts, 1995; Gubbins et al., 2003). This resistive heating, ohmic dissipation, is a non-reversible process resulting in an increase in entropy. Consideration of the entropy budget of the core may therefore contain information regarding the generation of magnetic field and will be shown to allow constraints to be placed upon the evolution of the core in order to power a dynamo.

2.2.2 Entropy balance of the core

An analogous procedure is taken here in deriving the energy budget so many equivalent terms will reappear in this section. The entropy change at a point within the core is given as (Hewitt et al., 1975; Gubbins et al., 2003; Nimmo, 2015)

$$\rho\frac{\mathrm{D}s}{\mathrm{D}t} = -\frac{\nabla\cdot\mathbf{q}}{T} + \frac{\mu\nabla\cdot\mathbf{i}}{T} + \frac{\rho h}{T} + \frac{\Phi}{T}, \tag{2.47}$$

where Φ/T is the combined entropy gain by viscous and ohmic dissipation. Both types of dissipation depend upon either the fluid flow or magnetic field throughout the outer core, in particular the small scale structure, which we cannot observe. As previously discussed we can infer the fluid motions at the CMB but not throughout the core. Likewise for the magnetic field, we can downward continue the surface field, but only the large scale field and only to the CMB due to the masking of the smaller scales by the crustal field. Braginsky and Roberts (1995) suggest that the viscous heating, Q_v, can be approximated as $Q_\mathrm{v} \approx \left(\frac{\nu}{\eta}\right) Q_\mathrm{j}$, where ν and η are the kinematic viscosity and magnetic diffusivity, and Q_j is the ohmic heating. Typical values of the core, $\eta \approx 0.6$ $\mathrm{m}^2\ \mathrm{s}^{-1}$ and $\nu \approx 5\times10^{-7}$ $\mathrm{m}^2\ \mathrm{s}^{-1}$ (Jones, 2015) gives the viscous dissipation about 6 orders of magnitude smaller than the ohmic dissipation. However, Q_v might be a larger fraction of the total dissipation if the length scale over which Q_v occurs is smaller than the relevant length scale for Q_j. Even if this is the case, it is unlikely that the ratio of length scales will be large enough for Q_v to be significant, so the total dissipation is therefore approximated to be only the ohmic dissipation, $\Phi = Q_\mathrm{j}$.

The first 2 terms on the RHS of 2.47 describe the entropy flux due to heat and mass flux. Using the vector identity (Eq. 2.4), we have

$$-\frac{1}{T}\nabla\cdot\mathbf{q} = -\nabla\cdot\left(\frac{\mathbf{q}}{T}\right) - \mathbf{q}\cdot\frac{\nabla T}{T^2} \tag{2.48}$$

$$\frac{\mu}{T}\nabla\cdot\mathbf{i} = \mu\left[\nabla\cdot\left(\frac{\mathbf{i}}{T}\right) + \mathbf{i}\cdot\frac{\nabla T}{T^2}\right], \tag{2.49}$$

where the quotient rule has been used to substitute $\nabla(T^{-1}) = -T^{-2}\nabla T$. Using the definitions of the heat flux (Eq 2.18) and adding together 2.48 and 2.49 gives

$$-\frac{1}{T}\nabla\cdot\mathbf{q} + \frac{\mu}{T}\nabla\cdot\mathbf{i} = -\nabla\cdot\left(\frac{\mathbf{q}}{T}\right) + k\left(\frac{\nabla T}{T}\right)^2 - \mathbf{i}\frac{\beta T}{\alpha_\mathrm{D}}\frac{\nabla T}{T^2} + \mu\nabla\cdot\left(\frac{\mathbf{i}}{T}\right). \tag{2.50}$$

From the definition of the mass flux (Eq. 2.19) the thermal gradient is

$$\nabla T = \frac{-\alpha_{\mathrm{D}} \nabla \mu - \mathbf{i}}{\beta} \tag{2.51}$$

$$\Rightarrow -\mathbf{i} \frac{\beta T}{\alpha_{\mathrm{D}}} \frac{\nabla T}{T^2} = \frac{\mathbf{i}^2}{\alpha_{\mathrm{D}} T} + \frac{\mathbf{i} \cdot \nabla \mu}{T}, \tag{2.52}$$

which finally gives 2.50 as

$$-\frac{1}{T} \nabla \cdot \mathbf{q} + \frac{\mu}{T} \nabla \cdot \mathbf{i} = -\nabla \cdot \left(\frac{\mathbf{q}}{T} \right) + k \left(\frac{\nabla T}{T} \right)^2 + \frac{\mathbf{i}^2}{\alpha_{\mathrm{D}} T} + \nabla \cdot \left(\frac{\mu \mathbf{i}}{T} \right), \tag{2.53}$$

once again employing the vector identity (Eq. 2.4) to simplify the chemical potential gradient, $\nabla \mu$, terms. Substitution of 2.53 back into the original description for changes in entropy, equation 2.47, yields

$$\rho \frac{\mathrm{D}s}{\mathrm{D}t} = -\nabla \cdot \left(\frac{\mathbf{q}}{T} \right) + k \left(\frac{\nabla T}{T} \right)^2 + \frac{\mathbf{i}^2}{\alpha_{\mathrm{D}} T} + \nabla \cdot \left(\frac{\mu \mathbf{i}}{T} \right) + \frac{\rho h}{T} + \frac{\Phi}{T}. \tag{2.54}$$

Terms on the right represent the entropy change associated with a heat flux, thermal conduction, mass diffusion, mass flux, internal heating and the ohmic dissipation. Integrating 2.54 over a volume V, transforming the divergence terms with the divergence rule yields

$$\int \rho \frac{\mathrm{D}s}{\mathrm{D}t} \mathrm{d}V = -\oint \frac{\mathbf{q}}{T} \cdot \mathrm{d}\mathbf{S} + \int k \left(\frac{\nabla T}{T} \right)^2 \mathrm{d}V + \int \frac{\mathbf{i}^2}{\alpha_{\mathrm{D}} T} \mathrm{d}V + \oint \frac{\mu \mathbf{i}}{T} \cdot \mathrm{d}\mathbf{S} + \int \frac{\rho h}{T} \mathrm{d}V + \int \frac{\Phi}{T} \mathrm{d}V. \tag{2.55}$$

As was done with the energy balance, $\rho \mathrm{D}s/\mathrm{D}t$ may be substituted with

$$\rho \frac{\mathrm{D}s}{\mathrm{D}t} = \rho \frac{C_p}{T} \frac{\mathrm{D}T}{\mathrm{D}t} - \alpha_T \frac{\mathrm{D}P}{\mathrm{D}t} - \rho \left(\frac{\partial \mu}{\partial c} \right)_{P,T} \frac{\mathrm{D}c}{\mathrm{D}t}, \tag{2.56}$$

to write 2.55 as

$$\begin{aligned} &\int \rho \frac{C_p}{T} \frac{\mathrm{D}T}{\mathrm{D}t} \mathrm{d}V - \int \alpha_T \frac{\mathrm{D}P}{\mathrm{D}t} \mathrm{d}V - \int \rho \left(\frac{\partial \mu}{\partial c} \right)_{P,T} \frac{\mathrm{D}c}{\mathrm{D}t} \mathrm{d}V = \\ &-\oint \frac{\mathbf{q}}{T} \cdot \mathrm{d}\mathbf{S} + \int k \left(\frac{\nabla T}{T} \right)^2 \mathrm{d}V + \int \frac{\mathbf{i}^2}{\alpha_{\mathrm{D}} T} \mathrm{d}V + \oint \frac{\mu \mathbf{i}}{T} \cdot \mathrm{d}\mathbf{S} + \int \frac{\rho h}{T} \mathrm{d}V + \int \frac{\Phi}{T} \mathrm{d}V. \end{aligned} \tag{2.57}$$

To produce the entropy budget for the whole core, the same approach as was taken

for the energy budget is used, integrating over the volumes of both the inner core and outer core applying the boundary conditions at the CMB and the ICB. At the CMB $\oint \mathbf{q}/T \cdot \mathrm{d}\mathbf{S}$ can be replaced by $Q_\mathrm{c}/T_\mathrm{c}$, where T_c is the temperature of the CMB, and the expression for Q_c from the energy budget (eq. 2.40) can be substituted in. At the ICB $\langle T \rangle = 0$ (Braginsky and Roberts, 1995) and so an equivalent condition on $\mathbf{q}$ shown previously (Eq. 2.30) may be used again, but without any gravitational term, including the factor involving the ICB temperature, T_i

$$\frac{1}{T_\mathrm{i}}\hat{\mathbf{n}} \cdot \mathbf{q_2} = \frac{1}{T_\mathrm{i}}\hat{\mathbf{n}} \cdot \mathbf{q_1} + \frac{1}{T_\mathrm{i}} L \rho_\mathbf{1} \frac{\mathrm{d}r_\mathrm{i}}{\mathrm{d}t}. \tag{2.58}$$

As previously assumed, the mass flux at the CMB is zero and at the ICB, $\langle \mu \rangle = 0$ since the ICB defines the phase boundary, $\langle T \rangle = 0$, and $\langle \mathbf{i} \rangle = 0$ to conserve mass. The total entropy budget for the whole core is therefore

$$\begin{aligned}\int k \left(\frac{\nabla T}{T}\right)^2 \mathrm{d}V + \int \frac{\mathbf{i}^2}{\alpha_\mathrm{D} T}\mathrm{d}V + \int \frac{\Phi}{T}\mathrm{d}V = &- \int \left(\frac{1}{T_\mathrm{c}} - \frac{1}{T}\right) \rho C_p \frac{\mathrm{D}T}{\mathrm{D}t}\mathrm{d}V \\ &+ \int \left(\frac{1}{T_\mathrm{c}} - \frac{1}{T}\right) \alpha_T T \frac{\mathrm{D}P}{\mathrm{D}t}\mathrm{d}V - \int \rho \left(\frac{\partial \mu}{\partial c}\right)_{P,T} \frac{\mathrm{D}c}{\mathrm{D}t}\mathrm{d}V \\ &+ \left(\frac{1}{T_\mathrm{c}} - \frac{1}{T_\mathrm{i}}\right) Q_\mathrm{l} + \frac{Q_\mathrm{g}}{T_\mathrm{c}} + \int \left(\frac{1}{T_\mathrm{c}} - \frac{1}{T}\right) \rho h \mathrm{d}V. \end{aligned} \tag{2.59}$$

On the LHS are the dissipative entropy sources arising from thermal conduction, E_k, mass diffusion, E_α, and ohmic heating, E_J. The first term on the RHS is the entropy change from secular cooling, E_s. The next 2 terms are the entropy changes from pressure changes, E_P, and the heat of reaction, E_H. The final 3 terms are entropy changes from latent heat release, E_L, gravitational energy, E_g, and finally radiogenic heating, E_r. The energy and entropy balances for the core may therefore be simply written as

$$Q_\mathrm{c} = Q_\mathrm{s} + Q_\mathrm{g} + Q_\mathrm{l} + Q_\mathrm{r} + Q_\mathrm{P} + Q_\mathrm{H} \tag{2.60}$$

$$E_\mathrm{k} + E_\alpha + E_\mathrm{J} = E_\mathrm{s} + E_\mathrm{P} + E_\mathrm{H} + E_\mathrm{L} + E_\mathrm{g} + E_\mathrm{r}. \tag{2.61}$$

Later, section 2.5 describes the method that calculates the cooling rate of the core from 2.60 allowing an estimation E_J from calculation of all other terms in 2.61. First, however, the next section details the representation of the stable layer to be included.

2.3 Stable stratification 1D representation

In the previous section, the energy and entropy balance was reviewed for a scenario in which convection maintains the isentropic basic state throughout the core, as is the standard model. From here on, I will detail the changes I make in order to model the stable layer. Within a stably stratified layer, there is no vigorous convection since vertical motion is suppressed, deviating away from the previously used time averaged basic state. An alternative state for the stable layer that merges with the basic state of the underlying convection is needed.

Although the density gradient is stabilising within the stable layer there can still be fluid motions. Forcing from the underlying convective region may induce dynamic waves but any vertical motion will be damped by the stabilising density gradient and contain even smaller density anomalies than that of convection. Some of the longest period waves associated with a stable layer inferred from observations are MAC waves, which have recently been used to explain variations in the dipole moment of the magnetic field and rotation rate of the Earth on the decadal timescale (Buffett et al., 2016). Predicted gravity waves from the same study would oscillate with a period of hours to days, much faster than my timescale of interest. I make the assumption that fluid velocity induced by waves are assumed to average out to zero in my model as they operate on these much smaller timescales, similar to the convective timescale. Horizontally driven flows within the layer, such as those that are driven by a possible heterogeneous heat flow (Christensen, 2018), are also assumed to have no net effect on the stability of the layer or the vertical transport of heat and mass.

Interfacial dynamics at the boundary between the stable layer and the convection below, such as penetrative convection or shear flow instabilities may still initiate vertical motion of fluid into the stable stratification (Turner, 1979; Lister, 1995; Takehiro and Lister, 2001; Bouffard et al., 2020) promoting mixing. As the stable density gradient becomes stronger towards the CMB, these dynamics are more greatly subdued and so I anticipate a zone with some thickness over which the transition from vigorous convection to stratified fluid takes place (figure 2.3).

The size of this transition zone will be dictated by the ability of turbulent motion of fluid to overcome the stabilising density gradient. Anomalies associated with a chemical layer are expected to be on the order of 1 wt% or more excess of light element at the CMB based on fits to seismological velocity models (Helffrich and Kaneshima, 2010; Brodholt and Badro, 2017). Given that the chemical expansivities, α_c, for light elements in the core are also on the order of 1 (Gubbins et al., 2004), the layer is predicted to have a peak density anomaly of around 1%. Assuming the density gradient is linear over a 300 km thick layer, this gives a stabilising density gradient on the order 10^{-3} % km^{-1}. Density anomalies associated with driving the dynamics in the transition zone

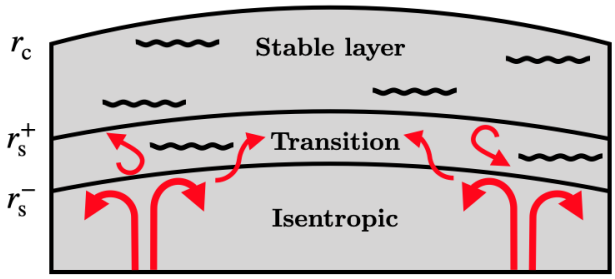

Figure 2.3: Cross section through the core showing the transition from the isentropic region to the stable layer. The transition region comprises of the zone over which fluid advection becomes less significant and diffusion becomes more important as the primary transport mechanism of heat and mass.

will be similar to the density anomalies driving convection, 10^{-6}% (Stevenson, 1987), and so are significantly smaller when compared to the change in density across even just the lower 1 km of the layer. Penetration of fluid into the stable layer is therefore limited to a small distance, resulting in a thin transition zone. This is consistent with Gubbins and Davies (2013) who argue that both shear flow instabilities and penetrative convection cannot penetrate into a layer formed via barodiffusion further than 1 km at most.

Takehiro and Lister (2001) suggest that for a Brunt-Väisälä frequency similar to that of Gubbins and Davies (2013) and Buffett and Seagle (2010), convective columns must be $\mathcal{O}$(1000 km) wide to penetrate through the layer. In the core, where the viscosity is very small, convective columns will only be on the order of 1 km wide (Gubbins and Davies, 2013) and so the penetrative depth is again very small. Layers of a thermal origin are typically predicted to have smaller stabilising gradients, giving Brunt-Väisälä frequencies up to an order of magnitude smaller than for a chemical origin (Lister and Buffett, 1998). This reduced strength however only reduces the requirement on the width of penetrating convective columns to $\mathcal{O}$(100 km) (Takehiro and Lister, 2001), still much larger than predicted for the Earth.

A further complication to the dynamics arises due to the different diffusive rates for mass and temperature. Double diffusive instabilities can be induced even when the net potential density stratification is stabilising, and can exhibit a range of behaviour depending upon both the relative gradients and diffusivities for mass and temperature. Finger convection may be induced in a thermal layer if the chemical gradient is destabilising, comprising of thin plumes of chemically enriched fluid that are able to penetrate through the stable temperature field (Turner, 1979; Radko, 2012). In the opposite case, when temperature is the destabilising component in a stable chemical layer, oscillating instabilities with increasing amplitudes can develop (Turner, 1979; Radko, 2012).

The nature of these primary double diffusive instabilities, and if they can induce further secondary instabilities, is uncertain in the context of planetary cores since the effects of rotation and magnetic forces on the phenomena are not clear (Garaud, 2018). I will therefore assume that they act only inside the transition zone. Since the transition region is thin, the region is assumed to have a negligible impact upon the global energy and entropy balance and so I make the simplifying assumption that the layer is infinitesimally thin. The assumption is also a practical one, as the complicated dynamics within the transition zone are not well understood, requiring expensive 3D dynamical studies to investigate, and so a more appropriate representation than the parameterised 1D approach used here is not yet clear. The dynamics of the transition zone will be simply represented by setting the boundary conditions on heat and mass to those regions adjacent to it, where specific choices of boundary conditions are discussed in section 2.7.

The averaging procedure on the stable layer therefore results in a hydrostatic 1D representation for the stable layer, the same as the rest of the core. The 1D profiles for temperature and composition are found by solutions to their respective spherical diffusion equations, rather than adiabatic and well mixed.

$$\rho C_p \frac{\partial T}{\partial t} = \nabla \cdot (-k \nabla T) \tag{2.62}$$

$$\rho \frac{\partial c}{\partial t} = -\nabla \cdot \left(-\rho D \frac{\partial c}{\partial r} + \alpha_c \alpha_D g \right), \tag{2.63}$$

where the mass flux, $\mathbf{i} = -\rho D \frac{\partial c}{\partial r} + \alpha_c \alpha_D g$. Terms in 2.63 represent the tendency of light elements to diffuse down the compositional gradient as well as a pressure gradient (barodiffusion), while thermodiffusion has been neglected since it is too uncertain to be reasonably included at this stage. (Gubbins et al., 2004).

2.4 Global energy and entropy equations with stable stratification

Based on the previous 1D representation of the bulk of the core and the stable layer, the core is separated into 2 main regions: the stable layer and isentropic interior. The isentropic interior comprises of the solid inner core and convecting liquid outer core, while the stable layer is assumed to be the static fluid above the isentropic interior and beneath the CMB, figure 2.4. Three key radii are the inner core radius, r_{i}, the stable layer interface, r_{s}, and the CMB, r_{c}. Some parameters, such as the mass fraction of light element may have distinctive values across all three regions and so for simplicity,

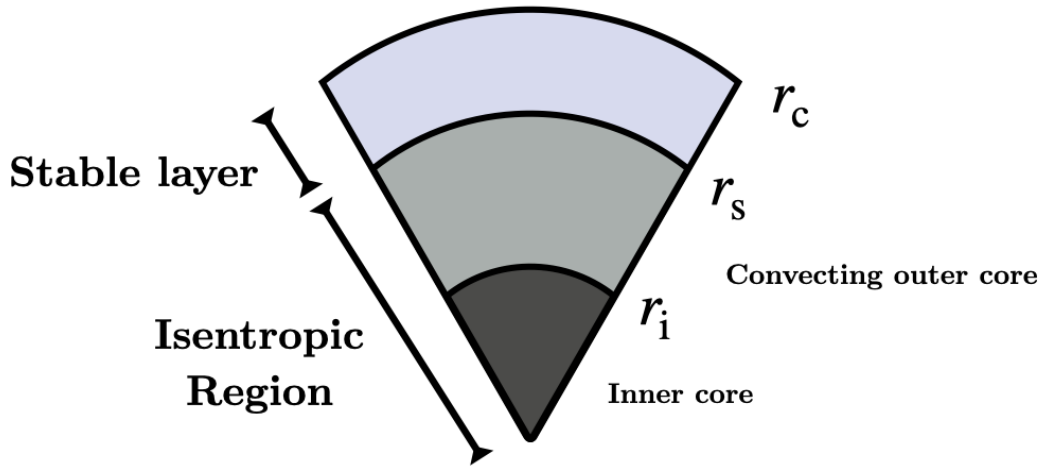

Figure 2.4: 1D representation of the core. The ICB is at the radius r_i, the stable layer interface at r_s, and the CMB at r_c. The isentropic region is defined as $0 \leq r \leq r_s$ and the stable layer at $r_s \leq r \leq r_c$.

the inner core, convecting outer core and stable layer will be referred to numerically as regions 1,2,and 3 respectively. This way, parameters with a bold numerical subscript will refer to the value in the corresponding region (e.g. $c_{\mathbf{1}}$, $c_{\mathbf{2}}$, $c_{\mathbf{3}}$).

The equations for conservation of energy and entropy at a point (Eq. 2.2 and 2.47) are still valid throughout the stable layer and so the same assumptions that lead to their integration over a volume are used here (Eq. 2.17 and 2.57). At the stable layer interface, r_s, there are no phase changes associated with the layer and so when integrating over the volume of the outer core, all terms in the energy balance take the same form except for the gravitational energy, Q_g, which is an integration over the volume over which the light element is redistributed, assumed to only include the convecting region of the outer core, $V_{\mathbf{2}}$ (Eq. 2.64 below). This assumes that the entire layer is sufficiently stabilising such that no compositionally enriched fluid below can mix into the layer, as the transition region is thin. Whilst terms like the secular cooling take the same form, the temperature and compositional profiles in the layer deviate away from the isentropic region, therefore introducing differences in the total integrals within the energy and entropy balances. Hence it will be useful to separate out the contributions between the isentropic interior and the stable layer to more transparently show their respective contributions and the impact of the boundary conditions on the 2 regions.

I will also make some more simplifying assumptions that I will use throughout this thesis. Firstly, the presence of potassium in the core, expected to be the main source of any radioactive isotopes present, is likely not large enough to impact the thermal history of the core (Xiong et al., 2018). I therefore neglect Q_r and E_r. Secondly, I

will neglect Q_{P} and E_{P} since Gubbins et al. (2003) show that they represent small contributions to the energy and entropy budgets, within the error of uncertainty of C_p, and hence Q_{s}.

Finally, the effects from heat of mixing, Q_{H} and E_{H}, are also ignored. As previously mentioned, if R_H is independent of radius then Q_{H} within the isentropic region is zero (Gubbins et al., 2004) since $\mathrm{D}c/\mathrm{D}t$ is also uniform throughout the convecting liquid. Calculations of $(\partial\mu/\partial c)_{P,T}$, which are required to evaluate R_H, predict a small contribution to E_{H}, 2 orders of magnitude smaller than other leading terms such as E_{k} or E_{s} (Davies, 2014) due to the small values of $(\partial\mu/\partial c)_{P,T}$ and $\mathrm{D}c/\mathrm{D}t$. Within the stable layer, $\mathrm{D}c/\mathrm{D}t$ will vary with radius as given by the diffusion solution for mass (Eq. 2.63) but is not 2 orders of magnitude larger and so can also be ignored in the layer as well. This is confirmed by calculations in chapter 4.

For the isentropic interior, for which integrals are evaluated over the volume, $V_{\mathbf{12}}$, the energy budget is

$$Q^{-}_{\mathrm{r_s}} = \overbrace{-\int \rho C_p \frac{\mathrm{D}T}{\mathrm{d}t}\mathrm{d}V_{\mathbf{12}}}^{Q^{\mathrm{is}}_{\mathrm{s}}} + \overbrace{4\pi r_{\mathrm{i}}^2 \rho_{\mathbf{1}} L \frac{\mathrm{d}r_{\mathrm{i}}}{\mathrm{d}t}}^{Q_{\mathrm{l}}} + \overbrace{\int \psi \rho \alpha_c \frac{\mathrm{D}c}{\mathrm{D}t}\mathrm{d}V_{\mathbf{2}}}^{Q_{\mathrm{g}}}, \tag{2.64}$$

where $Q^{-}_{\mathrm{r_s}}$ is the heat flow out of the isentropic region and into the transition zone at r_{s}. The superscript '-' refers to the heat flow into the bottom of the transition zone. The superscript 'is' in the secular cooling refers to the fact that this is not the full secular cooling of the core, Q_{s}, but just the contribution from the volume $V_{\mathbf{12}}$. The energy budget for the stable layer meanwhile is evaluated over the volume of the layer, $V_{\mathbf{3}}$, and is a simple balance between the secular cooling of the layer and the heat flows at the boundaries

$$Q_{\mathrm{c}} = \overbrace{-\int \rho C_p \frac{\mathrm{D}T}{\mathrm{d}t}\mathrm{d}V_{\mathbf{3}}}^{Q^{\mathrm{sl}}_{\mathrm{s}}} + Q^{+}_{\mathrm{r_s}}, \tag{2.65}$$

where $Q^{+}_{\mathrm{r_s}}$ is the heat flow out of the transition zone and into the layer, the superscript + referring to the top of the transition zone at r_{s}. The total secular cooling of the core is then $Q_{\mathrm{s}} = Q^{\mathrm{is}}_{\mathrm{s}} + Q^{\mathrm{sl}}_{\mathrm{s}}$.

The entropy budget is determined for the entire core, since I cannot know the radial distribution of E_{J} and therefore cannot construct an entropy budget separately for each region. Individual terms can be calculated for each region independently but the whole budget must be used to calculate a total value for E_{J}. After neglecting the pressure,

heat of reaction and internal heating terms, the entropy budget becomes

$$\overbrace{\int k\left(\frac{\nabla T}{T}\right)^2 \mathrm{d}V_{\mathbf{123}}}^{E_\mathrm{k}} + \overbrace{\int \frac{\mathbf{i}^2}{\alpha_\mathrm{D} T}\mathrm{d}V_{\mathbf{123}}}^{E_\alpha} + \overbrace{\int \frac{\Phi}{T}\mathrm{d}V_{\mathbf{123}}}^{E_\mathrm{J}} = \overbrace{-\int\left(\frac{1}{T_\mathrm{c}}-\frac{1}{T}\right)\rho C_p \frac{\mathrm{D}T}{\mathrm{D}t}\mathrm{d}V_{\mathbf{123}}}^{E_\mathrm{s}} + \overbrace{\left(\frac{1}{T_\mathrm{c}}-\frac{1}{T_\mathrm{i}}\right)Q_\mathrm{l}}^{E_\mathrm{L}} + \overbrace{\frac{Q_\mathrm{g}}{T_\mathrm{c}}}^{E_\mathrm{g}}, \tag{2.66}$$

where $V_{\mathbf{123}}$ is the volume of all 3 regions.

This concludes the derivation of the energy and entropy budgets for my 1D parameterised model of the core with stable stratification. The following sections will detail the numerical methods applied to estimates these terms, solving the diffusion solutions in the stable layer, and the scheme for evolving the layer size over time, in order to simulate the thermo-chemical evolution of the core.

2.5 Evaluating the energy and entropy budgets

This section describes the numerical methods for evaluating the energy and entropy budgets in order to compute the cooling rate of the core for both the isentropic region and the stable layer.

2.5.1 Isentropic region

In the isentropic core the numerical scheme employed is equivalent to those previously used for a fully isentropic core (Gubbins et al., 2003; Gubbins et al., 2004; Davies, 2014; Davies et al., 2015). The temperature is assumed to follow an adiabat, given previously (Eq. 1.3) and restated here

$$T_\mathrm{a}(r) = T_\mathrm{cen}\exp\left(-\int_0^r \frac{g\gamma}{\Phi_\mathrm{s}}\mathrm{d}r\right). \tag{2.67}$$

Assuming g, γ, and Φ_s are constant in time, $\frac{1}{T_\mathrm{a}}\mathrm{D}T_\mathrm{a}/\mathrm{D}t$ is constant allowing the spatially varying cooling rate along the adiabat to be normalised to the cooling rate at a particular radius (Gubbins et al., 2003)

$$\frac{\mathrm{D}T_\mathrm{a}}{\mathrm{D}t} = \frac{T_\mathrm{a}}{T_\mathrm{cen}}\frac{\mathrm{d}T_\mathrm{cen}}{\mathrm{d}t}, \tag{2.68}$$

where I have chosen to normalise to the temperature at the center of the core, T_cen.

The growth rate of the inner core may be related to the cooling rate by considering

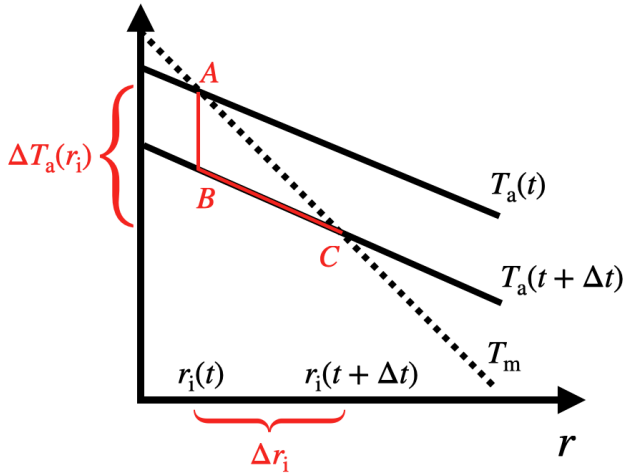

Figure 2.5: Schematic diagram showing how a change in inner core radius is related to a change in temperature as the core cools. The path A-B-C must represent the same change in temperature as the direct path A-C.

the relative gradients in the adiabat and the melting temperature (Gubbins et al., 2003). I assume that the melting curve is always steeper than the adiabat and so the inner core grows from the inside out as the core cools. For a drop in temperature of $\Delta T_{\rm cen}$, the ICB cools by $(T_{\rm i}/T_{\rm cen})\Delta T_{\rm cen}$. The ICB is defined by the intersection of the temperature profile and the melting curve, $T_{\rm m}$, which by the small cooling is advanced by $\Delta r_{\rm i}$ as shown on figure 2.5. When these changes in temperature and radius are small the gradients in $T_{\rm a}$ and $T_{\rm m}$ can be approximated as linear in the vicinity of the ICB. The change in temperature between points A and C must be the same as the change in temperature first between A and B and then B to C (Fig. 2.5). This gives the relation

$$\frac{T_{\rm i}}{T_{\rm cen}}\Delta T_{\rm cen} + \frac{\partial T_{\rm a}}{\partial r}\Delta r_{\rm i} = \frac{\partial T_{\rm m}}{\partial r}\Delta r_{\rm i}, \tag{2.69}$$

which gives

$$\frac{{\rm d}r_{\rm i}}{{\rm d}t} = \left(\frac{\partial T_{\rm m}}{\partial r} - \frac{\partial T_{\rm a}}{\partial r}\right)^{-1} \frac{T_{\rm i}}{T_{\rm cen}} \frac{{\rm d}T_{\rm cen}}{{\rm d}t} = C_r \frac{{\rm d}T_{\rm cen}}{{\rm d}t}. \tag{2.70}$$

The gravitational energy term depends upon the enrichment of the outer core due to inner core growth. From the previous relation of conservation of light element expelled form the inner core (Eq. 2.31)

$$\frac{{\rm D}c}{{\rm D}t} = \frac{\rho_1 4\pi r_{\rm i}^2 (c_2 - c_1)}{M_2} \frac{{\rm d}r_{\rm i}}{{\rm d}t} = C_c \frac{{\rm d}r_{\rm i}}{{\rm d}t} = C_c C_r \frac{{\rm d}T_{\rm cen}}{{\rm d}t}. \tag{2.71}$$

Substituting in for the cooling rate on the adiabat, inner core growth rate, and

the rate of enrichment of light element in the liquid using the relations above (2.68, 2.70 and 2.71) in the energy and entropy budgets (Eqs. 2.64 and 2.66) allows them to be normalised to the cooling rate of the core. The secular cooling terms $Q_{\mathrm{s}}^{\mathrm{is}}$ and $E_{\mathrm{s}}^{\mathrm{is}}$ become

$$Q_{\mathrm{s}}^{\mathrm{is}} = -\frac{\mathrm{d}T_{\mathrm{cen}}}{\mathrm{d}t} \int \rho C_p \frac{T_{\mathrm{a}}}{T_{\mathrm{cen}}} \mathrm{d}V_{\mathbf{12}} \tag{2.72}$$

$$E_{\mathrm{s}}^{\mathrm{is}} = -\frac{\mathrm{d}T_{\mathrm{cen}}}{\mathrm{d}t} \int \left(\frac{T_{\mathrm{a}}}{T_{\mathrm{c}}} - 1 \right) \frac{1}{T_{\mathrm{cen}}} \rho C_p \mathrm{d}V_{\mathbf{12}}. \tag{2.73}$$

Latent heat terms may be written

$$Q_{\mathrm{l}} = 4\pi r_{\mathrm{i}}^2 \rho_{\mathbf{1}} L C_r \frac{\mathrm{d}T_{\mathrm{cen}}}{\mathrm{d}t} \tag{2.74}$$

$$E_{\mathrm{L}} = \left(\frac{1}{T_{\mathrm{c}}} - \frac{1}{T_{\mathrm{i}}} \right) 4\pi r_{\mathrm{i}}^2 \rho_{\mathbf{1}} L C_r \frac{\mathrm{d}T_{\mathrm{cen}}}{\mathrm{d}t}. \tag{2.75}$$

So far the equations have been derived assuming only one alloying light element. To extend to multiple light elements, the summation across all light element species, 'x', can be taken. The gravitational energy terms become

$$Q_{\mathrm{g}} = \frac{\mathrm{d}T_{\mathrm{cen}}}{\mathrm{d}t} \int \psi \rho \sum_x \alpha_{c,x} C_{c,x} C_r \mathrm{d}V_{\mathbf{2}} \tag{2.76}$$

$$E_{\mathrm{g}} = \frac{\mathrm{d}T_{\mathrm{cen}}}{\mathrm{d}t} \frac{1}{T_{\mathrm{c}}} \int \psi \rho \sum_x \alpha_{c,x} C_{c,x} C_r \mathrm{d}V_{\mathbf{2}}. \tag{2.77}$$

The entropy change due to conduction and mass diffusion are not dependent upon the cooling rate and so can be simply calculated by numerically integrating the volume integrals. The chemical gradient is zero and so the mass flux only contains the barodiffusive contribution, $\mathbf{i} = -\rho D \nabla c + \alpha_c \alpha_D g = \alpha_c \alpha_D g$

$$E_{\mathrm{k}}^{\mathrm{is}} = \int k \left(\frac{\nabla T_{\mathrm{a}}}{T_{\mathrm{a}}} \right)^2 \mathrm{d}V_{\mathbf{12}} \tag{2.78}$$

$$E_{\alpha}^{\mathrm{is}} = \int \frac{\mathbf{i}^2}{\alpha_{\mathrm{D}} T_{\mathrm{a}}} \mathrm{d}V_{\mathbf{12}} \tag{2.79}$$

With the energy terms normalised to the cooling rate at the center of the core, the energy budget of the isentropic region can be simply written as

$$Q_{\mathrm{r_s}}^{-} = (\tilde{Q}_{\mathrm{s}}^{\ \mathrm{is}} + \tilde{Q}_{\mathrm{l}} + \tilde{Q}_{\mathrm{g}}) \frac{\mathrm{d}T_{\mathrm{cen}}}{\mathrm{d}t}, \tag{2.80}$$

where the tilde quantities have had the factor of $\mathrm{d}T_{\mathrm{cen}}/\mathrm{d}t$ removed. The tilde quantities can be calculated given the properties of the core and so for a given $Q_{\mathrm{r_s}}^{-}$, the cooling rate can be calculated. $Q_{\mathrm{r_s}}^{-}$ is fixed on any particular timestep and so the cooling rate of the isentropic region can be evaluated prior to the diffusion solutions in the stable layer.

2.5.2 Stable layer

In the stable layer the cooling rate cannot be normalised in any analogous way and so no tilde quantities can be defined, however the cooling rate can be directly solved from the thermal diffusion equation and used to numerically integrate any volume integrals (precise boundary conditions on this solution are detailed in 2.7). Since secular cooling is the only energy source in the layer, the secular cooling is simply the difference in heat flows at r_{c} and r_{s}^{+}

$$\overbrace{-\int \rho C_p \frac{\mathrm{D}T}{\mathrm{d}t} \mathrm{d}V_{\mathbf{3}}}^{Q_{\mathrm{s}}^{\mathrm{sl}}} = Q_{\mathrm{c}} - Q_{\mathrm{r_s}}^{+}, \tag{2.81}$$

which is just a restatement of 2.65. The contributions to the entropy budget are

$$E_{\mathrm{s}}^{\mathrm{sl}} = -\int \left(\frac{1}{T_{\mathrm{c}}} - \frac{1}{T}\right) \rho C_p \frac{\mathrm{D}T}{\mathrm{D}t} \mathrm{d}V_{\mathbf{3}} \tag{2.82}$$

$$E_{\mathrm{k}}^{\mathrm{sl}} = \int k \left(\frac{\nabla T}{T}\right)^2 \mathrm{d}V_{\mathbf{3}} \tag{2.83}$$

$$E_{\alpha}^{\mathrm{sl}} = \int \frac{\mathbf{i}^2}{\alpha_{\mathrm{D}} T} \mathrm{d}V_{\mathbf{3}} \tag{2.84}$$

All entropy terms are therefore estimated except for E_{J} which is solved by

$$E_{\mathrm{J}} = (E_{\mathrm{s}}^{\mathrm{is}} + E_{\mathrm{s}}^{\mathrm{sl}}) + E_{\mathrm{g}} + E_{\mathrm{L}} - (E_{\mathrm{k}}^{\mathrm{is}} + E_{\mathrm{k}}^{\mathrm{sl}}) - (E_{\alpha}^{\mathrm{is}} + E_{\alpha}^{\mathrm{sl}}) \tag{2.85}$$

Only the total integral of E_{J} can be calculated, indicating ohmic dissipation has occurred somewhere within the core but we cannot know where. E_{J} must be zero or greater, the dissipative process never leads to a decrease in entropy, however a negative value for E_{J} might be calculated by the budget. A negative E_{J} indicates an inconsistency somewhere in the assumptions built into the model in its current state, leading to an over/under estimation of one or more of the other entropy terms. Regardless, since we have observational evidence for a magnetic field for the majority of Earth's history (Tarduno et al., 2010), I will interpret models in which a negative E_{J} is predicted as not consistent with observations.

2.6 Core properties

In this section the numerical evaluation of core properties is explained in order that the integrals in the energy and entropy budgets might be calculated. All properties are expanded onto a radial grid such that they may be numerically integrated when calculating the volume integrals, where 500 radial nodes are ample to ensure convergence.

For core densities I use the data from PREM (Dziewonski and Anderson, 1981) which provides radial polynomials to parameterise the density in the form

$$\rho(r) = \begin{cases} \rho_{\mathbf{1}}(r) = \rho_0^{\mathrm{i}} + \rho_1^{\mathrm{i}} r + \rho_2^{\mathrm{i}} r^2 + \ \ldots\ \rho_N^{\mathrm{i}} r^N & \text{for } r \leq r_{\mathrm{i}} \\ \rho_{\mathbf{2}}(r) = \rho_0^{\mathrm{o}} + \rho_1^{\mathrm{o}} r + \rho_2^{\mathrm{o}} r^2 + \ \ldots\ \rho_N^{\mathrm{o}} r^N & \text{for } r_{\mathrm{i}} \leq r \leq r_{\mathrm{c}} \end{cases}, \tag{2.86}$$

where 2 sets of polynomials are provided, for the inner and outer cores respectively. The density of the stable layer is taken as $\rho_{\mathbf{2}}$ with an additional anomaly due to the

temperature and compositional profiles

$$\rho_{\mathbf{3}}(r) = \rho_{\mathbf{2}}(r) + \alpha_T(T_{\mathrm{a}}(r) - T_{\mathbf{3}}(r)) + \alpha_c(c_{\mathbf{2}} - c_{\mathbf{3}}(r)) \tag{2.87}$$

The PREM densities are based on the present day densities, however in the past when the inner core was smaller or entirely liquid, the outer core density was larger. The mass given by PREM is conserved by continuously adjusting ρ_0^{o} as the ICB changes without taking into account the density anomaly of the stable layer. This way the density anomaly of the layer can change in time and alter the total mass of the core, and the density profile in the isentropic region is changed in such a way to reflect the long term trend due to inner core growth. This neglects the change in $\rho_{\mathbf{2}}$ due to any mass flux at r_{s} enriching/depleting the underlying convective region however these alterations are very small, since entirely melting the inner core requires only a $\sim 0.2\%$ change to ρ_0^{o}, and so are safe to ignore.

The density anomaly in the stable layer is important for evaluating the stability of the layer, as will be discussed in section 2.7, but as the layer is only estimated to have a peak density deficit on the order of $\sim 1\%$ (Helffrich and Kaneshima, 2010), the layer has a negligible impact on the pressure and gravity, and so deviations from the isentropic state are ignored for their calculation.

Gravity across the inner core is found by

$$g(r) = \frac{4\pi G}{r^2}\int_0^r \rho_{\mathbf{1}}(r) r^2 \mathrm{d}r \quad \text{for } r \leq r_{\mathrm{i}}, \tag{2.88}$$

where G is the gravitational constant and ρ^{i} indicates the polynomials for the inner core are used. The integral is calculated analytically and can then be evaluated at the radial grid nodes. Gravity across the outer core is then given by

$$g(r) = \frac{4\pi G}{r^2}\int_0^r \rho_{\mathbf{2}}(r) r^2 \mathrm{d}r + \left(g(r_{\mathrm{i}}) - \frac{4\pi G}{r_{\mathrm{i}}^2}\int_0^{r_{\mathrm{i}}} \rho_{\mathbf{2}}(r) r^2 \mathrm{d}r\right)\left(\frac{r_{\mathrm{i}}^2}{r^2}\right) \quad \text{for } r_{\mathrm{i}} \leq r \leq r_{\mathrm{c}}, \tag{2.89}$$

which accounts for the density difference between the inner and outer cores and ensures gravity is continuous at the ICB.

The gravitational potential is required to calculate Q_{g} and is calculated such that $\psi(r_{\mathrm{c}}) = 0$ by

$$\psi(r) = -\int_r^{r_{\mathrm{s}}} g \mathrm{d}r, \tag{2.90}$$

which is found analytically and ψ is calculated on the radial grid. The choice of reference

point of ψ does not change the result since it is the change in ψ over the volume that controls Q_g.

Pressure is calculated by numerically integrating the hydrostatic pressure gradient given the fixed pressure at the CMB using the trapezoid rule

$$P(r) = -\int_{r_\mathrm{c}}^{0} \rho(r) g(r) \mathrm{d}r \quad \text{given } P(r_\mathrm{c}) = P_\mathrm{c}, \tag{2.91}$$

where the CMB pressure $P_\mathrm{c} = 136$ GPa (Dziewonski and Anderson, 1981).

I use the data of Davies et al. (2015) for values for thermal conductivity, adiabat and melting temperature. They provide a polynomial representation as a function of pressure for all 3 properties and for a range of assumed ICB density jumps. It is useful to have the adiabatic temperature and thermal conductivity as a function of radius when integrating over the volume of the core and also as their radial gradients will be used. Therefore the adiabat and conductivity pressure polynomials are refitted with radial polynomials in the form

$$T_\mathrm{a}(r) = T_\mathrm{cen} \left(1 + T_{\mathbf{1}} r + T_{\mathbf{2}} r^2 + \ \ldots \ T_N r^N\right), \tag{2.92}$$

$$k(r) = k_0 + k_{\mathbf{1}} r + k_{\mathbf{2}} r^2 + \ \ldots \ k_N r^N, \tag{2.93}$$

$$\tag{2.94}$$

where in the case of the data from Davies et al. (2015) $N = 3$ for the pressure polynomials and is kept at 3 when creating the radial polynomials. When refitting the polynomials coefficient for T_a, I normalise them to T_cen such that the polynomials are not time dependent. The choice of polynomials to represent the radial variation in core properties is motivated partly since other data I use are already represented by polynomials (PREM and the data from Davies et al. (2015)) and partly due to their simplicity to adequately fit data. Other representations have been used previously, notably for the density and adiabat which can be defined by exponential functions (Labrosse et al., 1997; Nimmo, 2015). Labrosse (2014) and Davies (2014) note that the exponential function for the adiabat produced a significantly different temperature gradient at the CMB when compared to those derived from a polynomial function. This is important when considering thermal stratification since a change in the adiabatic gradient changes the adiabatic heat flow and hence the conditions for growth of a stable layer.

The melting temperature of pure iron, $T_\mathrm{m,Fe}$, is kept as a pressure polynomial of the form

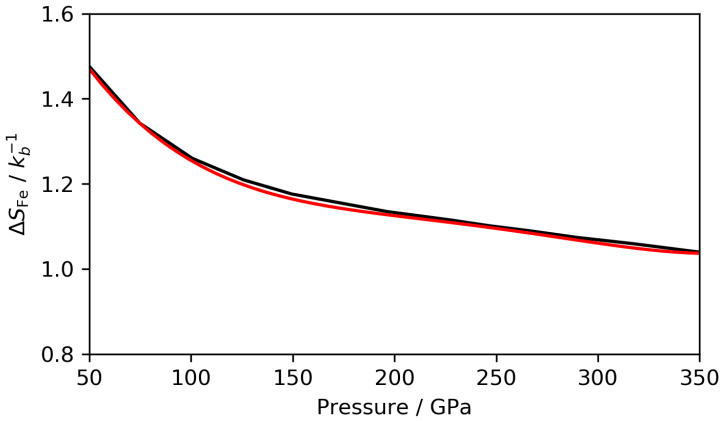

Figure 2.6: 3rd order polynomial fit (red) to the data of Alfè et al. (2002a) (black) for Δs_{Fe}, plotted in units of the Boltzmann constant k_b. RMS error of the polynomial fit is just 0.007 k_b^{-1}

$$T_{\mathrm{m,Fe}}(P) = T_{\mathrm{m}0} + T_{\mathrm{m}1}P + T_{\mathrm{m}2}P^2 + \ \ldots\ T_{\mathrm{m}N}P^N, \tag{2.95}$$

which is lowered based on the melting point depression for each light element present in the core, ΔT_{x}, calculated by the relation (Alfè et al., 2002a):

$$\Delta T_{\mathrm{x}} = \frac{T_{\mathrm{m,Fe}}}{\Delta s_{\mathrm{Fe}}}(\bar{c}_{\mathbf{1},x} - \bar{c}_{\mathbf{2},x}), \tag{2.96}$$

where Δs_{Fe} is the entropy change on freezing in pure iron at the ICB and $\bar{c}$ is the mole fraction of light element rather than the mass fraction c. Δs_{Fe} varies with pressure according to the data of Alfè et al. (2002a) which is fitted with a polynomial in the form

$$\Delta s_{\mathrm{Fe}}(P) = \Delta S_0 + \Delta S_1 P + \Delta S_2 P^2 + \ \ldots\ \Delta S_N P^N. \tag{2.97}$$

$N = 3$ gives a good fit to the data as shown on figure 2.6. This entropy change also defines the latent heat at the ICB by the relation

$$L = T_{\mathrm{m}} \Delta s_{\mathrm{Fe}}. \tag{2.98}$$

Assuming that each light element alters the melting temperature independently, the

total melting temperature is given as:

$$T_{\rm m} = T_{\rm m,Fe} + \sum_x \Delta T_x. \tag{2.99}$$

In order to calculate the light element concentration in the solid inner core, $c_x^{\rm s}$, the partitioning behaviour of light elements needs to be estimated. I use the theory of Alfè et al. (2002b) to express the equilibrium of chemical potentials between solid and liquid at the ICB as:

$$\mu_0^{\rm l} + k_b T_{\rm m} \ln(\bar{c}_x^{\rm l}) + \lambda_x^{\rm l} \bar{c}_x^{\rm l} = \mu_0^{\rm s} + k_b T_{\rm m} \ln(\bar{c}_x^{\rm s}) + \lambda_x^{\rm s} \bar{c}_x^{\rm s}, \tag{2.100}$$

where $\mu_0^{\rm s/l}$ is the chemical potential in either the solid or liquid, λ represents a linear correction to the chemical potentials to account for deviations from an ideal solution and k_b is the Boltzmann constant. Substitution of $T_{\rm m}$ using equations 2.99 and 2.96 for any one particular light element into 2.100 and rearranging yields:

$$\mu_0^{\rm l} - \mu_x^{\rm s} + \lambda_x^{\rm l} c_x^{\rm l} - \lambda_x^{\rm s} c_x^{\rm s} - k_b T_{\rm m,Fe} \ln\left(\frac{c_x^{\rm s}}{c_x^{\rm l}}\right)\left(1 + \frac{c_x^{\rm s} - c_x^{\rm l}}{\Delta S_{Fe}}\right) = 0. \tag{2.101}$$

where for a given $c_x^{\rm l}$, a value for $c_x^{\rm s}$ is found using the bisection method.

The workflow for the model is visualised by the flow chart in figure 2.7. The calculation of the energy terms allows the cooling rate to be solved by the energy budget (Eq. 2.80). The contribution of the isentropic region towards the entropy budget can also be calculated, although the full entropy budget, and hence $E_{\rm J}$, must wait until the stable layer evolution has been calculated. The stable layer evolution takes place immediately after the cooling rate is found and is detailed in the next section. $T_{\rm cen}$, the concentration of each light element, and $r_{\rm i}$ are updated by $\Delta t {\rm d}T_{\rm cen}/{\rm d}t$, $\Delta t {\rm d}c/{\rm d}t$, and $\Delta t {\rm d}r_{\rm i}/{\rm d}t$ respectively, where Δt is the time step used. A time step of 1 Myrs was found to be sufficient for convergence with <0.1% change when further increasing the timestep.

The full list of parameters used in this thesis are given in tables 2.1 and 2.2 for an iron core alloyed to silicon and oxygen

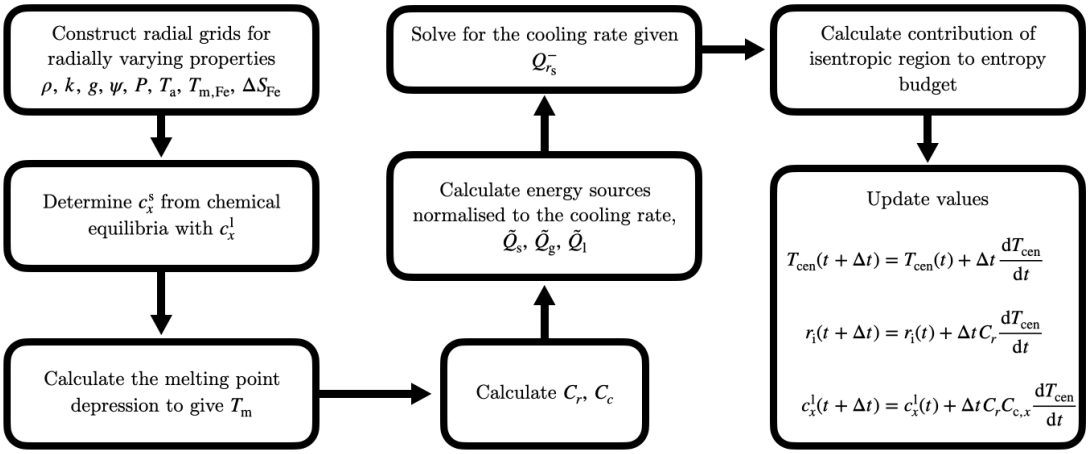

Figure 2.7: Flow chart for the numerical method of evolving the isentropic region in one times step, Δt.

Table 2.1: Parameter list. The bottom half of table splits values between oxygen and silicon.

Symbol	Meaning	Value		Units
ρ_1	Inner core density	$\rho_0^i = 13088.5$		kg m^{-3}
		$\rho_1^i = 0$		kg m $^{-4}$
		$\rho_2^i = -2.177\times10^{-10}$		kg m^{-5}
ρ_2	Outer core density	$\rho_0^i = 12581.5$		kg m^{-3}
		$\rho_1^i = -1.984\times10^{-4}$		kg m^{-4}
		$\rho_2^i = -8.974\times10^{-11}$		kg m^{-5}
		$\rho_3^i = -2.138\times10^{-17}$		kg m^{-6}
$T_{m,Fe}$	Fe melting temperature	$T_{m_0} = 1.68\times10^{3}$		K
		$T_{m_0} = 2.73\times10^{-8}$		K Pa^{-1}
		$T_{m_0} = -6.65\times10^{-20}$		K Pa^{-2}
		$T_{m_0} = 7.95\times10^{-32}$		K Pa^{-3}
α_T	Thermal expansivity	1×10^{-5}		K^{-1}
C_p	Specific heat capacity	800		J kg^{-1} K^{-1}
Δs_{Fe}	Entropy of melting	$\Delta S_0 = 1.91$		k_b
		$\Delta S_1 = -1.19\times10^{-11}$		k_bPa^{-1}
		$\Delta S_2 = 7.09\times10^{-23}$		k_b Pa^{-2}
		$\Delta S_3 = -1.94\times10^{-34}$		k_b Pa^{-3}
		$\Delta S_4 = 1.95\times10^{-46}$		k_b Pa^{-4}
		O	Si	
$\mu_x^l - \mu_x^s$	Change in chemical potential from liquid to solid Fe-x	-2.6	-0.05	eV per atom
λ_l^x	Linear correction to ideal solution in liquid Fe-x	3.25	3.6	eV per atom
λ_s^x	Linear correction to ideal solution in solid Fe-x	0	2.7	eV per atom
α_c	Chemical expansivity	1.1	0.86	-
D	Mass diffusivity	10^{-8}	5×10^{-9}	m^2 s^{-1}
$(\partial\mu/\partial c)_{P,T}$	Heat of mixing	16×10^{7}	8.6×10^{7}	J

Table 2.2: Parameters taken for different ICB density jumps, $\Delta\rho$.

Symbol	Meaning		Value			Units	
			$\Delta\rho$=600	$\Delta\rho$=800	$\Delta\rho$=1000		kgm^{-3}
T_a	Adiabatic temperature	T_1	-2.17	-5.70	-4.44	10^{-9}	K m^{-1}
		T_2	-1.98	-2.03	-1.88	10^{-14}	K m^{-2}
		T_3	-6.00	-2.12	-7.74	10^{-22}	K m^{-3}
k	Thermal conductivity	k_0	1.66	1.57	1.60	10^{2}	W m^{-1} K^{-1}
		k_1	0.59	-1.11	-2.41	10^{-6}	W m^{-2} K^{-1}
		k_2	-5.25	-4.04	-4.04	10^{-12}	W m^{-3} K^{-1}
		k_2	6.55	-7.58	-12.00	10^{-19}	W m^{-4} K^{-1}
$\bar{c}_x$	Mole fraction of light element	O	0.08	0.13	0.17		-
		Si	0.10	0.08	0.02		-

2.7 Numerical Method: Stable Layer

This section details the numerical scheme for computing the time evolution of the stable layer, and evolving the layer size in time. The diffusion equations used to compute the thermal and compositional profiles are detailed first, before the numerical methods for computing thermal stratification and chemical stratification are given in sections 2.7.1 and 2.7.2 respectively.

Within the stable layer I assume that there is no radial motion of fluid. As such, all heat and mass is transported by diffusion governed by

$$\frac{\partial T}{\partial t} = \kappa \frac{\partial^2 T}{\partial r^2} + \frac{2\kappa}{r}\frac{\partial T}{\partial r} + \frac{1}{\rho C_p}\frac{\partial k}{\partial r}\frac{\partial T}{\partial r} \tag{2.102}$$

$$\frac{\partial c}{\partial t} = D\frac{\partial^2 c}{\partial r^2} + \frac{2D}{r}\frac{\partial c}{\partial r} - \frac{\alpha_c \alpha_{\mathrm{D}}}{\rho}\left(\frac{\partial g}{\partial r} + \frac{2g}{r}\right), \tag{2.103}$$

where a radially varying thermal conductivity is accounted for in 2.62. While a radially varying diffusivity for mass can be accommodated in my numerical method, Pozzo et al. (2013) show that the mass diffusivity, D, for O, Si, and S can be reasonably taken as constant and so I neglect any variatation in radius of D. The term originating from a radially varying density in equation 2.103 was also neglected due to its very small contribution. A Crank-Nicolson discretisation is used to numerically solve 2.102 and 2.103 on an evenly spaced radial grid. The grid spacing is treated as an input parameter, throughout this thesis taken to be 1 grid point per km. 10 grid points are chosen when the layer is thinner than 10 km, necessary when the layer is first initialised to a thin region of 1 km. The domain size is never precisely an integer number of km's

in and so the closest resolution to 1 per km is taken. The Crank-Nicolson discretisation is stable given the condition

$$0.5 > \frac{Y\Delta t}{2\Delta r^2}, \tag{2.104}$$

where Y is the diffusivity. The grid spacing is an input and so if this condition is not met for the specified time step, the solution is run n times with a time step of $\Delta t/n$ such that $0.5 > Y\Delta t/2n\Delta r^2$. The same boundary conditions are fixed for all n calculations. This is only necessary when the layer is first initialised to a thin layer (1 km) and so the grid spacing is very small.

To find solutions to equations 2.102 and 2.103, relevant boundary conditions are required, which will depend upon the physical process that is generating stable stratification. I will explain the boundary conditions used in the case of either thermally stable or chemically stable layers separately in sections 2.7.1 and 2.7.2 respectively. I will only consider the diffusion of one light element species within the stable layer. Whilst the model may be extended to solve for the diffusion of multiple light elements, doing so significantly complicates the boundary conditions and numerical scheme for evolving the layer.

During one iteration of the model radial profiles within the isentropic region and stable layer are evolved independently. The cooling and enrichment in light element of the isentropic region is calculated by the methods detailed in the sections 2.7.1 and 2.7.2. The solutions to Eq. 2.102 and Eq. 2.103 provide the evolution of thermal and compositional profiles within the stable layer and there are 2 conditions that the new thermal and compositional profiles must satisfy in order to remain stably stratified and unmixed with the isentropic region. First, the potential density, ρ_Θ must be lower than the isentropic region, else the fluid will sink adiabatically into the convecting fluid, stated as

$$\rho_\Theta(r) = -\alpha_T(T_{\mathbf{3}}(r) - T_{\mathrm{a}}(r)) - \alpha_c(c_{\mathbf{3}}(r) - c_{\mathbf{3}}) \geq 0, \tag{2.105}$$

where I am defining the potential density as the density relative to the theoretical density of the fluid if extrapolated along the isentrope of the underlying isentropic region.

Secondly, the potential density gradient must be negative to ensure static stability

$$-\alpha_T\left(\frac{\partial T_{\mathbf{3}}}{\partial r} - \frac{\partial T_{\mathrm{a}}}{\partial r}\right) - \alpha_c\frac{\partial c_{\mathbf{3}}}{\partial r} \geq 0. \tag{2.106}$$

If these criteria are not met at any radius then the region of the stable layer below

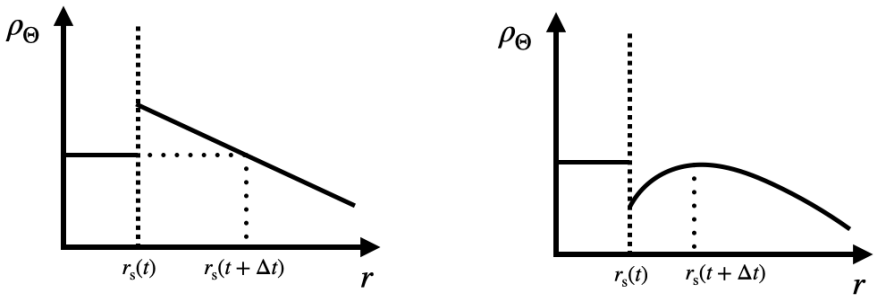

Figure 2.8: Conditions for the stable layer to recede. Either the potential density in the layer is higher (left) that the isentropic region or it has a positive gradient (right) which leads to vertical mixing. In either eventuality, the stable layer interface is moved such that the entire stable layer satisfies conditions 2.7 and 2.106

that radius is assumed to mix into the isentropic region, causing the layer to recede (Fig. 2.8). If the entire stable layer satisfies these criteria, discontinuities in temperature and/or composition at r_s between the isentropic region and stable layer are used to inform the growth of the stable layer as described below for both thermal (section 2.7.1) and chemical (section 2.7.2) stratification.

2.7.1 Thermal Stratification

Thermal stratification results from the mantle extracting a sub-adiabatic heat flow at the CMB, Q_c, from the core. The CMB heat flow provides a condition on the thermal gradient at r_c

$$\frac{\partial T_{\mathbf{3}}(r_\mathrm{c})}{\partial r} = -\frac{Q_\mathrm{c}}{4\pi r_\mathrm{c}^2 k(r_\mathrm{c})}. \tag{2.107}$$

The condition on temperature at the bottom of the stable layer, at r_s, depends upon the dynamics of the transition zone from convection through to stratified fluid. Unlike at the ICB, therefore no sources of heat, meaning the heat flux is continuous across the convecting fluid through the transition region and into the stable layer. The top of the convecting region is defined as the point at which the heat flow falls below the adiabatic heat flow, $Q_\mathrm{a}(r)$, therefore $Q^-_{\mathrm{r_s}} = Q_\mathrm{a}(r_\mathrm{s})$. In the absence of any entrainment of stratified fluid by dynamics at r_s the adiabatic heat flow is conducted into the static fluid in the stable layer. In reality however turbulent fluid motions in the convective region are likely to produce some entrainment which acts to mix hot fluid at the base of the layer back down again, reducing the overall heat flow into the stable layer. Entrainment of fluid will continue until the thermal gradient becomes sufficiently strongly stabilising. I write this thermal gradient at the top of the transition region in terms of the adiabatic

gradient and a dimensionless entrainment coefficient, E

$$\frac{\partial T_{\mathbf{3}}(r_{\mathrm{s}})}{\partial r} = (1-E)\frac{\partial T_{\mathrm{a}}}{\partial r}, \tag{2.108}$$

where now E represents all the interfacial dynamics collapsed into my 1D parameterisation. $E = 0$ corresponds to no entrainment of fluid, suggesting the transition from convecting fluid to stratified fluid occurs precisely when the thermal gradient becomes stabilising. With increasing E, the required thermal gradient to inhibit vertical motion of fluid is also increased and the lower the upwards flux of heat into the layer.

Due to the complicated nature of the interfacial dynamics, E is not yet known, related to the fluid properties, relative forces acting on the fluid and time. Lister and Buffett (1998) argue that E is negligibly small due to the strong influence of rotation on the fluid which has been shown to reduce mixing by entrainment at density interfaces (Fleury et al., 1991). At the moment, I can only demonstrate the evolution of the core for specific values of E, once stable stratification in the core is better understood in 3D dynamical models permitting a more precise value for E to be argued for. The heat flow into the base of the stable layer is therefore

$$Q^{+}_{\mathrm{r_s}} = -4\pi r_{\mathrm{s}}^2 k(r_{\mathrm{s}})(1-E)\frac{\partial T_{\mathrm{a}}(r_{\mathrm{s}})}{\partial r}. \tag{2.109}$$

Thermal diffusion throughout the layer, equation 2.102, is then solved with Neumann boundary conditions on the thermal gradient at the bottom and top of the layer given by 2.108 and 2.107 respectively.

I have so far neglected the impact of the compositional gradient upon the stability of the thermally stratified layer. Difficulties were encountered when solving for the joint thermo-chemical evolution of the layer when temperature was stabilising and composition was destabilising, seemly arising from incomplete knowledge of the complicated dynamics of the coupled system (discussed in the appendix A). As such, when thermally stratified layers are present in my model, only the diffusion of heat is computed. Composition within the layer is assumed to be identical to the underlying convecting fluid and hence composition plays no role in the stability of the layer.

Since the layer thickness may change in time, the domain over which the diffusion of heat must be calculated has a moving boundary at r_{s}. The domain is fixed in size on any particular time step in order to calculate the thermal diffusion solution and is then expanded in between time steps. The relative cooling rates between the isentropic region and the stable layer can then provide an estimate of how the layer interface should move, where a faster cooling isentropic region permits growth of the stable layer and the opposite results in a shrinking layer.

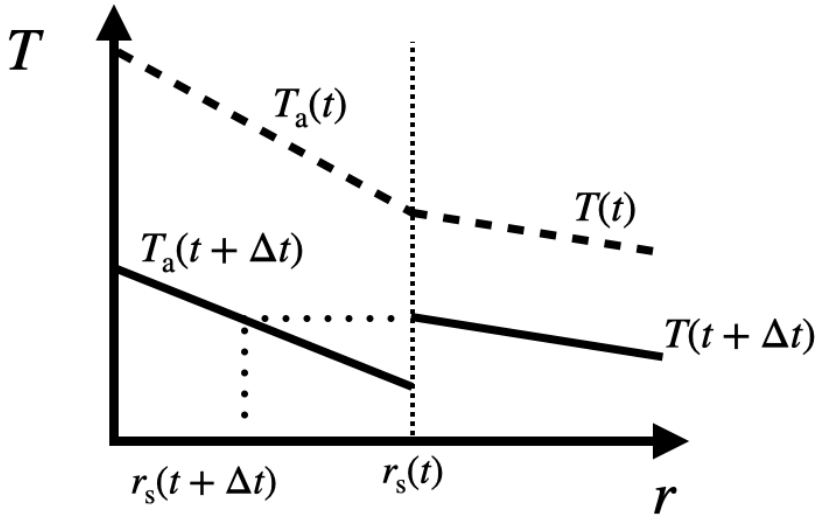

Figure 2.9: Temperature profiles for the isentropic region, T_a and stable layer, $T_{\mathbf{3}}$, at time t and $t + \Delta t$. The two regions are evolved independently, after which the layer interface moves to keep continuity of temperature.

Temperature is continuous throughout the core (Braginsky and Roberts, 1995) and so $\langle T \rangle = 0$. Assuming that the computed thermal profile in the layer satisfies the stability conditions (Eqs. 2.7 and 2.106), $T_{\mathbf{3}}(r_{\rm s}^{+}) \geq T_{\rm a}(r_{\rm s}^{-})$, where the superscript +/- refers to the upper side of lower side of the boundary respectively. Motivated by returning to continuity of temperature, the radius at which $T_{\rm a}(r) = T_{\mathbf{3}}(r_{\rm s}^{+})$ is found via the bisection method and it is this radius that is chosen as $r_{\rm s}(t + \Delta t)$ (Fig 2.9). The temperature profile is then regridded by linear interpolated onto the new domain $r_{\rm s}(t + \Delta t) \leq r \leq r_{\rm c}$ such that the temperature is continuous at $r_{\rm s}(t + \Delta t)$ and the stability conditions are still satisfied (Eqs. 2.7 and 2.106).

2.7.2 Chemical Stratification

I will consider a range of scenarios producing chemical stratification. Depending upon the physical process being represented I will either place a constraint upon the mass flux at the CMB, which leads to a condition on the compositional gradient by rearranging the definition of $\mathbf{i}$

$$\frac{\partial c_{\mathbf{3}}(r_{\rm c})}{\partial r} = \frac{\alpha_c \alpha_{\rm D} g - \mathbf{i} \cdot \hat{\boldsymbol{r}}}{\rho D}, \tag{2.110}$$

or I will place a constraint upon the mass fraction at the CMB at an elevated level relative to the underlying convective region

$$c_{\mathbf{3}}(r_{\rm c}) = c_{\rm eq}, \tag{2.111}$$

where c_{eq} is the fixed value used as the upper boundary condition. The subscript 'eq' stands for equilibrium as it will be assumed that the mantle maintains the core in chemical equilibrium with it, resulting in a flux of light element into the core as discussed more in section 2.8. Either 2.110 or 2.111 is used as the upper boundary condition on mass diffusion at the CMB and both may lead to a stable chemical gradient.

At the stable layer interface I adapt an existing method for setting the boundary condition on mass diffusion and evolving the position of r_{s} developed by Buffett and Seagle (2010). This method is valid for the scenario where the CMB heat flow is super-adiabatic. In theory there could be a scenario where both stabilising chemical and thermal gradients exist, however due to the much larger thermal diffusivity, I anticipate that the growth of the layer would be primarily controlled by thermal diffusion and therefore comparable with pure thermal stratification. For simplicity, the results presented in this thesis also focus on super-adiabatic heat flows when modelling a chemically stratified layer, although the model may be easily extended to represent a sub-adiabatic heat flow with chemical stratification.

Due to the stabilising chemical gradients, the stable layer can support a super-adiabatic temperature gradient and retain overall stability (unless Eqs. 2.7 or 2.106 are not met), allowing a super-adiabatic heat flow out of the isentropic region. Buffett and Seagle (2010) consider the onset of double diffusive convection at the point of neutral stability as the condition on the compositional gradient.

In the presence of a stable chemical gradient and a destabilising thermal gradient, oscillatory instabilities are observed (Turner, 1979). These instabilities are assumed to be limited to the vicinity of r_{s} where the weakest chemical gradients exist since the chemical gradient transitions to zero in the isentropic region. The diffusive instabilities organise the thermal and compositional profiles into a series of thin layers in a staircase pattern, where any individual layer has a uniform potential density but with a jump in potential density between successive layers (Turner, 1979). Buffett and Seagle (2010) argue that the compositional profile at the base of the layer may be reasonably extended throughout the staircase structure as an approximation and assume the whole region is still governed by mass diffusion (Eq. 2.103). The condition on the chemical gradient at r_{s} is therefore given by neutral stability when

$$\left(\frac{\partial c_{\mathbf{3}}}{\partial r}\right)_{r_{\mathrm{s}}^{+}} = -\frac{\alpha_T}{\alpha_c}\left(\frac{\partial T_{\mathbf{3}}(r_{\mathrm{s}})}{\partial r} - \frac{\partial T_{\mathrm{a}}(r_{\mathrm{s}})}{\partial r_{\mathrm{s}}}\right), \tag{2.112}$$

where double diffusive instabilities provide a mechanism for the mixing of light element out of the bottom of the layer.

In order to evaluate 2.112, the thermal gradient is required at r_{s}. Buffett and Seagle (2010) assume a constant super-adiabatic temperature gradient throughout the

layer and all time however I will relax this assumption by solving the thermal diffusion equation to produce a time dependent thermal profile. I solve 2.62 subject to a fixed thermal gradient condition at the CMB, given by Q_c, and a fixed temperature at r_s equal to the adiabatic temperature

$$\frac{\partial T_{\mathbf{3}}(r_\mathrm{c})}{\partial r} = -\frac{Q_\mathrm{c}}{4\pi r_\mathrm{c}^2 k(r_\mathrm{c})} \tag{2.113}$$

$$T_{\mathbf{3}}(r_\mathrm{s}) = T_\mathrm{a}(r_\mathrm{s}), \tag{2.114}$$

where the lower boundary condition is chosen based on continuity of temperature between the isentropic region and the stable layer. The solution to the thermal diffusion equation is computed first, then the thermal gradient is evaluated at r_s which then sets the lower boundary condition on mass diffusion with 2.112.

The method for evolving r_s in time is the same as used in Buffett and Seagle (2010). Assuming that $\langle c \rangle = 0$ on the stable layer interface and $\langle \nabla c \rangle = (\partial c/\partial r)_{r_\mathrm{s}^+}$, expressing continuity of composition on the moving interface with the advective derivative of c is given by

$$\left(\frac{\partial c_{\mathbf{2}}}{\partial t}\right)_{r_\mathrm{s}^-} = \left(\frac{\partial c_{\mathbf{3}}}{\partial t}\right)_{r_\mathrm{s}^+} + \frac{\partial r_\mathrm{s}}{\partial t}\left(\frac{\partial c_{\mathbf{3}}}{\partial r}\right)_{r_\mathrm{s}^+}, \tag{2.115}$$

remembering that the chemical gradient in the isentropic region is zero. The rate of change of $c_{\mathbf{2}}$ is attained by evaluating the energy budget in the isentropic region and is given by $C_c C_r(\mathrm{d}T_\mathrm{cen}/\mathrm{d}t)$. The rate of change of $c_{\mathbf{3}}$ at r_s^+ is given by the solution to mass diffusion (Eq. 2.103) and the chemical gradient at r_s^+ is the gradient used as the lower boundary condition on the diffusion solution given by 2.112. Rearranging 2.115 then allows estimation of the layer interface velocity.

The layer interface is moved by $\Delta t \times \mathrm{d}r_\mathrm{s}/\mathrm{d}t$ and both compositional and thermal profiles are interpolated on the new domain $r_\mathrm{s}(t + \Delta t) \leq r \leq r_\mathrm{c}$ such that they are continuous with the temperature and composition of the isentropic region (Fig. 2.10).

2.8 Benchmarks

In this section I show that aspects of the model that are based on previous numerical models are able to reproduce published results.

The evolution of the isentropic core is based upon the numerical model of Davies (2014) and Davies et al. (2015). I first reproduce a result from Davies et al. (2015) for a marginal dynamo scenario. In this model, the CMB heat flow is fixed at $Q_\mathrm{c} = 15.7$ TW post inner core nucleation whereas prior to the inner core the minimum CMB heat

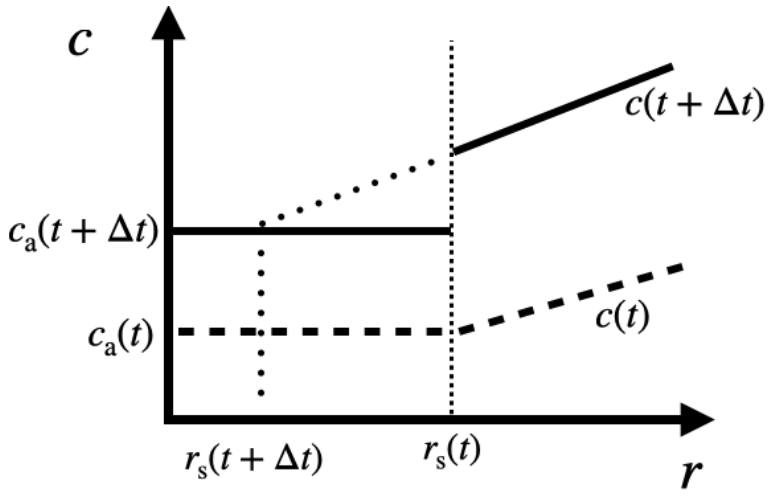

Figure 2.10: Compositional profiles for the isentropic region, $c_{\mathbf{2}}$ and stable layer, $c_{\mathbf{3}}$, at time t and $t + \Delta t$. The layer interface is advanced using 2.115 which is equivalent to extrapolating along the gradient of $c(t + \Delta t)$ until it intersects with $c_{\mathbf{2}}(t + \Delta t)$.

flow ensuring $E_\mathrm{J} > 0$ is imposed at r_c. This heat flow is calculated by setting $E_\mathrm{J} = 0$ in the entropy budget (Eq. 2.66) and solving for $\mathrm{d}T_\mathrm{cen}/\mathrm{d}t$ and then using the energy budget (2.80) to solve for Q_c. No stable layer is included in the model and so $r_\mathrm{s} = r_\mathrm{c}$ at all times. The particular result I match uses a present day ICB density jump of 800 kg m^{-3} for which Davies et al. (2015) derive radial polynomials for T_a, T_m, and k for an Fe-O-Si alloy. PREM density polynomials are used, with *ab initio* data from Alfè et al. (2002a) and Alfè et al. (2002b) providing Δs_Fe and the necessary partitioning data at the ICB, μ and λ (used in Eq. 2.100). All values used are included in tables 2.1 and 2.2 for $\Delta\rho = 800$ kg m^{-3}.

Figure 2.11 shows the comparison between the models for some key parameters. The time series all fit very closely with only some very small differences, most obvious in E_J during inner core growth. In Davies et al. (2015), the g and ψ are calculated analytically for the given density polynomials but ignore the density jump at the ICB, whereas I calculate them by numerically integrating the density polynomials and do account for the density jump at the ICB. This leads to very small differences in the total integrals in calculating the energy and entropy terms, manifesting in a slightly different value for E_J during inner core growth but the difference is very minor and does not alter the interpretation of the thermal history of the core.

To benchmark my Crank-Nicolson scheme for solving the diffusion equation, I compare to known analytical solutions for specific cases. Firstly, I can compare to time dependent solutions for a sphere of radius a and constant thermal diffusivity κ. The initial condition is taken to be a uniform temperature, T_1, and a lower boundary condition of zero temperature gradient at r=0.

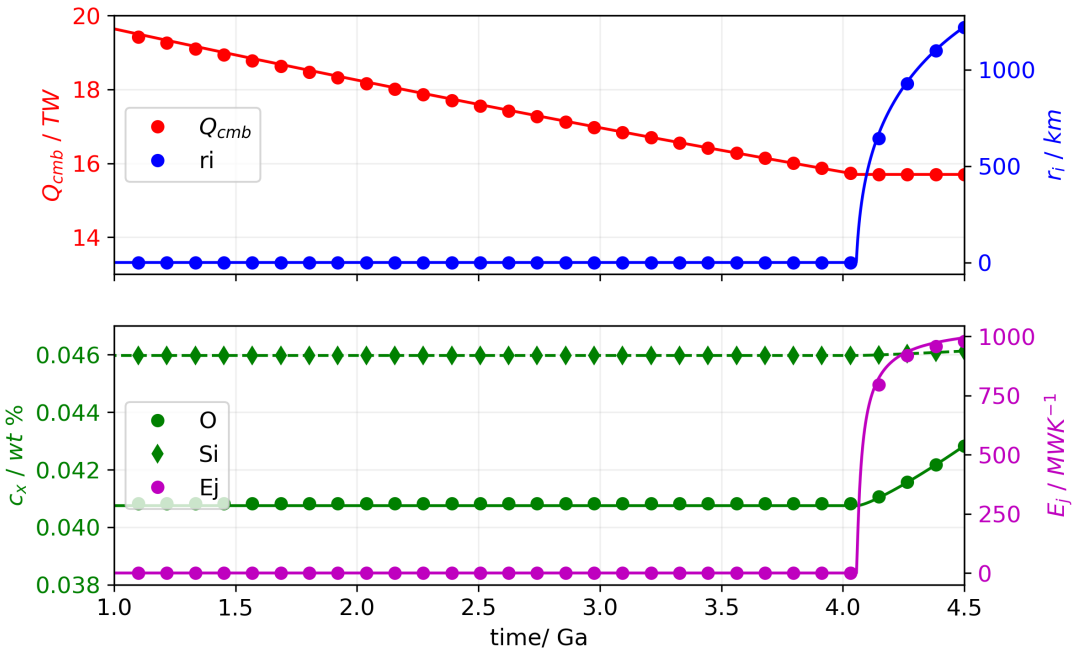

Figure 2.11: Comparison of my model (lines) for a purely isentropic core with one of the collection from Davies et al. (2015) (points). Plotted are the CMB heat flow history in red and the inner core radius in blue (top panel), and E_{J}, in purple and the concentrations of oxygen and silicon in green (bottom). Oxygen is denoted by the round points and solid green line, and silicon is denoted by the diamonds and dashed green line.

For an upper boundary condition at $r = a$ of fixed temperature, T_0, the time dependent solution for T is given as (Crank, 1975, Eq. 6.18):

$$\frac{T(r) - T_1}{T_0 - T_1} = 1 + \frac{2a}{\pi r} \sum_{n=1}^{\infty} \frac{(-1)^n}{n} \sin\left(\frac{n\pi r}{a}\right) \exp(-\kappa n^2 \pi^2 t / a^2) \tag{2.116}$$

and the solution for an upper boundary condition of fixed thermal gradient, $(\partial T/\partial r)_a$ is given as (Crank, 1975, Eq. 6.45)

$$T_0 - T = -a \left(\frac{\partial T}{\partial r}\right)_{r=a} \left[\frac{3\kappa t}{a^2} + \frac{1}{2}\frac{r^2}{a^2} - \frac{3}{10} - 2\frac{a}{r} \sum_{n=1}^{\infty} \frac{\sin(\alpha_n r)}{\alpha_n^2 a^2 \sin(\alpha_n a)} \exp(-\kappa \alpha_n t)\right], \tag{2.117}$$

where α_n are defined by the n^{th} root of $a\alpha_n \cot(a\alpha_n) = 1$. For the infinite sums, summing up to $n = 200$ provides a converged solution. Figure 2.12a) shows the results of my Crank-Nicolson scheme in comparison to these known anayltical solutions. The numerical scheme is for a spherical shell, appropriate for the application to a stable layer, yet the analytical solutions are for the whole sphere. As such the singularity at r=0 cannot be determined due to the factor of $1/r$ in the discretisation of the numerical scheme and so instead the solution is calculated for the domain $0.001 \leq r \leq 1$ introducing no significant error.

Figure 2.12b) shows the convergence of the solutions as the spatial resolution is increased. For the parameter choice used here, by only 10 radial grid points the error has dropped below 0.5% for both boundary condition types, showing rapidly achieved accuracy.

Analytical solutions also exist for a steady state within a spherical shell with a radially varying diffusivity, which my numerical method can accommodate, taking the form $\kappa = \kappa_0(1 + f(r))$, for some general $f(r)$. For a spherical shell with inner and outer surfaces at r_1 and r_2 which are held at constant temperature T_1 and T_2 respectively, the steady state solution takes the form (Crank, 1975, Eq. 9.18)

$$\frac{T_1 - T(r)}{T_1 - T_2} = \frac{I(r_1) - I(r)}{I(r_1) - I(r_2)}, \tag{2.118}$$

where I is defined as

$$I(r) = \int_{r_1}^{r} \frac{\mathrm{d}r}{r^2(1 + f(r))}. \tag{2.119}$$

Figure 2.12 c) shows results for my numerical solution compared to the analytical solutions for 3 functions $f(r)$, where in all cases $\kappa_0 = 1$. The 3 forms of $f(r)$ considered

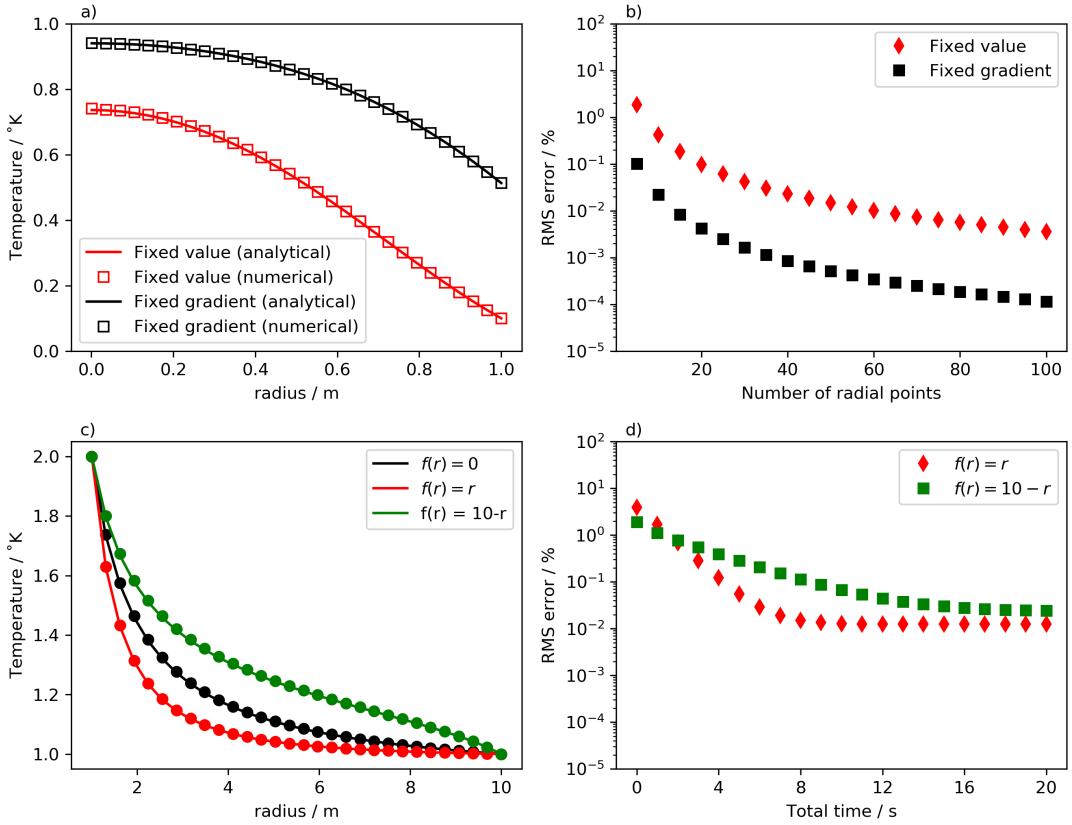

Figure 2.12: Comparison to analytical solutions for constant (top) and radially varying thermal conductivity (bottom). a) Analytical solutions Eqs. 2.116 and 2.117 in solid lines with numerical solutions as squares. An initial temperature of 1 K was taken for both solutions with a fixed temperature of 0 K (red) or fixed temperature gradient of -1 Km^{-1} (black), a thermal diffusivity of 1 ms^{-2} and a time step of 0.1 seconds. b) RMS error of numerical solutions in a) as the spatial resolution is increased. c) analytical (lines) and numerical (circles) solutions for a steady state with a radially varying diffusivity (Eq. 2.118). A total time of 20 s with fixed temperatures at the outer and inner boundaries was used. d) RMS error of the numerical solutions in c) as the time step is increased showing convergence to the steady state.

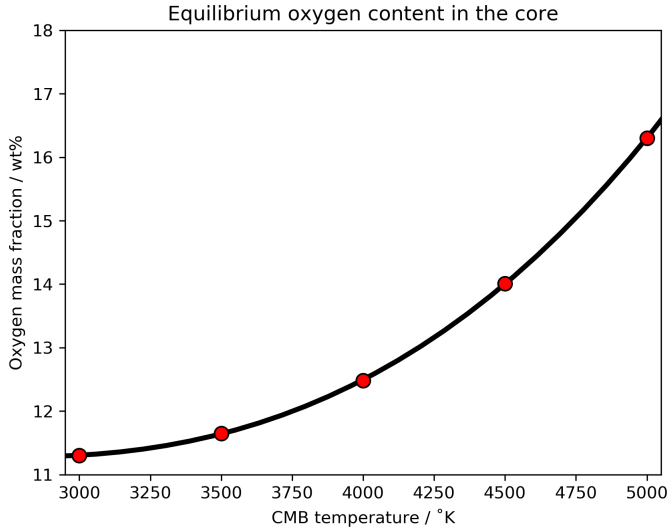

Figure 2.13: Equilibrium concentration of oxygenm c_{eq}, given 15% mole fraction of FeO in ferropericlase from Frost et al. (2010)). Red dots show data from Fig. 14 a) of Frost et al. (2010)) and the black line is a 3rd order polynomial fit to this data to calculate at intermediate temperatures.

are: the reference case when the diffusivity is constant, $f(r) = 0$, when the diffusivity increases with radius, $f(r) = r$, and when the diffusivity decreases with radius, $f(r) = 10 - r$. The solution is calculated for $r_1 = 1$ m, $r_2 = 10m$, $T_1 = 2$ K and $T_2 = 1$ K. The integral $I(r)$ is numerically integrated to calculate its value at the radial grid points. Since my numerical solution is a time dependent solution, the solution is calculated for a long enough time to converge to a steady state as demonstrated by the error with different time steps used in Figure 2.12 d).

Although these examples are for thermal diffusion, my scheme is written in a general form and the same discretisation is used for mass diffusion as well.

The final benchmark I may perform is to recreate the results of Buffett and Seagle (2010) given that I employ their method for evolving chemical stratification. Buffett and Seagle (2010) induce chemical stratification by using the thermodynamic model of Frost et al. (2010) of oxygen partitioning from mantle ferropericlase into the core alloy. At the CMB they fix the value of c to the temperature dependent equilibrium concentration, c_{eq} suggested by Frost et al. (2010), with the lower boundary condition at r_{s} given by equation 2.112 fixing the chemical gradient. Temperature is not solved for within the layer, instead they assume the super-adiabatic temperature gradient is a constant 1 Kkm^{-1} throughout the layer and that the temperature of the CMB decreases linearly from 5000 K to 4000 K over the age of the Earth. Corresponding values for the equilibrium concentration in the core as a function of CMB temperature is plotted in figure 2.13.

The evolution of the isentropic region is not coupled to the evolution of the stable layer. Instead they parameterise the time evolution of the adiabatic interior based on previous thermal history models (Buffett et al., 1996b). The necessary parameters are the inner core radius, which begins to grow at 3 Gyrs

$$r_{\mathrm{i}}(t) = 1221 \text{ km} \sqrt{\frac{t - 3 \text{ Gyrs}}{4.5 \text{ Gyrs} - 3 \text{ Gyrs}}}. \tag{2.120}$$

The subsequent source of oxygen, Φ, from a growing inner core assuming all oxygen partitions into the liquid is

$$\Phi(t) = 4\pi c_{\mathbf{2}}(t) \frac{\mathrm{d}r_{\mathrm{i}}}{\mathrm{d}t}, \tag{2.121}$$

where $c_{\mathbf{2}}(t)$ is the oxygen mass fraction in the liquid outer core in the adiabatic region whose time evolution is governed by

$$\frac{\mathrm{d}c_{\mathbf{2}}}{\mathrm{d}t} = \frac{\Phi(t)}{V_{\mathbf{2}}} - \frac{4\pi r_{\mathrm{s}}^2 \mathbf{i}(r_{\mathrm{s}}^-)}{M_{\mathbf{2}}}, \tag{2.122}$$

where $V_{\mathbf{2}}$ and $M_{\mathbf{2}}$ are the volume and mass of the convecting fluid in the isentropic region. Note that Eq. 2.122 divides the CMB flux term by the mass and not the volume, correcting a mistake in the print of Eq. 6 of Buffett and Seagle (2010). All available paramters are matched, where the key parameters are the initial oxygen concentration, taken as $c_{\mathbf{2}}(t = 0) = 0.05$, and the mass diffusivity, set to 3×10^{-9} m^{2}s^{-1}.

Figure 2.14 shows the comparison between the results, which agree with some minor deviations up to maximum of 3 km ($\sim 4\%$). My model was run at sufficiently high resolution spatially and temporally to have converged. Although I have employed a method as close to Buffett and Seagle (2010) as possible given available information, there may still be some differences in the specifics of the numerical discretisation of the diffusion equation. Further potential differences may exist in the procedure for re-gridding the solution as the domain expands, otherwise the methods are identical. These small differences in the numerical approach likely account for the small disparity in the final result, which are small enough that my model is shown to behave as expected for a growing chemically stratified layer.

The method outlined in section 2.7.1 for evolving thermal stratification is not based on any previously published results and so cannot be expected to precisely reproduce existing models for thermal stratification. In the next chapter, chapter 3, it is shown to behave in a similar fashion to a published model of thermal stratification in the Earth's core before the main results are presented.

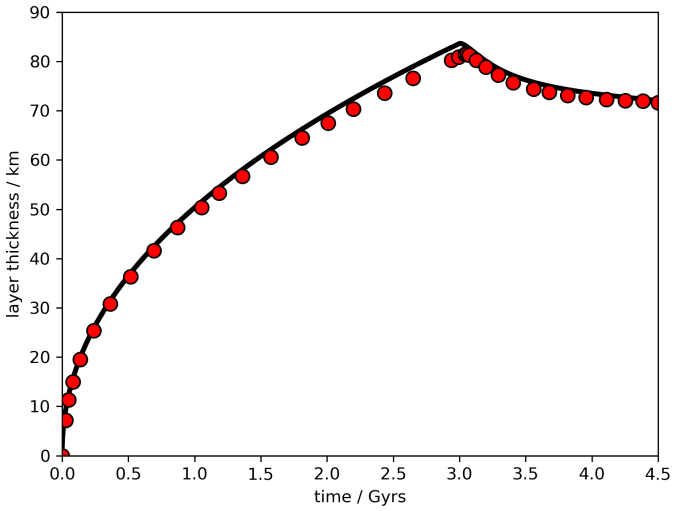

Figure 2.14: Stable layer thickness over time from Buffett and Seagle (2010) (red points) and my model (solid line).

2.9 Summary

This chapter has described a 1D parameterised model of the Earth's core with stable stratification beneath the CMB, dividing the core into 2 main regions. The isentropic region contains the solid inner core and the vigorously convecting region of the outer core and the stable layer contains static fluid, through which heat and mass is transferred only by diffusion.

In order to simulate the time evolution of the core, an energy balance is constructed, balancing sources of energy against the heat conducted away from the core at the CMB. The energy balance for the isentropic region may be written (Eq. 2.60) as

$$Q^-_{\mathrm{r_s}} = (\tilde{Q_\mathrm{s}}^{\mathrm{is}} + \tilde{Q_\mathrm{l}} + \tilde{Q_\mathrm{g}})\frac{\mathrm{d}T_{\mathrm{cen}}}{\mathrm{d}t}, \tag{2.123}$$

and the energy balance for the stable layer as (Eq. 2.65)

$$Q_\mathrm{c} = \overbrace{-\int \rho C_p \frac{\mathrm{D}T}{\mathrm{d}t}\mathrm{d}V_{\mathbf{3}}}^{Q_\mathrm{s}^{\mathrm{sl}}} + Q^+_{\mathrm{r_s}}. \tag{2.124}$$

Subject to a condition on $Q^-_{\mathrm{r_s}}$, equation 2.123 is numerically integrated to solve for the cooling rate of the core. In order to evaluate the potential for the core to maintain an internally generated magnetic field, an equivalent entropy balance is formulated, which for the entire core is written

$$E_\mathrm{k} + E_\alpha + E_\mathrm{J} = (\tilde{E_\mathrm{s}}^{\mathrm{is}} + \tilde{E_\mathrm{L}} + \tilde{E_\mathrm{g}})\frac{\mathrm{d}T_{\mathrm{cen}}}{\mathrm{d}t} - \int \left(\frac{1}{T_\mathrm{c}} - \frac{1}{T}\right)\rho C_p \frac{\mathrm{D}T}{\mathrm{D}t}\mathrm{d}V_{\mathbf{3}}, \tag{2.125}$$

where the integral on the RHS gives the contribution from the stable layer. E_J cannot be directly estimated and hence is solved for. The generation of magnetic field is observationally constrained to have persisted since ∼3.5 Ga (Tarduno et al., 2010) which requires $E_\mathrm{J} > 0$, providing a key constraint upon the thermal evolution of the core.

The stable layer may be either thermally or chemically stably stratified for which I detail 2 separate methods of solving the diffusion equations and estimating the change in size of the layer over time. For a thermal stratification, only temperature is assumed to control the growth of the layer, where the following conditions are applied at the top, r_c, and bottom, r_s, boundaries in order to numerically solve the diffusion equation (Eq. 2.62)

$$\left(\frac{\partial T}{\partial r}\right)_{r_\mathrm{c}} = -\frac{Q_\mathrm{c}}{4\pi r_\mathrm{c}^2 k(r_\mathrm{c})} \tag{2.126}$$

$$\left(\frac{\partial T(r_\mathrm{s})}{\partial r}\right)_{r_\mathrm{s}} = (1-E)\frac{\partial T_\mathrm{a}}{\partial r}, \tag{2.127}$$

where E is a non-dimensional coefficient representing entrainment of the layer at r_s by interfacial dynamics with the underlying convection. The layer interface is advanced deeper into the core to restore continuity of temperature at r_s by determining the radius where $T_\mathrm{a}(r) = T(r_\mathrm{s}^+)$.

For chemical stratification, both temperature and mass diffusion are calculated numerically within the layer. Conditions on the thermal diffusion solution are

$$\left(\frac{\partial T}{\partial r}\right)_{r_\mathrm{c}} = -\frac{Q_\mathrm{c}}{4\pi r_\mathrm{c}^2 k(r_\mathrm{c})} \tag{2.128}$$

$$T(r_\mathrm{s}) = T_\mathrm{a}(r_\mathrm{s}). \tag{2.129}$$

The solution to thermal diffusion then provides a condition on the chemical gradient at the interface, at neutral stability and the onset of doubly diffusive instabilities,

$$\left(\frac{\partial c}{\partial r}\right)_{r_\mathrm{s}} = \frac{\alpha_T}{\alpha_c}\left(\frac{\partial T}{\partial r}\right)_{r_\mathrm{s}}. \tag{2.130}$$

The upper boundary condition on the mass fraction of light element may be either fixed value or fixed gradient depending upon the physical scenario. Either the mass fraction is set to a specific value or the gradient is determined by a condition on the mass flux

$$\left(\frac{\partial c}{\partial r}\right)_{r_\mathrm{c}} = \frac{\alpha_c \alpha_\mathrm{D} g - \mathbf{i}\cdot\hat{\boldsymbol{r}}}{\rho D}. \tag{2.131}$$

Both types of boundary condition are used and discussed in more detail in chapter 4.

The layer interface, r_s, is advanced with the method of Buffett and Seagle (2010) using the relation, based on continuity of composition at the interface

$$\left(\frac{\partial c_\mathbf{2}}{\partial t}\right)_{r_\mathrm{s}^-} = \left(\frac{\partial c}{\partial t}\right)_{r_\mathrm{s}^+} + \frac{\partial r_\mathrm{s}}{\partial t}\left(\frac{\partial c}{\partial r}\right)_{r_\mathrm{s}^+}. \tag{2.132}$$

This framework provides a flexible model for simulating the coupled evolution of the Earth's core and a stably stratified layer beneath the CMB, with a wide range of applications. I will investigate a series of specific scenarios using this model for both thermal (chapter 3) and chemical (chapter 4) stratification in the context of the long term evolution of the core.

Chapter 3

Thermal Stratification

3.1 Introduction

The existence of thermal stratification in the present-day core depends on the relative magnitudes of the CMB heat flow, Q_{c}, and the adiabatic heat flow, Q_{a}. The CMB heat flow is estimated to lie in the range Q_{c}=5-17 TW (Lay et al., 2008; Nimmo, 2015). The adiabatic heat flow Q_{a} depends on the thermal conductivity k and temperature gradient at the top of the core. Assuming an adiabatic temperature gradient of $\sim$1 K km^{-1} (Davies, 2014), and k in the range $40 - 100$ W m^{-1} K^{-1} (De Koker et al., 2012; Pozzo et al., 2013; Gomi et al., 2013; Konôpková et al., 2016) gives Q_{a} $\sim$4-16 TW and so both strong stabilising and destabilising conditions are consistent with the available information. These simple estimates however do not constrain the thickness and strength of thermal stratification. More in depth analysis may predict the size of the stratification by considering the energy sources throughout the core for the present day, for which Gubbins et al. (2014) find to be limited to $\sim$700 km thick. Investigating the energy sources over time may then provide further constraint by required present day predictions be consistent with the evolution of the core over time. Modelling the long-term evolution of the core is the focus of this chapter.

When the CMB heat flow becomes sub-adiabatic, less heat is escaping the core than that supplied by convection. The effect is to heat up the top of the core developing a region in which heat is transferred by conduction only. A parcel of fluid that lies within this sub-adiabatic layer that is displaced vertically upwards (downwards) finds itself denser (lighter) than the ambient fluid in the stable layer and so experiences a buoyancy restoring force. Therefore the sub-adiabatic heat throughout the stable layer inhibits any radial motion.

Analysis of the energy and entropy budget for the core suggests that prior to an inner core, and neglecting radioactivity and mineral precipitation, the CMB heat flow

must exceed the adiabatic heat flow to sustain a dynamo (Nimmo, 2015). In the present day, inner core growth provides a source of chemical convection to power the geodynamo (Braginsky, 1963; Loper, 1978; Gubbins et al., 2004) and so a sub-adiabatic heat flow may be maintained whilst still generating a large scale magnetic field. Prior to the inner core however, the geodynamo would fail, something the paleomagnetic record indicates has not happened (Tarduno et al., 2010). Therefore if thermal stratification does exist in the core, it can only be as old as the inner core. Precipitation of MgO (O'Rourke et al., 2017; Badro et al., 2016) and/or SiO_2 (Hirose et al., 2017) could provide additional gravitational power prior to inner core formation, which would relax the constraint on the age of thermal stratification. However, precipitation rates are still under debate (Badro et al., 2018; Du et al., 2019) and the power that is made available by precipitation depends strongly on the abundance and coupled partitioning behaviour of iron, silicon and magnesium oxides (Mittal et al., 2020). Alternatively radioactive decay could provide an alternative source of power although quantities of radioactive potassium are negligible (Xiong et al., 2018). In view of these I do not consider mineral precipitation or radioactivity in the core.

Previous studies of Earth's core evolution have considered the time-dependent growth of a thermally stable region within an adiabatic and well-mixed core. These studies solve the heat diffusion equation in the stable layer and obtain its growth from continuity conditions imposed at the interface r_s with the well-mixed interior, the basic procedure followed in this work.

Previous models of thermal stratification within the core differ primarily in their choice of boundary conditions on the thermal diffusion solution and the numerical scheme for evolving the stable layer interface. Gubbins et al. (1982) fix the temperature at the CMB and the thermal gradient to the adiabatic gradient at r_s, then solve a time dependent solution for the thermal conduction profile within the layer. A growing inner core is present from t=0, releasing latent heat but not light element. They produce a >1000 km thick layer formed over the age of the Earth for a thermal conductivity of 15 W K^{-1} m^{-1}.

Labrosse et al. (1997) take a different approach, treating the moving interface as a Stefan problem, introducing a psuedo-latent heat at the interface. This allows both a temperature and the temperature gradient to be fixed at the layer interface, although the inclusion of the latent heat term means the temperature gradient cannot be continuous across the interface. They found that for a linearly decreasing CMB heat flow which becomes sub-adiabatic at around 3 Gyrs, a stable layer grows to ∼600 km in the remaining 1.5 Gyrs, about double the rate of growth in Gubbins et al. (1982), owing to the larger thermal conductivity of 60 W K^{-1} m^{-1}.

Lister and Buffett (1998) solve for both temperature and composition within the

stable layer requiring a continuity in density across r_s. By assuming that salt finger instabilities act to mix the composition uniformly across the layer, this provides a condition upon the temperature at the base of the layer. Using similar parameters to Labrosse et al. (1997), the stable layer grows to just 400 km thick in nearly 3 Gyrs, due to the lower relative compositional buoyancy in the layer than the well mixed region slowing down its advance.

Thermal stratification has been considered in the cores of other terrestrial bodies. Models of Mercury's interior structure (Dumberry and Rivoldini, 2015) and dynamo (Christensen and Wicht, 2008) suggest the presence of a thermally stable layer in the core, the evolution of which has been modelled using steady state solutions (Knibbe and Westrenen, 2018). A transition to subadiabatic conditions is usually invoked to explanation for the demise of the Martian dynamo around 4 Ga (Stevenson, 2001; Williams and Nimmo, 2004; Davies and Pommier, 2018). Venus may have a very low heat flux, below the adiabatic heat flow, across the CMB (Nimmo, 2002) to explain its lack of an internally generated magnetic field. The cores of Ganymede (Rückriemen et al., 2015) and the moon (Laneuville et al., 2014) are also thought to be thermally stratified at the present day. There is thus a broad utility for a general framework for modelling thermal stratification in terrestrial bodies.

The purpose of this chapter is twofold. First, I conduct a systematic parameter study in order to place constraints on the present-day thickness and strength of thermally stable layer. This will be achieved by producing models of the thermal history of the core which match available constraints such as persistent magnetic field generation and the correct inner core size. I explore a wide range of input parameters including low and high thermal conductivities (De Koker et al., 2012; Pozzo et al., 2013; Gomi et al., 2013; Konôpková et al., 2016), different core chemical and thermal properties, and CMB heat flows. Second, I consider the role of convective entrainment at the base of the layer, which has been neglected in the previous models of thermal stratification. Entrainment of buoyant fluid at the base of the stable layer can arise from downward mixing by flow in the bulk turbulent core (Turner, 1979), which acts to slow layer growth. Various parameterisations of the entrainment process have been considered and some can be shown to be equivalent (Lister, 1995). Here I implement a simple and flexible procedure that does not appeal to any specific mechanism and introduces a single 'entrainment coefficient', E, into the boundary conditions for the heat equation. The value of E probably depends on the details of the convective dynamics within the core (Lister, 1995) and may thus depend on time. However, in view of the current incomplete understanding of core dynamics (Jones, 2015) I consider a range of constant E values in this study.

This section is organised as follows. First a summary of the numerical method for evolving the core is provided in section 3.2. Benchmark cases demonstrating the models

behaviour are shown in section 3.3 along with the specific model parameters used here in section 3.2. Results are presented in section 3.4 and discussion and conclusions are presented in section 3.5.

3.2 Methods

Chapter 2 develops the thermal history model used in this thesis and so the following simply summarises its use for thermal stratification. The core is split into 2 main regions, the adiabatic interior and the stable layer. The stable layer comprises the region of the liquid outer core between r_s and r_c. The isentropic region contains the solid inner core and the liquid outer core up until r_s, where there is the sharp interface with the stable layer. Within the well mixed isentropic region, the temperature is assumed to follow an adiabat, whilst in the stable layer the temperature is described by a purely conductive profile. For this chapter, the compositional field within the stable layer is assumed to match the uniform composition of the liquid region in the adiabatic interior, so as to have no impact upon the density anomaly associated with the stable layer.

The time evolution of both regions is controlled by an imposed heat flow at r_c and the coupling between them. The conduction profile within the stable layer is found by numerically solving the time dependent diffusion equation for temperature, subject to fixed thermal gradients at both the top and bottom boundaries:

$$\rho C_p \frac{\partial T_{\mathbf{3}}}{\partial t} = \nabla \cdot (-k \nabla T_{\mathbf{3}}) \tag{3.1}$$

$$\frac{\partial T_{\mathbf{3}}}{\partial r} = \frac{Q_\mathrm{c}}{-k(r_\mathrm{c}) 4\pi r_\mathrm{c}^2} \qquad \text{at } r = r_\mathrm{c} \tag{3.2}$$

$$\frac{\partial T_{\mathbf{3}}}{\partial r} = (1 - E) \frac{\partial T_\mathrm{a}}{\partial r} \qquad \text{at } r = r_\mathrm{s}, \tag{3.3}$$

where $T_{\mathbf{3}}$, T_a are the temperature within the stable layer and adiabatic temperature respectively. The entrainment coefficient, E, is introduced into the lower boundary condition, decreasing the upwards flux of heat representing fluid entrained by the convecting region. When Q_c becomes sub-adiabatic, a 1 km thick stable layer with an adiabatic temperature profile is used as an initial condition. The Crank-Nicolson method (Crank, 1975) is employed to solve 3.1 with time and spatial resolution chosen to ensure accuracy as described in section 2.7.

For the isentropic region, in the absence of a stable layer, $Q_{r_\mathrm{s}} = Q_\mathrm{c}$, otherwise the

heat flow at the interface is the adiabatic heat flow:

$$Q_{r_\mathrm{s}} = -k(r_\mathrm{s})4\pi r_\mathrm{s}^2 \times \frac{\partial T_\mathrm{a}}{\partial r}. \tag{3.4}$$

The energy and entropy budgets for the whole core includes the stable layer, which for convenience are reiterated here. The energy balance of the isentropic region is

$$Q^-_{\mathrm{r_s}} = \overbrace{-\int \rho C_p \frac{\mathrm{D}T}{\mathrm{d}t}\mathrm{d}V_{\mathbf{12}}}^{Q^{\mathrm{is}}_\mathrm{s}} + \overbrace{4\pi r_\mathrm{i}^2 \rho_{\mathbf{1}} L \frac{\mathrm{d}r_\mathrm{i}}{\mathrm{d}t}}^{Q_\mathrm{l}} + \overbrace{\int \psi \rho \alpha_c \frac{\mathrm{D}c}{\mathrm{D}t}\mathrm{d}V_{\mathbf{2}}}^{Q_\mathrm{g}}, \tag{3.5}$$

and for the stable layer layer is (Eq. 2.65)

$$Q_\mathrm{c} = \overbrace{-\int \rho C_p \frac{\mathrm{D}T}{\mathrm{d}t}\mathrm{d}V_{\mathbf{3}}}^{Q^{\mathrm{sl}}_\mathrm{s}} + Q^+_{\mathrm{r_s}}, \tag{3.6}$$

The entropy balance is evaluated for the whole core and is used to evaluate the ohmic dissipation (Eq. 2.66

$$\overbrace{\int k\left(\frac{\nabla T}{T}\right)^2 \mathrm{d}V_{\mathbf{123}}}^{E_\mathrm{k}} + \overbrace{\int \frac{\mathbf{i}^2}{\alpha_\mathrm{D} T}\mathrm{d}V_{\mathbf{123}}}^{E_\alpha} + \overbrace{\int \frac{\Phi}{T}\mathrm{d}V_{\mathbf{123}}}^{E_\mathrm{J}} = \overbrace{-\int \left(\frac{1}{T_\mathrm{c}} - \frac{1}{T}\right)\rho C_p \frac{\mathrm{D}T}{\mathrm{D}t}\mathrm{d}V_{\mathbf{123}}}^{E_\mathrm{s}} + \overbrace{\left(\frac{1}{T_\mathrm{c}} - \frac{1}{T_\mathrm{i}}\right)Q_\mathrm{l}}^{E_\mathrm{L}} + \overbrace{\frac{Q_\mathrm{g}}{T_\mathrm{c}}}^{E_\mathrm{g}}. \tag{3.7}$$

Within the integrals over the entire volume of the core, $V_{\mathbf{123}}$, the appropriate profiles for temperature are used for either the isentropic or stable layer regions.

The interface at r_s is evolved in time depending upon the relative cooling of the isentropic region and the stable layer, advancing the layer if $T_{\mathbf{3}}(r_\mathrm{s}(t), t+\Delta t) > T_\mathrm{a}(r_\mathrm{s}(t), t+\Delta t)$ or receded the layer otherwise. The layer is advanced by seeking continuity of temperature, where the bisection method is used to find the radius, $r_\mathrm{s}(t+\Delta t)$ where $T_\mathrm{a}(r_\mathrm{s}(t+\Delta t) = T_{\mathbf{3}}(r_\mathrm{s}(t+\Delta t))$ as shown in Figure 2.9. The solution is then regridded using linear interpolation onto the expanded domain with $T_{\mathbf{3}}(r_\mathrm{s}(t+\Delta t)) = T_\mathrm{a}(r_\mathrm{s}(t+\Delta t))$ to ensure continuity of temperature at the interface.

Core properties are obtained for 3 different ICB density jumps, $\Delta\rho$, as this is only determined to approximately 800± 200 kgm^{-3}(Masters and Gubbins, 2003). A larger

$\Delta\rho$ results in more oxygen in the outer core, since this element is rejected by the solid inner core (Alfè et al., 2002b), and hence alters the properties of the outer core iron alloy. The core is taken as an Fe-O-Si alloy, with concentrations of light elements and associated core properties given previously in tables 2.1 and 2.2. Each set of core properties is named after the $\Delta\rho$ for which they represent leading to the designations D2015-600, D2015-800 and D2015-1000.

A key parameter for this study is the thermal diffusivity, κ, as this controls the growth rate of thermal stratification. A radially varying diffusivity is accommodated and so is calculated given the relation $\kappa = k/(\rho C_p)$, where k and ρ both vary in radius, yielding an approximate average κ of $\sim 1.2 \times 10^{-5} \mathrm{m}^2\mathrm{s}^{-1}$. This is 2-5$\times$ higher than used in previous models of thermal stratification in Earth (Gubbins et al., 1982; Labrosse et al., 1997; Lister and Buffett, 1998) chosen to be compatible with the recent large increase in estimates of k.

My model required a prescribed input of Q_c. It may be possible for recent times (500 Ma - present) using constraints on plate velocities with mantle convection models (Zhang and Zhong, 2011) to infer Q_c but the accuracy of these is dependent upon many other poorly constrained parameters. We have no observations for Q_c in the past and so strictly, Q_c should be determined simultaneously with the evolving core temperature using time-dependent dynamical models of mantle convection (e.g. Nakagawa and Tackley, 2015). However such an approach is very time-consuming and does not allow a systematic exploration of parameter space.

Another strategy is to employ a paremeterised model of mantle convection (e.g. Nimmo et al., 2004; Driscoll and Bercovici, 2014), which enables self-consistent calculation of Q_c and T_c but at the expense of introducing uncertain parameters such as the conductivity and viscosity of the upper and lower mantle thermal boundary layers. Moreover, a number of alternative parameterisations are available (e.g. Conrad and Hager, 1999; O'Rourke et al., 2017), which can significantly change the predicted heat flows. Here I write Q_c using a simple parameterised equation, which allows me to systematically sample a large range of plausible Q_c time-series.

Since I am only interested in modelling thermal stratification that forms after ICN in order to permit a dynamo, and the presence of stratification has a minimal impact upon the global energetics of the core, as discussed below, I only compute the thermal history of the Earth's core for the relatively short time since just before inner core nucleation through to the present day. Previous models of the coupled evolution of the mantle and core estimate a range of behaviour for Q_c (Fig. 3.1) in both the absolute value and rate of change. I therefore consider a wide range of both the present day Q_c and its rate of change through time.

In general, over the last $\sim$700 Myrs $Q_\mathrm{c}(t)$, previously published results may be fit

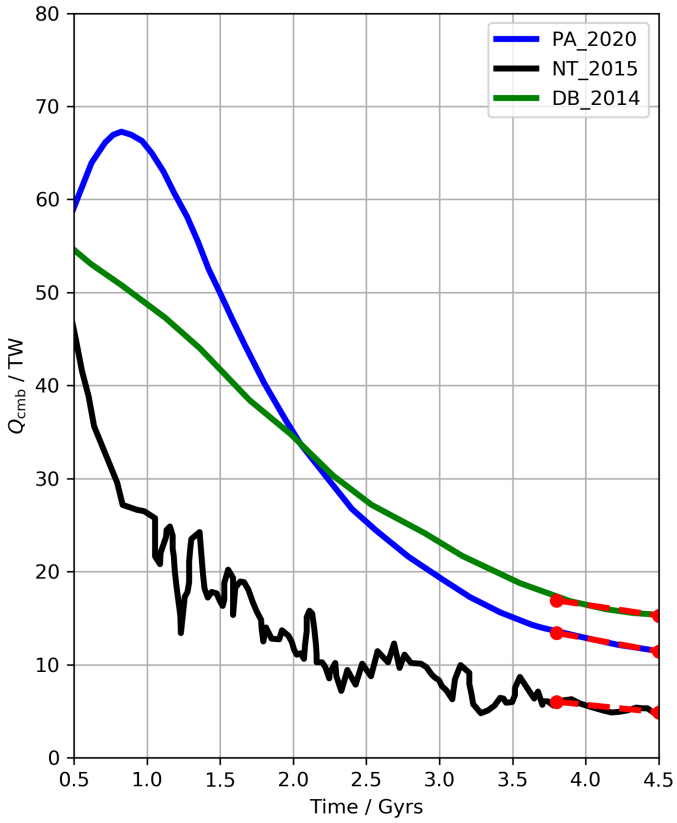

Figure 3.1: Published CMB heat flows from Patočka et al. (2020) (PA2020), Driscoll and Bercovici (2014) (DB2014) and Nakagawa and Tackley (2015) (NT2015). PA2020 used a mantle viscosity contrast of 5, with an activation energy of 300 kJ mol^{-1} as shown on their Figure 12. DB2014 is from their Earth case as shown in their Figure 5. NT2015 uses a friction coefficient of 0.02, shown in their Figure 9. Shown by the red dashed line and circles are linear best fits for the last 700 Myrs, during which all vary in Q_c by less than 3 TW/Gyrs.

by a simple linear parameterisation:

$$Q_c(t) = A + B(4.5\text{Gyrs} - t) \tag{3.8}$$

where A is the present day value for Q_c and B is the rate of decrease of the linear trend. Despite only iterated for the relatively recent past, models are still tied to constraints of the present day ICB radius and continued production of a dynamo during that period, they simply do not describe the evolution of the core prior to the inner core.

3.3 Benchmark Cases

I consider two cases to demonstrate the model behaviour. An equilibrium configuration in which the layer ceases to grow is obtained when the heat entering and leaving the layer are balanced: $Q_{r_s} = Q_c$. In general the approach to this state is hindered because both Q_{r_s} and Q_c vary in time, so for demonstration I set a constant heat flow 4 TW below the adiabatic value at the CMB (with $Q_a = 15$ TW, $Q_c = 11$) and $dT_a/dt = 0$ in the adiabatic interior, which requires the adiabatic heat flow at all radii is constant in time, and $E = 0$. Other parameters are $k = 100$ W m^{-1} K^{-1}, $\kappa = 10^{-6}$ m^2 s^{-1} and the adiabatic gradient corresponding to $\Delta\rho = 800$ kg m^{-3} (Davies et al., 2015). Figure 3.2 shows how the layer quickly grows and then converges to the radii at which $Q_{r_s} = Q_c$. The temperature profile in the layer is elevated above the adiabat until it merges with the adiabat at r_s.

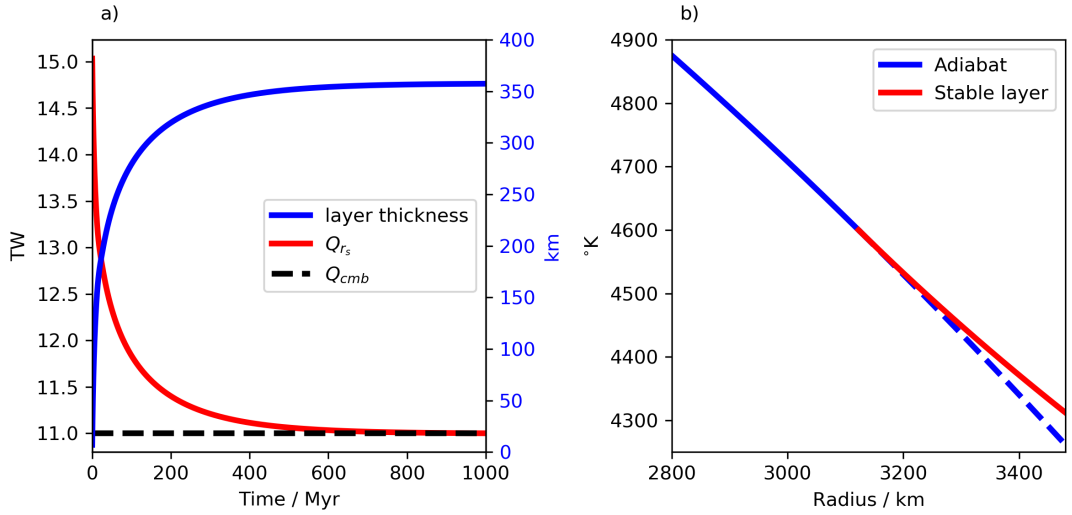

Figure 3.2: a) Heat flows at the CMB and at r_s (left axis) and layer thickness through time (blue, right axis). The model converges to the equilibrium point where the heat flows are equivalent. b) Temperature at the top of the core at 1 Gyr. The isentropic region is shown by the blue line (dashed blue line represents the theoretical adiabatic temperature within the layer). The temperature within the layer is shown in red.

I define the ADiabatic Ratio (ADR) as the ratio of the CMB heat flow to the adiabatic heat flow at the CMB:

$$ADR = \frac{Q_c}{Q_a(r_c)}, \tag{3.9}$$

in this test case $ADR \approx 0.73$. Clearly the condition for stabilising thermal stratification is $ADR < 1$, and the degree to which the stable layer can grow is limited by the ADR.

Finally, I reproduce the results of Labrosse et al. (1997). I parameterise their CMB

heat flow in the form

$$Q_{\mathrm{c}} = (q_0 + \beta t) \times 4\pi r_{\mathrm{c}}^2, \tag{3.10}$$

where q_0 =75 mW m^{-2} and β = -3.5 W $\mathrm{m}^{-2}\mathrm{s}^{-1}$. Key parameters are the thermal conductivity of the core, 60 W m^{-1} K^{-1}, and the thermal diffusivity, 5.8×10^{-6} m^2 s^{-1}, matching all other published parameters. The model matches that of Labrosse et al. (1997) well, producing a purely thermal stable layer of around 600 km thickness over the last 1.5 Gyr (Figure 3.3) with only ∼35km difference between them. The agreement is very good considering that different methods were used to model both the adiabatic interior, stable region and the evolution of the interface; these variations explain the small differences between the two cases.

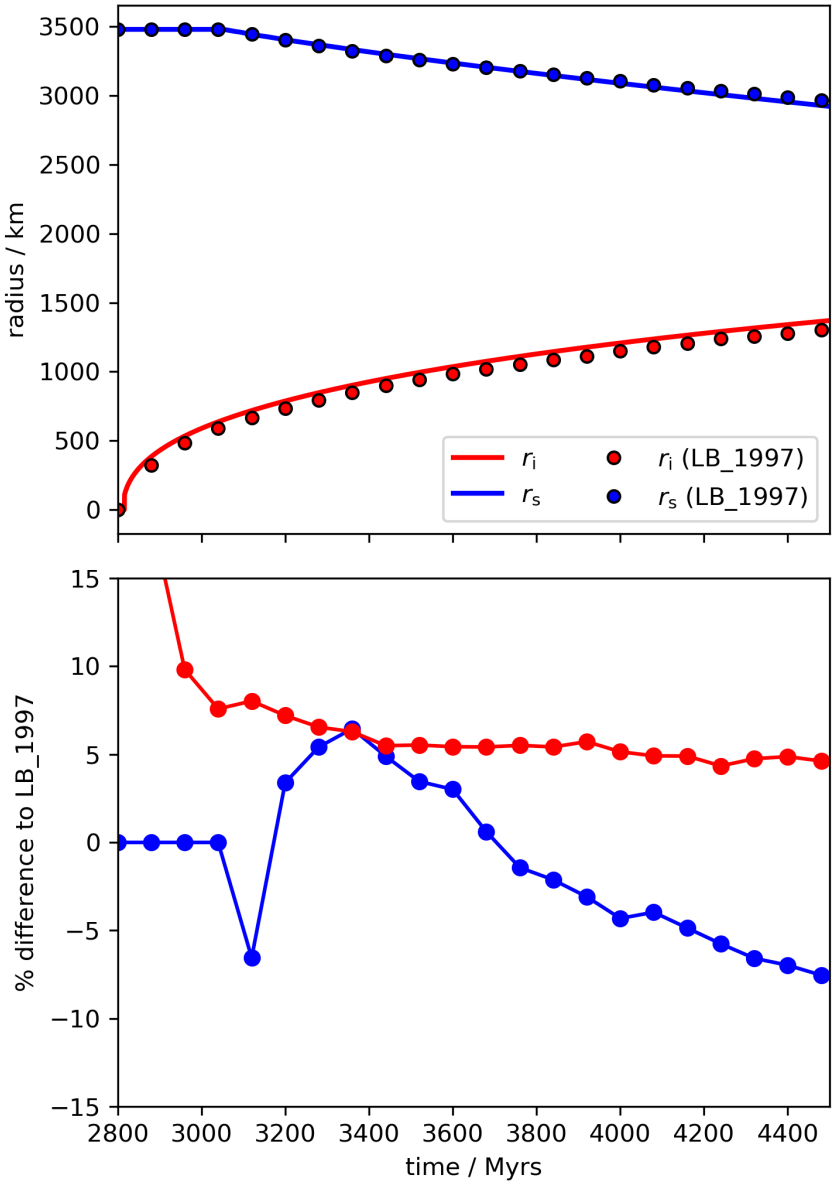

Figure 3.3: Benchmark case solutions (solid lines) matching the results of Labrosse et al. (1997) (circles, labelled LB_1997) (top) and the % difference between my solution compared to that of LB1997 (bottom). Inner core radius, r_i, is shown in red and the stable layer interface, r_s, is shown in blue. The solutions generally agree to within $\pm 7\%$.

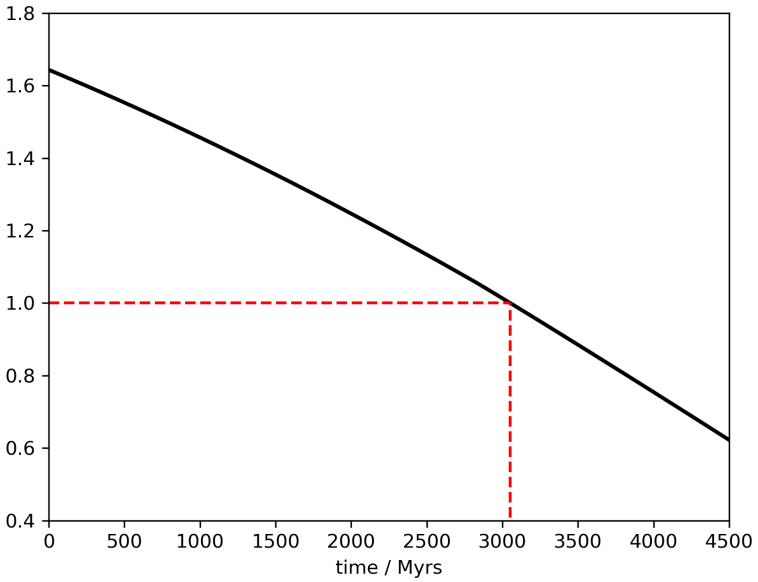

Figure 3.4: ADR from the results in Figure 3.3. The core becomes sub-adiabatic just after 3 Gyrs shown by the red dashed lines when the ADR falls below 1.

3.4 Results

I first show results from the model D2015-800 using A=10 TW and B= 8 TW/Gyrs to demonstrate the effects on the thermal evolution of the core. For this, 2 models are run, one that includes thermal stratification and one without. Both models share the same initial conditions in the past, just before the inner core forms such that differences between them are solely due to the presence of the stable layer. Figure 3.5a) shows r_i and r_s, where an approximately 400km thick layer grows in ∼300 million years. The inner core is marginally too large, about 10km in radius, at present in the simulation with the stable layer.

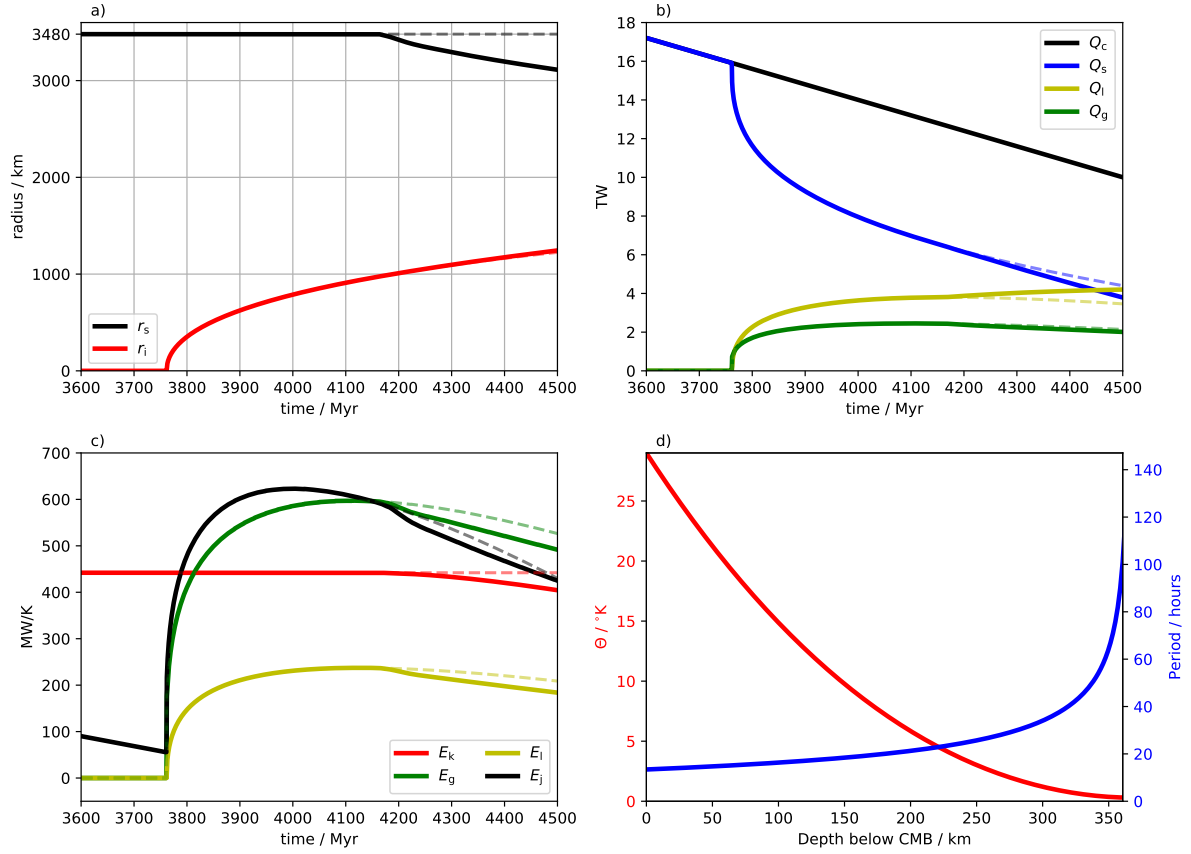

Figure 3.5: Results for model D2015-800, A=10 TW, B=8 TW/Gyr and E=0. Solid lines show the results from the calculation with a stable layer, dashed lines represent the calculation without a stable layer, where both started from the same initial conditions. Shown are the inner core and stable layer interface radii (a), the energy sources (b), the entropy sources (c) and the present day layer size and buoyancy period (d).

The energy terms are also similar (Figure 3.5b), with changes in Q_l and Q_g of 0.71 TW (+21%) and -0.13 TW (-6%) between cases with and without a layer. Note that although Q_g is increased due to the faster cooling rate in the stable layer case, the reduced volume in which the light elements are distributed leads to an overall reduction in Q_g. In general there is no significant impact upon the energy budget and hence the

cooling rate of the core and growth rate of the inner core as also noted by Labrosse et al. (1997).

The associated entropy sources are shown in Fig. 3.5c. Compared to the case without a layer $E_g = Q_g/T_c$ follows Q_g and is reduced relative to the case with no stable layer. Although Q_l is increased in the presence of a layer due to faster cooling, E_L is reduced due to the increased value for T_c in the efficiency factor $(T_i - T_c)/(T_i T_c)$. Since no chemical effects are considered within the stable layer, the entropy due to barodiffusion, E_α, is negligible in both cases as found in previous work (Gubbins et al., 2004; Davies, 2014). The largest contribution to E_k comes from the CMB region since the magnitude of the adiabatic gradient increases with radius and temperature decreases with radius. The presence of a stable layer therefore acts to reduce E_k, by around 9% in this example. The Ohmic dissipation E_J is slightly reduced in the presence of a stable layer because the decrease in E_L and E_g outweigh the decrease in E_k.

I conduct a large parameter search across A and B, together with the 3 sets of core properties. Initial temperatures for each individual model were chosen to ensure the correct size of the inner core at present is achieved. Figure 3.6 shows the present day stable layer thickness in this parameter space for zero entrainment, E=0. Models in which $E_J < 0$ at any time are ignored as shown by the white space in these figures and models in which the present day $ADR > 1$ produce no stratification shown by the grey colour.

As expected, there is a strong negative correlation between the layer thickness and A, with the thickest layers around 750 km in size for the D2015-800 and D2015-1000, while they are 600 km for D2015-600. The thermal conductivity in model D2015-600 is higher than the conductivities in D2015-800 or D2015-1000, increasing the adiabatic heat flow, hence why layers begin to form when A falls below 16 TW, as opposed to 13 TW for the other 2 core property sets using D2015-600 properties. Models in D2015-600 also always have a failing dynamo for $A > 9$ TW for the values of B searched.

The lower A is, the larger B must be to ensure that Q_c is sufficiently super-adiabatic prior to inner core nucleation (600 Ma) as shown by the boundary between models in which the dynamo fails and those that do not. For a fixed value of A, there is a weak negative correlation between layer thickness and B. As B is increased, heat flows in the past become higher and hence less sub-adiabatic (larger ADR), slowing the layer growth. This effect is only marginal since the thermal diffusion rate is relatively quick relative to the rate at which the ADR falls in these models. The main impact of B is in determining which models are able to sustain a dynamo. For a given A, B must be large enough to ensure that Q_c is super-adiabatic prior to the inner core. This lower bound on B increases as A is decreased shown by the boundary separating models that

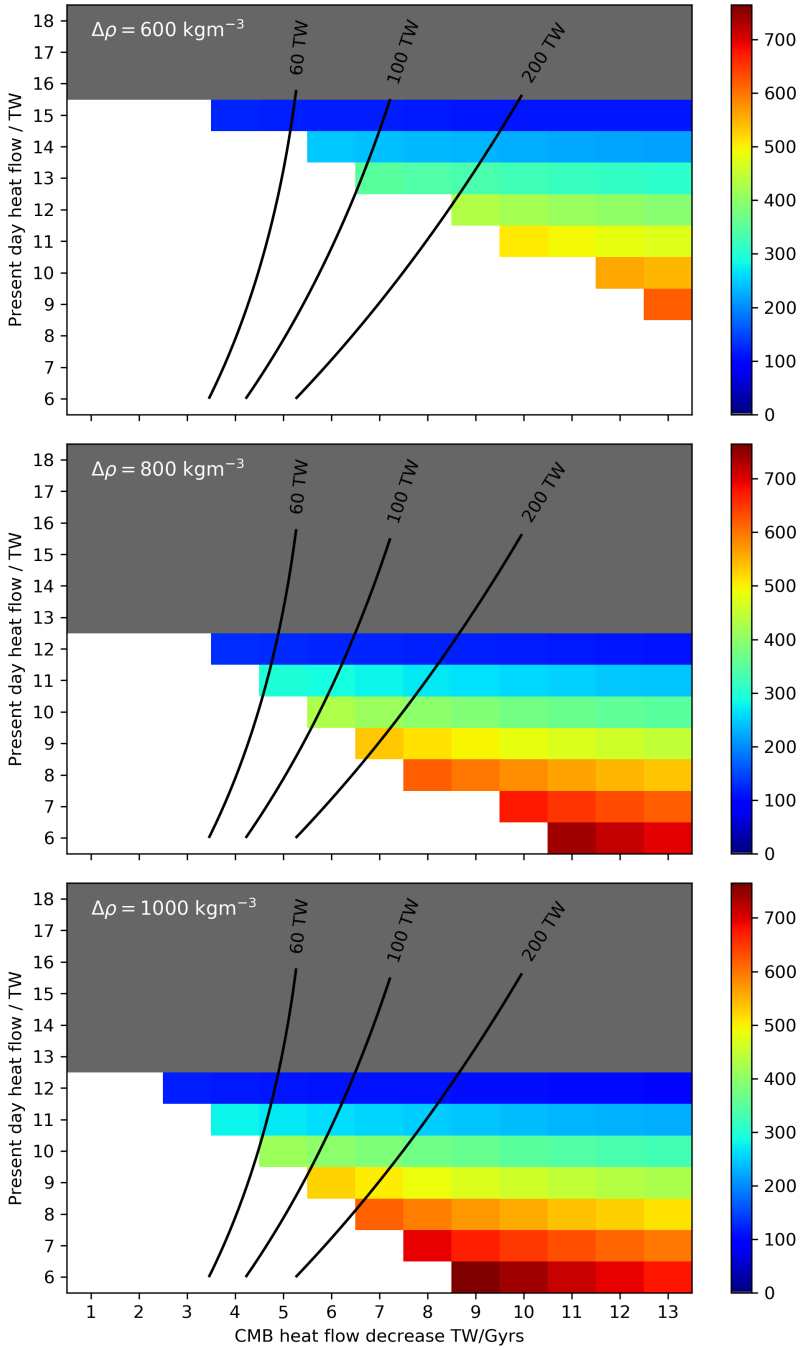

Figure 3.6: Present day layer thickness for models D2015-600 (top) D2015-800 (middle) and D2015-1000 (bottom) in km. Models in which E_J<0 are ignored as shown by the white space. Grey indicates that no stable layer forms. Black contours indicate the value for Q_c at t=500 Myr if the present day rate of change in Q_c were due to an exponential decay in Q_c over the last 4 Gyr, as discussed in 3.5

cannot sustain a dynamo (white space) and those that do.

Relatively large values for B are required to generate thermal stratification whilst maintaining a dynamo at all times. Extrapolating the linear heat flows I have used

back 4 Gyrs yields $Q_{\mathrm{c}}(t = 500$ Myrs) of anywhere between 25-70 TW, a range within conventional estimates (Fig. 3.1). However several studies (Davies, 2009; Nakagawa and Tackley, 2010, and most shown in Fig. 3.1) predict that Q_{c} follows an exponential decrease over the age of the Earth. I fit a theoretical heat flow Q_e that has an exponential form constrained to the present day A and B yielding:

$$Q_e(t) = A \times exp\left(\frac{4.5\mathrm{Gyrs} - t}{\tau}\right), \tag{3.11}$$

$$\tau = A/B, \tag{3.12}$$

where the decay constant τ has been chosen to ensure $Q_e = A$, $\mathrm{d}Q_e/\mathrm{d}t = -B$ at the present day. Extrapolating back along this theoretical exponential reveals predicted heat flows in the early Earth that gives rise to the recent trend in Q_{c}. Contours of the value of $Q_e(t = 500\mathrm{Myrs})$ are plotted on Figure 3.6, these are much higher than following the linear extrapolation in time. Many models plot in a region where the theoretical Q_e takes on extreme values (>200 TW) in the early Earth, with only a small corner of the parameter space producing thermal stratification and keeping this theoretical value for Q_e within the convectional predictions.

Altering the entrainment coefficient, E, alters the condition at which the stable layer will begin to grow, $ADR < (1 - E)$, and also slowing down the rate of advance by reducing the heat conducted into the stable layer. Figure 3.7 shows time series of the stable layer thickness for different values of E for a particular model (D2015-800, A=8 TW, B=8 TW/Gyr). This represents the dynamics of the underlying isentropic region entraining and mixing away the lower region of the stable layer to a point when the stabilising temperature gradient is too strong, given by the lower boundary condition in equation 3.3.

Figures 3.8-3.10 show the impact of including entrainment into the model with E=0.1, 0.2 and 0.3 respectively for all models simulated. In all cases, as expected, the overall layer thickness is reduced or was even stopped from forming in the first place as shown by the increased region in the parameter space where no layers form (grey coloured area).

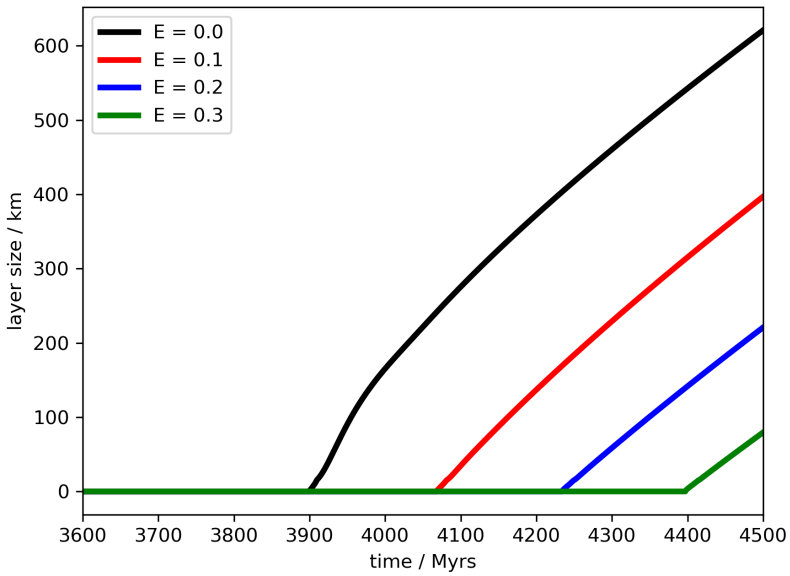

Figure 3.7: Time series of layer thickness for the model D2015-800, A=8 TW, B=8 TW/Gyr, with variations due to E.

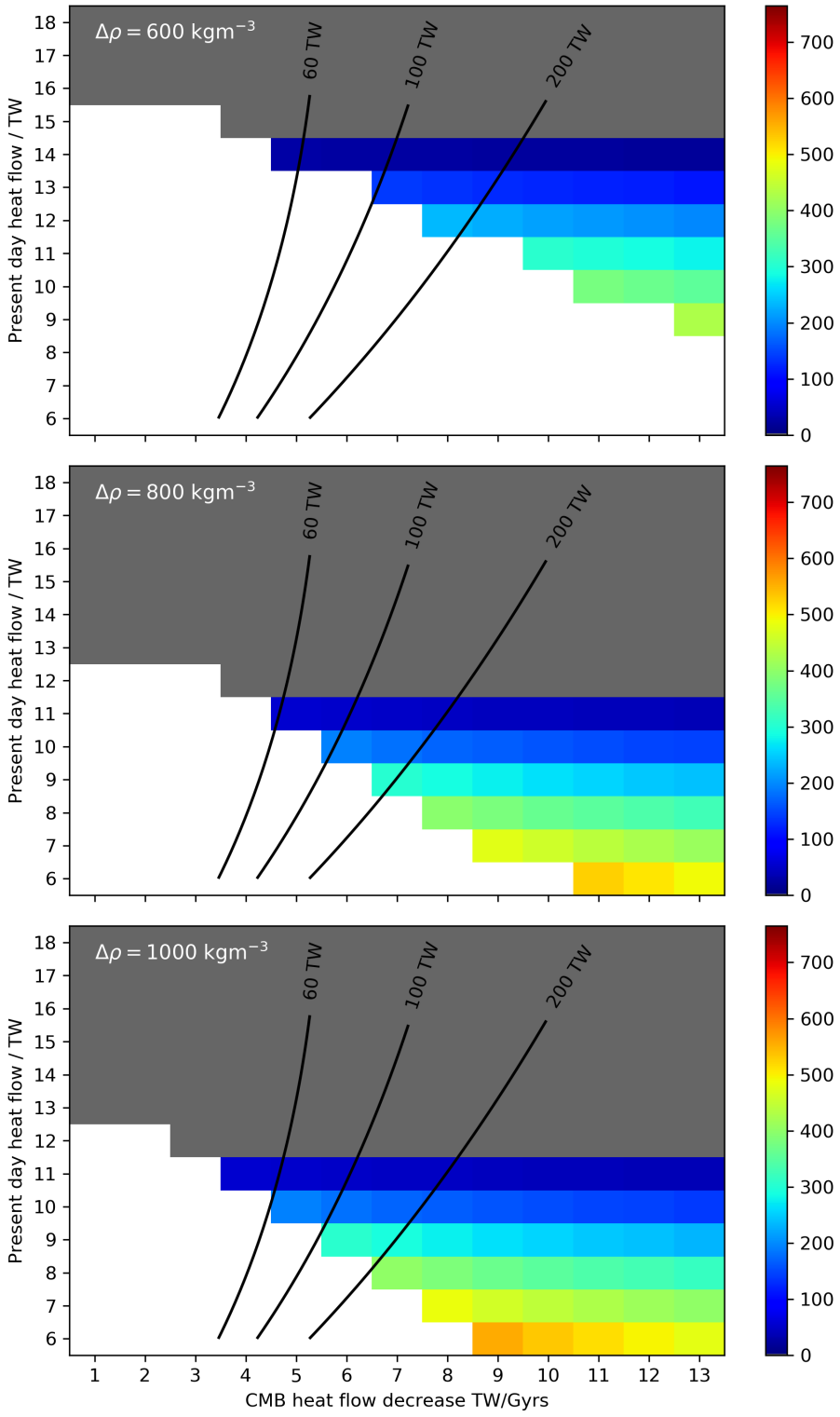

Figure 3.8: Same as 3.6 except with an entrainment coefficient of E=0.1

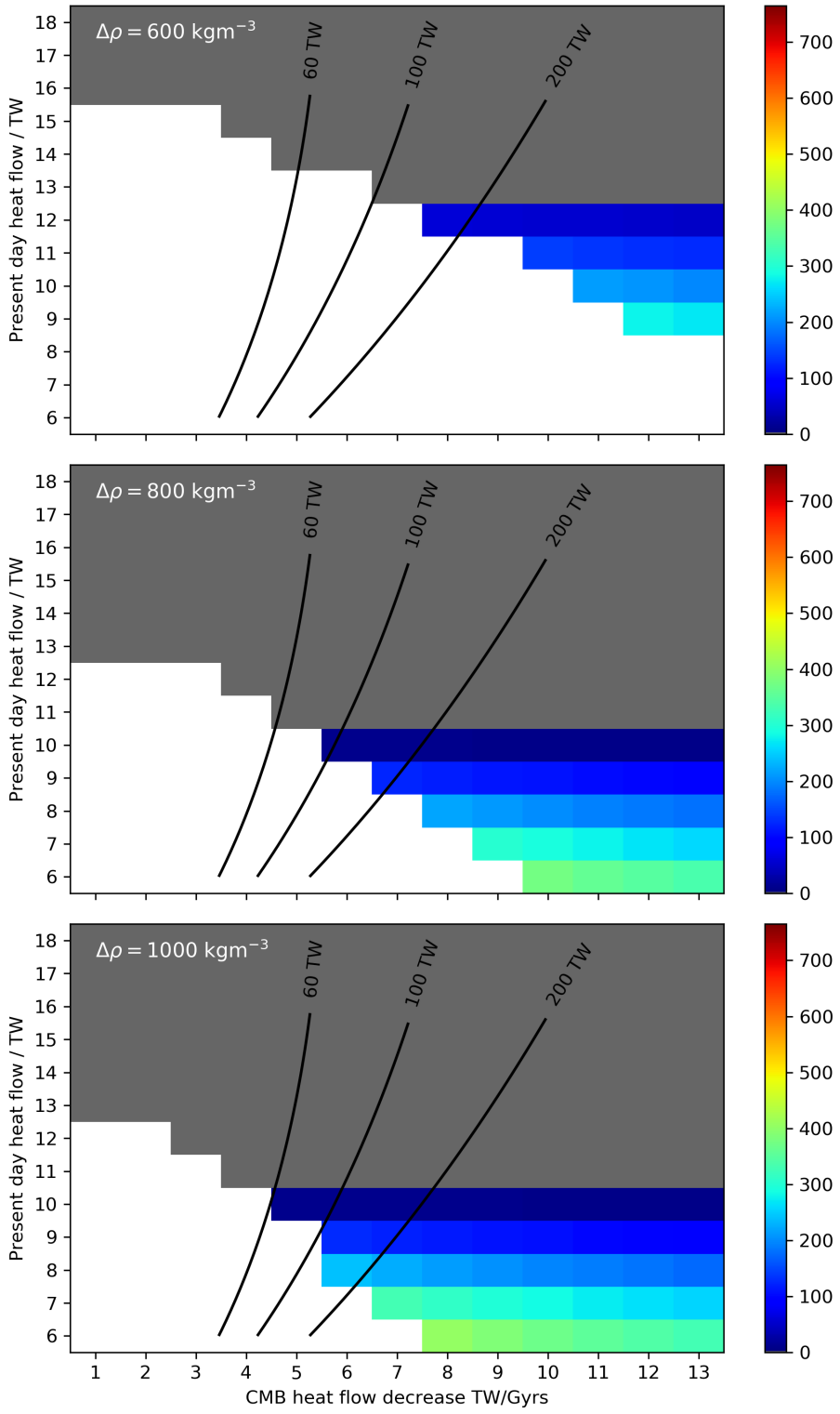

Figure 3.9: Same as 3.6 except with an entrainment coefficient of E=0.2

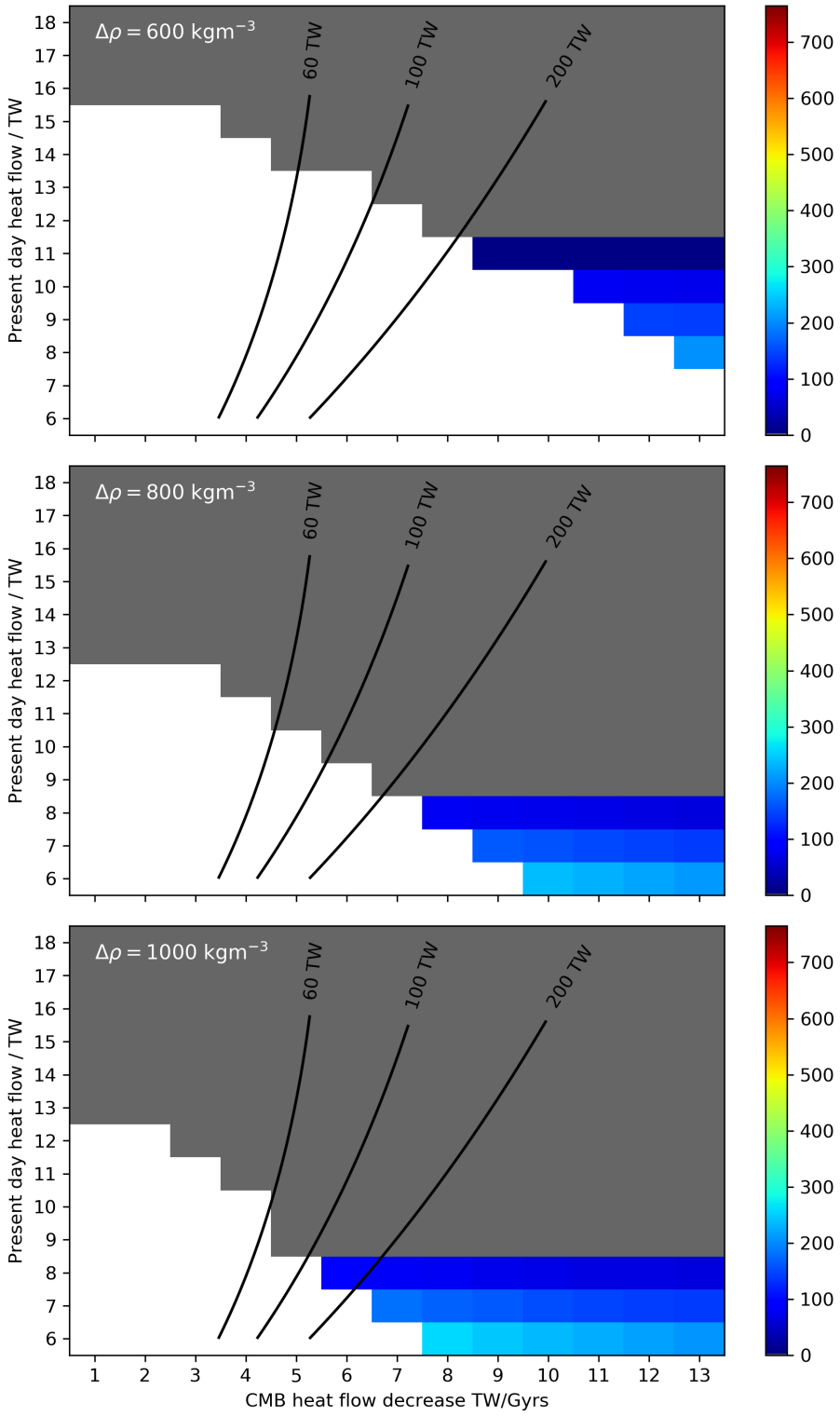

Figure 3.10: Same as 3.6 except with an entrainment coefficient of E=0.3

The stabilising thermal gradient determines the Brunt-Väisälä frequency N, the frequency of gravity waves in stably stratified fluid and a measure of the strength of stability defined as:

$$N = \sqrt{-\frac{g}{\rho_0}\frac{\partial \rho'}{\partial r}} \tag{3.13}$$

where ρ' is the potential density, $\rho' = \rho_0 (-\alpha_T \Theta)$, dependent upon the potential temperature $\Theta = T - T_a$. The period, $2\pi/N$, is plotted for a range of models on Figure 3.11 shows. Models are only shown as a function of ICB density jump and A, since there is no significant variation in either τ or E. As the ADR increases (increasing A) the stratification becomes weaker represented by longer periods and all models lie between 8-27 hours. The period of gravity waves, as inferred from geomagnetic observations lies in the middle of this range at ~19 hours (Buffett et al., 2016), although models with this 19 hour period have a layer thickness >200km, whereas Buffett et al. (2016) suggest only 140 km.

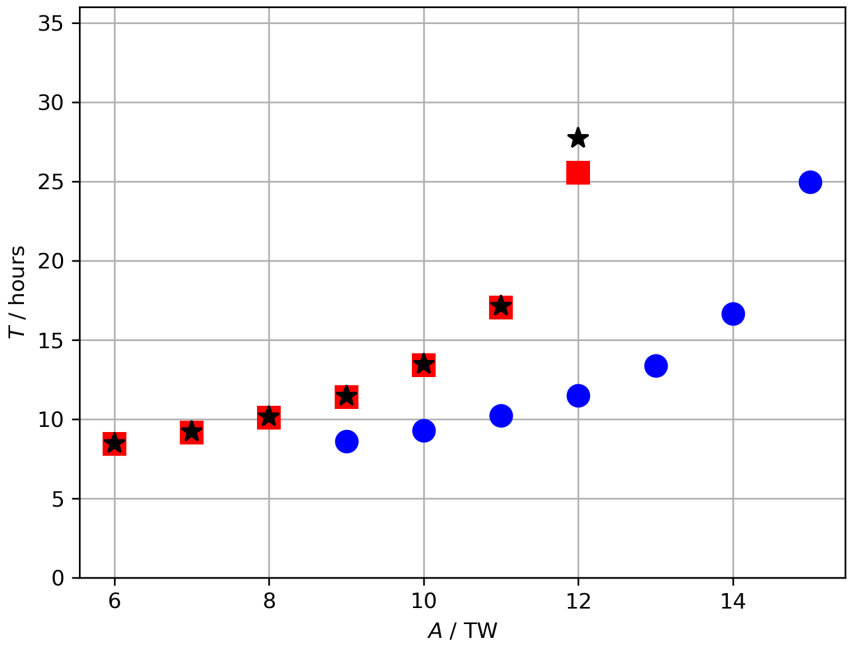

Figure 3.11: Peak buoyancy frequency shown by corresponding period in hours. No significant variation is found with B or E and so only models with B=13 TW/Gyr and $E = 0$ are shown. Symbols correspond to core properties D2015-600 (blue circles), D2015-800 (red squares) and D2015-1000 (black stars).

Comparing all stable layer thicknesses plotted as a function of $Q_e(t = 500Myrs)$ (Figure 3.12) reveals that most models either plot far beyond 200 TW in the early Earth or below 400 km. If the long term trend of Q_c can be well described by an exponential

then this further limits the extent of thermal stratification within the core to keep reasonable heat flows in the earth Earth. Introducing a small amount of entrainment, $E = 0.1$, reduces the upper bound to 300 km (circles on Fig. 3.12). No models with $E \geq 0.2$ produce layers where $Q_e(t = 500\text{Myrs}) < 100TW$.

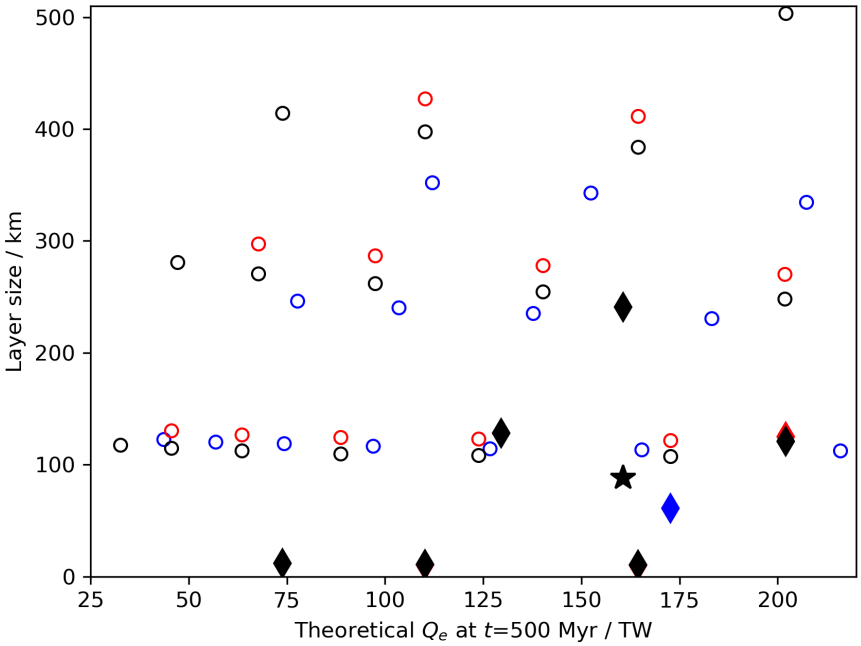

Figure 3.12: Layer thickness plotted against the theoretical value for Q_c at $t = 500$ Myr assuming an exponential trend. Blue, red, black colours refer to core properties D2015-600, D2015-800 and D2015-1000 respectively. Circles, diamonds, and stars refer to entrainment coefficients, E, of 0, 0.2, 0.3 respectively. Many models do not appear on the plot due to having a higher Q_c value than 200 TW or a stable layer thickness of zero.

3.5 Discussion

Simulating the recent past and prescribing a linear heat flow was chosen to avoiding specifying a complete, and unconstrained, history for Q_c, when only the last ∼700 Myrs is of consequence for the focus of this study. The temporal variance in Q_c from previous coupled core and mantle models, shown in Figure 3.1, show a range of behaviour due to specific modelling choices and the sensitivity of the results to relatively unconstrained parameters, such as the activation energy for the temperature dependence of mantle viscosity (O'Rourke et al., 2017). An exponential decay in Q_c is often found for coupled solutions using both lower estimates of k (e.g. Davies, 2009; Nakagawa and Tackley, 2010) and recent high estimates (e.g. DB2014, NT2015, PA2020 shown in Fig 3.1).

Assuming a theoretical exponential decay of Q_c, Q_e, of the form shown in equation 3.11, suggests extremely large heat flows in the early Earth shown by the black contours on Figures 3.6-3.10. Three (but not all) possibilities are that 1) the heat flow over the last ∼700 Myrs is representative of a longer exponential trend over the last 4 Gyrs, 2) the heat flow is instead representative of a longer linear trend for the past 4 Gyrs, or 3) neither 1 nor 2 is true. 3) is entirely plausible given dynamical models of mantle convection coupled to parameterised core models can produce more complicated temporal behaviour (e.g. Nakagawa and Tackley, 2010; Nakagawa and Tackley, 2015).

2) is appealing as sufficiently high heat flows would still be produced to ensure dynamo generation throughout Earth's full history, (e.g. Davies, 2014; Panovska et al., 2019) but few coupled models predict a linear trend in the CMB heat flow.

The consequence of 1) is that for most models that produce thermal stratification >200 km thick, very high or extreme (>200 TW) early CMB heat flows must have existed, in order to produce the required drop in Q_c over the age of the inner core. Increasing E makes the situation worse, pushing models with stable layers further towards these extreme heat flows. This would suggest very high core temperatures in the Earth, well above the mantle solidus which is calculated to be 4150 ±150 K at the CMB, and therefore widespread melting of the lower mantle. Furthermore the minimum value for B for all models presented here to produce any stable layers is 3 TW/Gyrs, larger than all of the published results from coupled models in Figure 3.1, which decrease at a rate of 2.8 (PA2020), 1.6 (NT2015), and 2.3 (DB2014) TW/Gyr respectively, in a region of the parameter space where I find no, or limited thermal stratification.

Seismic studies find a low velocity region interpreted as a distinct layer, though not all do (Alexandrakis and Eaton, 2010; Irving et al., 2018), at the top of the core to a range of depths: 50-100 km (Lay and Young, 1990; Garnero et al., 1993), 150 km (Tanaka, 2007), 300 km (Helffrich and Kaneshima, 2010; Kaneshima and Helffrich, 2013) or even 400 km (Kaneshima, 2018). Correlating with my results, this would

suggest the present day Q_c is somewhere between 1-3 TW below Q_a for each of the three $\Delta\rho$ values used.

Geomagnetic and length of day constraints favour the lower end of this range at around 140 km (Buffett et al., 2016) with a Brunt-Väisälä period (the theoretical period of gravity waves) of around 19 hours (0.8 days) which as shown in the results, is thinner than models produced here with approximately the same 19 hour period. However from my results, a 140 km thick layer would arise when A is around 1.5 TW below the adiabatic value, which would yield a period of only 23 hours, still the correct order of magnitude.

I have not modelled the chemistry of the stable layer, assuming it plays no role in determining stable layer growth, as I aim to focus upon pure thermal stratification. The presence of a chemical gradient in the layer may be sufficiently destabilising due to inner core growth, or give rise to destabilising double diffusive effects, to slow down or even halting/fully eroding the stable layer. It may be that double diffusive effects could be included into these parameterised models however at the moment understanding of these effects in the context of planetary cores is not yet understood sufficiently (Garaud, 2018). Regardless, these would act to reduce the layer thickness from those reported here and so they still stand as an upper bound.

In this study I introduced an entrainment parameter, E, to represent downwards mixing of stable thermal anomalies at the base of the layer. The precise value of E will depend upon the properties of the fluid and the dynamical regime it acts in (Fleury et al., 1991). In general the rate of entrainment across a stable density interface in a fluid has been observed to be inversely proportional to the Richardson number (Turner, 1979), a measure of the buoyancy relative to fluid shear, as increased vertical shear in the flow leads to Kelvin–Helmholtz instabilities. However the entrainment is also found to be proportional to the Rossby number (Levy and Fernando, 2002), which is small for the Earth's core ($\sim 3\times10^{-6}$) (Jones, 2015). Underlying thermal and/or compositional convection may penetrate into the stable stratification (Takehiro and Lister, 2001) depending on the scale of convective columns and the feedback of the Lorenz force on the fluid. Further work on understanding the dynamics of thermal stratification in highly conducting, rapidly rotating planetary cores is therefore key to further develop parameterised models of their evolution. As such, the value of E for the core is unknown although it has been demonstrated here that values < 0.4 are required to maintain some thermal stratification.

In summary I have produced a large suite of thermal history models using a range of input parameters, modelling thermal stratification at the top of the core. This was motivated by observations of the core suggesting a distinct stable layer may exist beneath the CMB (e.g. Helffrich and Kaneshima, 2010; Tanaka, 2007; Buffett et al.,

2016), coupled with recent revisions to the thermal conductivity in the core (e.g. De Koker et al., 2012; Gomi et al., 2013; Pozzo et al., 2013), a key parameter when considering thermal stratification.

Predicted buoyancy frequencies from all models of thermal stratification presented here give periods in the range of 8-28 hours. This is in agreement with the strength of stratification inferred from geomagnetic observations (Buffett et al., 2016)

The present day Q_c is the main control on the maximum layer thickness, which if the size of the layer is further constrained by observations, may provide a useful additional constraint upon Q_c if the layer has a thermal origin. This also depends upon the amount of entrainment, which I have included with a simple parameterisation, although the precise degree of entrainment is still uncertain. If $E > 0.4$ then it seems unlikely that any stable stratification may form, even given the more extreme scenarios of Q_c I have considered. Further understanding of E may come from dynamical studies of fluid convection focusing on the stability of the interface region between the stable layer and underlying bulk of the outer core.

In the absense of radioactivity or mineral precipitation, thermal stratification cannot exist prior to the inner core given constraints from the entropy budget on magnetic field generation. As such there are limits on the time dependence of the CMB heat flow to both be large enough prior to ICN to permit a dynamo and low enough at present to produce thermal stratification.

These limits suggest Q_c must have decreased over the age of the inner core at an average rate of $\geq$3 TW/Gyr, to produce even the thinnest layers, generally higher than found from calculated Q_c histories from coupled core and mantle models. Therefore it may be difficult to produce thermal stratification with persistent magnetic field generation within a coupled core and mantle model, although an approach of including thermal stratification into such models has not yet been attempted.

Chapter 4

Chemical Stratification

4.1 Introduction

Chemical stratification within the core relies upon a mechanism to enrich the fluid beneath the CMB with light elements, resulting in lower densities that are stable to convective motions. The source for this excess of light element at the CMB must be either an internal mechanism redistributing light element within the core, or be an external source of additional mass entering the core via the mantle.

Internally, as the inner core grows, light elements preferentially partition into the liquid (Braginsky, 1963; Alfè et al., 2002b) where the chemically light plumes from the ICB may pool beneath the CMB (Braginsky, 1993; Moffatt and Loper, 1994; Bouffard et al., 2019). Alternatively barodiffusion, the diffusion along the pressure gradient, may accumulate a chemical layer over the age of the Earth (Fearn and Loper, 1981; Gubbins and Davies, 2013).

Externally, a chemical layer may be a consequence of of Earth's differentiation. Differentiation of the planet formed the dense, iron core where siderophile elements are partitioned between the core and mantle depending upon the redox state (Frost et al., 2008). Collisions with the proto-Earth, including the hypothesised moon forming event (Asphaug, 2014), deliver large amounts of material to the Earth (Rubie et al., 2011) . Jacobson et al. (2017) suggest that at each progressive collision, accreted material undergoes differentiation at larger temperature and pressures, resulting in more O/Si partitioning into liquid iron as it descends through the mantle, creating stable chemical layering at the top of the core. Alternatively Landeau et al. (2016) perform experiments with liquid analogues to the Earth's mantle, core and the core of a large impactor. If the impactor core is relatively light, it can resist resist mixing, leaving a chemically stable layer beneath the CMB.

Finally, the light element transfer from the mantle has been investigated. Par-

titioning data of oxygen between solid mantle ferropericlase and the core from both experimental (Frost et al., 2010) and *ab initio* Davies et al. (2018) methods propose a higher equilibrium oxygen content in the core above current oxygen proposed concentrations Alfè et al. (2002b).

Buffett and Seagle (2010) use the data of Frost et al. (2010) to model the growth of a stratified layer due to an oxygen flux into the core assuming that the core and mantle are in chemical equilibrium at the CMB. Their model produces a present day layer thickness of around 80km assuming an mass diffusivity of oxygen in the core of 3×10^{-9} m^2s^{-1}. Nakagawa (2018) extends their result by including a steady state temperature solution for the layer and coupling to a thermal history model for the underlying adiabatic region of the core. The stable layer thickness varies between 140-250 km in their model depending upon the CMB heat flow and the oxygen diffusivity, for which they use up to 4.8×10^{-8} m^2s^{-1}.

Davies et al. (2018) argue the lower chemical boundary layer in the mantle limits the transport of O, making it difficult to explain a >100 km thick layer. Their model suggests that the upwards barodiffusive flux of O could actually be larger than the downward diffusion of O through the solid mantle, however, if the lower mantle was molten this would aid O transport into the core. Davies et al. (2020) use partitioning data of O between liquid mantle silicates and the core (Fischer et al., 2015; Pozzo et al., 2019) to modelling a Basal Magma Ocean (BMO) and the O transport across the CMB. Heightened transport of O due to the liquid silicates able to refresh the CMB with FeO allowed a ∼140 km thick layer to form in the core up until the end of their simulation (500 Ma). The thickness of the layer was determined by the radius where the chemical gradient from an analytical solution to diffusion balances a prescribed super-adiabatic temperature gradient to give neutral stability.

Buffett and Seagle (2010) do not simultaneously solve for the thermal evolution of the rest of the core, instead treating it as a time dependent input based on previous models without a stable layer (Buffett et al., 1996b). The consequence of this is that the evolution of the stable layer cannot impact the evolution. The calculations of Davies et al. (2018) and Davies et al. (2020) also do not couple the stable layer evolution to the thermal history of the core and avoid simulating times when inner core growth is expected. Nakagawa (2018) does calculate the ohmic dissipation for their coupled model following the method of Labrosse (2014), however, this method however does not include a parameterisation for a stable layer. It therefore seems that Nakagawa (2018) does not account for the stable layer when calculating the entropy terms. The impact of the layer upon the entropy budget of the core and hence power available to drive the dynamo is unknown in a chemical layer, something I will focus upon in this chapter.

I will consider two scenarios generating stable stratification in this chapter. I will revisit the same proposed fluxes of oxygen at the CMB but by modelling them with the model developed in chapter 2, I will investigate the impact of the layer upon the thermal evolution of the core, and vice versa, and the entropy budget. Secondly I will produce an equivalent set of results, investigating a primordial layer formed by incomplete mixing in the early Earth. So far, to my knowledge, there are no published models of a thermal history of the core under these conditions and so I will be able to examine the effects of a thick layer that exists from the onset of Earth's history. I will consider oxygen diffusion within the layer since oxygen is of interest for several key reasons. Firstly the discussed studies on oxygen partitioning advocate for a flux of oxygen into the core (Frost et al., 2010; Pozzo et al., 2019). Secondly oxygen has a relatively high molecular diffusivity at core pressure/temperatures compared to other light elements (Pozzo et al., 2013) and so will provide upper bounds on the thickness of chemical stratification. Oxygen is also thought to strongly partition into the liquid at the center of the core (Alfè et al., 2002b) during inner core growth and therefore provides a significant contribution to the inner core boundary density jump (Masters and Gubbins, 2003). Finally recent studies on oxide precipitates in the core (Badro et al., 2016; O'Rourke et al., 2017; Hirose et al., 2017; Badro et al., 2018; Du et al., 2019) have strong implications for the geodynamo and depend significantly on the presence of oxygen, particularly at the top of the core where this oxide precipitation is thought to occur.

The chapter is laid out as follows. Section 4.2 contains the methods for investigating the stable layer originating from both mass transfer with the mantle 4.2.1 and from a primordial layer 4.2.2. Results are shown in section 4.3 followed by a discussion in section 4.4.

4.2 Method

Chapter 2 develops the thermal history model used in this thesis; a general summary is given here for how chemical stratification will be treated. After, sections 4.2.1 and 4.2.2 will then cover the specific modelling choices for their respective scenarios of mass transfer with the mantle and a primordial layer.

The core is separated into 2 main regions, the isentropic region and the stable layer. The stable layer consists of the liquid outer core that is stably stratified at radii $r_\mathrm{s} \leq r \leq r_\mathrm{c}$. The isentropic region comprises the solid inner core and the convecting liquid outer core at radii $0 \leq r \leq r_\mathrm{s}$, where there is the sharp interface with the stable layer at r_s. Subscripts $\mathbf{1}, \mathbf{2}, \mathbf{3}$ will refer to values wihin the inner core, convecting outer core, or stable layer respectively. Within the well mixed isentropic region, the temperature is assumed to follow an adiabat, whilst in the stable layer the temperature is described

by a purely conductive profile. The composition of the liquid in the adiabatic region is constant whilst the composition in the stable layer is described by a diffusive profile.

The energy and entropy budgets for the whole core includes the stable layer, which for convenience are reiterated here. The energy balance for the isentropic region is (Eq. 2.64)

$$Q^-_{\mathrm{r_s}} = \overbrace{-\int \rho C_p \frac{\mathrm{D}T}{\mathrm{d}t}\mathrm{d}V_{\mathbf{12}}}^{Q_{\mathrm{s}}^{\mathrm{is}}} + \overbrace{4\pi r_{\mathrm{i}}^2 \rho_{\mathbf{1}} L \frac{\mathrm{d}r_{\mathrm{i}}}{\mathrm{d}t}}^{Q_{\mathrm{l}}} + \overbrace{\int \psi \rho \alpha_c \frac{\mathrm{D}c}{\mathrm{D}t}\mathrm{d}V_{\mathbf{2}}}^{Q_{\mathrm{g}}}, \tag{4.1}$$

and for the stable layer layer is (Eq. 2.65)

$$Q_{\mathrm{c}} = \overbrace{-\int \rho C_p \frac{\mathrm{D}T}{\mathrm{d}t}\mathrm{d}V_{\mathbf{3}}}^{Q_{\mathrm{s}}^{\mathrm{sl}}} + Q^+_{\mathrm{r_s}}, \tag{4.2}$$

Since I wish to focus upon chemical stratification, I will not consider CMB heat flows that are sub-adiabatic that generate thermal stratification, this was done in chapter 3. The temperature gradient at the base of the layer defines the heat into the base of the layer and is also used to define the heat flow out of the top of the isentropic region

$$Q^-_{\mathrm{r_s}} = Q^+_{\mathrm{r_s}} = -k(r_{\mathrm{s}}) 4\pi r_{\mathrm{s}}^2 \times \frac{\partial T_{\mathbf{3}}}{\partial r}. \tag{4.3}$$

where $T_{\mathbf{3}}$ is the temperature in the stable layer. The entropy balance is evaluated for the whole core and is used to evaluate the ohmic dissipation (Eq. 2.66

$$\overbrace{\int k \left(\frac{\nabla T}{T}\right)^2 \mathrm{d}V_{\mathbf{123}}}^{E_{\mathrm{k}}} + \overbrace{\int \frac{\mathbf{i}^2}{\alpha_{\mathrm{D}} T}\mathrm{d}V_{\mathbf{123}}}^{E_{\alpha}} + \overbrace{\int \frac{\Phi}{T}\mathrm{d}V_{\mathbf{123}}}^{E_{\mathrm{J}}} = \overbrace{-\int \left(\frac{1}{T_{\mathrm{c}}} - \frac{1}{T}\right) \rho C_p \frac{\mathrm{D}T}{\mathrm{D}t}\mathrm{d}V_{\mathbf{123}}}^{E_{\mathrm{s}}} + \overbrace{\left(\frac{1}{T_{\mathrm{c}}} - \frac{1}{T_{\mathrm{i}}}\right) Q_{\mathrm{l}}}^{E_{\mathrm{L}}} + \overbrace{\frac{Q_{\mathrm{g}}}{T_{\mathrm{c}}}}^{E_{\mathrm{g}}}. \tag{4.4}$$

The thermal and compositional radial profiles are give by solutions to the diffusion of heat and mass

$$\frac{\partial T_{\mathbf{3}}}{\partial t} = \kappa \frac{\partial^2 T_{\mathbf{3}}}{\partial r^2} + \frac{2\kappa}{r}\frac{\partial T_{\mathbf{3}}}{\partial r} + \frac{1}{\rho C_p}\frac{\partial k}{\partial r}\frac{\partial T}{\partial r} \tag{4.5}$$

$$\frac{\partial c_{\mathbf{3}}}{\partial t} = D \frac{\partial^2 c_{\mathbf{3}}}{\partial r^2} + \frac{2D}{r}\frac{\partial c_{\mathbf{3}}}{\partial r} - \frac{\alpha_c \alpha_{\mathrm{D}}}{\rho}\left(\frac{\partial g}{\partial r} + \frac{2g}{r}\right), \tag{4.6}$$

where the mass flux, $\mathbf{i} = -\rho D \nabla c + \alpha_c \alpha_{\mathrm{D}} g$, contains contributions from both a chemical gradient and barodiffusion along the hydrostatic pressure gradient.

Imposed boundary conditions on equation 4.5 are a fixed temperature at r_{s} and a fixed gradient at r_{c}:

$$\frac{\partial T_{\mathbf{3}}}{\partial r} = -\frac{Q_{\mathrm{c}}}{k(r_{\mathrm{c}}) 4\pi r_{\mathrm{c}}^2} \quad \text{at } r = r_{\mathrm{c}} \tag{4.7}$$

$$T_{\mathbf{3}} = T_{\mathrm{a}}(r_{\mathrm{s}}) \qquad \text{at } r = r_{\mathrm{s}}. \tag{4.8}$$

Once the solution to the thermal profile is found, the thermal gradient at r_{s} is used for a boundary condition on the chemical gradient for solving Eq. 4.6, such that at r_{s} there is neutral stability. Either a fixed value or fixed gradient at r_{c} is imposed as the upper boundary condition as described in section 4.2.1.

$$\frac{\partial c_{\mathbf{3}}}{\partial r} = \frac{\alpha_T}{\alpha_c}\frac{\partial T_{\mathbf{3}}}{\partial r} \quad \text{at } r = r_{\mathrm{s}}. \tag{4.9}$$

The interface at r_{s} is evolved in time by the condition of continuity of composition on the moving interface:

$$\left(\frac{\partial c_{\mathbf{2}}}{\partial t}\right)_{r_{\mathrm{s}}} = \left(\frac{\partial c_{\mathbf{3}}}{\partial t}\right)_{r_{\mathrm{s}}} + \frac{\partial r_{\mathrm{s}}}{\partial t}\left(\frac{\partial c_{\mathbf{2}}}{\partial r}\right)_{r_{\mathrm{s}}}, \tag{4.10}$$

as given in Buffett and Seagle (2010) and previously depicted in Figure 2.10. The solution for both temperature and composition is then linearly regridded onto the new domain with continuity in both temperature and composition at r_{s}, and therefore density.

I solve for the diffusion of only one light element within the layer. In theory all light elements present within the alloy will diffuse at different rates and whilst this can be done from a computational resource viewpoint, it significantly complicates the boundary conditions as they all will impact the density. For simplicity I choose to model just the light element that is considered most significant in controlling the evolution

of the layer, and I assume the other light elements within the layer are uniform and continuous with the adiabatic region, having no impact on the evolution of the layer growth. Additional light elements will be commented upon again in the discussion (section 4.4). Both diffusion solutions are found using a Crank-Nicolson discretisation on a uniform grid.

The CMB heat flow, Q_c, is difficult to estimate at present (Lay et al., 2008) and much less constrained in the past. Typically coupled models of the thermal evolution of both the core and the mantle produce exponentially decreasing trends for Q_c but with varying amplitudes and rates of decay (discussed in chapter 3, see Fig. 3.1). As such, I will search over a range of Q_c histories parameterised in the form

$$Q_c = Ae^{(4.5\text{Gyrs}-t)/\tau}, \tag{4.11}$$

where A is the present day value and τ is a decay constant.

The density jump at the ICB, $\Delta\rho$, is important for determining the core properties as discussed in section 2.6. I therefore consider multiple candidate models for core properties based on 3 different values for $\Delta\rho$: 600, 800 and 1000 kgm^{-3} given by Davies et al. (2015), where all parameters are summarised in tables 2.1 for parameters constant across all models, and 2.2 for parameters that vary depending on $\Delta\rho$. All 3 use a high thermal conductivity in a Fe-Si-O alloy (Fig. 4.1) and are given the model designations D2015-600, D2015-800 and D2015-1000, where the suffix denotes the value of $\Delta\rho$ from which they are derived.

The thermal conductivity of the core is still debated and to demonstrate the effects of a lower conductivity I use the estimates of Konôpková et al. (2016), replacing the conductivity values in models D2015-x with these lower estimates to create models K2016-x, where x denotes one of the 3 different possible density jumps (Fig. 4.1). The quoted values from Konôpková et al. (2016) are for an unspecified iron alloy and so other than thermal conductivity, there is no difference in any other parameter between D2015-x and K2016-x, for any particular density jump 'x'.

In the entropy balance (Eq.4.4), the only source of entropy balancing agains the dissipative sources prior to inner core growth is the contribution from secular cooling, E_s ($Q_l = Q_g = E_L = E_g = 0$). At these times the CMB heat flow needs to be high enough such that E_s is larger enough to ensure $E_J > 0$ which corresponds to $Q_c > Q_a$ where Q_a is the adiabatic heat flow at the CMB (Davies, 2014; Labrosse, 2014). For the high and low thermal conductivities I will use, Q_a is either $\sim$13 TW or < 6 TW respectively. Therefore for models D2015-X, A is varied between 13-19 TW and for low thermal conductivity models A is varied between 4-10 TW. For all models τ is varied between 3-9 Gyrs.

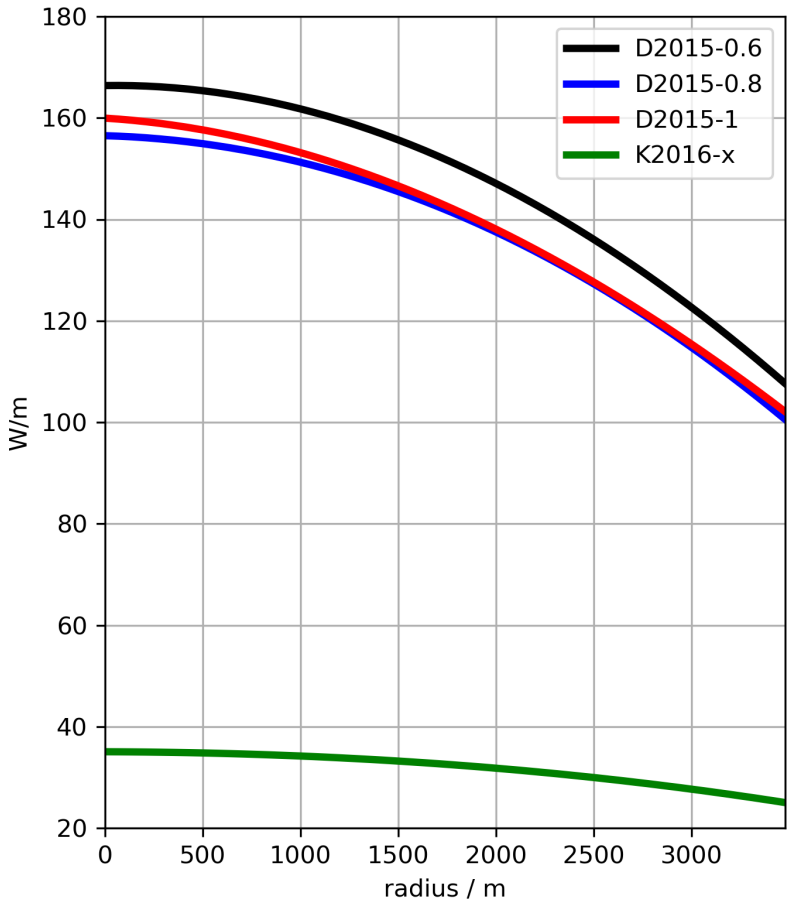

Figure 4.1: Radial conductivity profiles of models used in this section. For models based on Davies et al. (2015), 3 distinct conductivity profiles are provided depending on the density jump at the ICB. The data of Konôpková et al. (2016) is not dependent on the ICB density jump and hence I use the same conductivity values for any density jump 'x'.

4.2.1 Mass transfer with the mantle

I first revisit the scenario outlined consider by Buffett and Seagle (2010) and Nakagawa (2018). The mantle is assumed to sufficiently quickly replenish the CMB with FeO depleted material to maintain chemical equilibrium with the core. The equilibrium value is given by the temperature dependent thermodynamic partitioning model of Frost et al. (2010) which fixes the mass fraction of oxygen at the CMB, providing the upper boundary condition on mass diffusion (figure 4.2). The CMB temperature is given by the thermal diffusion solution as it varies in time and as such the equilibrium

concentration, c_{eq}, decreases in time as the core cools:

$$c_{\mathbf{3}} = c_{\mathrm{eq}}(T) \quad \text{at } r = r_{\mathrm{c}}. \tag{4.12}$$

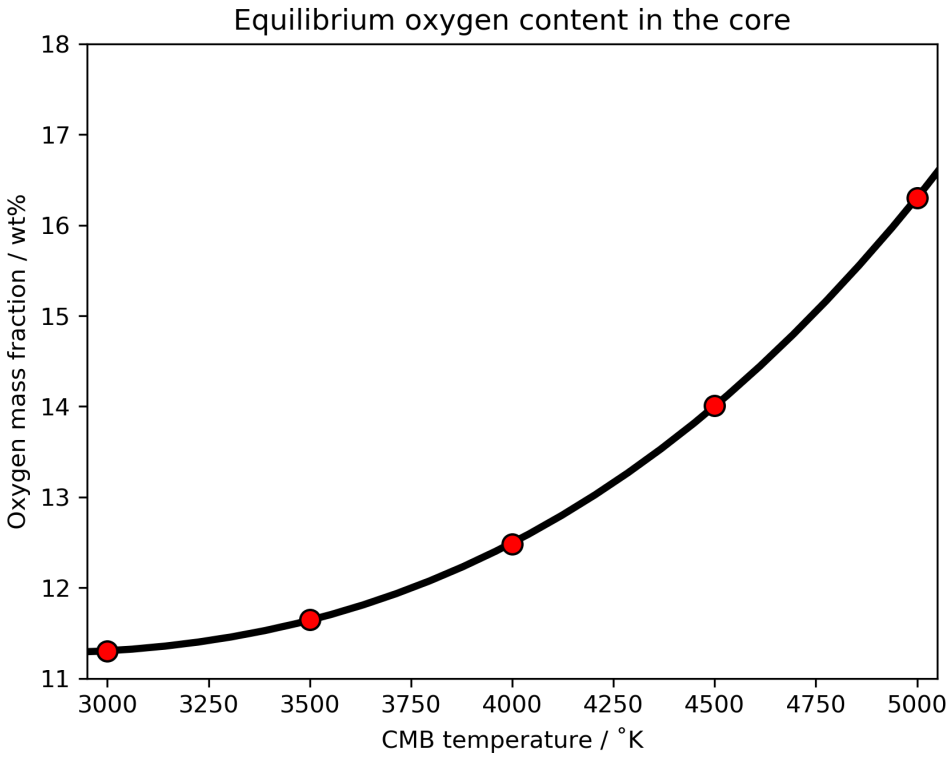

Figure 4.2: Equilibrium concentration of oxygen given 15% mole fraction of FeO in ferropericlase from Frost et al. (2010). Red dots show data from Fig. 14 a) of Frost et al. (2010) and the black line is a 3rd order polynomial fit to this data to calculate at intermediate temperatures.

Then I consider the results of Davies et al. (2020), in which transfer of Fe-O from a BMO into the core is modelled. They model the time evolution of the flux of Fe-O into the core, relaxing the assumption that the mantle can supply enough Fe-O to maintain chemical equilibrium; however they do not solve for the thermal history of the core which I will do. The flux of oxygen into the core depends upon the coupled system so that the concentration of oxygen in the core impacts the flux and vice versa. However, Davies et al. (2020) find the flux drops off with $1/\sqrt{t}$, with a magnitude depending upon the partitioning coefficient for Fe-O and the amount of Fe-O in the mantle. They considered a wide range of partition coefficients and BMO Fe-O content, consistently finding the $1/\sqrt{t}$ trend for Fe-O flux ranging 2 orders of magnitude. As such, I use 2 time series of Fe-O flux from Davies et al. (2020) representing the largest and lowest oxygen fluxes presented from their model and create a further two intermediate flux time series by simply scaling their amplitude (Fig. 4.3). In order of lowest to highest,

the time series represent a total of 7×10^{20}, 2×10^{21}, 7×10^{21}, and 2×10^{22} kg of oxygen into the core. For reference, in the core models I use the total mass of oxygen in the core is $\sim 4 \times 10^{22} - 9 \times 10^{22}$ kg.

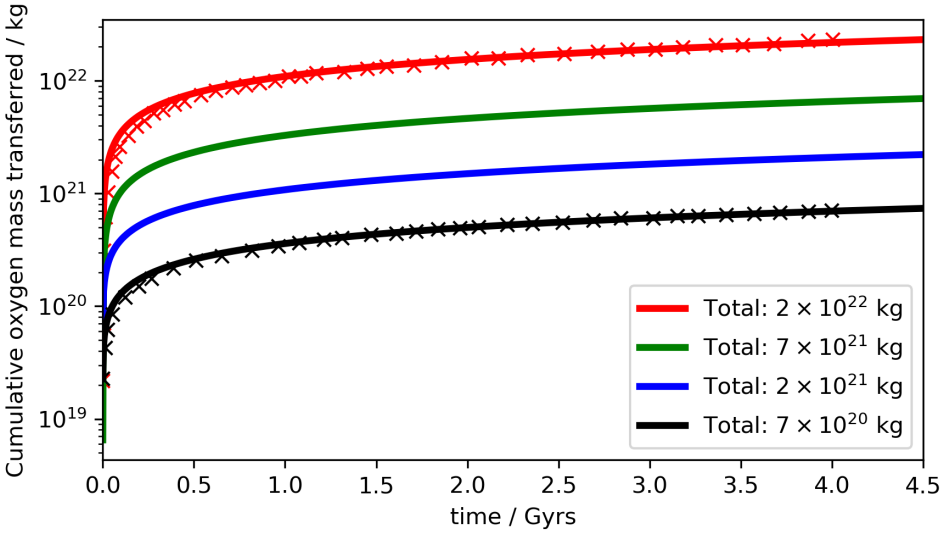

Figure 4.3: Time series of cumulative oxygen transfer into the core based upon the published results from Davies et al. (2020). The different time series are referred to by the total amount of oxygen flux into the core over 4.5 Gyrs as given in the legend. The highest and lowest flux cases (2×10^{20} and 2×10^{22}) relate to partition coefficients of 8 and 5 and mantle Fe-O mole fractions of 0.1 and 0.02 respectively from Davies et al. (2020). The middle 2 flux time series were made by scaling the lowest and highest by 3 and 0.3 respectively to represent intermediate partitioning. Original data is shown by the crosses for the highest and lowest flux cases.

The time series from Davies et al. (2020) for the cumulative total flux is fitted with a $\sqrt{t}$ function so that they may be extrapolated beyond 4 Gyrs to 4.5 Gyrs (as is on Figure 4.3). This will provide an upper bound upon the flux of oxygen into the core since the mantle at the CMB would be required to be molten to provide these fluxes. In reality the flux may either reduce or stop all together at a time prior to the present day when the lowermost mantle freezes. Note that the fluxes have been converted from mass of Fe-O to mass of oxygen by using the molecular weights (w) for oxygen and iron with the factor $w_{\mathrm{O}}/(w_{\mathrm{FeO}})$. In extrapolating to 4.5 Gyrs I have assumed that the inner core growth does not appreciably impact this $\sqrt{t}$ trend which the results confirm to be reasonable. The time derivative of the fit then yeilds the CMB flux, $\mathbf{i}_{\mathrm{c}}$ which is used as the upper boundary condition to solve mass diffusion in the layer

$$\frac{\partial c_{\mathbf{3}}}{\partial r} = -\frac{\mathbf{i}_{\mathrm{c}} - \alpha_c \alpha_{\mathrm{D}} g}{\rho D} \quad \text{at } r = r_{\mathrm{c}}. \tag{4.13}$$

Note that I include the barodiffusive contribution, whereas Davies et al. (2020) do not in calculating the mass flux. The barodiffusion contribution at the CMB is negligible when compared to the flux down the compositional gradient Davies et al. (2020) however, I

do want to include this term in general since it is not necessarily negligible near the base of the layer where the compositional gradient is much smaller.

In both cases of either fixed composition following Buffett and Seagle (2010) or fixed flux following Davies et al. (2020), there is originally no stable layer at t=0 Gyrs, growing by diffusion until the present day, coupled to the evolution of the underlying isentropic region.

4.2.2 Primordial Layers

I conclude my investigation into chemical stratification by modelling the scenario of a chemically stable layer produced as a result of the merging of cores of an ancient impactor with the proto-Earth. The fluid experiments of Landeau et al. (2016) show that for an impactor that has a light composition relative to the early core, an approximately linear profile in the mass fraction of the resulting chemical stratification is formed. As an initial condition I therefore impose a pre-existing stable layer of thickness $h = r_\mathrm{c} - r_\mathrm{s}$ with a linearly increasing mass fraction profile, $c_{\mathbf{3}}$. This profile merges with the underlying adiabatic region at r_s, $c_{\mathbf{3}}(r_\mathrm{s}) = c_{\mathbf{2}}$ and with a value $c_{\mathbf{3}}(r_\mathrm{c})$ at the CMB, chosen to give an imposed density contrast R, where $R = \alpha_c(c_{\mathbf{3}}(r_\mathrm{c}) - c_{\mathbf{2}})$. such that:

$$c_{\mathbf{3}}(r) = c_{\mathbf{2}} + \frac{r - r_\mathrm{s}}{h}\frac{R}{\alpha_c} \tag{4.14}$$

Estimates for R at the CMB at present are around 1% (0.01) (Helffrich and Kaneshima, 2010) and so I use R= 0.5%, 1% and 1.5% as the initial density contrasts. As the profile begins to diffuse the density contrast at the CMB will change in time however the diffusion of light element is slow and so I expect the present day value for R to be similar to the inital value, confirmed by my results. The temperature profile is initialised with a linear profile, with a gradient given by Q_c and a value ar r_s equal to the adiabatic temperature $T_\mathrm{a}(r_\mathrm{s})$. In theory there could be mass transfer with the mantle in this scenario however I wish to demonstrate the evolution of the core focusing on just the primordial layer and so for simplicity I set the condition of zero total flux at the CMB:

$$\frac{\partial c_{\mathbf{3}}}{\partial r} = -\frac{\alpha_c \alpha_\mathrm{D} g}{\rho D} \quad \text{at } r = r_\mathrm{c}. \tag{4.15}$$

To summarise, I consider 2 different scenarios resulting in chemical stratification: mass transfer with the mantle and a primordial layer. I produce 2 set of models for the first scenario. Case 1 uses a fixed value on composition representing the oxygen partitioning from solid ferropericlase into the core and maintaining the chemical equi-

librium. Case 2 fixes the flux of oxygen to a time varying value which represents the oxygen partitioning from a BMO into the core. Finally, in the second scenario, case 3 considers a pre-exisiting primordial layer with no mass transfer with the mantle. Each of these scenarios are calculated with the 6 different sets of core properties using D2015-600/800/1000 and K2015-600/800/1000 and a range of CMB heat flows.

4.3 Results

In this section, results for cases 1,2, and 3 are shown in that order. In each case an example solution for a particular choice of parameters is given, before demonstrating the more broad trends across the full parameter space.

4.3.1 Case 1: Mass flux via chemical equilibrium with the mantle

I first show results for the CMB heat flux, equation 4.11 for $A = 15$ TW and $\tau = 6$ Gyrs for the core properties D2015-800. Plotted for comparison to this model is an identical simulation with the same heat flow and core properties that matches the current inner core size but no mass transfer with the mantle and hence no stable layer forms. The stable layer thickness can be seen on Figure 4.4 a), growing to around 200 km at its peak before being eroded as the inner core grows to it's present day thickness of around 130 km. As expected this is approximately the same size as found by Nakagawa (2018) for roughly the same oxygen diffusivity despite their inner core being double the age than presented here. The erosion on the layer by inner core growth is primarily due to oxygen rejected by the inner core enriching the concentration in the well mixed interior, rather than an effect due to the extra energy sources. Therefore, if a similar total amount of oxygen is released by the inner core, the interface will recede by a similar distance not heavily dependent upon the inner core age.

The energy sources (Fig. 4.4 b)) are not significantly impacted by the presence of the layer. The inner core growth rate is marginally different leading to small differences in Q_l and Q_g and so the total secular cooling Q_s is also very similar. The entropy sources E_J, E_k and E_α, along with the entropy due to secular cooling, E_s, are plotted on Figure 4.4 c). Note that E_J only just stays positive prior to inner core nucleation, and so if the heat flow were reduced much further, the dynamo would fail which would be inconsistent with observations at that time. In the stable layer the conductive profile is both colder and has a steeper gradient than an adiabatic temperature profile, with a greater deviation at the CMB than at r_s. Therefore, given $E_k \propto (\nabla T/T)^2$ and the fact that the larger contributions to the total integral of E_k come from the outermost region of the core (due to spherical geometry), E_k is significantly increased due to the presence of the stable layer.

The entropy due to mass diffusion, E_α, is very small at present, however was very

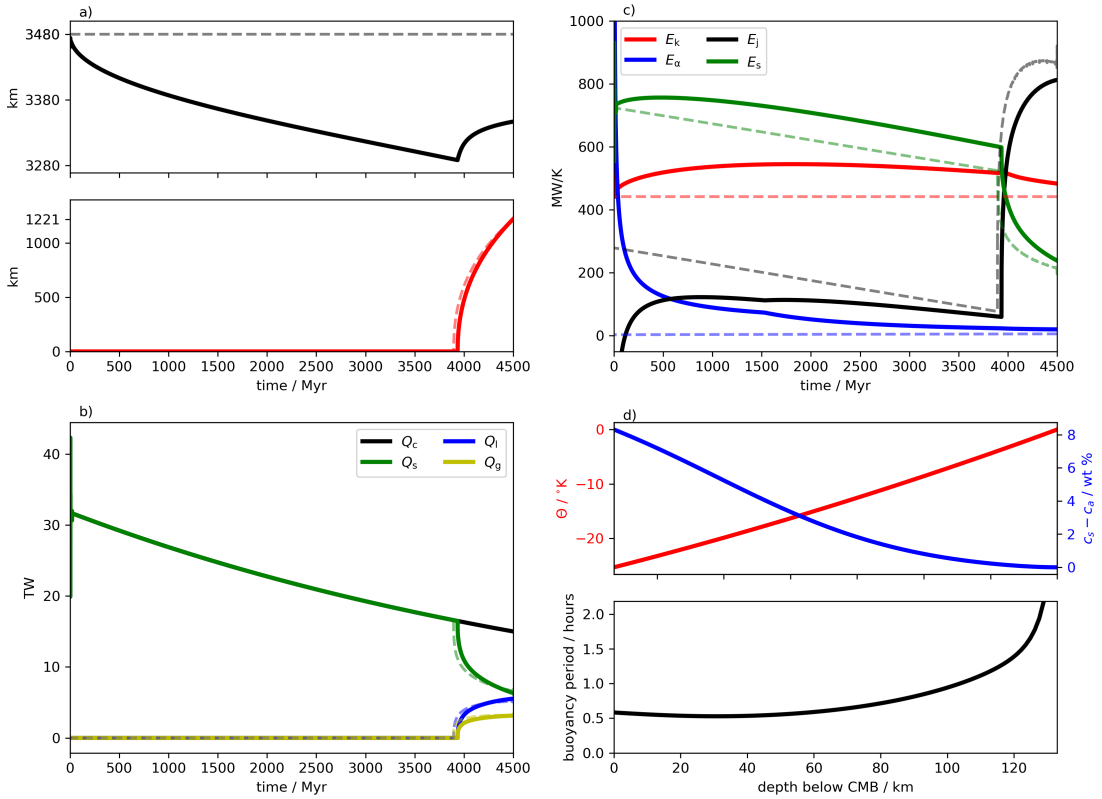

Figure 4.4: Results for case 1 using model D2015-800 with $A = 15$ TW, $\tau = 6$ Gyrs. In panels a),b) and c) dashed lines show results for an identical case without a stable layer. a) Radii of r_s (top) and r_i (bottom) through time. b) Energy sources through time. c) Entropy sources through time. E_L and E_g are not shown for clarity of the other terms but their effect on the entropy budget can be seen post inner core nucleation in E_J. d) Thermal and compositional profiles relative to the isentrope of the adiabatic region (top) and the period of gravity waves (bottom), equal to $2\pi/N$ where N is the Brunt-Väisälä frequency.

large in the 500 Myrs due to a large flux which reduces over time. Despite these significant increases to the dissipative E_k and E_α, E_J remains positive, except for very early times, due to E_s also increasing relative to the case with no stable layer. We have no reliable paleomagnetic observations in the first 500 Myrs of Earth's history and so this model may still be considered successful since $E_\mathrm{J} < 0$ is confined to this period. In the stable layer the thermal profile is free to cool below an adiabatic temperature and so $\mathrm{D}T/\mathrm{D}t$ is larger at radii $r > r_\mathrm{s}$ than if the entire outer core were convecting and adiabatic. Furthermore, the CMB temperature is lower when the chemical layer is present for the same reason and so for the entire core, the factor $(1/T - 1/T_\mathrm{c})$ becomes larger, making the secular cooling more thermodynamically efficient. There is still an overall reduction in E_J as the increase in E_s is not great enough to overcome the increases in E_α and E_k, therefore the presence of a chemical stable layer does marginally increase the lower bound on the CMB heat flow in the more distant past to ensure an active dynamo for the past 3.5 Gyrs.

The destabilising thermal and stabilising compositional profiles throughout the layer are shown in Figure 4.4 d) (top panel). Both profiles are plotted relative to the isentrope of the isentropic region at that radius, i.e. relative to an extrapolation along the adiabat and the constant oxygen concentration of the isentropic region, for the definition of the potential temperature as $\Theta(r) = T(r) - T_{\rm a}(r)$. These profiles determine the Brunt-Väisälä frequency N a typical measure of the strength of stability which gives the frequency of gravity waves in stably stratified fluid defined as:

$$N = \sqrt{-\frac{g}{\rho_0}\frac{\partial \rho'}{\partial r}} \tag{4.16}$$

where ρ_Θ is the potential density, $\rho_\Theta = \rho_0 \left(-\alpha_T \Theta - \alpha_c (c_{\mathbf{3}} - c_{\mathbf{2}})\right)$.

The period, $2\pi/N$ is plotted on the lower panel of Figure 4.4 d) which is relatively short at around 30 minutes near the CMB (note the period tends to infinity at $r_{\rm s}$ as the buoyancy profile tends to neutrally stability).

For a full parameter search I calculate models with a variety of core properties: D2015-600/0.8/1 and K2015-600/0.8/1. For the low conductivity models, K2015-X, I vary the heat flow parameter A between 4-10 TW, whilst the high conductivity models, D2015-X, A is varied between 13-19 TW. For all models τ is varied between 3-9 Gyrs.

Figure 4.5 shows the present day layer thickness for all models. Missing results for lower values of A and τ for models D2015-600/800 are due to $E_{\rm J}$ becoming negative at a time just before the inner core formed. Decreasing τ or increasing A increases $Q_{\rm c}$ although the results show very little variation with the $Q_{\rm c}$ history. A larger density jump, $\Delta\rho$, increases the quantity of oxygen expelled by inner core growth resulting in thinner layers, reducing by around 10 km for each successive value of $\Delta\rho$.

Figure 4.6 shows the different time evolution of high and low thermal conductivity models. D2015-X models initially grow faster since $A = 15$ TW represents a slightly less super-adiabatic heat flow than 6 TW does for K2015-X models but the main difference is the inner core age. In K2015-X models the inner core is much older due to a much lower requirement on the secular cooling to ensure $E_{\rm J} > 0$ and so the layer begins to recede much earlier at around 3.2 Gyrs. However, a slower growing inner core releases light element much more slowly and so the layers in D2015-X models are eroded much faster to produce almost an identically sized layer at the present day. Higher $\Delta\rho$ values have reduced thermal conductivity values since the presence of light element depresses k. Therefore, for the same $Q_{\rm c}$, a lower k results in steeper super-adiabatic temperature gradients and therefore more entrainment of the layer and a reduced growth rate.

In general, regardless of core properties or heat flow, a chemically stable layer is produced between ∼120-150 km thick at present with a peak Brunt-Väisälä frequency

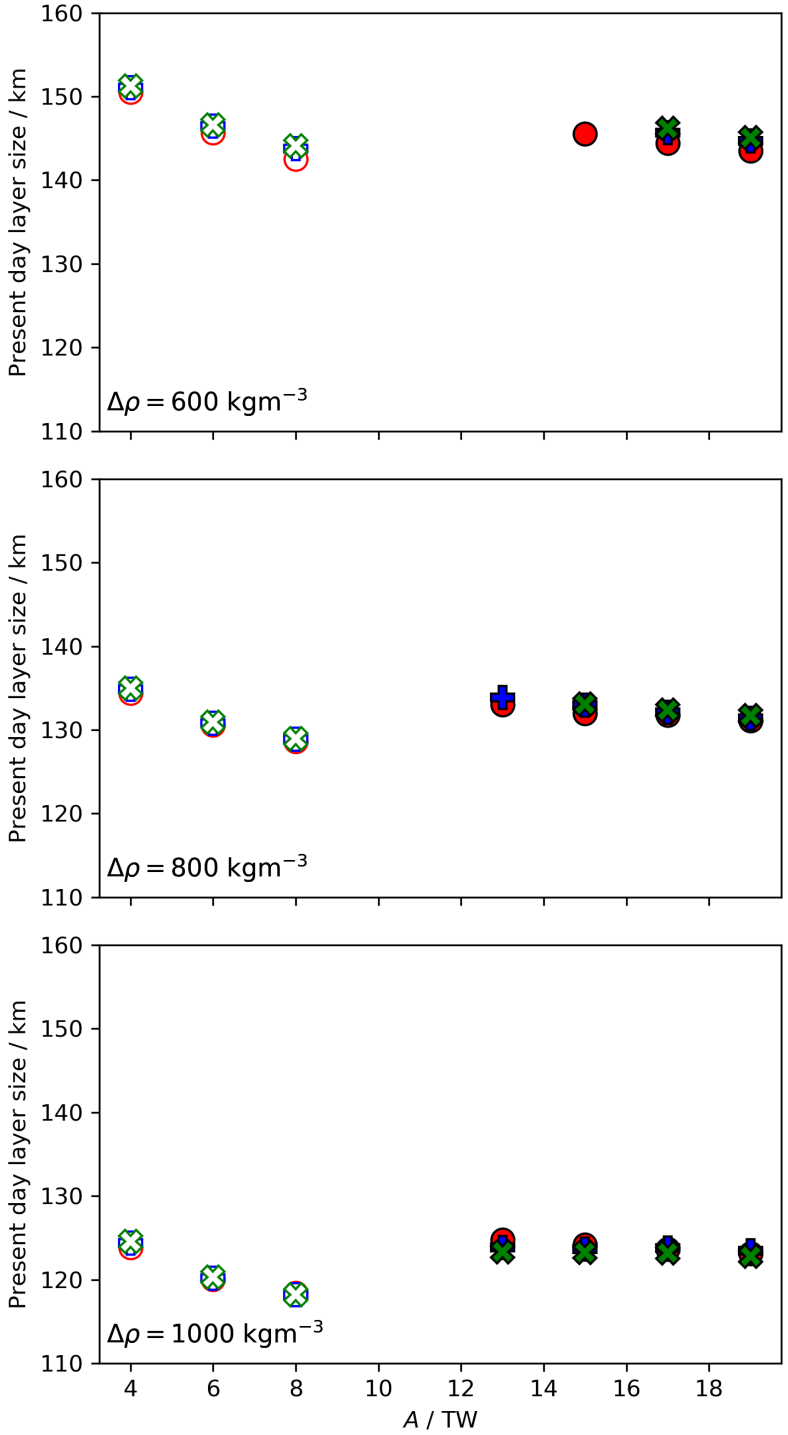

Figure 4.5: Present day layer thickness from the parameter search for case 1 as a function of A. Top, middle and bottom panels represent the 3 different inner core density jumps of 600, 800 and 1000 kgm^{-3} respectively. Solid symbols and empty symbols represent either a high (D2015-X) or low (K2015-X) thermal conductivity. Finally symbols represent $\tau = 3$ (circles), 6 (crosses) and 9 (plusses) Gyrs.

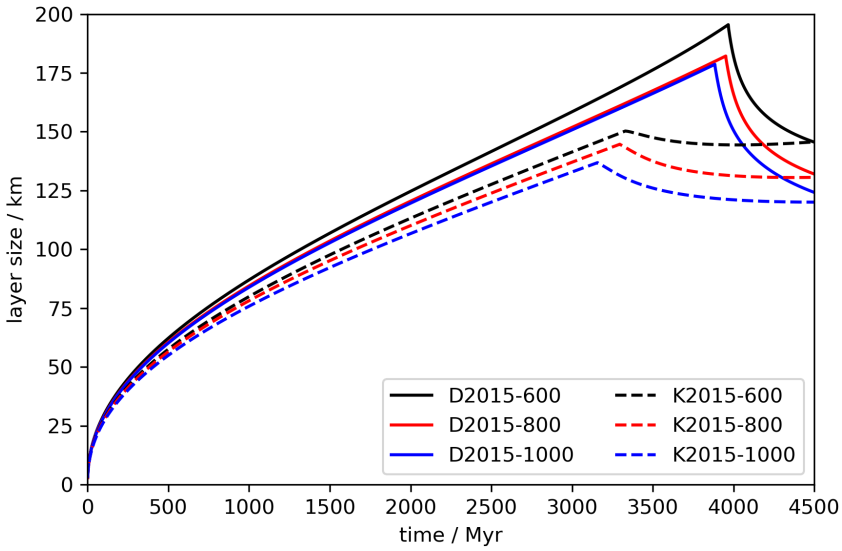

Figure 4.6: Time series of layer thickness for lower conductivity models (K2015-X) vs higher conductivity models (D2015-X). Results are shown for $\tau = 3$ Gyrs and then either $A = 15$ TW for D2015-X or $A = 6$ TW for K2015-X for all density jumps used.

relating to periods between 25-37 minutes since the chemical anomaly is always very large relative to the super-adiabatic temperature gradients (Fig. 4.7).

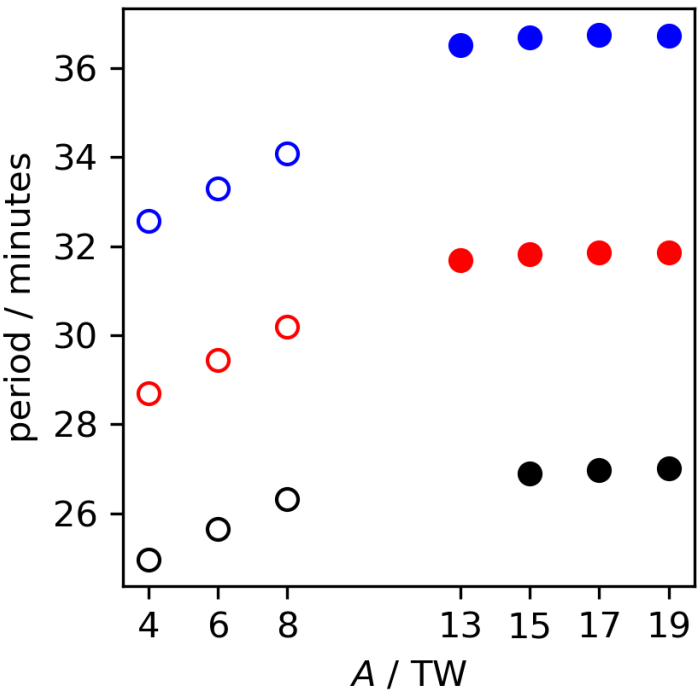

Figure 4.7: Period of gravity waves, $2\pi/N$, in the present day layers for high (filled) and low(open) conductivites. Colors refer to different density jumps of 600 (black), 800 (red), 1000 (blue) kg m^{-3}. Results are only shown for $\tau = 3$ Gyrs since there is no significant variation with varying τ.

4.3.2 Case 2: Mass flux with the mantle from a BMO

Section 4.3.1 presented results when the mantle is able to maintain the flux of oxygen into the core such that the two are in equilibrium at the CMB, based upon the partitioning data of Frost et al. (2010). In this section I present results based upon the findings of Davies et al. (2020) in which the flux of oxygen into the core is limited by the chemical boundary layer at the base of the mantle, calculated using their partitioning behaviour between molten silicates and the core (Fischer et al., 2015; Pozzo et al., 2019). Based on their study I use 4 different time series of oxygen flux into the core, a range from the lowest to highest fluxes found by Davies et al. (2020) (Fig. 4.3). As before I first show a result for a single set of core properties and CMB heat flow parameters before the summary of the full parameter search.

Figure 4.8 shows the results for the model with core properties D2015-800 using the Q_c parameters A=15 TW and $\tau = 6$ Gyrs (the same set of parameters in figure 4.4). As expected the higher flux case generates a thicker layer (Fig. 4.8 a) upper panel) than the low flux case, reaching to 200 km thick at it's peak before inner core nucleation. Despite nearly 2 orders of magnitude more oxygen transferred into the core, the layer is only moderately thicker than the low flux case as its growth is limited by the slow speed of diffusion of oxygen in the core.

However, there is a strong difference in the entropy budget for the two cases (Fig. 4.8 c). In the high flux case the entropy due to mass diffusion, E_α, is orders of magnitude larger since $E_\alpha \propto \mathbf{i}^2$. For this model, the dynamo cannot operate for the majority of the simulation in contrast to the low flux case in which E_α is small and $E_J > 0$. Reducing this flux of oxygen to the second highest flux case, using a total flux of 7×10^{22} kg, shown in Figure 4.9, lowers E_α enough to keep E_J positive for the period of time constrained by paleointensity data ($>$ 3.5 Ga) (Tarduno et al., 2010) to produce a viable model. Differences between the energy budget and hence inner core growth are minimal (Fig. 4.8a lower panel, and b).

The high flux case produces an extremely large O concentration at the CMB, 30 wt% above the isentropic region (Fig. 4.8 d) upper panel) compared to just 1% in the low flux case. The much larger anomaly of the high flux case produces the shorter period of gravity waves at $\sim$ 20 minutes whereas the low flux case produces an 80 minute period. Although 80 minutes is longer than the highest flux case, it is still much shorter than the 8-28 hours produced by thermal stratification (see figure 3.11).

All results from the parameter search are shown on Figure 4.10. E_J in all the highest flux models (2×10^{22} kg) follows the same trend as shown above giving E_J¡0 for the majority of the simulation and so none of those models are compatible with observations. The present day layer thickness is relatively insensitive to the heat flow history or core properties as was the case with the previous results (Fig. 4.5). Layer

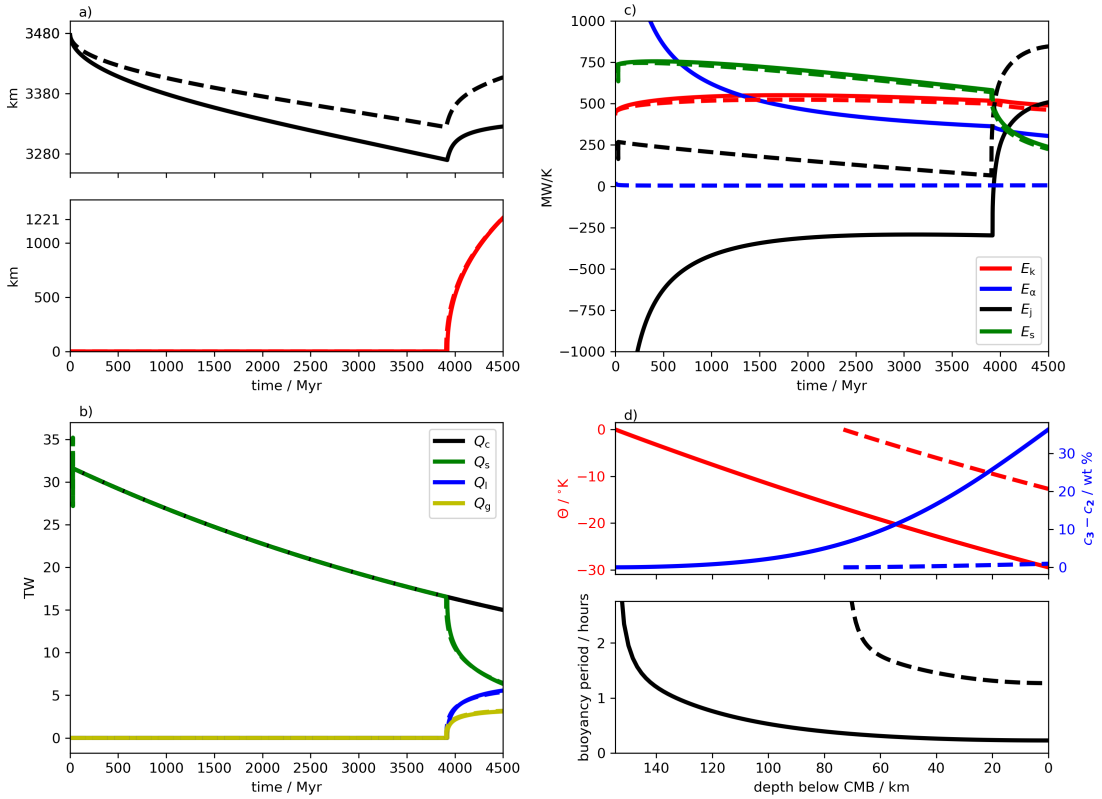

Figure 4.8: Results for case 2 using model D2015-800 with $A = 15$ TW, $\tau = 6$ Gyrs. In all panels, solid lines show results for the highest flux case and dashed lines show results for the lowest flux case. a) Radii of r_s (top) and r_s (bottom) through time. b) Energy sources through time. c) Entropy sources through time. E_L and E_g are not shown but the effect on their entropy budget can be seen post inner core nucleation in E_J. d) Thermal and compositional profiles relative to the isentrope of the adiabatic region (top) and the period of gravity waves as given by the $2\pi/N$ (bottom).

thickness decreases slightly with increasing $\Delta\rho$ as more light element is attributed to oxygen in the bulk core composition, and so more is released upon freezing of the inner core. As expected the layer thickness decreases with reduced flux at the CMB.

Figure 4.11 shows the present day layer thickness for all models based on a mass flux at the CMB as a function of the total flux of oxygen. Both case 1 and case 2 results show the same trend, despite the different modelling approaches, demonstrating that the main control upon the layer thickness across all the results presented here is the total amount of light element introduced at to the core. The layer size quickly increases as more oxygen is introduced into the core before the growth of the layer is limited by the rate of diffusion. Nakagawa (2018) showed that the layer size is $\propto \sqrt{D}$ and so this along with total oxygen flux are the two primary controls of the present day layer size. The predicted Brunt-Väisälä follow a similar trend for all models from cases 1 and 2, giving periods that decrease with increasing total flux (Fig. 4.12.

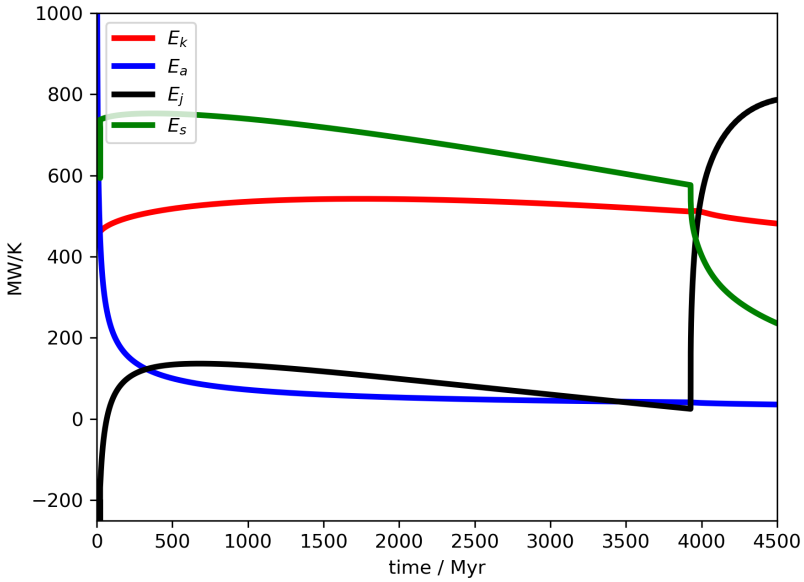

Figure 4.9: Same as Figure 4.8 c) except the imposed flux of oxygen is 30% that of the highest flux case yielding a total flux of 7×10^{21} kg, Figure 4.3.

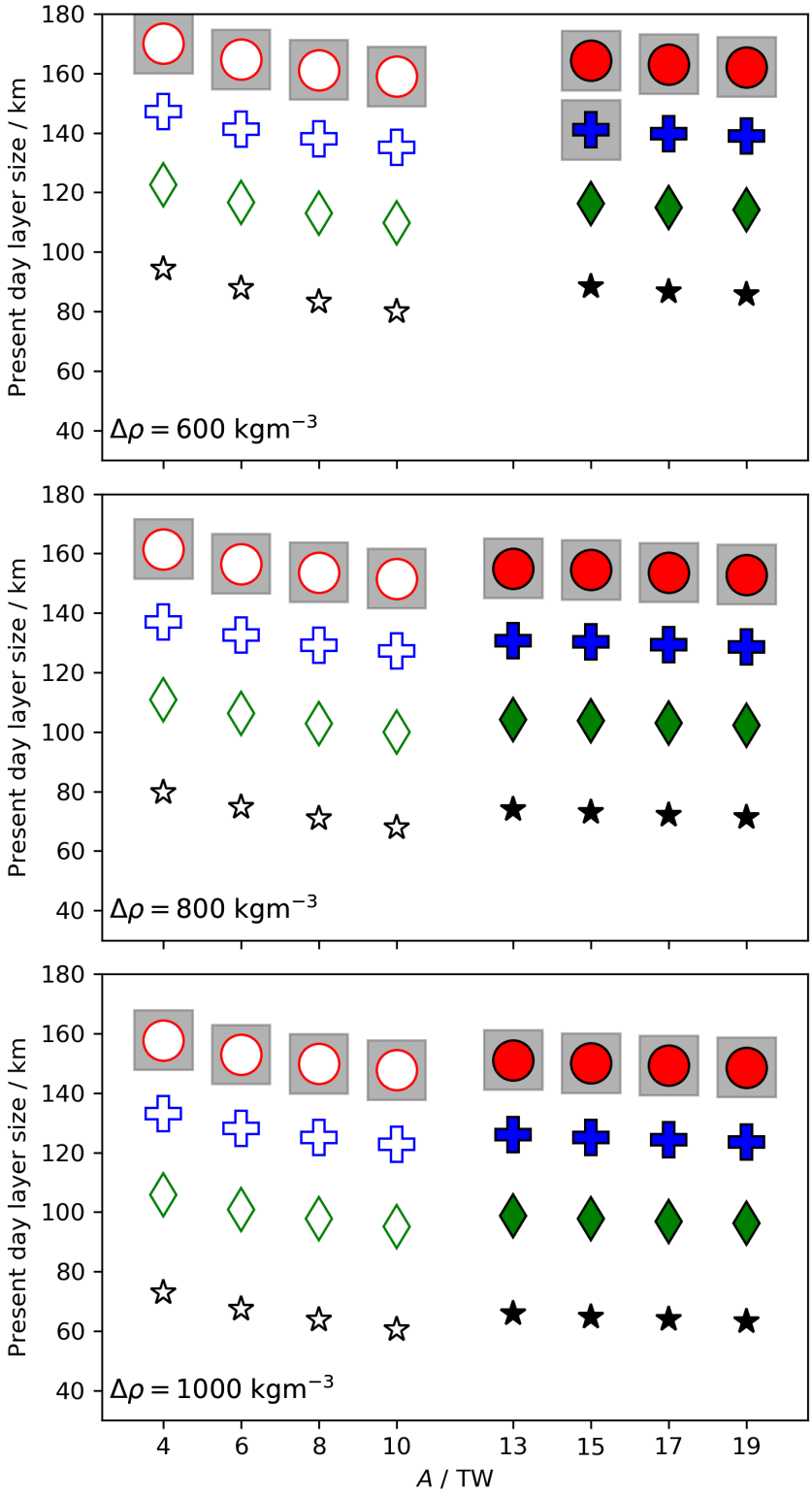

Figure 4.10: All results from the parameter search for case 2 as a function of A. Top, middle and bottom panels represent the 3 different inner core density jumps of 600, 800 and 1000 kgm^{-3} respectively. Solid symbols and empty symbols represent either a high (D2015-X) or low (K2015-X) thermal conductivity. Symbols represent $\tau = 3$ (circles), 6 (crosses) and 9 (plusses) Gyrs. Larger and smaller symbols represent the higher and lower fluxes from figure 4.3 respectively. Models in which the presence of the stable layer resulted in $Ej < 0$ at a time constrained by paleomagnetic measurements ($t > 3.7$ Ga) are shown with a grey box behind them.

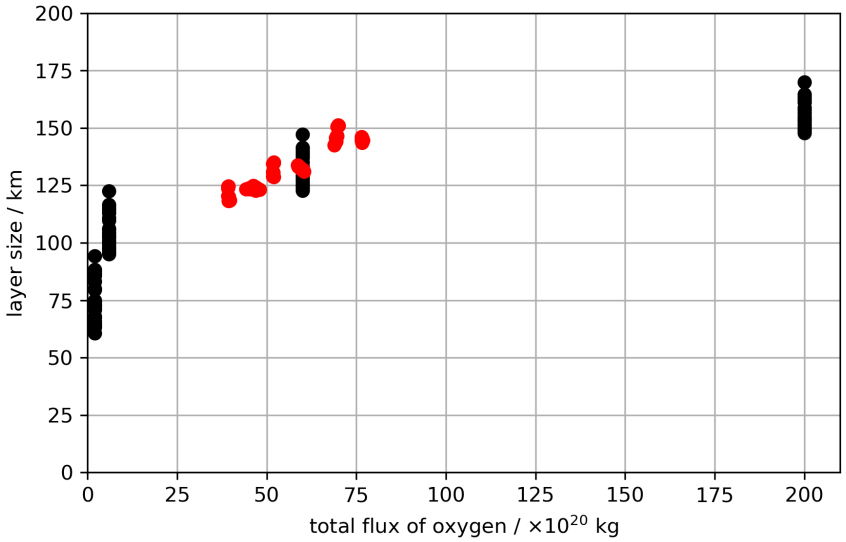

Figure 4.11: All models both case 1 (red) and case 2 (black) plotted as the present day layer thickness vs the total oxygen flux into the core.

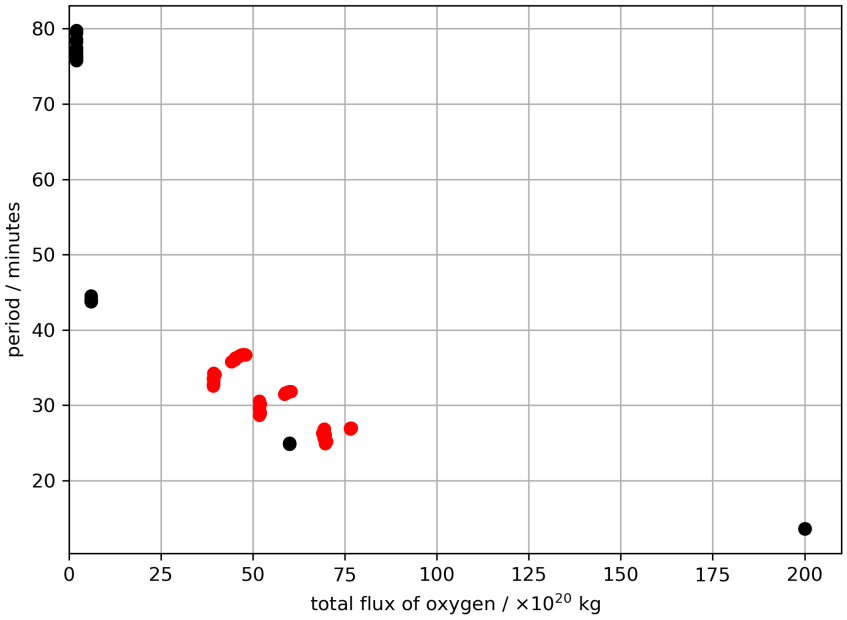

Figure 4.12: All models both case 1 (red) and case 2 (black) plotted as the period corresponding to the peak Brunt-Väisälä frequency vs the total oxygen flux into the core.

4.3.3 Case 3: Primordial layer

Finally I show results for chemical stratification formed via an ancient impactor resulting in a primordial layer. The layer is initialised at t=0 with a linear profile in oxygen composition which is continuous with the well mixed region at r_s and increases to an anomaly at r_c given by a specified density anomaly of R =0.5, 1, 1.5%. I first show the result for the same core properties and heat flow model as used in the previous results sections: D2015-800 with A=15 TW and τ=6 Gyrs with a density anomaly at the CMB of R=1% in an initially 300 km thick layer. As done in section 4.3.1, the results are compared to a simulation in which no primordial layer exists and no chemical stratification grows (dashed lines).

Figure 4.13 summarises the results showing that the layer grows by diffusion before being eroded back due to the inner core enriching the well mixed region with oxygen. The CMB density anomaly of 1% is retained as diffusion has not sufficiently smoothed out the compositional profile in the layer (Fig 4.13d, top panel) to reduce the initialised oxygen mass fraction. Once again we see the effect on the entropy budget (Fig 4.13b) where a larger production of entropy by thermal conduction, E_k, is roughly balanced with an increase in the secular cooling E_s, therefore still permitting Ej>0 throughout this simulation. In my parameter search I do not find any models in which the presence of the primordial layer reduces E_J below zero for which Ej remains positive in an identical simulation with no initial primordial layer. The period of gravity waves throughout the layer are longer than in the previous results due to weaker chemical gradients but are still relatively short at around 2-3 hours (Fig 4.13d bottom panel).

For the full parameter search (Figs. 4.14 and 4.15) layers were initialised at thicknesses of 100, 200, 300 and 400 km thick with a density anomaly of 0.5%, 1% and 1.5%. All models follow a similar trend to the model shown in Figure 4.13, growing via diffusion a small amount before receding due to inner core growth. Exceptions to this trend are shown by the models in which the present day layer thickness is zero. For a given initial layer thickness, there comes a point where the heat flow at $t = 0$ is sufficiently destabilising to cause the layer to rapidly recede and fully erode the layer. Furthermore for a fixed density anomaly R, increasing the initial layer thickness, h, gives a smaller gradient in the initial linear profile. As the initial layer thickness increases, there reaches a point where again the super-adiabatic temperature gradient is sufficiently destabilising. Therefore, on figures 4.14 and 4.15, increasing Q_c or h (upwards and to the right on each of the sub-plots) moves towards the region of the parameter space where the layer is quickly eroded away within the first 20 Myrs.

In the case of a low thermal conductivity (Fig. 4.15) a notable number of models have their primordial layers quickly eroded away at only moderate heat flows, since a fixed heat flow becomes more super-adiabatic the lower the thermal conductivity. This

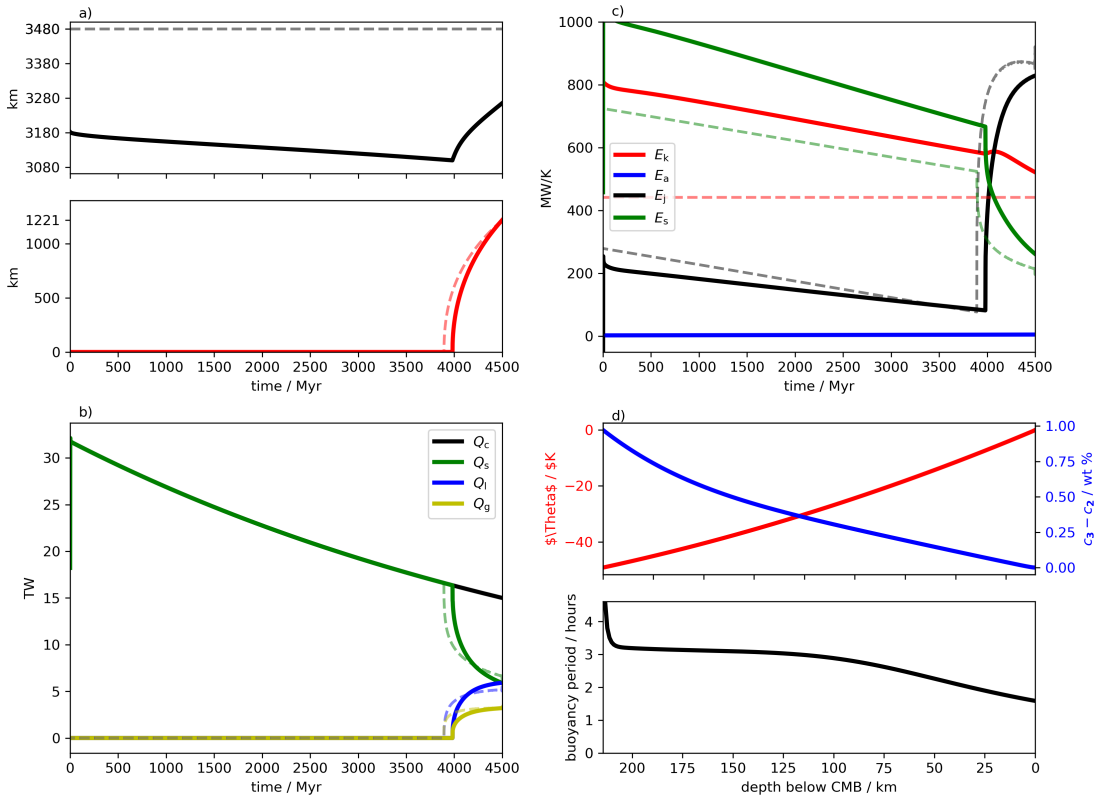

Figure 4.13: Results for case 3 using model D2015-800 with A=14 TW, τ=6 Gyrs, an initial layer thickness of 300 km and a density anomaly of 1%. In panels a),b) and c) dashed lines show results for an identical case without a stable layer. a) Radii of r_s (top) and r_i (bottom) through time. b) Energy sources through time. c) Entropy sources through time. E_L and E_g are not shown but their effect on the entropy budget can be seen post inner core nucleation in E_J. d) Thermal and compositional profiles relative to the isentrope of the adiabatic region (top) and the period of gravity waves as given by the Brunt-Väisälä frequency, $2\pi/N$ (bottom).

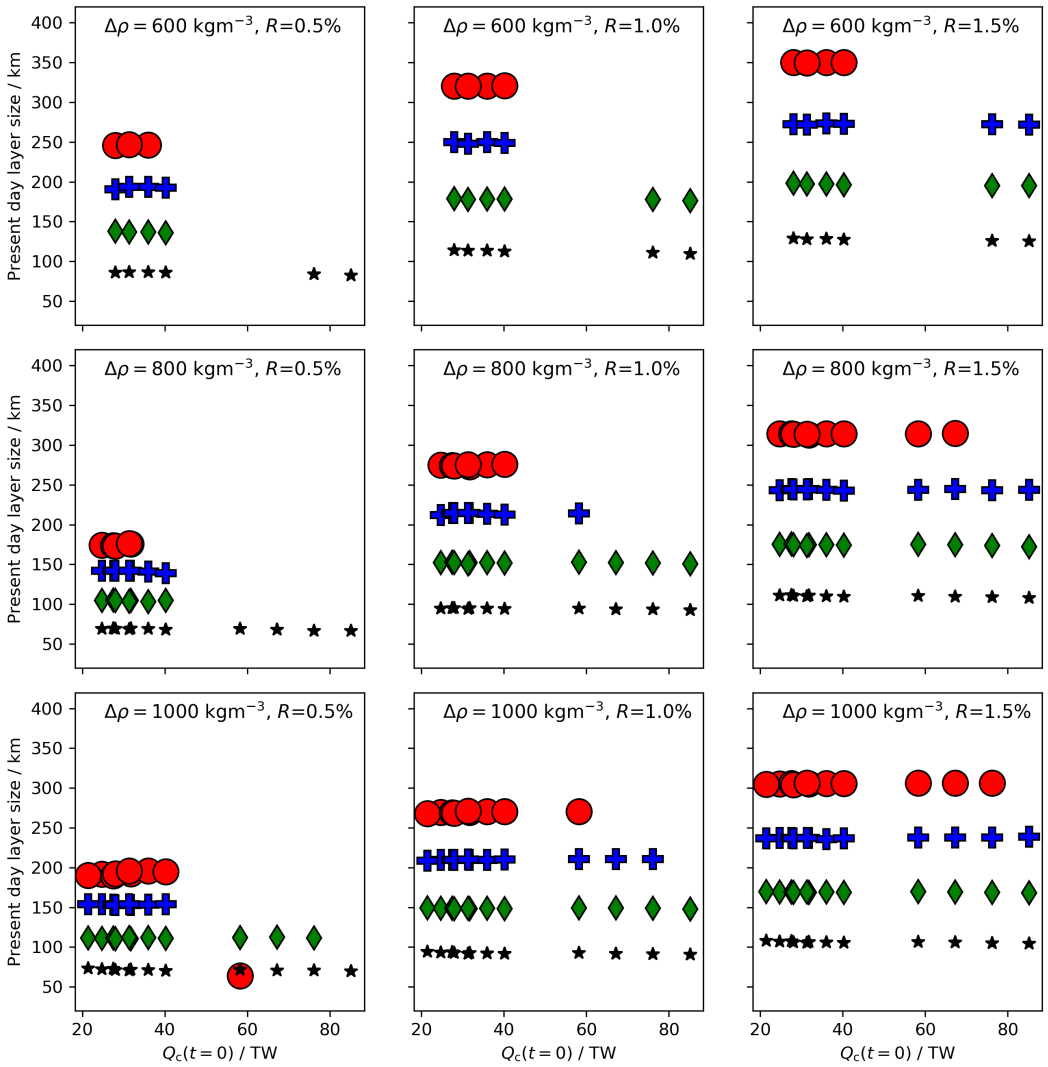

Figure 4.14: Results for case 3 using the high thermal conductivity models D2015-600 (top row), D2015-800 (middle row) and D2015-1000 (bottom row) and 3 different initial density anomalies of 0.5% (left column), 1% (middle column) and 1.5% (right column). Symbols represent different initial layer sizes, h: 100 km (black stars), 200 km (green diamonds), 300 km (blue plusses), and 400 km (red circles). Models are plotted with their present day layer thickness as a function of $Q_c(t = 0)$.

places a strong constraint upon the maximum thickness a primordial layer could persist to until the present. If the early Q_c was above 20 TW then the maximum present day layer thickness is $\sim$ 150 km in my parameter space. This upper bound comes from $R = 1.5\%$, whereas below this value the upper bound is reduced to $\sim$100 km. In the high thermal conductivity case, the heat flow required to generate equally strong super-adiabatic thermal gradients is greatly increased, allowing numerous parameter combinations to retain stable layers thicker than 300 km and above $Q_c(t = 0) = 80$ TW.

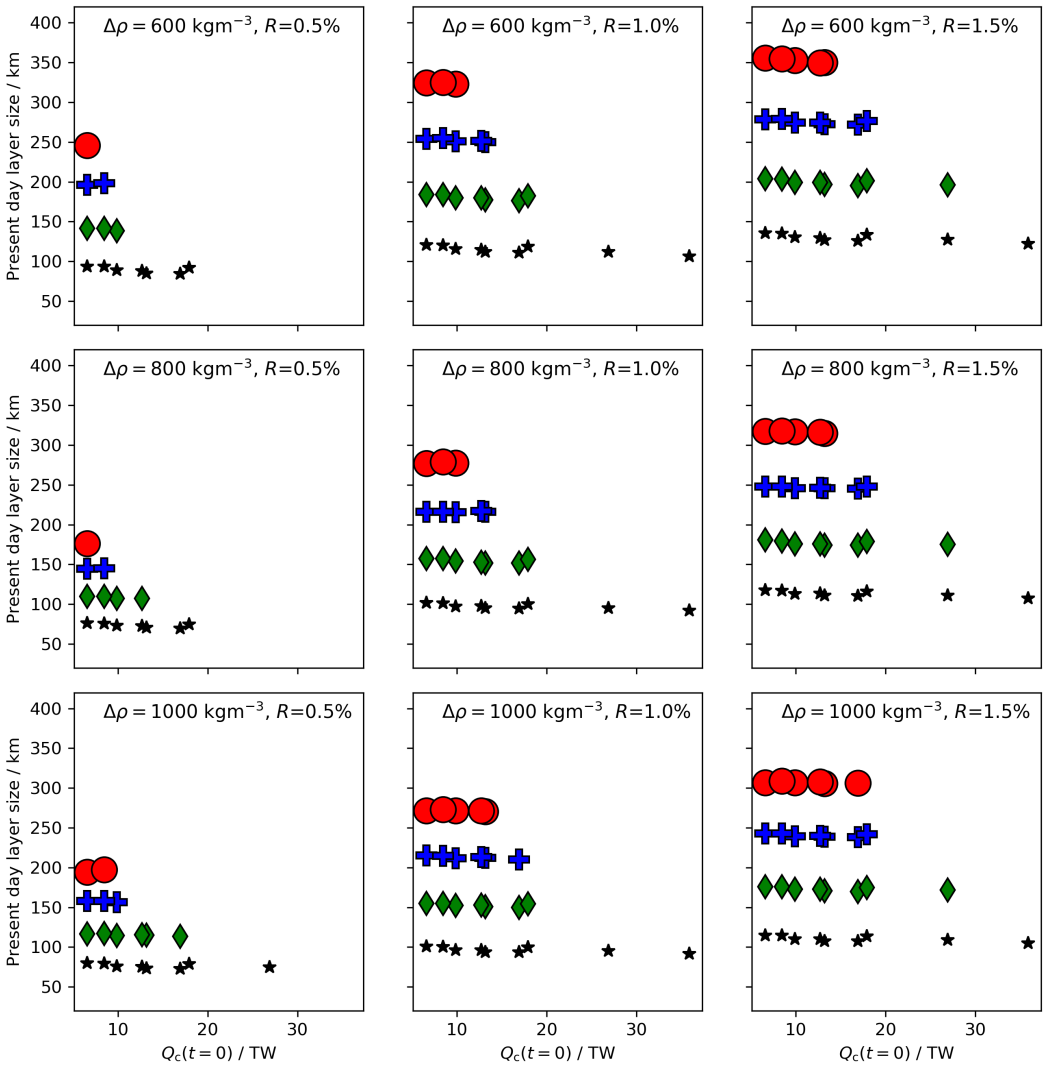

Figure 4.15: The same as Figure 4.14 except for low thermal conductivity models K2015-600 (top row), K2015-800 (middle row) and K2015-1000 (bottom row). Note the different x axis scale compared to Fig. 4.14.

All results give a similar Brunt-Väisälä frequency, in the range 1.5-4 hours (Fig. 4.16). Greater layer thicknesses result from a larger initial layer thickness and therefore a weaker stabilising gradient for the same initial R. Larger R gives stronger stabilising gradients and hence a shorter period. In general, over the entire parameter search the Brunt-Väisälä frequency is relatively insensisitve to the input parameters.

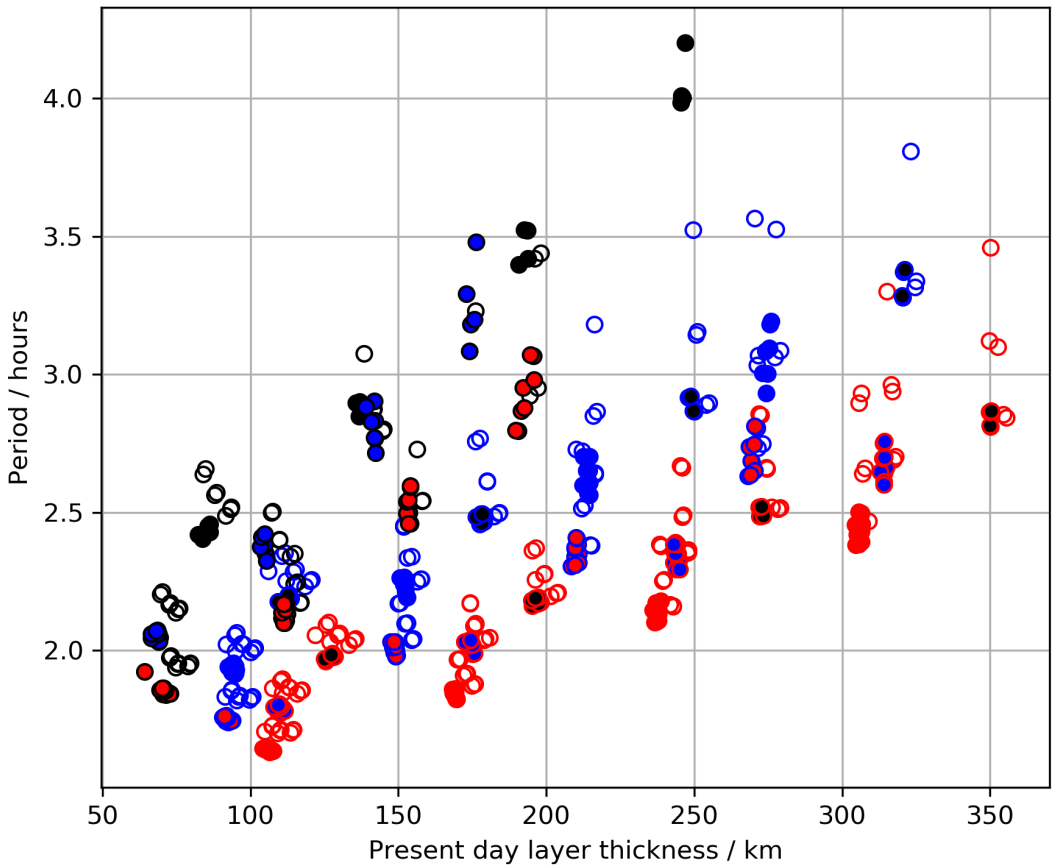

Figure 4.16: Period of gravity waves given the mean Brunt-Väisälä frequency within the layer. Colours refer to initial density anomaly: $R = 0.5\%$ (black), 1.0% (blue), and 1.5% (red). Open symbols are models with low thermal conductivity (K2015-X) and filled symbols are models with a high conductivity (D2015-X).

4.4 Discussion

There are a few key assumptions and features within the models throughout this chapter that I will discuss. The discussion is broken up into 2 main sections, one on the first 2 cases of mass transfer with the mantle and one on the primordial layer results. Finally some discussion relevent to all models is given before concluding remarks.

4.4.1 Mass transfer with the mantle

In the first case I consider, in which the mantle supplies oxygen to the core such that the top of the core is in chemical equilibrium, there is a large flux early in the simulation that results in $E_{\mathrm{J}} < 0$ (Fig. 4.4). When the layer begins to grow, the fluid at the CMB must rapidly increase in oxygen concentration to go from the initial bulk concentration to the equilibrium concentration with the mantle. A similar exponential decrease in the flux was used in section 4.3.2. These may partially originate from initial discontinuities in the model rapidly adjusting. Initially the isentropic region encompasses the entire core, with no initial stable layer, within an initial uniform oxygen concentration. On the first time step, the model must initialise a small layer with the upper boundary condition at the elevated level given by chemical equilibrium with the mantle. This sets up a steep chemical gradient and hence a very large flux at the CMB. When the Earth was undergoing differentiation, physical processes such as diffusion would still have occurred and so the last masses of iron that sank into the core will have begun to equilibriate with the mantle. Indeed, this is how the model of Jacobson et al. (2017) forms an initial chemical layer, and so by the time the mantle and core had fully differentiated, there may have already been a thin layer of chemically enriched fluid beneath the CMB. I therefore therefore consider the short lived, huge flux of oxygen not necessarily representative of the first 100 Myrs in reality but rather the numerical model rapidly readjusting from the discontinuity in the initial conditions. Regardless, the main consequence of this short lived large flux is to massively reduce the power available to the dynamo at a time unconstrained by paleointensity data (Tarduno et al., 2015).

In case 2, I imposed the flux of oxygen into the core based upon the results of Davies et al. (2020), where in their study they only simulated the time before the inner core formed. I have extrapolated their flux time series for the full 4.5 Gyrs on the assumption that inner core formation would not significantly alter the long term trend, an assumption I will evaluate here. The flux into the core is dependent upon the concentration of oxygen within the core at the CMB, which could be altered by the growing inner core. Figure 4.17 shows the time series of oxygen mass fraction at the CMB for the model presented in figure 4.8 with the lowest flux. The lowest flux model will be the greatest impacted by the presence of the inner core due to the weakest

stabilising chemical gradient present. Although the inner core alters the growth rate of the layer by eroding away at the base, the chemical layer acts as a strong buffer between the CMB and r_s, with no change in the oxygen concentration, inhibiting the effects of the inner core from propagating upwards to alter the partitioning behaviour. The extrapolation of the flux time series to 4.5 Gyrs is therefore sensible given the scope of this chapter.

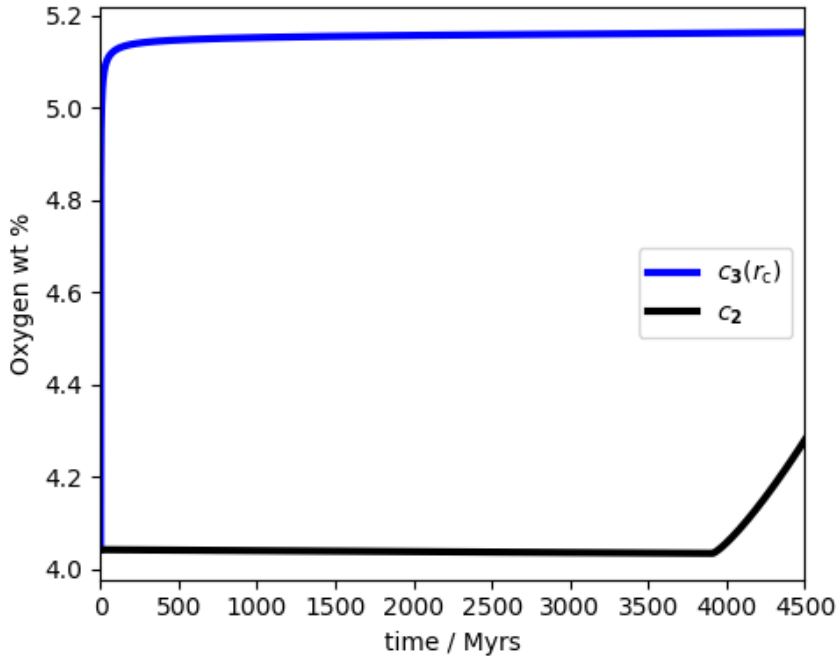

Figure 4.17: Oxygen mass fraction at the CMB for the lowest flux case in Figure 4.8. The oxygen mass fraction in the underlying adiabatic region, c_2, changes due to inner core growth but has no effect on the value at the CMB at the top of the chemical layer.

In the development of the energy and entropy budgets in chapter 2, a zero mass flux at the CMB was assumed at 2 points which I will now address. The heat flux vector, $\mathbf{q}$, is due to a thermal gradient and a mass flux $\mathbf{i}$:

$$\mathbf{q} = -k\nabla T + \mathbf{i}\left(\mu + \frac{\beta T}{\alpha_D}\right), \tag{4.17}$$

which may be rewritten using the Onsager reciprocal relationships (eq. 59.12, Landau and Lifshitz, 1987)

$$\mathbf{q} = -k\nabla T + \left[k_T\left(\frac{\partial \mu}{\partial c}\right)_{p,T} - T\left(\frac{\partial \mu}{\partial T}\right) + \mu\right]\mathbf{i}, \tag{4.18}$$

where k_T is the thermal diffusion ratio that is unknown and so assumed to be negligible (Gubbins et al., 2004). The heat flow at the CMB is the surface integral of the heat

flux across the CMB

$$Q^c_{cmb} = -\oint k^c \nabla T \cdot \mathrm{d}\mathbf{S} + \oint R^c_h \mathbf{i} \cdot \mathrm{d}\mathbf{S}, \tag{4.19}$$

where as defined chapter 2, $R_h = \mu - (\partial\mu/\partial T)$ and the superscript c denotes values on the core side of the CMB. This form of the CMB heat flow includes the heat of reaction associated with a mass flux, which I have assumed zero by assuming $\mathbf{i} = 0$ at the CMB in the energy and entropy equations. As with the heat of reaction at the ICB, it is the change in R_h between the core and mantle that is important, otherwise the same amount of heat is absorbed on one side as is released on the other side of the CMB. The heat flow at the CMB in the mantle has the same form, except depending on the mantle properties:

$$Q^m_{cmb} = -\oint k^m \nabla T \cdot \mathrm{d}\mathbf{S} + \oint R^m_h \mathbf{i} \cdot \mathrm{d}\mathbf{S} \tag{4.20}$$

The heat of reaction due to the mass flux is therefore (Davies et al., 2020):

$$Q_h = \oint \langle R_h \rangle \mathbf{i} \cdot \mathrm{d}\mathbf{S}. \tag{4.21}$$

Using a value for $\langle R_h \rangle$ for Fe-O of 3.5 ev per formula unit (Pozzo et al., 2019) yields a value of $\langle R_h \rangle$=7.4×10^5 Jkg^{-1} for oxygen. The heat of reaction for the highest mass flux from Fig. 4.3 only represents 1.5 TW at early times, that rapidly decays to around 16 GW and is therefore negligible in the energy budget. The contribution of the heat of reaction to the entropy budget must be zero as the heat generated by the process is also removed at the CMB at the same temperature and so must have a zero Carnot efficiency.

I have only considered one light element in the layer, whereas more light elements are present in the core and may have anomalous values in the layer. Brodholt and Badro (2017) required a deficit of at least one light element in order to produce both a seismically slower and lighter fluid. The silicon concentration of the isentropic region increased marginally during inner core growth and so the fluid within the stable layer away from r_s will be relatively depleted in Si. The total change in Si content due to inner core growth is small, < 0.2 wt%, and so not enough according to the results of Brodholt and Badro (2017). If Si also partitions out of the core into the mantle, whilst oxygen partitions into the core, the layer might have the correct deficit, however the core model used in this study has a relatively low amount of Si and so the core is still likely undersaturated in Si relative to the mantle (Brodholt and Badro, 2017).

(Helffrich and Kaneshima, 2010) and Komabayashi (2014) however, suggest a deficit in another light element alongside an excess of oxygen is not necessary. Whilst oxygen has a relatively large diffusivity compared to other light elements (Pozzo et al., 2013),

another light element anomaly could be driven by barodiffusion throughout the layer whilst oxygen controls the layer growth; in essence a smaller chemical layer within the larger oxygen enriched chemical layer. Gubbins and Davies (2013) show that Si and/or S diffusing by barodiffusion could produce an anomaly within $\sim$ 100 km of the CMB but only with an anomaly of around 0.3 wt%, small enough to not significantly alter the stability of the layer beyond the oxygen anomaly. The presence of diffusion of Si or S within the layer is therefore unlikely to change the time evolution of the layer by influencing its stability.

4.4.2 Primordial layers

The third and final case I consider is the pre-existing presence of a chemical layer as a result of core merging during Earth's accretion. The initial composition of the chemical layer depends upon the composition of the impactor that collided with the proto-Earth and so the lower relative density of the impactor could be attributed in theory to many different light elements. My choice of oxygen was motivated by finding an upper bound on the present day layer thickness given oxygen has a larger mass diffusivity than other siderophile elements such as silicon or sulphur (Gubbins et al., 2004). The layer thickness is $\propto \sqrt{D}$ and so if the layer were instead enriched in silicon, which has a diffusivity approximately half that of oxygen (Pozzo et al., 2013), the layer would grow by diffusion at 70% the speed. When the inner core grows, the erosion of the layer is controlled by the need to satisfy continuity of density and so would erode the layer just as far, irrespective of the light element responsible for the imposed initial density anomaly.

There could be a situation where, once the primordial layer is emplaced, there may be subsequent mass transfer with the mantle. I have not considered this here in order to focus on specifically the thermal history of the core with a primordial layer however this may lead to a range of potential scenarios for future study. Additional mass transfer into the pre-existing layer may bolster the layer growth although any pre-exisiting oxygen anomaly will reduce the partitioning of oxygen into the core and additional light element may not have enough time to diffuse down to r_{s}, especially if the layer size ¿200 km, to increase the growth rate. Additional mass transfer would also not likely impact the result where higher heat flows have the ability to erode away the layer in the first few 10's Myrs, due to the destabilising thermal gradients diffusing more rapidly throughout the layer than the additional stabilising chemical gradients. Subsequent mass transfer would allow a chemical layer to regrow although this would be indistinguishable from a case in which the primordial layer never existed.

4.4.3 Conclusions

I have performed a large range of simulations of the thermal history of the core with chemical stratification beneath the CMB using a variety of core properties and heat flow histories spanning current estimates. I have first extended the results of Buffett and Seagle (Buffett and Seagle (2010)) and Nakagawa (Nakagawa (2018)) for a chemical layer formed via oxygen transfer with the mantle to model the full entropy budget for the core. I have found the impact upon E_{J} is relatively small, except in early times when a large flux of oxygen inhibited a dynamo. From a paleomagnetic standpoint, this is not an issue given no paleomagnetic data are available to constrain the magnetic field of the Earth in its few 10's Myrs of history.

Secondly, I have considered a second case, in which a chemical layer forms by oxygen transfer with the mantle, except based upon oxygen flux results from a recent paper (Davies et al., 2020) on BMO evolution. The large fluxes of oxygen into the core predicted by models (larger than a total of $\sim 7 \times 10^{21}$ kg of oxygen) contained in that study lead to extreme increases in E_{α}, reducing E_{J} below zero for the majority of the simulation time. Lower flux cases are therefore preferred since they permit a dynamo for the last 3.5 Gyrs and produce stable layers with oxygen concentrations more consistent with seismic observations (Helffrich and Kaneshima, 2010). This limits the layer thickness to around 140 km at present for a layer produced by transfer of oxygen with the mantle. This limit may be increased if the mass diffusivity for oxygen is larger than used in this study however this would also lead to an increase in E_{α} and hence reduction in E_{J}. Otherwise, models are relatively insensitive to both CMB heat flow and core properties used. For both case 1 and case 2, the maximum layer thicknesses achieved from successful models was 150 km, and a maximum Brunt-Väisälä frequency corresponding to a period of 25 minutes.

Lastly, the scenario of a primordial layer formed during Earth's accretion is simulated for the first time in a thermal history model. When the early CMB heat flow is high it may fully erode away some of the stable layers modelled, particularly if the core has a low thermal conductivity. There are a number of plausible models in which the estimate of the entropy due to ohmic dissipation, E_{J}, is positive at all times, therefore the dynamo may operate even when a thick (¿300 km) layer persists for 4.5 Gyrs. If the thermal conductivity of the core is relatively low, this places a strong constraint upon the present day layer thickness as many thicker (¿200 km) layers are eroded in the early Earth for moderate CMB heat flows due to weaker initial chemical gradients.

Strong stratification develops in all models presented in this chapter, yielding gravity wave periods of a couple of hours to 30 minutes. Geomagnetic observations along with length of day changes interpretted as the signature of MAC waves in the core suggest much weaker stratification with gravity wave periods on the order of 1 day (Buffett

et al., 2016) in an approximately 140 km thick layer. However, the size of the inferred layer from that study is consistent with the majority of chemical layers produced in all 3 cases in this chapter.

Chapter 5

Conclusions and Future Work

This thesis has been concerned with the long term evolution of the Earth's core containing stable stratification beneath the CMB. In this chapter I will summarise the main findings presented and revisit the aims and objectives set out in chapter 1. Finally, I will discuss future avenues for research that may further improve our understanding of stable stratification in the Earth.

5.1 Conclusions

My objectives were:

1. Develop a thermal history model, with a generalised representation of thermal and chemical stratification.
2. Constrain the structure and evolution of stable layers resulting from purely thermal stratification, focusing on the implications of high core thermal conductivity.
3. Constrain the structure and evolution of stable layers resulting from chemical stratification due to FeO enrichment and incomplete mixing at core formation.

5.1.1 Develop a thermal history model, with a generalised representation of thermal and chemical stratification.

Chapter 2 highlighted that the growth of the stable layer is controlled by the diffusion of heat and/or mass over very long timescales (100's Myrs to Gyrs). Thermal history models are therefore required since these timescales are outside the reach of dynamical models. A key constraint on thermal history models is the estimation of the ohmic dissipation in order to determine models that are consistent with the paleomagnetic rock record. Previous models of stable stratification have not typically estimated the ohmic dissipation. Finally, since it is uncertain if the layer has a thermal or chemical

origin, both types of stratification need to be considered, for which there are a range of possible scenarios. Chapter 2 therefore presented a thermal history model that includes a stable layer, calculates the ohmic dissipation, and has a general framework for considering either thermal or chemical stratification, something that so far has not been published.

The model I developed in chapter 2 separated the core into 2 main regions, the stable layer and the isentropic region. The isentropic region is treated in the same manner as previous thermal history models (Gubbins et al., 2003; Gubbins et al., 2004; Nimmo, 2015; Davies, 2014) and so adopts an equivalent mathematical representation. The size of the isentropic region changes to accommodate the stable layer beneath the CMB in which diffusion profiles dictate the radial transport of heat and/or mass. The contributions to the energy and entropy budget from the stable layer are derived from the same conditions as for the isentropic region, namely conservation of mass and entropy, but are dependent upon the solutions to the radial diffusion within the layer. This allows the global entropy change from ohmic dissipation to still be estimated for the entire core with appropriate contributions from both the isentropic region and stable layer.

The layer size is time dependent and as such a numerical scheme is required to evolve the interface between the stable layer and the isentropic region. I include fully time dependent solutions for both heat and mass diffusion, where The Crank-Nicolson discretisation I use accepts Dirchlet or Neumann boundary condition types at either boundaries allowing flexibility in the methods. I have made particular choices in boundary conditions but this is not a limitation of the code, which is written in a manner to facilitate easy sharing and manipulation with other researchers, for example should somebody wish to use a fixed temperature where I have use a fixed temperature gradient. Furthermore my model does not require that the initial state of the core was entirely isentropic and I later uses this in order to model an initial chemical layer produced from ancient impactors (Landeau et al., 2016).

The transition from the isentropic region to stable layer is treated as a sharp interface. Entrainment of stable fluid due to non-linear dynamics at the transition is represented in the boundary conditions at the base of the layer. The onset of doubly diffusive instabilities defines the boundary condition for chemical stratification, also providing the entrainment mechanism of light element out of the layer and into the isentropic region. This boundary condition was first proposed by Buffett and Seagle (2010) which I have extended by including a time dependent solution for temperature in the layer to control the estimation of the chemical gradient at the interface. In the case of thermal stratification, entrainment is represented by a dimensionless coefficient, in a similar manner to Lister (1995) and Lister and Buffett (1998), reducing the heat flow into the stable layer by entraining stable hot fluid downwards.

5.1.2 Constrain the structure and evolution of stable layers resulting from purely thermal stratification

In chapter 3 I applied my numerical model to the case of a sub-adiabatic heat flow at the CMB, Q_c, resulting in thermal stratification. I focus upon recent high estimates of the thermal conductivity (Pozzo et al., 2012; Gomi et al., 2013; De Koker et al., 2012), increasing the likelihood that a given CMB heat flow is less than the heat conducted down the adiabat. Prior to the inner core the heat flow must be super-adiabatic in order to provide enough power to drive the geodynamo, limiting the age of thermal stratification to be younger than the inner core. I therefore modelled only the recent past, just prior to the inner core until the present day, for a range of linear heat flows and core properties.

I defined the adiabatic ratio, ADR, as the ratio of Q_c to the adiabatic heat flow. The further below 1 the present day ADR is, the thicker the thermal stratification produced but also the faster Q_c must decrease over the age of the inner core in order to be super-adiabatic ($ADR > 1$) prior to ICN. Previous models of the coupled evolution of the core and mantle that calculate Q_c (Driscoll and Bercovici, 2014; Panovska et al., 2019; Nakagawa and Tackley, 2015; O'Rourke and Stevenson, 2016) typically find an exponentially decaying decrease over time in Q_c, predicting at most a decrease of 3 TW Gyr^{-1} over the last ∼700 Myrs. The results depend upon the density jump at the ICB ($\Delta\rho$) since this controls the core composition and subsequently thermal conductivity. My results that use a decrease in Q_c of 3 TW Gyr^{-1} limit the present day layer thickness to around 100-150 km ($\Delta\rho = 600, 800$ kg m^{-3}) or potentially up to 300 km if $\Delta\rho = 1000$ kg m^{-3}. Thicker layers are possible but require more rapid changes in Q_c than these coupled models typically predict.

The entrainment coefficient, E, alters the condition for stratification to require at the present day $ADR < 1 - E$. Increasing E results in fewer models producing thermal stratification and those that do manage to produce a layer are thinner. When $E = 0.1$, no thermal layers form when the recent decrease in Q_c is 3 TW Gyr^{-1} and by E=0.3, layers are confined to the regions of the parameter space with very high rates of change in Q_c (> 6 TW Gyr^{-1}).

Assuming that the long term trend in Q_c is accurately described by an exponential, I extrapolated the heat flows I imposed along an exponential fit to estimate the the early Q_c to the first 500 Myrs of Earths history. Many of my successful models producing thermal stratification correspond to very high early heat flows in excess of 100 TW, when the previously mentioned coupled models that solve for Q_c do not find $Q_c > 70$ TW.

Finally predicted Brunt-Väisälä frequencies across all solutions found vary only by a factor of 3.5, giving periods of 8-28 hours, similar to that inferred from modelled

MAC waves in the core (Buffett and Seagle, 2010) (19 hours). Predicted periods from fitting compositional anomalies to seismic observations have given shorter periods at 1.5-3.5 hours (Helffrich and Kaneshima, 2010), significantly shorter than even the the most strongly stratified thermal layer I produce.

5.1.3 Constrain the structure and evolution of stable layers resulting from chemical stratification due to FeO enrichment and incomplete mixing at core formation.

In chapter 4 I considered chemical origins for the stable layer. I first reproduced the conditions modelled by Buffett and Seagle (2010) and Nakagawa (2018), where oxygen partitions into the core from solid ferropericlase in the mantle, based on the data of Frost et al. (2010). The layer thickness and Brunt-Väisälä frequencies I found are consistent with those previous studies as expected however the ohmic dissipation, E_J I calculated is significantly different to that of Nakagawa (2018) (Buffett and Seagle (2010) do not calculate this). I found that E_J is negative in the very early Earth, suggesting a magnetic field cannot be generated, which is not the case in Nakagawa (2018). I concluded that this was due to my inclusion of the entropy due to molecular diffusion, E_α, into the entropy budget. This is not necessarily an issue given E_J was only negative for the first 100 Myrs, a period where there are no observational constraints on the geodynamo; however, it does foreshadow the next set of results as an important effect.

Next I considered FeO partitioning from molten silicates representative of a magma ocean following the recent work of Davies et al. (2020). The magma ocean promotes larger fluxes of oxygen into the core, however larger mass fluxes also leads to increasing E_α. I found that the larger fluxes I used predicted $E_\mathrm{J} < 0$ for the majority of the simulation time and hence are not consistent with paleomagnetic observations. This provides a limit on the mass flux into the core and hence the layer thickness to around 140 km at present. All else being equal, a larger mass diffusivity, D, leads to a larger layer thickness but also a larger contribution to E_α and so this 140 km limit is not trivially increased by increasing D. Otherwise, models are relatively insensitive to both CMB heat flow and core properties used. The layer thickness has a clear variation with the total mass of oxygen fluxed into the core. The thickness rapidly increases with an increased total flux before levelling off at ~ 150 km due to be limited by the diffusion rate. The Brunt-Väisälä frequencies are all fast, giving short periods around 30 minutes, the same as Buffett and Seagle (2010).

Lastly, I perform the first thermal history models for an initial primordial layer formed during Earth's accretion. I am interested in upper limits on the layer thickness and so I considered a layer enriched purely in oxygen, a faster diffusing light element than S/Si, enabling it to reach the largest possible present day size. When the early

Q_c is high it may fully erode away the weaker initial layers modelled, particularly if the core has a low thermal conductivity. There are, however, a number of plausible models that produce a history consistent with observations given the lack of constraint on the initial layer. I confirmed that the dynamo may operate even when a thick ($>$ 300 km) layer persists for 4.5 Gyrs. If the thermal conductivity of the core is relatively low, relatively thick ($>$ 200 km) layers are quickly eroded by high heat flows forming strongly destabilising thermal gradients within the layer.

Brunt-Väisälä frequencies resulting from thermal stratification gives periods of 8-28 hours, from mass transfer with the mantle ∼30 minutes, and finally from a primordial layer 1.5-4 hours. Additional future constraints upon the Brunt-Väisälä frequency may be able to distinguish between the different origins of the layer.

Table 5.1: The same as table 1.2 including the results from this thesis. Values given from this study are the reasonable upper limits found, e.g. very thick ($>$ 600 km) thermal layers were found but they require extreme heat flows inconsistent with previous studies of the coupled evolution of the core and mantle. Notable limits given particular parameter choices are listed. Values are for present day layer thickness, h, and period of gravity waves, $2\pi/N$

Publication	Stratification type	h (km)	$\frac{2\pi}{N}$ (hours)
This study (thermal, $\Delta\rho = 600, 800$ kg m^{-3})	T	150	25
This study (thermal, $\Delta\rho = 1000$ kg m^{-3})	T	300	28
This study (thermal, $E = 0.3$)	T	0	-
This study (O flux from ferropericlase)	C(T)	150	0.5
This study (O flux from BMO)	C(T)	150	0.4
This study (primordial layer, $R = 0.5\%$)	C(T)	250	4
This study (primordial layer, $R = 1.5\%$)	C(T)	350	3.5
Labrosse et al. (1997)	T	600	-
Lister and Buffett (1998)	T(C)	400	>17
Buffett and Seagle (2010)	C	80	0.5
Nakagawa (2018)	C(T)	80-270	0.05
Gubbins and Davies (2013)	C	100	1.2
Davies et al. (2020)	C	60-140	-

5.2 Future research

I have developed a numerical model to compute the evolution of the core given a specified Q_c throughout time. For consistency, Q_c should be solved for in tandem with computing the thermal evolution of the mantle. So far, no coupled history models of both the core and mantle with a stable layer beneath the CMB have been published for the Earth and so it is not yet clear how the mantle reacts to the presence of a stable layer. A chemical layer, which I have found for the most part to be insensitive to Q_c, is not likely to alter the behaviour significantly away from models that do not

include a stable layer. If the chemical layer has its origins in mass transfer from a BMO, then a parameterisation such as that of Davies et al. (2020) would need to be included into the mantle history calculation, significantly complicating the model by requiring a search over a large parameter range. There is not a certain parameterisation of mantle dynamics and so a fully dynamical model can more accurately represent the mantle evolution however are expensive to run and introduce more uncertain parameters into the parameter search.

An obvious extension to my model would be to incorporate the diffusion of multiple light elements into the stable layer. If more than 2 components of the fluid influence the density, the boundary conditions at the stable layer interface become more complicated since multiple light elements all contribute to the stability of the fluid to varying degrees. Similar coupling of multiple light elements can arise at the CMB with multipl elements partitioning with the mantle that depend upon the concentrations of each other. Inclusion of more light elements would require alterations to the numerical scheme advancing the layer interface, however computationally calculating the diffusion profiles is cheap and can use the same Crank-Nicolson scheme used in this thesis for oxygen.

A potential additional source of power for the dynamo prior to ICN is the suggestion of steady mineral precipitation of either MgO (O'Rourke and Stevenson, 2016; Badro et al., 2018; Du et al., 2019) or SiO_2 (Hirose et al., 2017). As the light elements precipitate out, dense fluid is left behind, sinking and liberating gravitational energy. The dense liquid sinking could destabilise a stable layer if the precipitation occurs at/near the CMB and so might not be compatible with any layer at all. Alternatively, the dense fluid may be able to sink through the layer without major disruption to the stratification. This would introduce flexibility for thermal stratification to begin forming prior to the inner core, requiring a less extreme Q_c history since precipitation contributes to the dynamo. Finger convection resulting from doubly diffusive instabilities represents the inverse scenario: chemically light upwellings rather than dense downwellings. Finger convection has been shown to not disrupt a thermally stratified layer in a dynamical study of Mercury's core (Manglik et al., 2010) but dynamical studies specific to Earth and mineral precipitation would be required to establish if precipitation at the CMB and stable stratification are compatible.

This thesis has focused upon the long term evolution of the stable layer in a 1D representation but there are a number of 3D dynamics associated with the interaction between a stable layer and underlying convection that are still poorly understood. My model is dependent upon the boundary conditions chosen at the stable layer interface, which dynamical studies can help to constrain. For thermal stratification I have included a dimensionless entrainment coefficient but we do not know its value in the Earth. A useful study would be to impose an initial thermal layer into a spherical

3D model of the core and then to quantitatively measure how the interface between the layer and convection behaves over time, potentially reaching a steady state, giving a constraint upon E. Entrainment may depend upon the both Rossby number and Richardson number (Levy and Fernando, 2002), the latter of which is very difficult to estimate in the core since it is based on the small scale shear of the fluid. An equivalent study was recently performed for an initial chemical layer (Bouffard et al., 2020). They found that very little entrainment is observed in their case but that is not necessarily the same for a thermal layer due to the much more rapid diffusivity and impact upon density of the fluid. It is also worth noting that defining the interface between stable stratification and convecting interior within a dynamical study is not trivial since there is no single radius where an obvious transition occurs.

The stable layer may not be a global feature. Due to the constrained geometry of sources and receivers, seismic studies do not have the resolution to be able to determine lateral variations in the layer. Both the dynamics studies of Mound et al. (2019) and Bouffard et al. (2019) found lateral variations in stable stratification although under significantly different scenarios. Mound et al. (2019) suggest a thermally stable layer is disrupted under regions of high heat flux, whilst persisting under regions of low heat flux. A quantitative analysis into the conditions that lead to the transition between disruption and persistence of the layer in terms of the entrainment could be useful to constrain E. Bouffard et al. (2019) considers a chemical layer growing by pooling of light element release from the inner core beneath the CMB. They too notice a lateral variation in the thickness of the layer however in their case it is attributed to plumes inside the tangent cylinder being mixed and diluted less efficiently than outside the tangent cylinder. Schaeffer et al. (2017) performed dynamo models that are some of the closest to realistic Earth parameters to date and surprisingly found chemically enriched plumes also tended to form a stable density gradient within the tangent cylinder.

Finally, largely uncertain processes in the core are the formation of double diffusive instabilities. Laboratory experiments have been performed but generally focus upon applications to the more localised regions of the atmosphere and ocean (Turner, 1974; Kelley et al., 2003) and so the combined influence of rotation, spherical geometry and magnetic field upon the instabilities are not clear. Doubly diffusive codes are available for use for planetary cores (e.g. Bouffard et al., 2017) and so future studies that utilise these methods will go a long way to improving our knowledge of 1D parameterisations of these instabilities, although will have to make the concessions that all dynamical studies of the core make in not attaining the true Earth parameter regime.

5.3 Final Thoughts

The development of the numerical model used in this thesis was a challenging yet stimulating process; a tale of discovering methods that fail more often than they succeed and finally being able to settle upon the work presented here. I have attempted to exploit the opportunity a thesis affords in providing a detailed description of the assumptions and specifics of the model to promote future authors ability to reproduce results, a roadblock I encountered myself during this study.

One aspect I am most interested in seeing developed are entrainment rates of stabilising thermal gradient, such that the unknown entrainment parameter, E, I introduced in chapter 3 might be constrained. It is interesting that successful models exist in a relatively narrow region of the parameter space, which if $E > 0$, reduces further leaving few models that could be considered consistent with other studies, particularly the time variance of Q_c. The Brunt-Väisälä frequencies from chemical layers showed little variation with the input parameters, remaining distinct from those produced by thermal stratification, and so gives hope to future constraints on N being able to distinguish between the two possible origins.

Bibliography

Alexandrakis, Catherine and David W. Eaton (2010). "Precise seismic-wave velocity atop Earth's core: No evidence for outer-core stratification". In: *Physics of the Earth and Planetary Interiors* 180.1-2, pp. 59–65.

Alfè, D., M. J. Gillan, and G. D. Price (Apr. 2002a). "Ab initio chemical potentials of solid and liquids solutions and the chemistry of the Earth's core". In: *Journal of Chemical Physics* 116.16, pp. 7127–7137.

— (Jan. 2002b). "Composition and temperature of the earth's core constrained by combining ab initio calculations and seismic data". In: *Earth and Planetary Science Letters* 195.1-2, pp. 91–98.

— (2007). "Temperature and composition of the Earth's core". In: *Contemporary Physics* 48.2, pp. 63–80.

Alfè, D., G. D. Price, and M. J. Gillan (2002c). "Iron under Earth's core conditions: Liquid-state thermodynamics and high-pressure melting curve from ab initio calculations". In: *Physical Review B - Condensed Matter and Materials Physics*.

Alfè, Dario (2009). "Temperature of the inner-core boundary of the Earth: Melting of iron at high pressure from first-principles coexistence simulations". In: *Physical Review B - Condensed Matter and Materials Physics* 79.6.

Allègre, Claude, Gérard Manhès, and Éric Lewin (2001). "Chemical composition of the Earth and the volatility controlon planetary genetics". In: *Earth and Planetary Science Letters* 185.1-2, pp. 49–69.

Amit, Hagay (2014). "Can downwelling at the top of the Earth's core be detected in the geomagnetic secular variation?" In: *Physics of the Earth and Planetary Interiors* 229, pp. 110–121.

Anzellini, S., A. Dewaele, M. Mezouar, P. Loubeyre, and G. Morard (2013). "Melting of iron at earth's inner core boundary based on fast X-ray diffraction". In: *Science* 340.6131, pp. 464–466.

Asphaug, Erik (2014). "Impact Origin of the Moon?" In: *Annual Review of Earth and Planetary Sciences* 42.1, pp. 551–578.

Avery, Margaret S., Catherine G. Constable, Christopher J. Davies, and David Gubbins (2019). "Spectral methods for analyzing energy balances in geodynamo simulations". In: *Physics of the Earth and Planetary Interiors*.

Badro, James, Julien Aubert, Kei Hirose, Ryuichi Nomura, Ingrid Blanchard, Stephan Borensztajn, and Julien Siebert (2018). "Magnesium Partitioning Between Earth's Mantle and Core and its Potential to Drive an Early Exsolution Geodynamo". In: *Geophysical Research Letters* 45.24, pp. 240–13.

Badro, James, Alexander S. Côté, and John P. Brodholt (2014). "A seismologically consistent compositional model of Earth's core". In: *Proceedings of the National Academy of Sciences of the United States of America* 111.21, pp. 7542–7545.

Badro, James, Julien Siebert, and Francis Nimmo (2016). "An early geodynamo driven by exsolution of mantle components from Earth's core". In: *Nature* 536.7616, pp. 326–328.

Belonoshko, Anatoly B., Jie Fu, Taras Bryk, Sergei I. Simak, and Maurizio Mattesini (2019). "Low viscosity of the Earth's inner core". In: *Nature Communications* 10.1.

Biggin, Andrew J., Geert H.M.A. Strik, and Cor G. Langereis (2009). "The intensity of the geomagnetic field in the late-Archaean: New measurements and an analysis of the updated IAGA palaeointensity database". In: *Earth, Planets and Space* 61.1, pp. 9–22.

Birch, Francis (1952). "Elasticity and constitution of the Earth's interior". In: *Journal of Geophysical Research* 57.2, pp. 227–286.

Blanc, Nicolas A., Dave R. Stegman, and Leah B. Ziegler (2020). "Thermal and magnetic evolution of a crystallizing basal magma ocean in Earth's mantle". In: *Earth and Planetary Science Letters* 534.

Bloxham, Jeremy (1986). "The expulsion of magnetic flux from the Earth's core". In: *Geophysical Journal of the Royal Astronomical Society*.

Boehler, R. (1993). "Temperatures in the Earth's core from melting-point measurements of iron at high static pressures". In: *Nature*.

— (2000). "High-pressure experiments and the phase diagram of lower mantle and core materials". In: *Reviews of Geophysics*.

Borlina, Cauê S., Benjamin P. Weiss, Eduardo A. Lima, Fengzai Tang, Richard J.M. Taylor, Joshua F. Einsle, Richard J. Harrison, Roger R. Fu, Elizabeth A. Bell, Ellen W. Alexander, Heather M. Kirkpatrick, Matthew M. Wielicki, T. Mark Harrison, Jahandar Ramezani, and Adam C. Maloof (2020). "Reevaluating the evidence for a Hadean-Eoarchean dynamo". In: *Science Advances*.

Bouffard, M., M. Landeau, and A. Goument (2020). "Convective erosion of a primordial stratification atop Earth's core". In: *Geophysical Research Letters* 47, e2020GL087109.

Bouffard, Mathieu, Gaël Choblet, Stéphane Labrosse, and Johannes Wicht (2019). "Chemical convection and stratification in the earth's outer core". In: *Frontiers in Earth Science* 7.

Bouffard, Mathieu, Stéphane Labrosse, Gaël Choblet, Alexandre Fournier, Julien Aubert, and Paul J. Tackley (2017). "A particle-in-cell method for studying double-diffusive convection in the liquid layers of planetary interiors". In: *Journal of Computational Physics*.

Braginsky, S I (1963). "Structure of the F layer and reasons for convection in the Earth's core". In: *Soviet Phys. Dokl.* 149, pp. 8–10.

— (1964). "Magnetohydrodynamics of the Earth's core". In: *Geomag. Aeron.* 4, pp. 698–712.

— (1993). "MAC-oscillations of the hidden ocean of the core." In: *Journal of Geomagnetism and Geoelectricity* 45, pp. 1517–1538.

Braginsky, Stanislav I. and Paul H. Roberts (1995). "Equations governing convection in earth's core and the geodynamo". In: *Geophysical & Astrophysical Fluid Dynamics* 79.1-4, pp. 1–97.

Brodholt, John and James Badro (2017). "Composition of the low seismic velocity E′ layer at the top of Earth's core". In: *Geophysical Research Letters* 44.16, pp. 8303–8310.

Buffett, B. A. and J. Bloxham (2002). "Energetics of numerical geodynamo models". In: *Geophysical Journal International*.

Buffett, Bruce, Nicholas Knezek, and Richard Holme (2016). "Evidence for MAC waves at the top of Earth's core and implications for variations in length of day". In: *Geophysical Journal International* 204.3, pp. 1789–1800.

Buffett, Bruce A., Herbert E. Huppert, John R. Lister, and Andrew W. Woods (1996a). "On the thermal evolution of the Earth's core". In: *Journal of Geophysical Research: Solid Earth* 101.B4, pp. 7989–8006.

— (1996b). "On the thermal evolution of the Earth's core". In: *Journal of Geophysical Research: Solid Earth* 101.B4, pp. 7989–8006.

Buffett, Bruce A. and Christopher T. Seagle (2010). "Erratum: Stratification of the top of the core due to chemical interactions with the mantle (Journal of Geophysical Research (2011) 116 (B07405) DOI:10.1029/2011JB008376)". In: *Journal of Geophysical Research: Solid Earth* 116.7.

Bullen, K. E. (1963). "An Index of Degree of Chemical Inhomogeneity in the Earth". In: *Geophysical Journal of the Royal Astronomical Society* 7.5, pp. 584–592.

Charbonneau, Paul (2014). "Solar Dynamo Theory". In: *Annual Review of Astronomy and Astrophysics* 52.1, pp. 251–290.

Christensen, U. R. (2018). "Geodynamo models with a stable layer and heterogeneous heat flow at the top of the core". In: *Geophysical Journal International* 215.2, pp. 1338–1351.

Christensen, Ulrich R. and Johannes Wicht (2008). "Models of magnetic field generation in partly stable planetary cores: Applications to Mercury and Saturn". In: *Icarus* 196.1, pp. 16–34.

Conrad, Clinton P. and Bradford H. Hager (1999). "The thermal evolution of an earth with strong subduction zones". In: *Geophysical Research Letters* 26.19, pp. 3041–3044.

Cox, G. A., P. W. Livermore, and J. E. Mound (2014). "Forward models of torsional waves: Dispersion and geometric effects". In: *Geophysical Journal International*.

Crank, J (1975). *The Mathematics of Diffusion*. Oxford University Press.

Davies, C. J., M. Pozzo, D. Gubbins, and D. Alfè (2018). "Partitioning of Oxygen Between Ferropericlase and Earth's Liquid Core". In: *Geophysical Research Letters* 45.12, pp. 6042–6050.

Davies, Christopher, Monica Pozzo, David Gubbins, and Dario Alfè (2015). "Constraints from material properties on the dynamics and evolution of Earth's core". In: *Nature Geoscience* 8.9, pp. 678–685.

Davies, Christopher J. (2014). "Cooling history of Earth's core with high thermal conductivity". In: *Physics of the Earth and Planetary Interiors* 247, pp. 65–79.

Davies, Christopher J. and Anne Pommier (2018). "Iron snow in the Martian core?" In: *Earth and Planetary Science Letters* 481, pp. 189–200.

Davies, Christopher J., Monica Pozzo, David Gubbins, and Dario Alfè (2020). "Transfer of oxygen to Earth's core from a long-lived magma ocean". In: *Earth and Planetary Science Letters* 538.

Davies, Geoffrey F. (2009). "Effect of plate bending on the Urey ratio and the thermal evolution of the mantle". In: *Earth and Planetary Science Letters* 287.3-4, pp. 513–518.

De Koker, Nico, Gerd Steinle-Neumann, and Vojtěch Vlček (2012). "Electrical resistivity and thermal conductivity of liquid Fe alloys at high P and T, and heat flux in Earth's core". In: *Proceedings of the National Academy of Sciences of the United States of America* 109.11, pp. 4070–4073.

Driscoll, P. and D. Bercovici (2014). "On the thermal and magnetic histories of Earth and Venus: Influences of melting, radioactivity, and conductivity". In: *Physics of the Earth and Planetary Interiors* 236, pp. 36–51.

Du, Zhixue, Asmaa Boujibar, Peter Driscoll, and Yingwei Fei (2019). "Experimental Constraints on an MgO Exsolution-Driven Geodynamo". In: *Geophysical Research Letters* 46.13, pp. 7379–7385.

Dumberry, Mathieu and Attilio Rivoldini (2015). "Mercury's inner core size and core-crystallization regime". In: *Icarus* 248, pp. 254–268.

Dziewonski, Adam M. and Don L. Anderson (1981). "Preliminary reference Earth model". In: *Physics of the Earth and Planetary Interiors* 25.4, pp. 297–356.

Encyclopedia of Geomagnetism and Paleomagnetism (2007).

Fearn, David R. and David E. Loper (1981). "Compositional convection and stratification of Earth's core". In: *Nature* 289.5796, pp. 393–394.

Fischer, Rebecca A., Yoichi Nakajima, Andrew J. Campbell, Daniel J. Frost, Dennis Harries, Falko Langenhorst, Nobuyoshi Miyajima, Kilian Pollok, and David C. Rubie (2015). "High pressure metal-silicate partitioning of Ni, Co, V, Cr, Si, and O". In: *Geochimica et Cosmochimica Acta* 167, pp. 177–194.

Fleury, M., M. Mory, E. J. Hopfinger, and D. Auchere (1991). "Effects of rotation on turbulent mixing across a density interface". In: *Journal of Fluid Mechanics* 223, pp. 165–191.

Frost, D. J., U. Mann, Y. Asahara, and D. C. Rubie (2008). "The redox state of the mantle during and just after core formation". In: *Philosophical Transactions of the Royal Society A: Mathematical, Physical and Engineering Sciences* 366.1883, pp. 4315–4337.

Frost, Daniel J., Yuki Asahara, David C. Rubie, Nobuyoshi Miyajima, Leonid S. Dubrovinsky, Christian Holzapfel, Eiji Ohtani, Masaaki Miyahara, and Takeshi Sakai (2010). "Partitioning of oxygen between the Earth's mantle and core". In: *Journal of Geophysical Research: Solid Earth* 115.2.

Fu, Roger R., Benjamin P. Weiss, Eduardo A. Lima, Pauli Kehayias, Jefferson F.D.F. Araujo, David R. Glenn, Jeff Gelb, Joshua F. Einsle, Ann M. Bauer, Richard J. Harrison, Guleed A.H. Ali, and Ronald L. Walsworth (2017). "Evaluating the paleomagnetic potential of single zircon crystals using the Bishop Tuff". In: *Earth and Planetary Science Letters*.

Garaud, Pascale (2018). "Double-Diffusive Convection at Low Prandtl Number". In: *Annual Review of Fluid Mechanics* 50.1, pp. 275–298.

Garnero, Edward J., Donald V. Helmberger, and Stephen P. Grand (1993). "Constraining outermost core velocity with SmKS waves". In: *Geophysical Research Letters* 20.22, pp. 2463–2466.

Gillet, Nicolas, Dominique Jault, Elisabeth Canet, and Alexandre Fournier (2010). "Fast torsional waves and strong magnetic field within the Earthg's core". In: *Nature*.

Gomi, Hitoshi, Kenji Ohta, Kei Hirose, Stéphane Labrosse, Razvan Caracas, Matthieu J. Verstraete, and John W. Hernlund (2013). "The high conductivity of iron and thermal evolution of the Earth's core". In: *Physics of the Earth and Planetary Interiors* 224, pp. 88–103.

Gubbins, D (1977). "Energetics of the Earth's core". In: *Journal of Geophysics-Zeitschrift f r Geophysik* 43.1, pp. 453–464.

Gubbins, D. and C. J. Davies (2013). "The stratified layer at the core-mantle boundary caused by barodiffusion of oxygen, sulphur and silicon". In: *Physics of the Earth and Planetary Interiors* 215, pp. 21–28.

Gubbins, D., T. G. Masters, and J. A. Jacobs (1979). "Thermal evolution of the Earth's core". In: *Geophysical Journal of the Royal Astronomical Society* 59.1, pp. 57–99.

Gubbins, D., C. J. Thomson, and K. A. Whaler (1982). "Stable regions in the Earth's liquid core". In: *Geophysical Journal of the Royal Astronomical Society* 68.1, pp. 241–251.

Gubbins, David (2001). "The Rayleigh number for convection in the Earth's core". In: *Physics of the Earth and Planetary Interiors*.

— (2007). "Geomagnetic constraints on stratification at the top of Earth's core". In: *Earth, Planets and Space* 59.7, pp. 661–664.

Gubbins, David, Dario Alfè, Chris Davies, and Monica Pozzo (2014). "On core convection and the geodynamo: Effects of high electrical and thermal conductivity". In: *Physics of the Earth and Planetary Interiors* 247, pp. 56–64.

Gubbins, David, Dario Alfè, Guy Masters, G. David Price, and M. J. Gillan (Nov. 2003). "Can the Earth's dynamo run on heat alone?" In: *Geophysical Journal International* 155.2, pp. 609–622.

Gubbins, David, Dario Alfè, Guy Masters, G. David Price, and Michael Gillan (June 2004). "Gross thermodynamics of two-component core convection". In: *Geophysical Journal International* 157.3, pp. 1407–1414.

Hardy, Colin M, Philip W Livermore, and Jitse Niesen (2020). "Enhanced magnetic fields within a stratified layer". In: *Geophysical Journal International*.

Helffrich, George and Satoshi Kaneshima (2010). "Outer-core compositional stratification from observed core wave speed profiles". In: *Nature* 468.7325, pp. 807–812.

— (2013). "Causes and consequences of outer core stratification". In: *Physics of the Earth and Planetary Interiors* 223, pp. 2–7.

Hewitt, J. M., D. P. McKenzie, and N. O. Weiss (1975). "Dissipative heating in convective flows". In: *Journal of Fluid Mechanics*.

Hirose, Kei, Stéphane Labrosse, and John Hernlund (2013). "Composition and State of the Core". In: *Annual Review of Earth and Planetary Sciences* 41.1, pp. 657–691.

Hirose, Kei, Guillaume Morard, Ryosuke Sinmyo, Koichio Umemoto, John Hernlund, George Helffrich, and Stéphane Labrosse (2017). "Crystallization of silicon dioxide and compositional evolution of the Earth's core". In: *Nature* 543.7643, pp. 99–102.

Hirst, I. L. and D. A. Carter (2002). "Another look at the core density deficit of Earth's outer core". In: *Physics of the Earth and Planetary Interiors* 131.1, pp. 19–27.

Holme, R. (2015). "Large-Scale Flow in the Core". In: *Treatise on Geophysics: Second Edition*. Vol. 8, pp. 91–113.

Ichikawa, Hiroki and Taku Tsuchiya (2014). "Atomic transport property of Fe-O liquid alloys in the Earth's outer core P, T condition". In: *Physics of the Earth and Planetary Interiors* 247, pp. 27–35.

Irving, Jessica C.E., Sanne Cottaar, and Vedran Lekic (2018). "Seismically determined elastic parameters for Earth's outer core". In: *Science Advances* 4.6.

Jackson, A. and C. Finlay (2015). "Geomagnetic Secular Variation and Its Applications to the Core". In: *Treatise on Geophysics: Second Edition*.

Jackson, Andrew, Art R.T. Jonkers, and Matthew R. Walker (2000). "Four centuries of geomagnetic secular variation from historical records". In: *Philosophical Transactions of the Royal Society A: Mathematical, Physical and Engineering Sciences* 358.1768, pp. 957–990.

Jacobson, Seth A., David C. Rubie, John Hernlund, Alessandro Morbidelli, and Miki Nakajima (2017). "Formation, stratification, and mixing of the cores of Earth and Venus". In: *Earth and Planetary Science Letters* 474, pp. 375–386.

Jones, C. A. (2015). "Thermal and Compositional Convection in the Outer Core". In: *Treatise on Geophysics: Second Edition*. Vol. 8, pp. 115–159.

Kaneshima, Satoshi (2018). "Array analyses of SmKS waves and the stratification of Earth's outermost core". In: *Physics of the Earth and Planetary Interiors* 276, pp. 234–246.

Kaneshima, Satoshi and George Helffrich (2013). "Vp structure of the outermost core derived from analysing large-scale array data of SmKS waves". In: *Geophysical Journal International* 193.3, pp. 1537–1555.

Kelley, D. E., H. J.S. Fernando, A. E. Gargett, J. Tanny, and E. Özsoy (2003). *The diffusive regime of double-diffusive convection*.

Keszei, Ernö (2013). *Chemical thermodynamics: an introduction*. Springer Science & Business Media.

Knibbe, Jurriën Sebastiaan and Wim van Westrenen (2018). "The thermal evolution of Mercury's Fe–Si core". In: *Earth and Planetary Science Letters* 482, pp. 147–159.

Koelemeijer, P., J. Ritsema, A. Deuss, and H. J. van Heijst (2016). "SP12RTS: A degree-12 model of shear- and compressional-wave velocity for Earth's mantle". In: *Geophysical Journal International* 204.2, pp. 1024–1039.

Komabayashi, Tetsuya (2014). "Thermodynamics of melting relations in the system Fe-FeO at high pressure: Implications for oxygen in the Earth's core". In: *Journal of Geophysical Research: Solid Earth*.

Konôpková, Zuzana, R. Stewart McWilliams, Natalia Gómez-Pérez, and Alexander F. Goncharov (2016). "Direct measurement of thermal conductivity in solid iron at planetary core conditions". In: *Nature* 534.7605, pp. 99–101.

Korte, Monika, Catherine Constable, Fabio Donadini, and Richard Holme (2011). "Reconstructing the Holocene geomagnetic field". In: *Earth and Planetary Science Letters*.

Labrosse, Stéphane (2014). "Thermal evolution of the core with a high thermal conductivity". In: *Physics of the Earth and Planetary Interiors* 247, pp. 36–55.

Labrosse, Stéphane, Jean Paul Poirier, and Jean Louis Le Mouël (1997). "On cooling of the Earth's core". In: *Physics of the Earth and Planetary Interiors* 99.1-2, pp. 1–17.

Laio, A. (2000). "Physics of iron at earth's core conditions". In: *Science*.

Landau, L. D. and E. M. Lifshitz (1987). *Fluid mechanics: Landau and Lifshitz: course of theoretical physics*.

Landeau, Maylis, Peter Olson, Renaud Deguen, and Benjamin H. Hirsh (2016). "Core merging and stratification following giant impact". In: *Nature Geoscience* 9.10, pp. 786–789.

Laneuville, M., M. A. Wieczorek, D. Breuer, J. Aubert, G. Morard, and T. Rückriemen (2014). "A long-lived lunar dynamo powered by core crystallization". In: *Earth and Planetary Science Letters* 401, pp. 251–260.

Larmor, Joseph (1919). "How could a rotating body such as the Sun become a magnet". In: *Rep. Brit. Adv. Sci.*, pp. 159–160.

Lay, Thome and Christopher J. Young (1990). "The stably-stratified outermost core revisited". In: *Geophysical Research Letters* 17.11, pp. 2001–2004.

Lay, Thorne, John Hernlund, and Bruce A. Buffett (2008). "Core-mantle boundary heat flow". In: *Nature Geoscience* 1.1, pp. 25–32.

Lesur, V., K. Whaler, and I. Wardinski (2015). "Are geomagnetic data consistent with stably stratified flow at the core–mantle boundary?" In: *Geophysical Journal International* 201.2, pp. 929–946.

Levy, M. A. and H. J.S. Fernando (2002). "Turbulent thermal convection in a rotating stratified fluid". In: *Journal of Fluid Mechanics* 467, pp. 19–40.

Li, Yunguo, Lidunka Vočadlo, Tao Sun, and John P. Brodholt (2020). "The Earth's core as a reservoir of water". In: *Nature Geoscience*.

Lister, John R. (1995). "On Penetrative Convection at Low Péclet Number". In: *Journal of Fluid Mechanics* 292, pp. 229–248.

Lister, John R. and Bruce A. Buffett (1998). "Stratification of the outer core at the core-mantle boundary". In: *Physics of the Earth and Planetary Interiors* 105.1-2, pp. 5–19.

Loper, David E. (1978). "The gravitationally powered dynamo". In: *Geophysical Journal of the Royal Astronomical Society* 54.2, pp. 389–404.

Lui, A. T. Y. (1996). "Current disruption in the Earth's magnetosphere: Observations and models". In: *Journal of Geophysical Research: Space Physics*.

Manglik, Ajay, Johannes Wicht, and Ulrich R. Christensen (Jan. 2010). "A dynamo model with double diffusive convection for Mercury's core". In: *Earth and Planetary Science Letters* 289.3-4, pp. 619–628.

Martorell, Benjamí, John Brodholt, Ian G. Wood, and Lidunka Vočadlo (2013). "The effect of nickel on the properties of iron at the conditions of Earth's inner core: Ab initio calculations of seismic wave velocities of Fe-Ni alloys". In: *Earth and Planetary Science Letters* 365, pp. 143–151.

Masters, Guy and David Gubbins (2003). "On the resolution of density within the Earth". In: *Physics of the Earth and Planetary Interiors* 140.1-3, pp. 159–167.

Matyska, Ctirad and David A. Yuen (2002). "Bullen's parameter η: A link between seismology and geodynamical modelling". In: *Earth and Planetary Science Letters* 198.3-4, pp. 471–483.

McDonough, W. F. and S. s. Sun (1995). “The composition of the Earth”. In: *Chemical Geology* 120.3-4, pp. 223–253.

Metman, Maurits C., Philip W. Livermore, Jonathan E. Mound, and Ciarán D. Beggan (2019). “Modelling decadal secular variation with only magnetic diffusion”. In: *Geophysical Journal International*.

Mittal, Tushar, Nicholas Knezek, Sarah M. Arveson, Chris P. McGuire, Curtis D. Williams, Timothy D. Jones, and Jie Li (2020). “Precipitation of multiple light elements to power Earth’s early dynamo”. In: *Earth and Planetary Science Letters* 532.

Moffatt, H. K. and D. E. Loper (1994). “The Magnetostrophic Rise of A Buoyant Parcel In the Earth’s Core”. In: *Geophysical Journal International* 117.2, pp. 394–402.

Morard, Guillaume, Denis Andrault, Daniele Antonangeli, and Johann Bouchet (2014). “Properties of iron alloys under the earth’s core conditions”. In: *Comptes Rendus - Geoscience* 346.5-6, pp. 130–139.

Mound, Jon, Chris Davies, Sebastian Rost, and Jon Aurnou (2019). “Regional stratification at the top of Earth’s core due to core–mantle boundary heat flux variations”. In: *Nature Geoscience*.

Nakagawa, Takashi (2018). “On the thermo-chemical origin of the stratified region at the top of the Earth’s core”. In: *Physics of the Earth and Planetary Interiors* 276, pp. 172–181.

Nakagawa, Takashi and Paul J. Tackley (2010). “Influence of initial CMB temperature and other parameters on the thermal evolution of Earth’s core resulting from thermochemical spherical mantle convection”. In: *Geochemistry, Geophysics, Geosystems* 11.6.

— (2015). “Influence of plate tectonic mode on the coupled thermochemical evolution of Earth’s mantle and core”. In: *Geochemistry, Geophysics, Geosystems* 16.10, pp. 3400–3413.

Nakajima, Miki and David J. Stevenson (2015). “Melting and mixing states of the Earth’s mantle after the Moon-forming impact”. In: *Earth and Planetary Science Letters* 427, pp. 286–295.

Nguyen, Jeffrey H. and Neil C. Holmes (2004). “Melting of iron at the physical conditions of the Earth’s core”. In: *Nature* 427.6972, pp. 339–342.

Nimmo, F. (2015). “Energetics of the Core”. In: *Treatise on Geophysics: Second Edition*. Vol. 8, pp. 27–55.

Nimmo, F., G. D. Price, J. Brodholt, and D. Gubbins (2004). “The influence of potassium on core and geodynamo evolution”. In: *Geophysical Journal International* 156.2, pp. 363–376.

Nimmo, Francis (2002). “Why does Venus lack a magnetic field?” In: *Geology* 30.11, pp. 987–990.

O'Brien, David P., Alessandro Morbidelli, and Harold F. Levison (2006). "Terrestrial planet formation with strong dynamical friction". In: *Icarus* 184.1, pp. 39–58.

O'Rourke, Joseph G., Jun Korenaga, and David J. Stevenson (2017). "Thermal evolution of Earth with magnesium precipitation in the core". In: *Earth and Planetary Science Letters* 458, pp. 263–272.

O'Rourke, Joseph G. and David J. Stevenson (2016). "Powering Earth's dynamo with magnesium precipitation from the core". In: *Nature* 529.7586, pp. 387–389.

Oldham, Richard Dixon (1906). "The constitution of the interior of the earth, as revealed by earthquakes". In: *Quarterly Journal of the Geological Society of London* 62.1-4, pp. 456–475.

Panovska, S., M. Korte, and C. G. Constable (2019). *One Hundred Thousand Years of Geomagnetic Field Evolution.*

Patočka, V., O. Šrámek, and N. Tosi (2020). "Minimum heat flow from the core and thermal evolution of the Earth". In: *Physics of the Earth and Planetary Interiors* 305, p. 106457.

Poirier, J.-P. and T J Shankland (1993). "Dislocation melting of iron and the temperature of the inner core boundary, revisited". In: *Geophysical Journal International* 115.1, pp. 147–151.

Poirier, Jean Paul (1994). "Light elements in the Earth's outer core: A critical review". In: *Physics of the Earth and Planetary Interiors* 85.3-4, pp. 319–337.

Posner, Esther S., David C. Rubie, Daniel J. Frost, and Gerd Steinle-Neumann (2017). "Experimental determination of oxygen diffusion in liquid iron at high pressure". In: *Earth and Planetary Science Letters* 464, pp. 116–123.

Pourovskii, L. V., J. Mravlje, A. Georges, S. I. Simak, and I. A. Abrikosov (2017). "Electron-electron scattering and thermal conductivity of -iron at Earth's core conditions". In: *New Journal of Physics.*

Pozzo, Monica, Chris Davies, David Gubbins, and Dario Alfè (2012). "Thermal and electrical conductivity of iron at Earth's core conditions". In: *Nature* 485.7398, pp. 355–358.

— (2013). "Transport properties for liquid silicon-oxygen-iron mixtures at Earth's core conditions". In: *Physical Review B - Condensed Matter and Materials Physics* 87.1.

— (2019). "FeO Content of Earth's Liquid Core". In: *Physical Review X* 9.4.

Radko, Timour (2012). *Double-diffusive convection.*

Roberts, P. H. and S. Scott (1965). "On analysis of the secular variation 1. A hydromagnetic constraint : Theory". In: *Journal of geomagnetism and geoelectricity.*

Roberts, Paul H. and Gary A. Glatzmaier (Oct. 2000). "Geodynamo theory and simulations". In: *Reviews of Modern Physics* 72.4, pp. 1081–1123.

Rost, Sebastian, Edward J. Garnero, and Quentin Wiliams (2006). "Fine-scale ultralow-velocity zone structure from high-frequency seismic array data". In: *Journal of Geophysical Research: Solid Earth* 111.9.

Rubie, David C., Daniel J. Frost, Ute Mann, Yuki Asahara, Francis Nimmo, Kyusei Tsuno, Philip Kegler, Astrid Holzheid, and Herbert Palme (2011). "Heterogeneous accretion, composition and core-mantle differentiation of the Earth". In: *Earth and Planetary Science Letters* 301.1-2, pp. 31–42.

Rückriemen, T., D. Breuer, and T. Spohn (2015). "The Fe snow regime in Ganymede's core: A deep-seated dynamo below a stable snow zone". In: *Journal of Geophysical Research E: Planets* 120.6, pp. 1095–1118.

Schaeffer, N., D. Jault, H. C. Nataf, and A. Fournier (2017). "Turbulent geodynamo simulations: A leap towards Earth's core". In: *Geophysical Journal International*.

Shanker, J., B. P. Singh, and S. K. Srivastava (2004). "Volume-temperature relationship for iron at 330 GPa and the Earth's core density deficit". In: *Physics of the Earth and Planetary Interiors* 147.4, pp. 333–341.

Shearer, P. and G. Masters (1990). "The density and shear velocity contrast at the inner core boundary". In: *Geophysical Journal International*.

Sinmyo, Ryosuke, Kei Hirose, and Yasuo Ohishi (2019). "Melting curve of iron to 290 GPa determined in a resistance-heated diamond-anvil cell". In: *Earth and Planetary Science Letters*.

Souriau, Annie and Georges Poupinet (1991). "The velocity profile at the base of the liquid core from PKP(BC+Cdiff) data: An argument in favour of radial inhomogeneity". In: *Geophysical Research Letters* 18.11, pp. 2023–2026.

Stacey, F. D. and D. E. Loper (2007). "A revised estimate of the conductivity of iron alloy at high pressure and implications for the core energy balance". In: *Physics of the Earth and Planetary Interiors* 161.1-2, pp. 13–18.

Stacey, Frank D (2010). "Thermodynamics of the Earth". In: *Reports on Progress in Physics* 73.4, p. 46801.

Stevenson, D. J. (Jan. 1987). "Limits on lateral density and velocity variations in the Earth's outer core". In: *Geophysical Journal of the Royal Astronomical Society* 88.1, pp. 311–319.

— (2001). "Mars' core and magnetism". In: *Nature* 412.6843, pp. 214–219.

Takehiro, Shin ichi and John R. Lister (2001). "Penetration of columnar convection into an outer stably stratified layer in rapidly rotating spherical fluid shells". In: *Earth and Planetary Science Letters* 187.3-4, pp. 357–366.

Tanaka, Satoru (2007). "Possibility of a low P-wave velocity layer in the outermost core from global SmKS waveforms". In: *Earth and Planetary Science Letters* 259.3-4, pp. 486–499.

Tarduno, John A., Rory D. Cottrell, William J. Davis, Francis Nimmo, and Richard K. Bono (2015). "A Hadean to Paleoarchean geodynamo recorded by single zircon crystals". In: *Science* 349.6247, pp. 521–524.

Tarduno, John A., Rory D. Cottrell, Michael K. Watkeys, Axel Hofmann, Pavel V. Doubrovine, Eric E. Mamajek, Dunji Liu, David G. Sibeck, Levi P. Neukirch, and

Yoichi Usui (Mar. 2010). “Geodynamo, solar wind, and magnetopause 3.4 to 3.45 billion years ago”. In: *Science* 327.5970, pp. 1238–1240.

Tateno, Shigehiko, Kei Hirose, Yasuo Ohishi, and Yoshiyuki Tatsumi (2010). “The structure of iron in earth’s inner core”. In: *Science*.

Tauxe, Lisa (2010). *Essentials of paleomagnetism*. Univ of California Press.

Thébault, Erwan, Christopher C. Finlay, Ciarán D. Beggan, Patrick Alken, Julien Aubert, Olivier Barrois, Francois Bertrand, Tatiana Bondar, Axel Boness, Laura Brocco, Elisabeth Canet, Aude Chambodut, Arnaud Chulliat, Pierdavide Coïsson, François Civet, Aimin Du, Alexandre Fournier, Isabelle Fratter, Nicolas Gillet, Brian Hamilton, Mohamed Hamoudi, Gauthier Hulot, Thomas Jager, Monika Korte, Weijia Kuang, Xavier Lalanne, Benoit Langlais, Jean Michel Léger, Vincent Lesur, Frank J. Lowes, Susan Macmillan, Mioara Mandea, Chandrasekharan Manoj, Stefan Maus, Nils Olsen, Valeriy Petrov, Victoria Ridley, Martin Rother, Terence J. Sabaka, Diana Saturnino, Reyko Schachtschneider, Olivier Sirol, Andrew Tangborn, Alan Thomson, Lars Tøffner-Clausen, Pierre Vigneron, Ingo Wardinski, and Tatiana Zvereva (2015). “International geomagnetic reference field: The 12th generation international geomagnetic reference field - The twelfth generation”. In: *Earth, Planets and Space* 67.1.

Tilgner, A. (2005). “Precession driven dynamos”. In: *Physics of Fluids*.

— (2007). “Rotational Dynamics of the Core”. In: *Treatise on Geophysics*.

Turner, J S (1974). “Double-Diffusive Phenomena”. In: *Annual Review of Fluid Mechanics*.

— (1979). *Buoyancy effects in fluids*. Cambridge university press.

Umemoto, Koichiro and Kei Hirose (2020). “Chemical compositions of the outer core examined by first principles calculations”. In: *Earth and Planetary Science Letters* 531.

Valley, John W., Aaron J. Cavosie, Takayuki Ushikubo, David A. Reinhard, Daniel F. Lawrence, David J. Larson, Peter H. Clifton, Thomas F. Kelly, Simon A. Wilde, Desmond E. Moser, and Michael J. Spicuzza (2014). “Hadean age for a post-magma-ocean zircon confirmed by atom-probe tomography”. In: *Nature Geoscience*.

Walter, Michael J. and Reidar G. Trønnes (2004). “Early earth differentiation”. In: *Earth and Planetary Science Letters* 225.3-4, pp. 253–269.

Whaler, K. A. (1980). “Does the whole of the earth’s core convect?” In: *Nature* 287.5782, pp. 528–530.

— (1986). “Geomagnetic evidence for fluid upwelling at the core-mantle boundary”. In: *Geophysical Journal of the Royal Astronomical Society*.

Wicht, J. and A. Tilgner (2010). “Theory and modeling of planetary dynamos”. In: *Space Science Reviews* 152.1-4, pp. 501–542.

Williams, John Pierre and Francis Nimmo (2004). “Thermal evolution of the Martian core: Implications for an early dynamo”. In: *Geology* 32.2, pp. 97–100.

Xiong, Zhihua, Taku Tsuchiya, and Takashi Taniuchi (2018). "Ab Initio Prediction of Potassium Partitioning Into Earth's Core". In: *Journal of Geophysical Research: Solid Earth* 123.8, pp. 6451–6458.

Xu, Junqing, Peng Zhang, K. Haule, Jan Minar, Sebastian Wimmer, Hubert Ebert, and R. E. Cohen (2018). "Thermal Conductivity and Electrical Resistivity of Solid Iron at Earth's Core Conditions from First Principles". In: *Physical Review Letters*.

Zhang, Nan and Shijie Zhong (2011). "Heat fluxes at the Earth's surface and core-mantle boundary since Pangea formation and their implications for the geomagnetic superchrons". In: *Earth and Planetary Science Letters* 306.3-4, pp. 205–216.

Ziegler, L. B., C. G. Constable, C. L. Johnson, and L. Tauxe (2011). "PADM2M: A penalized maximum likelihood model of the 0-2 Ma palaeomagnetic axial dipole moment". In: *Geophysical Journal International*.

Ziegler, L. B. and D. R. Stegman (2013). "Implications of a long-lived basal magma ocean in generating Earth's ancient magnetic field". In: *Geochemistry, Geophysics, Geosystems* 14.11, pp. 4735–4742.

Appendices

Appendix A

Chemical instability in a thermal layer

In chapter 2, section 2.7.1 the numerical method for evolving a thermally stratified layer was given. It was noted that the chemistry of the layer was omitted due to numerical difficulties, which are outlined here.

In the presence of a sub-adiabatic heat flow, the thermal profile within the layer is elevated above the adiabatic temperature which grows downwards by diffusion. The thermal gradient at the CMB is controlled by the imposed CMB heat flux, whilst the thermal gradient at the interface is controlled by a stability criteria. In the absence of any chemical gradient, the condition for neutral stability is simply

$$\frac{\partial T}{\partial r} = \frac{\partial T_{\mathrm{a}}}{\partial r}. \tag{A.1}$$

I included the impacts of entrainment into this stability criterion by supposing that the thermal gradient at the base of the layer is represented by the required thermal gradient to be sufficiently stabilising so as to resist dynamical mixing, given by

$$\frac{\partial T}{\partial r} = (1 - E)\frac{\partial T_{\mathrm{a}}}{\partial r}, \tag{A.2}$$

where E is a dimensionless entrainment coefficient. Larger values of E required the fluid be more strongly stabilising in order to resist mixing and reduces the upwards flux of heat due to anomalously hot fluid from the base of the layer being entrained away.

In the presence of a destabilising chemical gradient, the neutral stability condition

(Eq. A.1) becomes

$$\frac{\partial T}{\partial r} = \frac{\partial T_{\mathrm{a}}}{\partial r} - \frac{\alpha_c}{\alpha_T}\frac{\partial c}{\partial r}. \tag{A.3}$$

This is an analogous condition as was employed for the opposite scenario, when chemical gradients are stabilising and thermal gradients are destabilising, where the method of Buffett and Seagle (2010) gives the condition on the chemical gradient (Eq. 2.112, restated here)

$$\frac{\partial c}{\partial r} = -\frac{\alpha_T}{\alpha_c}\frac{\partial T}{\partial r} - \frac{\partial T_{\mathrm{a}}}{\partial r}, \tag{A.4}$$

In order to establish the required thermal gradient for neutral stability in A.3, the chemical gradient needs to be known. Whilst the inner core grows, the light element concentration in the underlying convective region increases and so as the layer grows, the fluid that is incorporated into the layer has a progressively larger light element concentration. Ignoring any diffusion, and considering that the light element is 'frozen' into the stable layer as it grows, the approximate form of the chemical profile within the layer is shown in figure A.1 (Labrosse et al. (1997) gives a similar analysis).

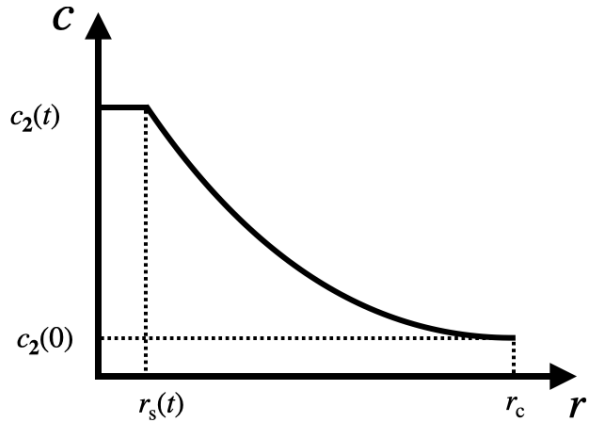

Figure A.1: Chemical profile throughout a thermally stratified layer that begins to grow from time 0 until time t, whilst the inner core is also growing. The light element mass fraction in the underlying convective region, $c_{\mathbf{2}}$, steadily increases over time due to inner core growth. This increasing light element fraction is captured by the growth of the stable layer down from the CMB.

In this scenario, the chemical gradient at r_{s} is dependent upon the rate of enrichment of $c_{\mathbf{2}}$ and the rate of advancement of the layer interface

$$\frac{\partial c}{\partial r} = \frac{\mathrm{d}c_{\mathbf{2}}}{\mathrm{d}t}\left(\frac{\mathrm{d}r_{\mathrm{s}}}{\mathrm{d}t}\right). \tag{A.5}$$

As the inner core grows $\mathrm{d}c_{\mathbf{2}}/\mathrm{d}t$ increases and the growth rate of the stable layer, being controlled by diffusion, slows over time since r_s is approximately $\propto \sqrt{t}$. These relations create the greatly increasing chemical gradient towards the base of the layer depicted in figure A.1. The required thermal gradient for stability at r_s therefore increases over time.

If equation A.3 is used as the lower boundary condition on the thermal diffusion solution, then progressively less heat is conducted into the layer and so, assuming the heat conducted out of the top of the layer into the mantle remains the same, the layer may start to cool more rapidly than the underlying convective region. In one timestep, if the temperature at the interface in the stable layer, $T_{\mathbf{3}}(r_\mathrm{s})$ is lower than the adiabatic temperature, $T_\mathrm{a}(r_\mathrm{s})$, then since the composition is continuous, the fluid in the stable layer would be more dense and would sink to mix with the convection, moving r_s upwards.

Diffusion of light element throughout the layer will act to smooth the chemical gradient, however mass diffusion is very slow at around 1000 times slower than thermal diffusion (e.g. Gubbins et al., 2004) and so will not act to vary the chemical profile much.

To demonstrate this effect I perform a calculation in which equation A.3 is used as the lower boundary condition to solve the diffusion of heat in the layer. In order to find the chemical gradient I solve the chemical diffusion equation to find $c_3(t+\Delta t)$ subject to a zero mass flux condition at the CMB and $c_{\mathbf{3}}(r_\mathrm{s}, t+\Delta t)$ is fixed to $c_{\mathbf{2}}(t+\Delta)t$. This condition of continuity of c at r_s is motivated by the previous argument that as the layer grows, chemical enriched fluid is incorporated into the stable layer. This produces a profile similar to figure A.1 which gives the chemical gradient in A.3. The thermal diffusion solution is then calculated subject to the thermal gradient in A.3 at r_s and the thermal gradient given the the CMB heat flow at r_c. Q_c is chosen to be a fixed sub-adiabatic value, 10 TW, and core properties for a value of $\Delta\rho = 800$ kg m^{-3} are used (tables 2.1 and 2.2). The temperature of the core is chosen such that T_cen is just above the melting temperature at the center of the core in order for the inner core to start growing at the beginning of the simulation. The results for just the first 100 iterations of the calculation are shown on figure A.2.

The sawtooth like pattern in the layer size (Fig. A.2, top) results from the thermal layer initially growing until the chemical gradient becomes too large, resulting in a low heat flux into the layer and the fluid at r_s becomes too dense and is mixed away. When the layer has either been entirely eroded away, the layer beins to regrow out of 'fresh' fluid with no initial chemical gradient and the process repeats. Over time the amplitude if size the layer reaches decreases as $\mathrm{d}c_{\mathbf{2}}/\mathrm{d}t$ increases over time, more rapidly causing the erosion of the layer. Also as the core cools over time, the imposed 10 TW

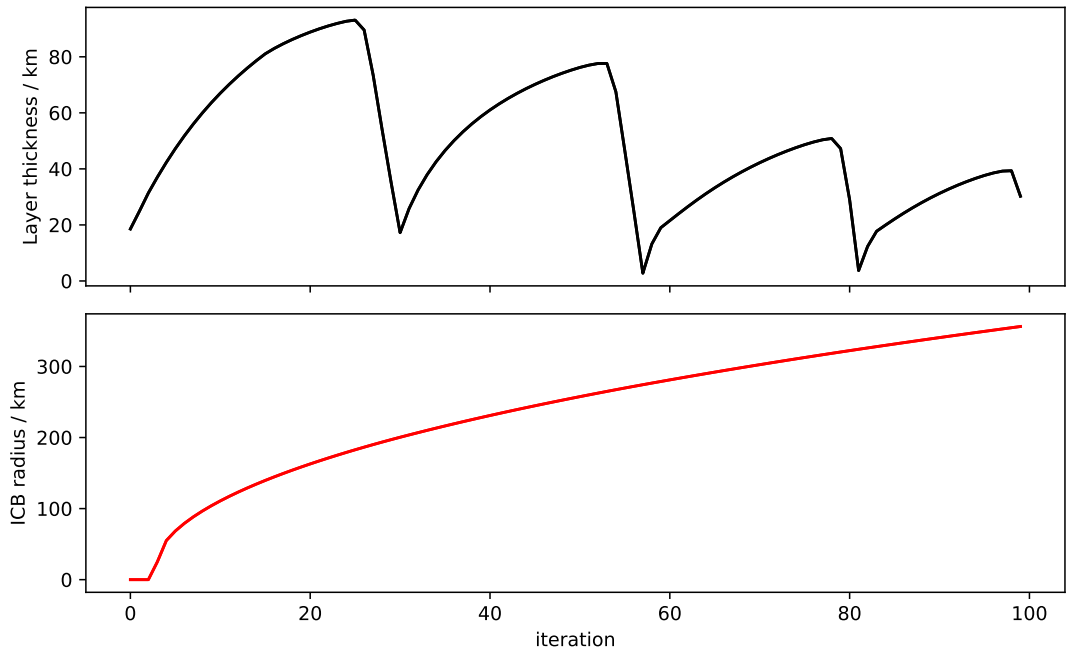

Figure A.2: First 100 iterations of the calculation described in the text with the time step is set to 0.5 Myrs. Top panel shows the layer size and the bottom panel shows the inner core radius.

at the CMB also begins to approach the adiabatic heat flow since $\nabla T_{\mathrm{a}} \propto T_{\mathrm{a}}$, reducing the extent to which the thermal layer will grow regardless of compositional effects.

Lister and Buffett (1998) use an alternative method to handle the chemistry of a thermal layer. They assumed that the double diffusive finger convection acts to uniformly mix the compositional field to uniform in the layer. This value is lower than in the underlying convective region giving a jump in c at r_{s} which they use to provide a condition on the temperature at T assuming that density is continuous at r_{s}, $\alpha_T(T_3 - T_2) + \alpha_c(c_3 - c_2) = 0$. Manglik et al. (2010) perform double diffusive convection for a thermally stratified Mercurian core, finding that finger convection can smooth out the compostiional field in the layer without disrupting it, however without a significant jump in composition between the two regions. Lister and Buffett (1998) do not quote a value for the jump in T/c at the interface and a lack of key numerical details inhibited me from recreating their model, so I cannot know precisely what values their model achieved.

An estimate can be found by making some simple assumptions. Lister and Buffett (1998) have a growing inner core for all 4.5 Gyrs and so assuming the inner core grows $\propto \sqrt{t}$, a good approximation (Buffett et al., 1996b), I can write

$$r_{\mathrm{i}}(t) = 1221 \text{ km} \sqrt{\frac{t}{4.5}}. \tag{A.6}$$

Lister and Buffett (1998) find a 400 km thick layer grows from time $t = 2$ Gyrs, again approximately $\propto \sqrt{t}$ giving

$$r_{\mathrm{s}} = \begin{cases} 3480 \text{ if } t \leq 2 \text{ Gyrs} \\ 3480 - \frac{400}{\sqrt{2.5}} \text{ if } t > 2 \text{ Gyrs} \end{cases} . \tag{A.7}$$

Assuming all light element is excluded from the inner core as it grows and that the core has a uniform density, then the rate of change of $c_{\mathbf{2}}$ is given by

$$\frac{\mathrm{d}c_{\mathbf{2}}}{\mathrm{d}t} = \frac{4\pi r_{\mathrm{i}}^2 \frac{\mathrm{d}r_{\mathrm{i}}}{\mathrm{d}t} \rho c}{\frac{4}{3}\pi(r_{\mathrm{s}}^3 - r_{\mathrm{i}}^3)\rho}. \tag{A.8}$$

Numerically integrating equation A.8 with an initial condition of $c_{\mathbf{2}} = 0.041$ at $t = 0$ gives the concentration in the convecting region as a function of time. Assuming that the light element is 'frozen' into the layer as it grows, allows a calculation of the chemical profile throughout the layer, figure A.3. If this light element were to evenly redistribute across the stable layer gives an integrated average value of 4.20 wt%, 0.13 wt% less than the convecting region at $t = 4.5$ Gyrs. The total change in light element mass fractino due to crystalisation of the whole core was around 0.2 wt%, consistent with thermal history models (e.g. Davies et al., 2015). This jump in composition gives a required jump in temperature of 130 K to ensure continuity of density (assuming $\alpha_c = 1$ and $\alpha_T = 10^{-5}$ K^{-1}). In the model of Lister and Buffett (1998) light element is incorporated into the stable layer in an equivalent manner, just that the integrated average is calculated at every time step.

In the core, temperature is continuous (Braginsky and Roberts, 1995), and so a jump of 130 K is a large deviation away from this condition. I decided I wanted to maintain continuity of temperature, however all methods have their pros and cons due to our current lack of understanding of these interfaces. The entrainment parameter in my model (Eq. A.2) could theoretically be used to represent the impact of a chemical gradient and so could relate to my results presented in chapter 3 for $E > 0$. The sawtooth behaviour in my model, could represent real physical behaviour since the cause is readily identified and might be interesting to delve into deeper, although I experienced some unsatisfactory spurious behaviour is some cases. I conceded to instead focus upon pure thermal stratification for the purpose of this study and leave a more detailed study into the complex interplay between temperature and chemistry within the layer for future work.

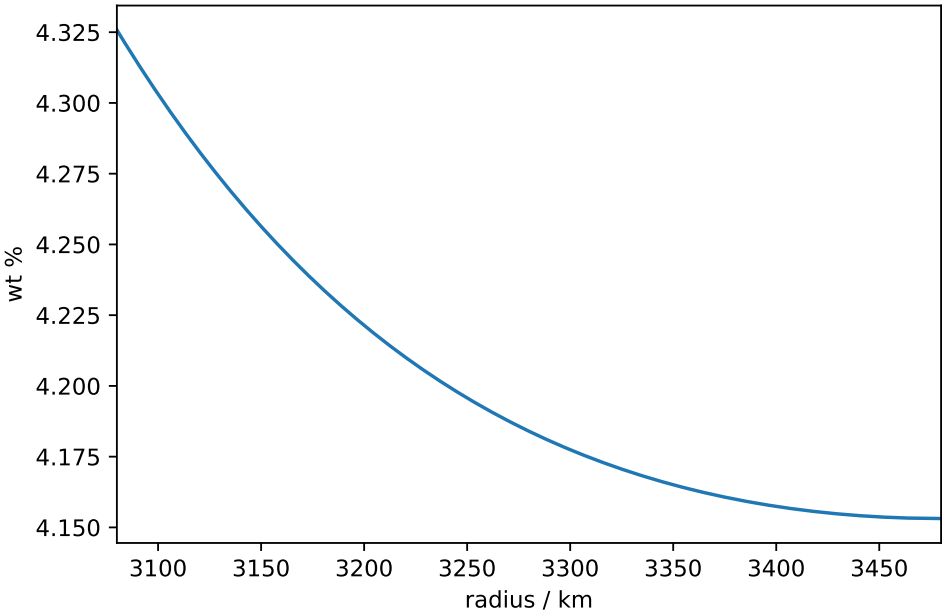

Figure A.3: Chemical profile through the thermal layer at $t = 4.5$ Gyrs.